ABSTRACT

Title of Dissertation: ELECTROSTATIC MEMS ACTUATORS USING GRAY-SCALE TECHNOLOGY

Brian Carl Morgan, Doctor of Philosophy, 2006

Dissertation directed by: Professor Reza Ghodssi
Department of Electrical and Computer Engineering
Institute for Systems Research

The majority of fabrication techniques used in micro-electro-mechanical systems (MEMS) are planar technologies, which severely limits the structures available during device design. In contrast, the emerging *gray-scale technology* is an attractive option for batch fabricating 3-D structures in silicon using a single lithography and etching step. While gray-scale technology is extremely versatile, limited research has been done regarding the integration of this technology with other MEMS processes and devices.

This work begins with the development of a fundamental empirical model for predicting and designing complex 3-D photoresist structures using a pixilated gray-scale technique. A characterization of the subsequent transfer of such 3-D structures into silicon using deep reactive ion etching (DRIE) is also provided. Two advanced gray-scale techniques are then introduced: First, a *double exposure* technique was developed to exponentially increase the number of available gray-levels; improving the vertical resolution in photoresist. Second, a design method dubbed *compensated aspect ratio*

dependent etching (CARDE) was created to anticipate feature dependent etch rates observed during gray-scale pattern transfer using deep reactive ion etching (DRIE).

The developed gray-scale techniques were used to integrate variable-height components into the actuation mechanism of electrostatic MEMS devices for the first time. In static comb-drives, devices with 3-D comb-fingers were able to demonstrate >34% improvement in displacement resolution by tailoring their force-engagement characteristics. Lower driving voltages were achieved by reducing suspension heights to decrease spring constants (from 7.7N/m to 2.3N/m) without effecting comb-drive force. Variable-height comb-fingers also enabled the development of compact, voltage-controlled electrostatic springs for tuning MEMS resonators. Devices in the low-kHz range demonstrated resonant frequency tuning >17.1% and electrostatic spring constants up to 1.19 N/m (@70V).

This experience of integrating 3-D structures within electrostatic actuators culminated in the development of a novel 2-axis optical fiber alignment system using 3-D actuators. Coupled in-plane motion of electrostatic actuators with integrated 3-D wedges was used to deflect an optical fiber both horizontally and vertically. Devices demonstrated switching speeds <1ms, actuation ranges >35μm (in both directions), and alignment resolution <1.25μm. Auto-alignment to fixed indium-phosphide waveguides with <1.6μm resolution in <10 seconds was achieved by optimizing search algorithms.

ELECTROSTATIC MEMS ACTUATORS USING GRAY-SCALE TECHNOLOGY

by

Brian Carl Morgan

Dissertation submitted to the Faculty of the Graduate School of the
University of Maryland, College Park, in partial fulfillment
of the requirements for the degree of
Doctor of Philosophy
2006

Advisory Committee:
Professor Reza Ghodssi, Chair
Professor John Melngailis
Professor Thomas Murphy
Professor Gottleib Oehrlein
Professor Gary Rubloff

Dedication

To the Morgan's: Richard, Tina, Kelly, Wayne, and my wife Susan.

Acknowledgements

While I am the one receiving a degree, the accomplishments in this dissertation would not be possible without significant contributions from my colleagues, friends, and family.

I would like to thank my advisor, Professor Reza Ghodssi for his guidance and support over the past 4 ½ years, as well as my Dissertation Defense Committee, Professor John Melngailis, Professor Tom Murphy, Professor Gottlieb Oehrlein, and Professor Gary Rubloff. Generous financial support was provided to me through a U.S. Army Research Laboratory Fellowship and two fellowships from the Achievement Rewards for College Scientists (ARCS) Metropolitan Washington Chapter – a wonderful organization of women who have supported the graduate research of U.S. citizens for almost 50 years.

I was fortunate to collaborate with numerous talented people throughout my research at UMD. From the Collaborative Technology Alliance (CTA), I would like to acknowledge Dr. Mark Allen (Georgia Tech), Dr. David Veazie (Clark Atlanta), Dr. Stuart Jacobsen (MIT), and Dr. Allan Epstein. From a collaboration with Toshiba Corporation, I would like to recognize Mr. Taizo Tomioka (Toshiba), Mr. Tomohiro Iguchi (Toshiba), Dr. Gottlieb Oehrlein (UMD), and Dr. Xuefeng Hua (UMD). Finally, through a long collaboration with the NASA-Goddard Space Flight Center I have had the opportunity to work with a tremendous team led by Dr. John Krizmanic and Dr. Robert Streitmatter.

I would like to express my gratitude to numerous members of the U.S. Army Research Laboratory for graciously allowing me to conduct a large part of my research within their facility. Specifically, Mr. Madan Dubey, Dr. Eugene Zakar, and Ms. Teresa Kipp were instrumental in establishing my initial internship at ARL, while Mr. John Hopkins and Mr. Bruce Geil continued support of my work in the years beyond. A big thank you also goes to ARL cleanroom manager Dr. Brett Piekarski and his staff for keeping all that critical equipment running. I must also extend a thank you to the Laboratory for Physical Sciences for allowing me extensive use of their cleanroom, specifically cleanroom manager Mr. Toby Olver and stepper guru Mr. Steve Brown

I would like to thank the current and past members of the MEMS Sensors and Actuators lab for many useful discussions and occasional comic relief. Specifically, Mr. Mike Waits served as an excellent mentor early on in my graduate career, and my office-mate Mr. Nima Ghalichechian helped me stay sane throughout the marathon of graduate school. I also appreciate the great patience and care demonstrated by Mr. Stephan Koev when reviewing this manuscript.

Finally, I am extremely grateful to my family and friends for their unending support, especially my wife Susan who had to put up with me throughout graduate school.

To those listed above and to those whom I may have forgotten: Thank You.

Sincerely,

Brian Carl Morgan
August 2006

Table of Contents

List of Tables

List of Figures

CHAPTER 1: INTRODUCTION

1.1. Introduction

The role of technology in today's society is ever present. From iPod's to cell phones to the internet, technology is continually transforming the global landscape. As this trend continues, the push for smaller, faster, cheaper, components continually challenges engineers at all levels of product development. These challenges often go beyond cramming more transistors on a chip, towards integrating multiple technologies into a single package for overall system density. It is here that the area of microelectromechanical systems (MEMS) becomes quite attractive, whereby lithography, deposition, and etching techniques used in the microelectronics industry are exploited to create complex structures and systems at the micro-scale.

Some commercial MEMS products have recently seen success, with Analog Devices shipping over 200 million MEMS accelerometers[*], and Texas Instruments introducing Digital Light Processing (DLP) chips for projection displays. However, the majority of fabrication techniques used in the integrated circuit (IC) and MEMS industries are considered planar technologies. Simply put, the user defines the horizontal dimensions of a structure through a series of lithography steps, while subsequent processes, such as etching or deposition, define the structure vertical dimensions. The structures possible using such conventional fabrication technologies are extremely limited. Consequently, MEMS designers have typically limited themselves to structures/designs possible using the preferred fabrication technologies rather than designs capable of yielding the highest performance.

[*] As of 1/14/06 (http://www.analog.com/en/cat/0,2878,764,00.html)

Alternative fabrication techniques have been introduced over the years that are capable of creating complicated 3-D geometries. Yet previous research has often focused on creating stand-alone features for rapid prototyping and are rarely batch fabrication compatible (i.e. microstereolithography [1]), which negates many of the potential advantages for MEMS, such as high volume and low cost. In contrast, the emerging *gray-scale technology* is an attractive fabrication technique for producing 3-D structures in silicon using batch fabrication tools [2-17]. While gray-scale technology is extremely versatile (able to produce a variety of 3-D structures in a single lithography and etching step), limited work has been done regarding the integration of this technology with standard MEMS processes and specific devices. In addition, gray-scale technology relies heavily on deep reactive ion etching (DRIE), a relatively new technology (last 10 years) whose limits and applications are still being explored. The integration of such a 3-D fabrication technology with conventional fabrication techniques could not only improve upon existing devices, but also enable a class of MEMS actuators previously thought impossible or impractical.

This dissertation will focus on developing the emerging *gray-scale technology* to improve upon existing MEMS actuators and develop new actuation schemes for optoelectronics packaging. Consequently, the topics discussed in this dissertation will be broken into three primary categories: 3-D fabrication, in-plane MEMS actuators, and optical fiber alignment. First, newly developed gray-scale technology design and fabrication techniques will be described, with an emphasis on technology collaborations pursued as part of this work. Next, the developed techniques were used to integrate 3-D components into the actuation mechanism of electrostatic MEMS comb-drive actuators to

improve their resolution and provide tailored force-engagement profiles. This principle is subsequently extended to the development of tunable MEMS resonators that are more compact than corresponding devices fabricated with planar techniques. Finally, a novel device for aligning an optical fiber in 2-axes using 3-D shaped actuators is proposed, fabricated, and tested, as a platform towards the integrated packaging of optoelectronics components.

1.2. Summary of Thesis Accomplishments

The specific accomplishments of this research are as follows:

- **Gray-scale Technology Development**:

  Starting with my masters thesis work [18], a methodology for designing complex optical masks to create 3-D profiles in photoresist was developed. The subsequent pattern transfer of such structures into silicon via deep reactive ion etching (DRIE) was characterized, with a focus on etch selectivity. This work was extended to include novel design methods to alleviate two primary limitations within gray-scale technology: First, a *double exposure technique* was developed to exponentially increase the number of gray-levels available in photoresist and improve the vertical resolution in photoresist. Second, a design technique dubbed *compensated aspect ratio dependent etching (CARDE)* was created to anticipate feature dependent etch rates observed during gray-scale DRIE pattern transfer.

  The general utility of gray-scale technology for create complex static topographies was demonstrated through 3 technology collaborations:

  1. *Development of a variable span microcompressor (U.S. Army Research Laboratory and Massachusetts Institute of Technology)*

2. *Design and Fabrication of 3-D substrates for packaging of a MOSFET relay (Toshiba Corporation)*
3. *Design, Fabrication, and Testing of X-ray Phase Fresnel Lenses (NASA-Goddard Space Flight Center)*

- **Compact Tailored Electrostatic MEMS Comb-drives:**

Comb-drive actuators incorporating variable height gray-scale structures were designed, fabricated, and tested for the first time. Analytical and 3-D finite element analysis (FEA) methods were developed to establish a theoretical framework for analyzing improvements in resolution, range of operation, and deflection stability. Comb-drive actuators with reduced height suspensions were also demonstrated as a simple method to decrease suspension spring constants, and thus reduce driving voltages.

Testing of variable height comb-finger designs demonstrated >34% improvement in displacement resolution (from 344nm/V to 227nm/V), while reduced height suspensions exhibited a 70% decrease in spring constant (from 7.7 N/m to 2.3 N/m). The design and fabrication techniques developed for integrating gray-scale technology within an electrostatic MEMS actuator process help these devices serve as a platform for developing more complex 3-D shaped actuators.

- **Vertically Shaped Tunable MEMS Resonators**:

The work on vertically shaped comb-drive actuators was extended to create a new class of compact, tunable MEMS resonators. The traditional theoretical framework of voltage-controlled electrostatic springs was modified using a combination of 2-D and 3-D Finite Element Analysis (FEA), enabling tuning of the

resonant frequency both Up and Down in a compact layout not previously achieved. This framework can be adapted to use a new weighted, variable finger engagement design to minimize non-linear stiffness coefficients when driving the resonator with large amplitudes.

MEMS resonators in the low kHz range were designed, fabricated, and tested to demonstrate these configurations. Electrostatic springs as strong as 1.19 N/m (@70V) enabled tuning of the resonant frequency by up to 17.1%.

- **<u>On-Chip 2-axis Optical Fiber Alignment</u>**:

An on-chip 2-axis optical fiber alignment system using opposing wedges fabricated with gray-scale technology was created for the first time. Devices with various actuator layouts and gray-scale wedge designs were fabricated, assembled, and tested. An optical test station was developed and utilized to evaluate fiber displacement range and resolution for various configurations. New auto-alignment algorithms were developed and implemented to demonstrate the ability to align the optical fiber to a specific target, with particular emphasis on comparing overall alignment time and final resolution. Methods to evaluate Cartesian control and possible hysteresis effects of these actuators were also developed.

Switching speeds were measured to be consistently <1ms. Alignment times of <10sec to a fixed 2μm square indium phosphide (InP) waveguide with <1.6μm resolution were commonly achieved by optimizing search algorithms and parameters. Ultimately, MEMS aligners were able to achieve alignment ranges as large as 40μm (at fiber tip) in both the in-plane and out-of-plane directions, with alignment resolution of <1.25μm.

1.3. Literature Review:

The area of MEMS has evolved over the past 20 years, and as such, the three primary topics discussed in this thesis (3-D fabrication, in-plane MEMS actuators, and optical fiber alignment) have been investigated to various extents by other groups. The following sections will review the relevant work found in the literature regarding each of these topics.

1.3.1. 3-D Fabrication Techniques

While many 3-D fabrication techniques have been developed over the years, they can be broadly categorized as being either a serial unit process, where each unit is fabricated in a sequential fashion, or a batch fabrication process, where many devices can be fabricated at one time on a given wafer.

1.3.1.1. Serial Unit Processes

One of the most versatile 3-D fabrication techniques is that of microstereolithography [1, 19, 20], an extension of stereolithography techniques patented in 1986 [21] for rapid-prototyping. Microstereolithography uses the light-induced, spatially resolved polymerization of a liquid resin into a solid polymer. A sequence of deposition and exposure steps of a thin photosensitive polymer are used, where each exposure contains a 2-D pattern of the appropriate cross section of the desired structure. After all exposures are finished, a single development step removes the unexposed areas of polymer, leaving a 3-D polymer mold with virtually arbitrary shape.

The exposure system could be a set of photomasks with flood exposures, or a scanning technique using a rastered laser beam. To achieve sufficient vertical resolution at minimal cost, the laser technique has become far more prevalent, and structures with >1000 levels are common. Using a He-Cd laser (325nm), *Takagi et al* reported structures

as large as 20mm x 20mm x 20mm, with a minimum resolution of 5μm x 5μm x 3μm (x,y,z) [22]. However, such a scanning technique requires a long write time for each layer, particularly over large areas. In addition, one must repeatedly spread a liquid resin between exposures, slowing the process significantly. To this end, two-photon microstereolithography [23, 24] could be used where two-photon absorption is used to expose confined areas within a solid medium.

With the advent of high resolution projection displays, some groups have moved to 'integral microstereolithography', where a dynamic pattern generator can quickly expose an entire layer, and be reconfigured quickly. *Bertsch et al* successfully implemented a liquid crystal display (LCD) based system (260 x 260 pixels) capable of 90 layers per hour with 5μm x 5μm x 5μm resolution [19]. Yet, even as screen resolutions improve, there is an obvious trade-off between resolution and maximum structure size. This limitation notwithstanding, microstereolithography has already been used in RF MEMS applications to create a phase shifter [25], and can create intricate structures such as the fluidic connector shown in Figure 1.1.

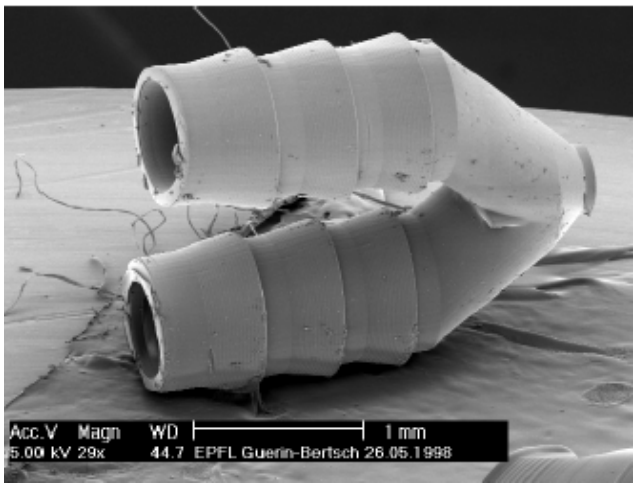

Figure 1.1: Fluidic connector fabricated using microstereolithography (Bertsch et al, *MEMS '98*).

Current microstereolithography research has been more focused on the use of ceramic composites, in order to open up the opportunity of manufacturing complex 3-D parts that can be sintered into pure alumina microcomponents [19]. However, some limitations of microstereolithography cannot be ignored, particularly in MEMS applications. First, regardless of advances in processing speed, it is inherently a slow process because only a single device is fabricated at one time, which cannot compare to large wafer throughput. Second, it is limited to polymer materials, limiting its integration with silicon microelectronic circuits, and preventing its use in many MEMS applications.

If one moves towards more silicon-friendly 3-D fabrication technologies, focused ion-beam (FIB) fabrication techniques are quite versatile [26-29]. FIB can provide localized maskless milling and deposition of both conductors and insulators with very high precision. *Khan-Malek et al* used this technique to fabricate 3-D diffractive optical elements (DOEs), demonstrating zone plates with 32nm outer rings [29]. While FIB enables 3-D structures in/on silicon with superior resolution, fabricating each structure is quite time consuming (hours), making them better candidates for low volume tasks such as photomask error correction.

1.3.1.2. Batch Fabrication

It is clear that for high volume manufacturing, any 3-D fabrication technique must be batch fabrication in some respect, and preferably compatible with the IC workhorse material, silicon, for later system integration. The crystallographic properties of various substrates (such as silicon) may enable angled features to be created using wet chemical etching (such as potassium hydroxide, for silicon), but flexibility in this angle cannot be accommodated. In some cases, simple stepped structures can be used to mimic a 3-D

profile, possibly using multiple embedded masking layers to create 3-4 levels in silicon with heights in the 10's to 100's of micrometers [30]. However, the goal of any technique should be the fabrication of nearly arbitrary angles, for maximum flexibility to be used in myriad applications.

Some research has been conducted utilizing inclined/rotated UV lithography [31, 32]. *Beuret et al* were able to use multiple integrated metal masks to create cones of exposed resist as the light source is rotated, resulting in angled structures in the photoresist [31]. Metal structures with angled sidewalls were then achieved by electroplating. While this technique can create conductive structures with small angles (<20º reported), it requires multiple integrated metallic masks that complicate processing significantly. Alternatively, *Han et al* used a negative thick photoresist (SU-8), which was exposed using multiple inclined and/or rotated exposures, and reported angles in resist up to 39º [32]. However, the author's technique results in polymer 3-D structures, with no discernable way to transfer this process into the underlying silicon, severely inhibiting its use in many applications.

In silicon, *Pham et al* have used anisotropic etching of silicon to create 3-D inductors, but anisotropic etching provides only one fixed angle (54.7º from the vertical using a <100> wafer) [33]. *Ayon et al* have used a buried dielectric layer to deflect charged ions during Deep Reactive Ion Etching (DRIE) [34] to achieve angled etch profiles, reporting angles as large as 32º [35]. Yet, setting up this buried dielectric layer is non-trivial. Often multiple bonding steps are required, and the handle wafer must be sacrificed entirely due to notching effects. This handle wafer also limits the density and configuration of angled etch profiles, prohibiting all but the simplest angled trenches to

be fabricated. For MEMS devices demanding high levels of density and integration with other MEMS fabrication steps, this option is quite insufficient.

More recently, an alternative fabrication method for creating 3-D silicon structures using a single lithography and etching step, *gray-scale technology*, has been developed by multiple groups [2-14], including research conducted at UMD as part of the preliminary work for this thesis [15-17, 36-38]. In this technique, a variable transmission optical mask is used to partially expose a conventional photoresist layer, often in a standard projection lithography tool. After a development step, different thicknesses of photoresist remain (called '*gray levels*') that correspond to the intensity through the mask at that point. A dry-anisotropic etching step, such as DRIE, then transfers this pattern into the underlying silicon.

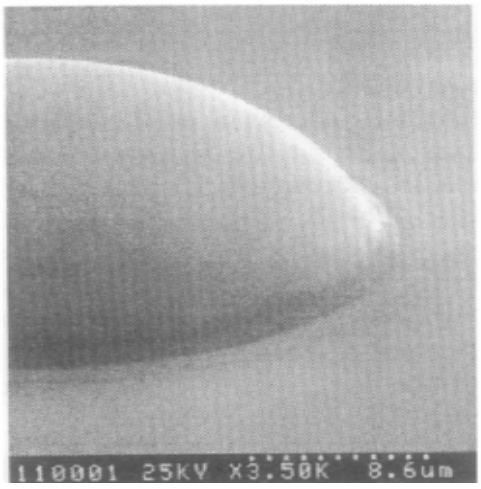

Figure 1.2: Positive lens in silicon, 10µm tall, 30µm diameter (Wagner, Henke, et al, 1995).

Both *Gal* [2] and *Henke et al* [3-5] used the diffraction effects between sub-resolution transparent pixels in a projection lithography system to create an intensity corresponding to the pixel size, enabling sloped photoresist structures of various size that could be transferred into a substrate (see Figure 1.2). *Whitley et al* [6] then briefly

demonstrated the transfer of these structures into the underlying silicon using DRIE, resulting in deep sloped structures in silicon, towards optics applications. This work was then built upon by *Waits et al* [13-15] to extend this work into the MEMS domain, where a light-field pixilated implementation was used, as well as detailed pattern transfer characterizations begun. While the gray-scale process is quite sensitive and requires extensive characterization and optimization, it has the ability to create variable height structures in silicon over a wide range of dimensions (μm to mm) in a batch manner.

Simple gray-scale structures have been demonstrated previously, yet few (if any) MEMS devices have been developed to take advantage of this newfound capability. This versatility, coupled with the fact that only standard MEMS fabrication equipment is required, makes gray-scale technology an attractive option for integrating 3-D components within MEMS devices. Since the technology is still in its infancy, Chapter 2 of this thesis will discuss the gray-scale process in greater detail, and describe the steps taken to further develop and optimize the process to enable increased flexibility, resolution, and integration within MEMS devices.

1.3.2. Traditional MEMS Actuators

Many MEMS actuation schemes have been developed using planar technologies, and not all will necessarily benefit from the integration of 3-D components. The following sections will discuss two primary categories for MEMS actuators, those used for static actuation and those developed for resonator applications. Specific comments will be made on the potential for 3-D components to enhance their performance.

1.3.2.1. Static Actuation

Numerous research groups have developed MEMS actuation techniques, such as magnetic [39], piezoelectric [40], scratch drives [41], and shape memory alloys (SMA) [42]. Magnetic and piezoelectric actuators are typically inhibited by fabrication difficulties and material concerns (such as containing toxic lead compounds), which often limit their applications. Scratch drive actuators can create relatively large forces and displacements (*Akiyama et al* report 100μN and 150μm respectively [41]), but scratch drives have a severe disadvantage because they typically only operate in one direction. Shape memory alloys on the other hand, can produce large displacements in two directions, with *Krulevitch et al* reporting displacements >50μm [42]. Bi-morph SMAs can be used to produce large deflections with small forces, but these simply alternate between two fixed positions. Alternatively, free standing SMAs achieve reversible motion by requiring extra springs for a restoring force, or special thermomechanical treatments (that exhibit less recoverable formation), which would not be compatible with most batch fabrication techniques [42].

Another class of actuators, electrothermal, has also received much attention because they can generate large forces and displacements, while being fabricated with planar IC-compatible techniques [43-45]. *Que et al* have reported forces in the mN range, with displacements >10μm, using relatively low voltages <12V [43]. However, electrothermal actuators use Joule heating and therefore require large currents (increasing power consumption) and often reach temperatures of >600 C, which may be prohibitive.

An alternative MEMS actuation scheme that can be fabricated using planar techniques, electrostatic actuation [46-49], is based on capacitive actuation, resulting in minimal current/power consumption. As a result, planar comb-drive actuators have been

developed in multiple materials, including silicon [50], polysilicon [47], and electroplated metals [51]. While each finger of a comb-drive produces minimal force, cascading the comb-fingers with careful suspension design can result in large forces and displacements.

The first boom in comb-drive design centered on achieving large static displacements using standard planar technologies [50, 52-57]. One group identified that with the ability to fabricate 3-D components, they could significantly reduce the spring constant of their suspension without reducing the comb-drive force, resulting in a significant increases in displacement. Thus, *Lee et al* reported static deflections of up to 130μm at only 37V [58]. However, to achieve this structure took a complicated fabrication process including 3 plasma enhanced chemical vapor depositions (PECVD), 4 DRIE etches, and 2 isotropic sulfer-hexafluoride (SF_6) etches, followed by aluminum metallization [58]. In contrast, such a structure could be fabricated in a single etch using gray-scale technology and will be demonstrated in Chapter 3 of this thesis.

The second wave of comb-drive research centered around the fact that electrostatic actuation relies on the capacitance between two surfaces, which is heavily dependent on the geometry of each surface. For rectangular planar comb-drives, there is a constant change in capacitance per unit length, resulting in a simple quadratic relation between displacement (Δx) and voltage (V) (i.e. $\Delta x \sim V^2$) [46]. Using planar technologies multiple groups have proposed altering this capacitance-position profile by changing the gap between the stationary and moving comb-fingers, see Figure 1.3 [55, 59-61]. *Ye et al* [60] used numerical 2-D simulation to design variable comb-finger shapes and gaps for linear, quadratic, and cubic force-engagement profiles. *Jensen et al* [61] used a parallel plate approximation model to calculate the capacitance between overlapping comb-

fingers with a lithographically-defined variable gap. These results enabled tuning of both displacement and resolution of the comb-drive actuators, but at the expense of significantly increasing the size of each comb-pair. For example, most designs proposed by *Ye et al* (or *Jensen et al*) required more than twice the area for each comb-pair [60]. The result is a device with a much larger footprint, an unacceptable consequence in most cases where miniaturization is a concern.

Figure 1.3: (a) Top view of a typical planar comb-drive finger, where the gap remains constant as the finger engages. (b) Top view of a variable gap design (from Jensen *et al* JMEMS, 2003), where the area required for a single comb-pair is greatly increased.

Further work by *Ye et al* [62] attempted to simulate variable capacitance/force profiles by optimizing comb-finger geometry in the vertical dimension to address the problem of increased device size. While the authors present simulation of complex comb-finger geometries (shaping both top and bottom surfaces of the comb-finger), they concede that their designs cannot be fabricated due to the limitations of current manufacturing techniques. However, with the advent of gray-scale technology, 3-D shaping of individual comb-fingers is possible, enabling variable force-engagement profiles for improved resolution without affecting device area.

The design, fabrication, and testing of comb-drive actuators with altered force-engagement profiles, as well as reduced spring constants, is discussed in more detail in Chapter 3 of this thesis.

1.3.2.2. MEMS Resonators

Besides static deflection applications, one of the primary uses for electrostatic MEMS actuators is for micromechanical resonators. For example, MEMS varactors for tuning electrical resonance have been developed by multiple groups [63, 64]. Micromechanical resonators for signal processing/filtering applications [65-67], gyroscopes[68], and charge and field sensors[69], have been demonstrated previously.

A natural extension of static MEMS resonators is to make them tunable, something first accomplished by *Nathanson et al* in 1967 [70]. The basic premise was to use a third electrode for tuning in a parallel plate configuration, where the quadratic dependence of capacitance on the gap creates an electrostatic spring. More recently, other groups have used this concept to develop MEMS resonators towards RF tunable filters, capable of tuning the resonant frequency down by 1% of 760KHz device [71], or by ~5% for a ~1MHz resonator with Q factor = 4370 [72]. However, bi-directional tuning of a MEMS resonator (particularly over wide range) is much more challenging.

Adams et al took the approach of using fringing field actuators, basically non-overlapping comb-drives moving perpendicular to their traditional direction [73, 74]. While this technique was able to tune both linear and non-linear stiffness coefficients, the range of motion was quite small (on order of 1μm) and tune fingers arranged perpendicular to the stroke makes the design less compact and increases damping. *Jensen et al* chose to use variable gap (i.e. variable force-engagement) planar comb-fingers to create an electrostatic spring for larger ranges of resonator displacements and bi-directional tuning [61]. But again, the variable gap design requires that the size of each comb-pair be increased, dramatically increasing overall device size. However, using gray-scale technology to create the required variable force-engagement profiles

could produce similar effects over a large travel range without increased the device footprint. The design, fabrication, and testing of such resonators is discussed in more detail in Chapter 4 of this thesis.

1.3.3. On-Chip Optical Fiber Alignment

Packaging of optoelectronic components, often in the form of fiber-pigtailing, usually requires alignment of the fiber by large, expensive, macro-scale systems capable of aligning each fiber to high accuracy using precision actuators. However, these machines are typically expensive and have low throughput due to the tight alignment tolerances required for aligning the fiber (in the micron to sub-micron range). For example, pick-and-place assembly systems with 20-30μm accuracy are an order of magnitude faster than those requiring 1-2μm accuracy, severely affecting throughput [75]. Optoelectronic packaging costs can easily exceed 50% of the total module cost [76]. In fact, the 2003 International Technology Roadmap for Semiconductors (ITRS) identified a key issue with packaging optoelectronic devices to be aligning the optical path in an automated manor, as alignment between components currently dominates the cost of packaging of most hybrid systems [77].

While silicon is not suitable for producing active optoelectronic devices, hybrid packaging approaches using micro-fabricated silicon packaging platforms to move the alignment mechanism 'on-chip' have been of particular interest. Such systems offer the potential for low cost, high volume, integrated packages, with potentially high accuracy fiber alignment placement. In general, the approaches developed fall into two categories, either passive or active, each of which is discussed below.

1.3.3.1. Passive Techniques

For the purposes of this research, 'passive' alignment techniques will refer to methods where the final alignment and assembly is performed without any light propagating in the optical path. Essentially, the goal is to fabricate and assemble all components extremely accurately and hope that the result is acceptable when the light is turned 'on.' Since the 1970's, anisotropically etched v-grooves in silicon have been used to create precise optoelectronic packaging platforms for passive alignment of an optical fiber to optoelectronic components [78-83]. The boundaries of the v-groove are defined during the lithographic process to be precisely aligned with other features on the wafer, forming what is commonly called a "silicon waferboard," as shown in Figure 1.4 [81]. The optical fiber is secured in the v-groove, while optoelectronic chips are flip-chip bonded to pre-fabricated solder pads, often using surface tension for self-alignment of the chip and substrate, see Figure 1.5 [84].

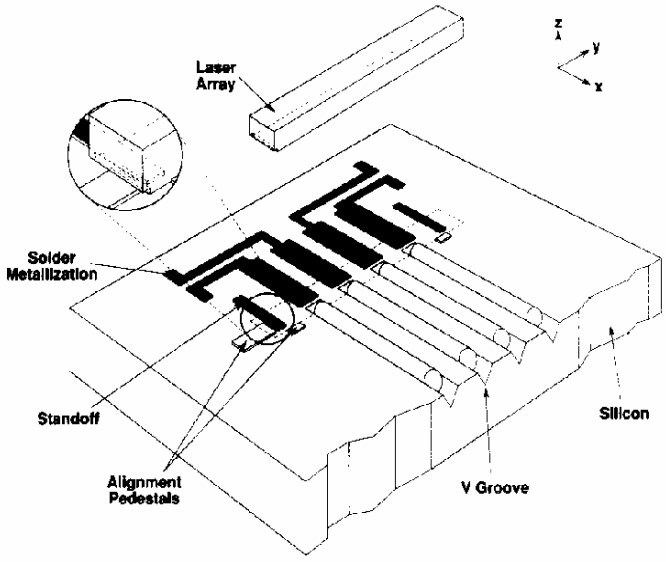

Figure 1.4: Prototype silicon waferboard for passive laser/fiber alignment (Armiento *et al,* 1991).

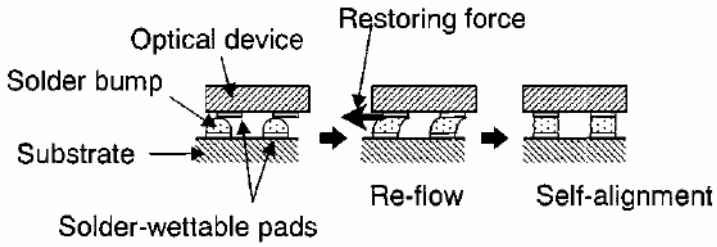

Figure 1.5: Surface tension of solder bumps during re-flow can be used for self-alignment (Sasaki et al, 2001).

By maintaining strict fabrication and assembly tolerances, such approaches report alignment in the range of 1-2μm [81, 82], which will not meet the needs for future devices that will require sub-micron tolerances [85]. Limiting factors often include the tolerance of fiber diameter, core/cladding concentricity, and imperfect mounting in the V-groove [83]. An additional challenge to such v-groove/flip-chip approaches is to control the vertical alignment of each component, as vertical shifts due to changes in solder ball/paste volume are common.

Even if these challenges can be overcome, such passive alignment schemes rely on extremely precise fabrication tolerances to cumulatively guarantee alignment, which can significantly increase processing costs. Therefore, an attractive alternative approach is to relax fabrication and assembly tolerances and instead use on-chip actuation to optimally position each fiber for maximum coupling – essentially performing the role of the expensive macro-aligner at the micro-scale.

1.3.3.2. Active Techniques

Active fiber alignment involves monitoring the amount of coupled power through the system while changing the location of the optical fiber. The fiber is then fixed at the location where maximum coupling is measured. The primary benefits of on-chip active alignment systems using MEMS are:

1. *Relaxed fabrication and assembly tolerances:* Final alignment is no longer solely dependent on cumulative fabrication tolerances of multiple components, reducing the required accuracy of individual components
2. *Potentially high-volume and high throughput:* actuation mechanisms are batch fabricated and contained inside each optoelectronic module, enabling individually optimized alignment
3. *Sub-micron actuation capability:* MEMS actuators with sub-micron displacement resolution are common

Multiple on-chip active fiber alignment systems using MEMS approaches have been proposed and demonstrated, using a variety of actuation schemes. Alignment in the plane of the wafer (1-D) has been achieved using electrothermal actuators [86, 87] or asymmetric laser trimming of films with residual stress [88]. However, as with the passive alignment techniques, the lack of vertical actuation capability is extremely limiting. *Kaneko et al* provided a small amount of vertical shift by using a partially metal coated fiber in a V-groove, yet the rotation of the fiber was done externally and the motion was discrete (only 4 separate points could be reached) [89].

When it comes to MEMS devices providing multi-axis alignment, there have been three primary devices developed. An electromagnetic-based actuator was developed by *T. Frank*, shown in Figure 1.6, that was capable of deflecting an optical fiber cantilever over 100μm [90, 91]. The actuator used large coils in a multiple wafer stack to actuate a permanent magnet attached to the end of the fiber. However, this technique requires the attachment of a permanent magnet to the fiber, making this technique impractical as a high volume, high-throughput packaging option.

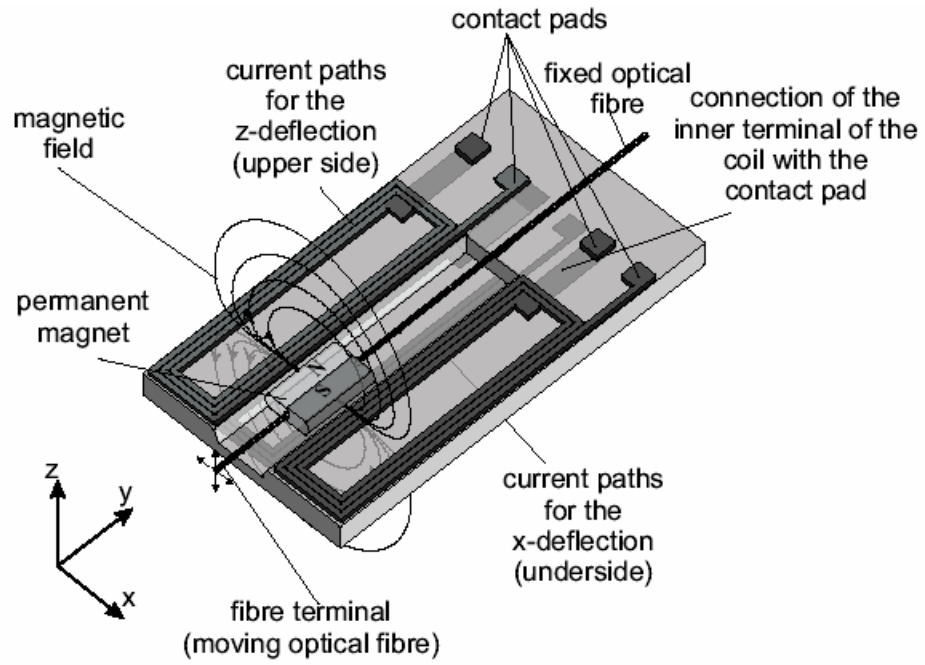

Figure 1.6: **Micro-alignment machine requiring a permanent magnet attached to the optical fiber (Frank, 1998).**

An electrostatic actuator developed by *Kikuya et al* used multiple anisotropically etched v-grooves to create an optical fiber cantilever [92, 93]. By patterning electrodes on the sidewalls of the deeply etched v-grooves, the applied voltages created an attractive force on a metallized optical fiber, bending the fiber into appropriate alignment in 2-axes. While this technique achieves 2-D fiber alignment in a relatively compact (narrow) manner, it has two main limitations: First, the electrostatic nature requires that the component being manipulated is a conductor or has a conductive coating already applied. Second, electrostatic attraction of the fiber is subject to the pull-in phenomenon, where the fiber will 'snap' to the substrate after only moving a fraction of the gap size (in parallel plate actuators, this happens at 1/3 of the original gap [94]). Thus, tradeoffs between fiber to v-groove gap, range of motion, and applied voltages, make it difficult to scale their design to shorter/stiffer cantilevers (<10mm).

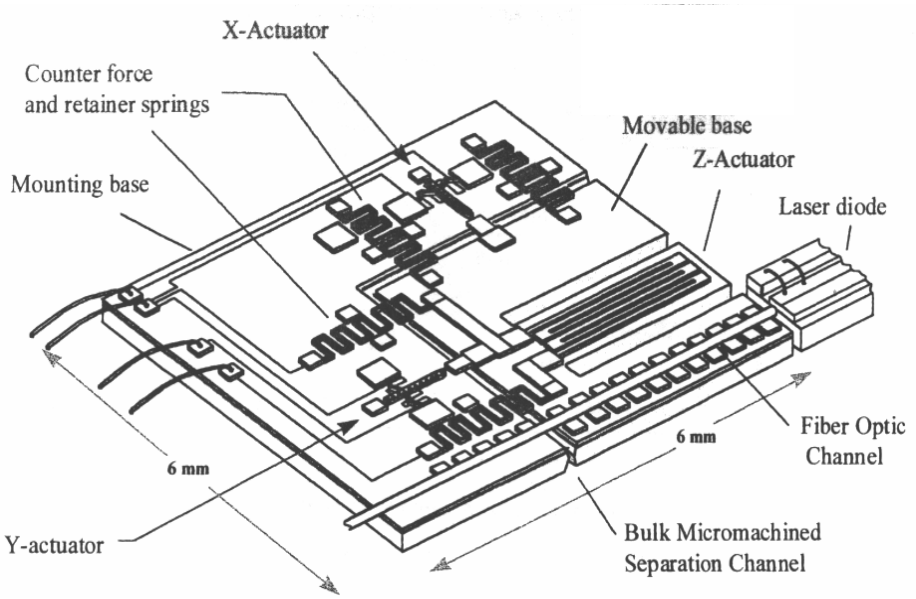

Figure 1.7: In-package micro-aligner requiring specialized fabrication equipment (Haake *et al*, 1998).

The most capable on-chip MEMS packaging system so far has been that of *Haake et al* [95, 96], see Figure 1.7, which is capable of alignment in all 3 axes,. The authors report fiber tip actuation of over 20μm in each direction. However, device design and fabrication is quite complicated as the large force actuators require the LIGA process [97], which needs an x-ray synchrotron radiation source – limiting the widespread adoption of such a device. Additionally, typical configurations are not conducive to dense fiber integration.

In contrast, electrostatic comb-drive actuators with 3-D shaped components could provide an on-chip actuation packaging platform capable of high-resolution active optical fiber alignment within an optoelectronic module in both the in-plane and out-of-plane directions. Such a system could be batch fabricated in potentially dense configurations, would require no previous fiber preparation, and could be integrated with 3-D gray-scale actuators for tailoring displacement/alignment resolution. The principles, design,

fabrication and testing of the on-chip 2-axis MEMS fiber alignment system developed in this work are discussed in Chapters 5 and 6 of this thesis.

1.4. Thesis Objectives and Structure

The purpose of this research is two-fold: First, to develop gray-scale technology as an integrative MEMS-based 3-D fabrication tool, and second, to demonstrate the first MEMS actuators of any kind to utilize gray-scale fabricated features for improved performance and capabilities. The advances in gray-scale technology pioneered in this work firmly establish gray-scale as an attractive platform technology for MEMS device development. As part of this research on the core technology, multiple novel static devices were demonstrated, including: static micro-compressors, 3-D packaging substrates for MOSFET relays, and soft X-ray phase Fresnel lenses. The variable-height comb-drive actuators and resonators developed in this work are the first demonstration of achieving tailored electrostatic actuator behavior while maintaining a compact device layout. This dissertation also reports the first 2-axis on-chip optical fiber alignment system that uses the coupled in-plane motion of gray-scale shaped actuators to create actuation both in- and out- of the plane of the wafer. Alignment of an optical fiber cantilever in 2-axes over a large range (40μm x 40μm), with high resolution (<1μm), and fast alignment times (routinely <20 seconds), establish this device as a realistic on-chip platform for the packaging and integration of optoelectronic devices.

This PhD dissertation is organized as follows: Chapter 1 has reviewed the motivation behind this research, summarized the main contributions contained in this dissertation, and briefly reviewed the relevant literature.

Chapter 2 will discuss the gray-scale technology process in detail. Specific attention will be paid to profile control and pattern transfer. Three demonstrations of static 3-D applications developed with gray-scale technology will be presented as technology collaborations with different partners: the U.S. Army Research Laboratory, the Toshiba Corporation, and the NASA-Goddard Space Flight Center.

The development of the first electrostatic MEMS actuators integrating variable height structures fabricated with gray-scale technology will be presented in Chapter 3. Issues related to the design and integration of gray-scale structures into a comb-drive actuator will be reviewed, while test results will confirm their improved performance. Chapter 4 will build upon this work and discuss a more specific application of gray-scale tailored actuators: tunable MEMS resonators. The theoretical framework for such actuators will be presented, along with test results from multiple embodiments.

Chapters 5 and 6 will discuss the development of a new on-chip 2-axis optical fiber alignment system developed using gray-scale technology. The concept, design, and fabrication of the basic system will be discussed in detail in Chapter 5, while Chapter 6 will review all optical testing and alignment results.

Chapter 7 has been reserved for discussions on potential extensions of the work presented in this dissertation, as well as concluding remarks. Topics to be covered include: low frequency tunable resonator applications, prospects for miniaturizing fiber alignment systems towards dense array packaging, and methods for clamping optical fibers after alignment has been achieved.

CHAPTER 2: GRAY-SCALE TECHNOLOGY

This chapter will review the research performed on the core gray-scale technology process, which serves as the cornerstone of this dissertation. The developments presented here demonstrate gray-scale technology as a flexible platform for 3-D actuator development. The initial portions of this work, most notably the 3-D profile control and etch selectivity characterization, were conducted as part of my Master's Thesis research, "Development of a Deep Silicon Phase Fresnel Lens using Gray-scale Lithography and Deep Reactive Ion Etching" [18]. For clarity, the term "gray-scale *lithography*" will refer to a photolithography process using a "gray-scale optical mask," while the term "gray-scale *technology*" will refer to the combination of "gray-scale *lithography*" and a dry-anisotropic etching step used to transfer the photoresist pattern into the silicon.

2.1. Introduction

As discussed in Chapter 1, gray-scale technology is a batch fabrication technique capable of creating variable height structures in silicon using a single lithography and etching step. Gray-scale lithography was first developed for use in diffractive optics in the mid 1990's [8, 11, 12]. One method uses commercially available high energy beam sensitive (HEBS) glass (www.canyonmaterials.com) that uses the chemical reduction of silver ions in a silver-alkali-halide material to produce coloring specks of silver atoms, directly modulating the opacity of each point on a photomask [9, 10]. However, the cost of HEBS masks can be up to one order of magnitude more than standard chrome on quartz plates and there is only one known vendor, which together limit the widespread adoption of this technique. Thus, the method of gray-scale implementation chosen for this research is based on the pixilated approach described by *Waits et al* [14, 15], which

uses many sub-resolution opaque pixels on a standard chrome optical mask in a projection lithography system.

During a UV exposure, the projection lithography system filters out all spatial diffraction orders, creating intermediate transmitted intensities proportional to the pixel size [3, 4]. Each intensity partially exposes a positive photoresist film to a certain depth. This exposure renders the top portion of the photoresist layer more soluble in a developer solution, while the bottom portion of the photoresist layer remains unchanged. Therefore, after a standard development step, an intermediate thickness of photoresist, called a '*gray level,*' will remain behind in areas that received a partial exposure. By locally modulating this intensity pattern with a specially designed gray-scale optical mask, many gray levels may be created at once to form a 3D structure in the photoresist, where each pixel size on the mask results in a different height *gray level* in photoresist.

By patterning the photoresist on a silicon wafer, a dry-anisotropic etching technique, such as reactive ion etching (RIE) or deep reactive ion etching (DRIE), may be used to subsequently transfer this pattern into the silicon [2]. A schematic of this entire process is shown in Figure 2.1. By distributing many appropriately sized pixels on the optical mask, step approximations to various 3-D shapes can be replicated in the photoresist and/or underlying silicon.

The following sections will review the theoretical background of gray-scale technology, and then review developments in both lithography and etching performed during this work. Finally, three collaborations with organizations outside UMD will be presented as applications of static 3-D silicon structures fabricated using gray-scale technology.

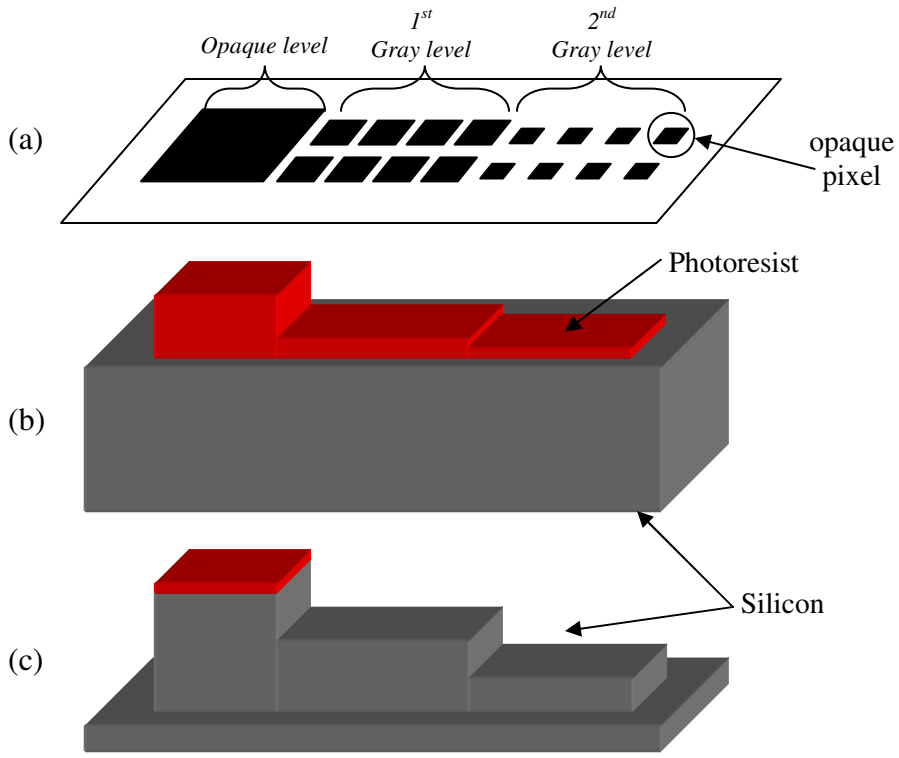

Figure 2.1: Schematic of the gray-scale technology process. (a) An example pixilated gray-scale optical mask design using 2 different size pixels, or gray levels. (b) The corresponding pattern in a positive photoresist after exposure and development. (c) Final silicon structure after transfer into underlying substrate using dry plasma etching.

2.2. Gray-scale Background

Before discussing advancements in gray-scale technology developed as part of this dissertation, the theoretical framework and design limitations for the chosen gray-scale implementation must be discussed.

2.2.1. Theoretical Background

The chosen method of pixilated gray-scale lithography relies on a standard projection lithography system, a simplified schematic of which is shown in Figure 2.2. When a pixilated optical mask is placed in this system, a fraction of the incident light is blocked and transmitted light will diffract. It is this diffraction between closely spaced opaque pixels that leads to a uniform intermediate intensity at the wafer surface.

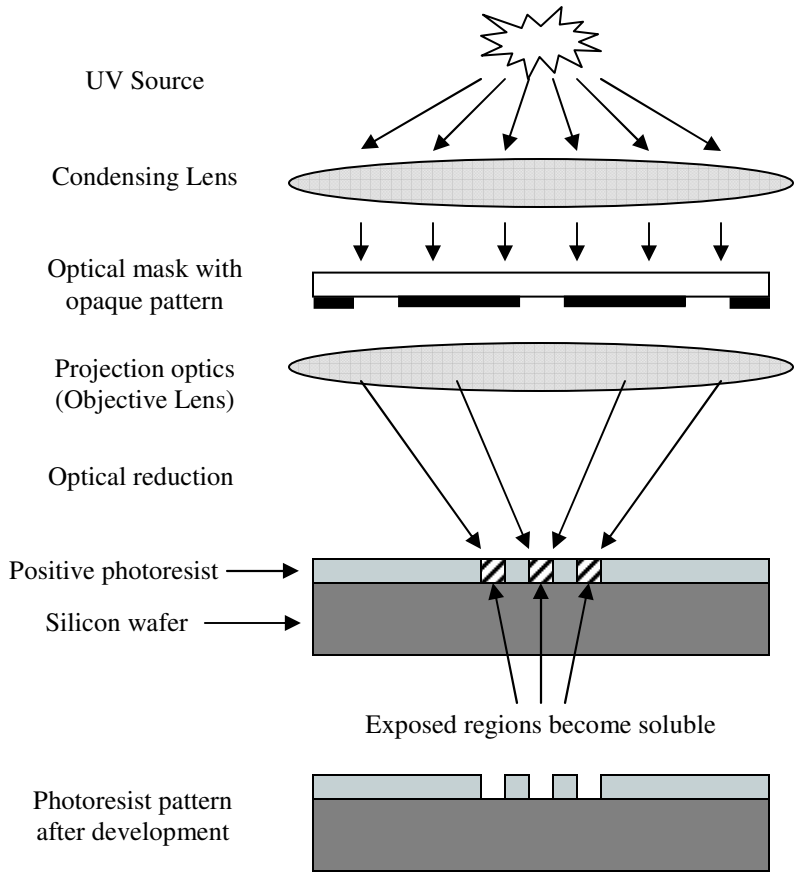

Figure 2.2: A generic projection lithography system with reduction optics (usually 5X or 10X).

To understand this phenomenon more closely, we will follow the reasoning of Henke *et al* [4, 5], where we consider the projection optics (objective lens) to act as a spatial frequency filter on a one dimensional grating, such as set of chrome lines, with a pitch of *p*. We can define the amplitude transmission function of the mask as *T(x)*, where the values *0* and *1* are assigned to locations on the mask with or without chrome, respectively. The Fourier spectrum, *T'(k),* of this amplitude transmission function, *T(x),* is obtained through the standard Fourier relations:

$$T(x) = \int_{-\infty}^{\infty} T'(k) \cdot \exp(ikx)dk \qquad \textbf{(1)}$$

and

$$T'(k) = \frac{1}{2\pi} \int_{-\infty}^{\infty} T(x) \cdot \exp(-ikx)dx\,. \qquad \textbf{(2)}$$

A diffraction limited optical system will cut off higher spatial frequencies in the Fourier spectrum, *T'(k)*. Thus, the complex amplitude, *A(x')*, in the image plane (i.e. at the wafer surface), is given by:

$$A(x') = \int_{-k_c}^{+k_c} T'(k) \cdot \exp(ikx')dk \,. \tag{3}$$

The parameter k refers to a lateral wave vector on the mask, whose 1st diffraction order corresponds to:

$$k = \frac{2\pi}{\lambda} \sin\theta = 2\pi\upsilon \tag{4}$$

where λ is the wavelength of illumination light used in the stepper and υ is a spatial frequency of the grating lines. The numerical aperture (NA) of the system then defines the maximum angle, θ_c, capable of passing through the system:

$$NA = \sin\theta_c \,. \tag{5}$$

For normal incidence plane wave illumination, this *NA* determines the critical spatial frequency, υ_c, or critical pitch, p_c, necessary on the optical mask for the 1st diffraction order to reach the critical angle, θ_c:

$$p_c = \frac{1}{\upsilon_c} = \frac{\lambda}{NA}. \tag{6}$$

For periodic features below this critical pitch, the ±1 and higher diffraction orders are prevented from passing through the projection system. Since all spatial information is contained in the higher diffraction orders, only a uniform 'DC' component of light (0th diffraction order) is transmitted through the optical system, and all spatial information regarding the shape of individual pixels is lost. In a true lithography system, the partial

coherence of the light source, σ, will also play a role in determining the critical pitch of the system [5]:

$$p_c = \frac{\lambda}{(1+\sigma)NA}. \tag{7}$$

For the research performed in this dissertation, the pitch has been held constant, at or near the critical pitch in order to maintain this condition. The 'DC' component of the optical mask transmission was then locally modulated by varying the size of rectangular sub-resolution opaque pixels contained therein, as shown in Figure 2.3.

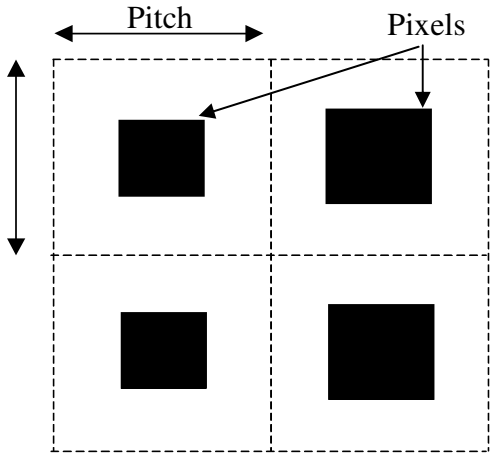

Figure 2.3: Optical mask design scheme using sub-resolution pixels and a constant sub-resolution pitch. By calculating the area of each pixel and the area of the pitch, the percent transmission through the mask is estimated.

Now, the complex amplitude at the wafer surface can be determined by a simple integral over the mask transmission function, which only includes *k=0*:

$$A(x') = T'(k=0) = \frac{1}{2\pi}\int_{-\infty}^{\infty} T(x)dx. \tag{8}$$

For a pixilated approach, this integral calculates the percentage of light transmitted through the optical mask (*Tr*), which can be calculated using the area of each pixel (A_{pixel}) and the area of the square pitch (A_{pitch}):

$$Tr = 1 - \frac{A_{pixel}}{A_{pitch}}. \quad \textbf{(9)}$$

This results in a normalized aerial image intensity at the wafer surface of:

$$I(x') = \left|A(x')\right|^2 = Tr^2 = \left(1 - \frac{A_{pixel}}{A_{pitch}}\right)^2. \quad \textbf{(10)}$$

2.2.2. Optical Mask Constraints

The projection lithography system used in this research was a 5X reduction stepper (CGA-Ultratech) in the clean-room facilities at the Laboratory for Physical Sciences (LPS) in College Park, MD. Since the estimated resolution of this system is between 0.5-0.6μm on the wafer, the critical pitch used on our gray-scale optical mask is on the order of 2.5-3.0μm, meaning each pixel must be even smaller. All optical masks for this research were obtained through Northrop Grumman Corp., Linthicum, MD, but the design rules discussed here can be applied to any mask vendor.

Optical masks cannot be fabricated with arbitrarily small features, so the number of different size pixels that will fit inside a particular pitch is finite. The result is a discrete set of available pixels (each with an associated transmission, *Tr*) that depends on the selected pitch and the mask vendor limitations. Since each pixel is sub-resolution, the actual shape of the pixel (i.e. square or circle) should not be reconstructed and therefore only the total area of the pixel should be important.

When designing a pixilated gray-scale mask, there are 2 main parameters that determine your pixel constraints: (1) minimum feature size (F_m) and (2) mask address size, usually the electron beam spot size (S_0). The minimum feature size is the smallest feature dimension, opaque or clear, expected to be resolved after mask fabrication (i.e. all

dimensions of an opaque box must be larger than F_m and two adjacent edges cannot be spaced closer than F_m). The spot size of the electron beam used to fabricate a mask is also important because it often defines the smallest possible increment between subsequent pixel sizes. Smaller spot sizes are advantageous because they can lead to larger pixel sets as the permutations of pixel sizes can be increased while remaining within the F_m constraints. Masks obtained from Northrop Grumman had limitations of $F_m = 0.5\mu m$ and $S_0 = 0.1\mu m$.

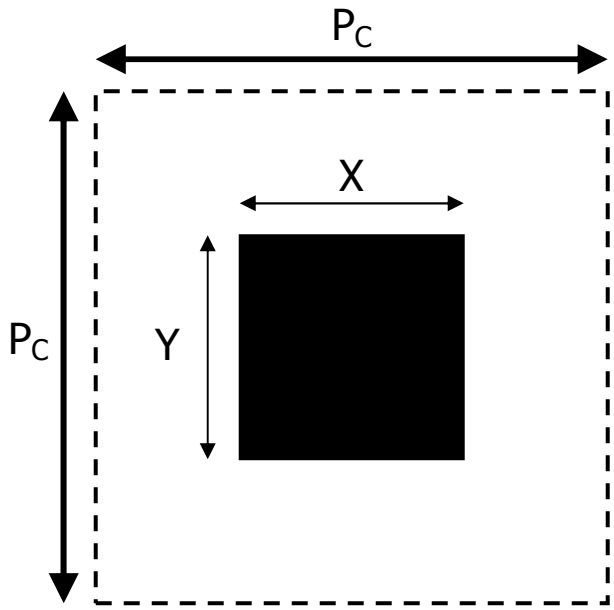

Figure 2.4: Rectangular pixilation schematic used to define mask design constraints.

Thus, to create a set of useable sub-resolution pixels for a gray-scale optical mask design, the dimensions of each rectangular pixel, height(X) vs. width(Y) must satisfy the following 3 identities derived from Figure 2.4:

$$X, Y \geq F_m \tag{11}$$

$$X, Y \leq \left(P_C - F_m\right) \tag{12}$$

$$\left.\begin{aligned} X &= F_m + n * S_0 \\ Y &= F_m + m * S_0 \end{aligned}\right\} \quad \textbf{where} \quad n, m = 0,1,\ldots \frac{P_C - 2 * F_m}{S_0} \tag{13}$$

where P_C is the critical pitch, or resolution limit, discussed earlier. The limiting case of 11 will result in the largest transmission through the mask, while the limit of Equation 12 will define the smallest transmission through the mask. Equation 13 will determine the final number of pixels (or transmissions) available. We can now modify Equation 9 for each pixel (i) to fit the rectangular case shown in Figure 2.4:

$$Tr(i) = 1 - \frac{X(i) * Y(i)}{(P_C)^2}. \quad \textbf{(14)}$$

Any pixels with identical (or extremely close) *Tr* values may be eliminated from a pixel set since they will be redundant. One must also keep in mind that every pixel will not necessarily result in a repeatable gray level in photoresist, since the development process must be considered, which often eliminates many smaller pixels. The final pixel set will be determined through the use of a calibration mask to experimentally establish the useable range of pixels (gray levels). In some instances, a mask pitch above the critical pitch could be used for gray-scale design to increase the number of available gray-levels, but with the danger of introducing oscillations in the photoresist surface as higher diffraction orders are collected by the objective lens.

2.2.3. Standard Lithography Process

Establishing a standard photolithography process enables the lithography processing to be considered a constant, which in turn allows all 3-D structures to be designed using only pixel selection. When developing a gray-scale lithography process, low-contrast thick photoresists are preferred to increase the range of intermediate intensities that generate different development rates, resulting in more *gray levels*. Clariant's AZ9245 was chosen as the photoresist for this research because it has relatively low contrast and can be spun to a nominal thickness of >6μm with ease. The

developer solution was Clariant's AZ400K, mixed in a concentration of 5:1, DI water to developer. This yielded development times in the 5-6 minute range, much longer than conventional development times of 1-2 minutes. Slower development steps are preferred in order to avoid over-development, which will cause a loss of lower gray levels.

Exact lithography parameters were optimized using a calibration mask [18] and the 5X projection lithography system at LPS with an observed resolution of 0.56μm, corresponding to a critical pitch of 2.8μm on the optical mask. The process details are given in Table 2.1. Note that no hard bake step is used (as suggested by the photoresist manufacturer) to avoid any photoresist re-flow during hard bake. Further details on the lithography process can be found in [14, 15, 18]. Unless otherwise noted, this gray-scale lithography process was used for processing all 3-D structures discussed in the rest of this dissertation. An example of a gray-scale photoresist wedge is shown in Figure 2.5.

Table 2.1: The standard gray-scale lithography process.

Photoresist	Spin Coating (rpm : sec)	Soft Bake (°C : sec)	Focus (μm)	Exposure (mJ)	Developer : Time (min)
AZ9245	2500 : 60 (6.0μm thick)	110 : 120	-1.0	250	AZ 400K 1:5 DI water : 5

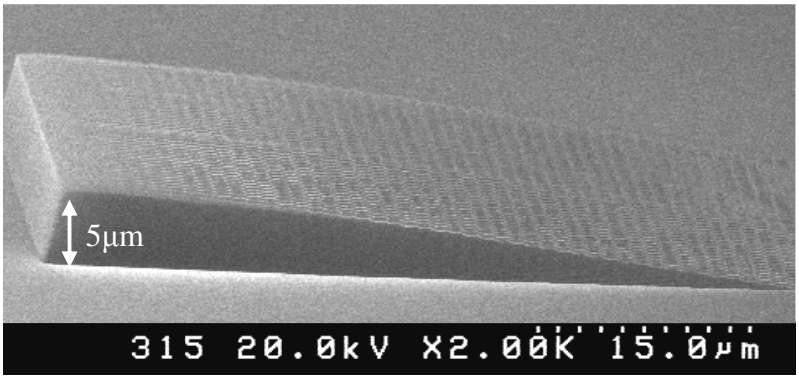

Figure 2.5: An example gray-scale wedge in photoresist using >45 gray levels.

2.3. Design and Lithography Advancements

The previous section established the capability to achieve multiple intermediate intensities through a pixilated gray-scale optical mask, as well as described a photoresist process to realize these intensities as differential height photoresist structures after development. To extend this work into MEMS and other applications, it was imperative that methods to control the 3-D profile's horizontal and vertical resolution be developed, as discussed in the following sections.

2.3.1. Minimum Feature Limitations

The analysis and discussion provided in Section 2.2 assumes an infinitely periodic array of gray-scale pixels. However, a real MEMS structure is usually finite, leading to a definitive 'edge' where the pixels stop and some higher diffraction orders are collected. On large MEMS structures, this edge effect could be small compared to the overall device size, yet on smaller structures (<10μm), the effects can be severe. Shown in Figure 2.6 is an opaque structure next to an attempted gray level, using a pitch of 2.0μm and only 10 pixels. As evident from the SEM, the edge effects on both side of this structure effectively remove the entire intended gray level.

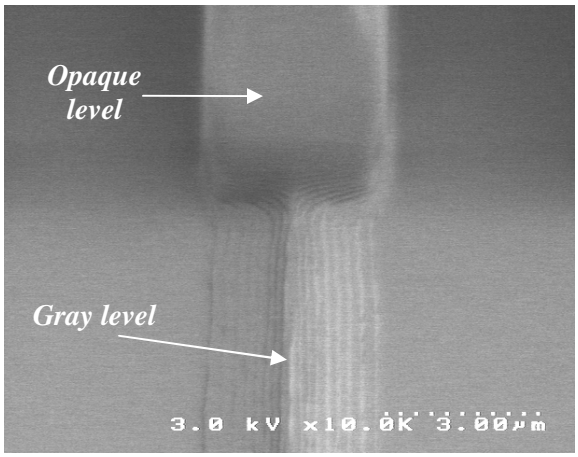

Figure 2.6: Attempted gray level in photoresist using 10 pixels on a 2.0μm mask pitch, where edge effects have effectively removed the gray-level.

As the size of the gray-scale structure increases, this edge effect stays approximately constant at around a 1-1.5μm indent to each side. The 8μm opaque structure in Figure 2.7 shows that a ~5μm gray level is now achieved. Thus, for gray-scale structures with critical minimum features <10μm, a simple bias of ~1μm can be included in the gray-scale design to offset the change in dimension due to edge effects. After pattern transfer, only a small amount of mask erosion at the corners is observed due to the lack of verticality at the photoresist edge. We estimate that a minimum gray-scale feature size of 4-5μm can be realistically reproduced.

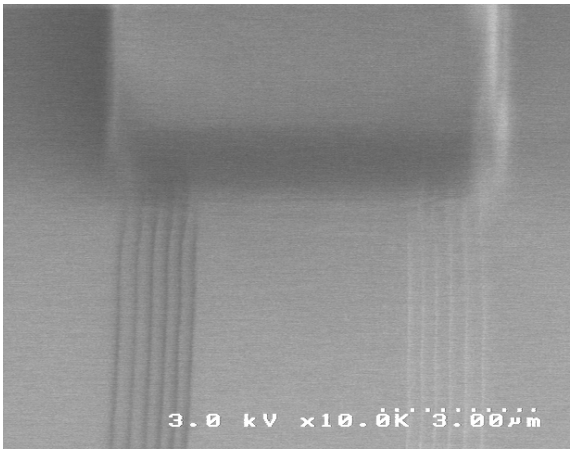

Figure 2.7: A gray level in photoresist using 20 pixels on a 2.0 mask pitch.

2.3.2. 3-D Profile Control

Given the small size of each pixel at the wafer level (~0.5 x 0.5μm), it is crucial that the method developed for controlling 3-D profiles in photoresist be conducive to automation, in order to facilitate placement of the thousands of pixels required to create MEMS structures of appreciable size.

Our investigation begins with the basic law of absorption, where we know that as the incident UV light travels through the thickness of the photoresist, the intensity decreases exponentially [98]:

$$I(z) = I_0 \exp(-\alpha z). \quad \textbf{(15)}$$

Considering only this exponential decay of intensity through the photoresist, linear changes in transmission (i.e. I_0) through an optical mask will create a logarithmic change in the exposure depth (z) at which a desired intensity is reached. Combining this logarithmic behavior with an initial uniform photoresist thickness and exposure time could determine exposure dose contours within a photoresist layer. However, there are other more factors that also influence the exact thickness of photoresist that remains after development, such as bake conditions, development rate, etc. Thus, a gray-scale profile control model must account for all these process variables.

An empirical model was developed based on the use of a calibration mask and the standard optimized lithography process. The calibration mask contained long stepped structures with different constant pitch, and each contained a limited number of pixel permutations. The height of each gray level in photoresist was measured and correlated to the pixel and pitch on the optical mask that produced the particular height. Measuring multiple levels creates an empirical relation between the initial pixel size on the optical mask and the final photoresist height. Note that the exact pixel shape on the mask after fabrication is unknown, so the calculated *Tr* is an approximation. It is thus more important that the mask vendor be consistant than accurate because systematic errors will be accounted for in the empirical model. The normalized height in photoresist (*Hp*) for many pixels with the same pitch was then plotted against the corresponding *Tr* value, as done in Figure 2.8.

A Gaussian curve was then used to approximate the trend of these data points, creating a simple relation between any *Tr* and *Hp* [16, 18]:

$$H_P = A_0 * \exp\left(-(Tr)^2 * \gamma\right) \quad \textbf{(16)}$$

where A_0 and γ are the empirically determined fit parameters for the particular photoresist being used. Ideally, the fit parameters will be identical for different pitches, but due to approximations in *Tr* value and measurement uncertainty, they tend to vary slightly. A Gaussian fit to this data was chosen for two specific reasons. First, a decaying logarithm or exponential type function with intensity is expected due to the exponential decay in intensity with increasing depth. Since the intensity is proportional to Tr^2 (Equation 10), a decaying exponential appears Gaussian when plotted against the *Tr* value derived from the pixel size (Equation 9). The second reason for a Gaussian curve lies in the simplicity of inverting the equation.

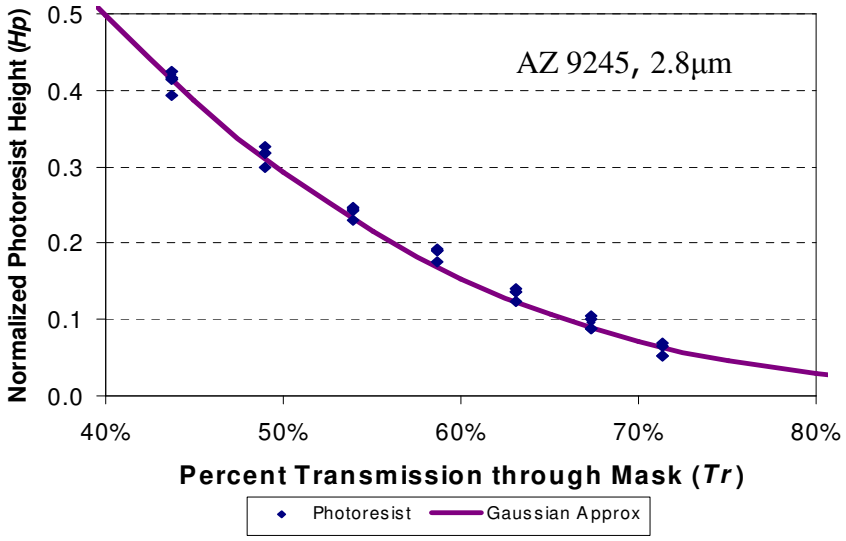

Figure 2.8: Gaussian curve fit through data points relating normalized photoresist heights to the percent transmission through the mask [16].

The result is an intuitive design tool, where a simple expression can be used to calculate the percent transmission, *Tr*, required on the mask to produce the desired height in photoresist, *Hp*:

$$Tr = \sqrt{\frac{-\ln\left(\frac{H_P}{A_0}\right)}{\gamma}}. \qquad \textbf{(17)}$$

When designing a specific structure, the ideal calculated *Tr* value is cross referenced with the available *Tr* values from a set of available pixels.

By using the Gaussian approximation method described above, much of the modeling behind the gray-scale lithography process may be abbreviated, and gray-scale masks may be designed to mimic any desired slope. As shown later in Section 2.5, this technique has demonstrated precise profile control over a wide range of structure sizes.

2.3.3. Double Exposures

While the pixilated technique makes gray-scale mask design and fabrication simple, one disadvantage is the inherent tradeoff between horizontal and vertical resolution. A small pitch will yield the best horizontal resolution, but few pixel permutations are possible, limiting vertical resolution. By choosing a large pitch, more gray-levels can be designed to fit the criteria outlined in Section 2.2.2, but the horizontal resolution in the plane of the wafer becomes poor. Even if vertical resolution is the only concern, the pitch (and therefore # of pixels) cannot be increased arbitrarily due to the finite resolution of the projection lithography system.

It is instructive to introduce typical values for each of the constraints outlined in Section 2.2.2. Using a critical pitch (P_c) of 2.5μm and a minimum feature size (F_m) of 0.5μm, we can calculate the minimum and maximum *Tr* values to be 36% and 96%, respectively. The useable range of *Tr* is actually even smaller in practice because pixels with *Tr* values above 80% are rarely realized in photoresist after development. Since the first (highest) gray level is created using *Tr=36%,* only approximately the bottom ½ of the photoresist thickness will have gray levels. Using a spot size (S_0) of 0.1μm, only ~40 unique pixels could be designed in this range, and that requires working at the extremes

of mask vendor capability, which often does not yield consistent results. And even 40 gray levels may be insufficient for MEMS structures that span 100's of micrometers. Thus, a new method of mask design is necessary whereby high resolution in horizontal and vertical domains can be maintained, while relaxing mask fabrication tolerances.

In this research, an exponential increase of photoresist gray levels has been demonstrated through the addition of a 2nd exposure step before photoresist development. By tuning the time of each of the two exposures, the entire range of photoresist can be utilized for gray-scale structure creation. A double exposure test mask was designed and fabricated to demonstrate this capability. A pitch of 2.6μm was chosen to remain close to the diffraction limit, while F_m was increased to 0.8μm and S_0 was assumed to be 0.2μm (both values relaxing previous mask tolerances). Only square pixels were chosen for this demonstration, yet the results can be scaled to include rectangular pixels as well. The square pixel dimensions used and their corresponding *Tr* values are shown in Table 2.2.

Table 2.2: Pixels and percent transmissions used in double exposure experiments, with 2.6μm pitch.

Pixel Size	Tr
2.6	0%
1.8	52.1%
1.6	62.1%
1.4	71.0%
1.2	78.7%
1.0	85.2%
0.8	90.5%
0.0	100%

Note that pixel sizes of 2.6μm and 0.0μm correspond to completely opaque and completely transparent areas, respectively. Assuming all gray levels could be reproduced in photoresist, using a single exposure would result in 8 distinct levels for use in structure design: the full photoresist thickness, 6 intermediate gray level heights, and no remaining photoresist. Each size pixel was arrayed to make 200μm by 200μm pads that were

arranged in columns by pixel size, creating a square matrix of gray-scale pads with identical columns. This square matrix was then repeated with a 90º rotation, as shown below in Figure 2.9, and placed on the opposite side of a single mask.

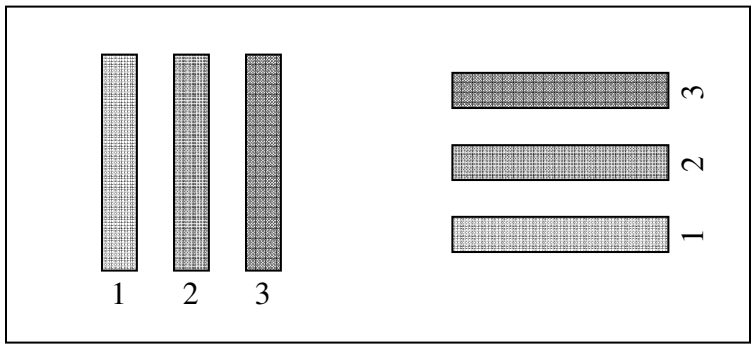

Figure 2.9: Schematic of the mask layout for the double-exposure experiment, where each column (or row) corresponds to gray-scale pads using a single pixel size and constant pitch.

A silicon wafer was prepared with the standard gray-scale lithography process outlined earlier, with the exception of the exposure step. Rather than a single exposure of say 1.5 seconds to achieve the correct dosage, the wafer was exposed in two steps. The first exposure corresponds to the pattern in Figure 2.9. The mask was then removed from the system and rotated 180º. After rotation, the two orthogonal columns of gray-scale pads overlap, so that during the second exposure, a complete matrix of exposure combinations is create, resembling Figure 2.10.

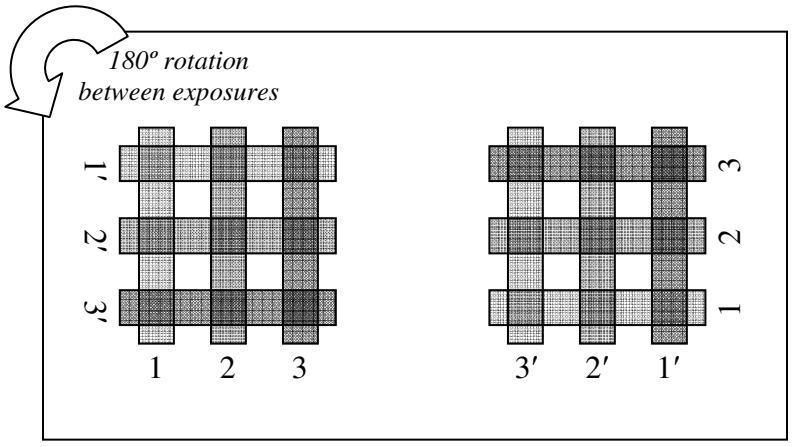

Figure 2.10: Schematic of exposure matrix after 180º rotation of mask between 2 exposures, where the primed numbers indicate the 2nd exposure pattern.

Using simply two ½ exposures, the number of unique exposure combinations possible with N intensity levels is $N^2/2$ (in this case, 32). Yet, by exposing with a weighted exposure technique, say 1/3 and 2/3 doses, a full complement of N^2 intensity levels (64) can be achieved. Figure 2.11 shows measured photoresist heights for each pad in the double exposure matrix for a combination of 0.95 + 0.55 second exposures, plotted as a function of the effective total percent transmission, Tr_{eff}:

$$Tr_{eff} = \frac{(Tr_1 \times Time_1) + (Tr_2 \times Time_2)}{Time_1 + Time_2}. \quad \textbf{(18)}$$

The large points in the figure correspond to those levels where an identical pixel was used during both partial exposures, and thus represent the gray levels possible using only a single exposure technique.

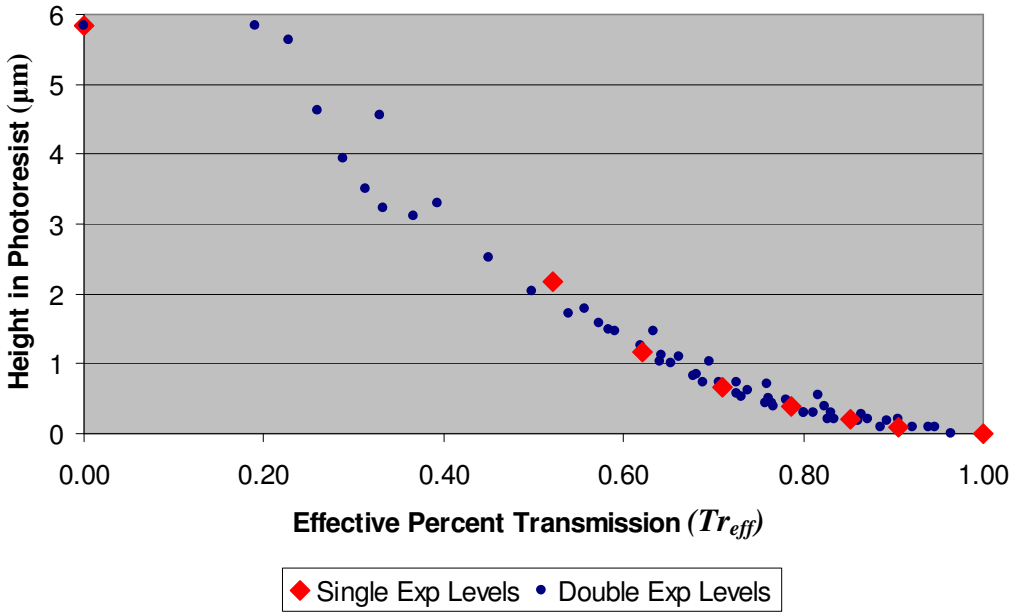

Figure 2.11: Achieved gray levels using the double exposure technique with 6 pixel sizes. The levels achieved using identical pixels for both partial exposures correspond to a single exposure technique.

Previously with single exposures, gray levels could not be created in the higher portions of the photoresist due to pixel limitations, rendering approximately the top ½ of photoresist unusable. In addition, the spacing of gray levels was uneven, leading to large

vertical steps between high gray levels. However, it is clear from Figure 2.11 that not only has the number of gray levels increased, but the distribution throughout the thickness of photoresist has also improved dramatically.

The power of this technique is easily realized when you consider that the pixel set used for this demonstration was limited to 6 square pixels with conservative spacing. Simply extending the initial pixel set to include 16 pixel permutations should result in >200 gray levels in photoresist, covering the majority of the photoresist thickness. It must also be reiterated, that these improvements can all be achieved without sacrificing any horizontal resolution.

While the design of an optical mask becomes more complicated when using the double exposure technique, empirical modeling similar to the Gaussian approximation method described in Section 2.3.1 should be possible to automate the process. Depending on the required horizontal and vertical resolution required for a particular application, the double exposure technique may or may not be necessary. However, the flexibility to create 3-D structures in this expanded design space lends further weight to the importance and significance of gray-scale technology as an enabling tool within the micro-fabrication and MEMS communities.

2.4. Pattern Transfer

Once a variable height photoresist structure is created, it is subsequently used as a mask during a plasma-etching step to transfer the pattern into the underlying substrate material. For shallow structures (<10μm), reactive ion etching (RIE) can be used, while for deeper structures in silicon, deep reactive ion etching (DRIE) has become the dominant technique. The following sections will describe the basic DRIE process and

how the gray-scale pattern is transferred into silicon. A detailed etch selectivity characterization for controlling the amplification of the photoresist structure into the final 3-D silicon structure will be presented.

2.4.1. Deep Reactive Ion Etching (DRIE)

Robert Bosch GmbH established the basic DRIE process in 1996 [99], where cycles of etching and passivation are used to create deep, vertical, high aspect ratio features in silicon. Much research has been done regarding the various processes at work in the plasma, including [34, 100-107], so the basic operation is only briefly summarized below. The remaining focus will be on its application to gray-scale pattern transfer.

The starting material is typically a silicon wafer patterned with a masking material such as photoresist or silicon dioxide. A short etching step is first executed using an inductively coupled plasma (ICP) containing SF_6 (and sometimes Ar or O_2 gases). This etch is relatively vertical over small depths (usually <1μm), however there will be a limited amount of isotropic lateral etching of the silicon. A passivation step follows, where C_4F_8 gas is cycled into the chamber to create a conformal teflon-like film over the entire surface. When the etching step is repeated, the passivation layer is preferentially removed from horizontal surfaces by charged ions in the plasma, allowing vertical etching to continue. Simultaneously, this passivation layer temporarily protects the silicon sidewall from further etching by F ions and radicals. Etch and passivation steps are cycled until a desired etch depth is achieved in the silicon, resulting in a deep vertical etch with slight scalloping on the sidewalls, as shown in Figure 2.12. Etch rates of 1-5μm per minute are achievable.

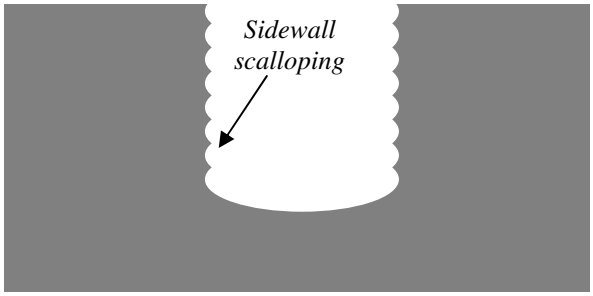

Figure 2.12: Cross section of a silicon trench fabricated using DRIE, where the sidewalls exhibit slight scalloping due to the cyclic nature of the etch.

During the DRIE process, the masking material is simultaneously etched along with the substrate. However, the etch rate of the masking material, in our case photoresist, is many times lower than the etch rate of silicon. This ratio of the silicon to photoresist etch rates is referred to as the '*etch selectivity*.' Etch selectivity for a photoresist mask is typically around 60 to 1, usually written as 60:1 or just 60. *Whitley et al* [6] briefly demonstrated and received a patent on the transfer of gray-scale structures into silicon using DRIE in 2002, showing simply that tuning the cycle times could produce sidewall facets with sufficient quality for their optical devices. However, full characterization of the etch selectivity within a DRIE system is required for gray-scale technology as the difference in the etch rates between the two materials amplifies the vertical dimensions of each gray-scale structure.

Figure 2.13 shows an example photoresist wedge on a silicon substrate. As this wedge is etched in a DRIE process, any exposed silicon will etch quickly, while the photoresist nested mask etches more slowly (the photoresist is primarily etched by ion bombardment). As the etch proceeds, the photoresist wedge will slowly recede, exposing more silicon to the high etch rate plasma. The transferred gray-scale structure will retain its original horizontal dimensions, while the vertical dimensions are amplified by the etch

selectivity. Therefore, etch selectivity control is an absolute necessity for the fabrication of precise 3D structures in silicon.

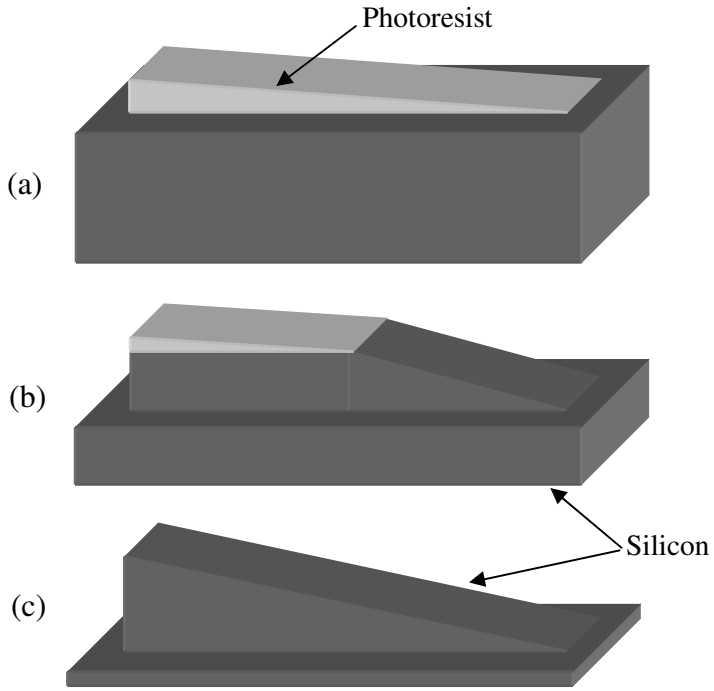

Figure 2.13: (a) Initial sloped photoresist structure on silicon. (b) Sloped pattern begins to transfer into the silicon with a particular selectivity. (c) Final structure in silicon retains lateral dimensions while vertical dimensions are amplified by the etch selectivity.

2.4.2. Selectivity Characterizations

Precisely controlling the vertical scaling of the photoresist into the final silicon structure (i.e. etch selectivity) during DRIE is one of the major challenges in the gray-scale technology process. Many factors contribute to the etch rate of both the silicon and photoresist, and often the effects are difficult to de-couple entirely. During each etch cycle of DRIE, the silicon is etched by a combination of chemical reactions and ion-assisted etching, while the photoresist is etched by sputtering via ion bombardment.

A number of experiments were carried out to assess the effect of changing various etch parameters on etch selectivity [16-18]. The starting etch recipe, termed *Base Etch I*, is shown in Table 2.3, and consists of separate passivation and etch steps within a time

multiplexed cycle. Changes were made to *Base Etch I* regarding temperature, electrode power, and silicon loading because of anticipated effects on the etch selectivity. For example, increasing the electrode power will increase the rate at which the photoresist is sputtered from the surface due to ion bombardment, causing a corresponding decrease in etch selectivity. These results were presented in more detail in my Masters Thesis [18], but are summarized in Table 2.4.

Table 2.3: DRIE process parameters for Base Etch I.

Step	Ar (sccm)	C_4F_8 (sccm)	SF_6 (sccm)	Pressure (mTorr)	Water Temp(°C)	Electrode Power (W)	Time (sec)
Passivation	40	70	0	19	20	1	5
Etch	40	0	100	19	20	10	8

Table 2.4: DRIE etch selectivity characterization results.

Parameter	Silicon Loading (%)	Si Etch Rate (μm/min)	PR Etch Rate (μm/min)	Etch Selectivity	Sidewall Angle (Inside/Outside)
Base Etch I	**41**	**0.71**	**0.010**	**75**	**-0.1˚/-2.0˚**
Base Etch II	57	0.73	0.016	42	-0.1˚/-2.0˚
Base Etch III	27	0.90	0.010	92	-0.3˚/-2.1˚
Higher Electrode Power	41	0.71	0.013	55	-0.5˚/-2.2˚
Lower Electrode Power	41	0.54	0.005	103	2.3˚/0.4˚
Increased Temperature	41	0.75	0.015	48	-1.3˚/-2.9˚

While the process changes described above may be applied in many cases, achieving extremely low etch selectivity (<20) may be difficult while maintaining other etch characteristics, such as sidewall profile. An alternative approach for coarse tuning of etch selectivity was also developed that uses an intermediate *Oxygen-only* step added to each passivation-etch cycle [16, 18], as shown in Table 2.5. Oxygen plasma steps are

commonly used in MEMS and the IC industry for photoresist removal, and have minimal structural impact on silicon surfaces. But by adding a short Oxygen-only plasma step to each cycle, a thin layer of photoresist is removed during each cycle, effectively increasing the photoresist etch rate. The silicon etch rate should remain largely unaffected since the Oxygen plasma step is separate from the etching portion of the time-multiplexed cycle. By modulating the length of the Oxygen-only plasma step, the amount of photoresist removed during each cycle, and hence etch selectivity, can be coarsely controlled, as shown in Table 2.6.

Table 2.5: Modified Bosch process using an Oxygen-only step for etch selectivity reduction.

Step	Ar (sccm)	C_4F_8 (sccm)	SF_6 (sccm)	O_2 (sccm)	Pressure (mTorr)	Chamber Temp(°C)	Electrode Power (W)	Time (sec)
Passivation	40	70	0	0	19	20	1	5
Etch	40	0	100	0	19	20	10	8
Oxygen-step	40	0	0	70	19	20	8	0-6

Table 2.6: Modulating the length of the O2 etch step coarsely controls resulting etch selectivity.

Etch	Length of O_2 Step (sec)	Etch Selectivity
1	0	70.4
2	2	37.2
3	4	25.6
4	6	13.7

The etch recipes and trends seen above are intended to serve as guidelines for etch development of specific structures. It must also be noted that while the selectivity can be changed over a wide range, there are nearly always tradeoffs with other etch parameters that may or may not be important, such as etch rate or sidewall angle/roughness. However, given the design flexibility afforded during the gray-scale lithography process, it is often possible to design for an etch selectivity range where other etch parameters are

acceptable, and use the results above to fine-tune the process to achieve the appropriate final 3-D silicon structure. An example gray-scale wedge after being transferred into the silicon is shown in Figure 2.14.

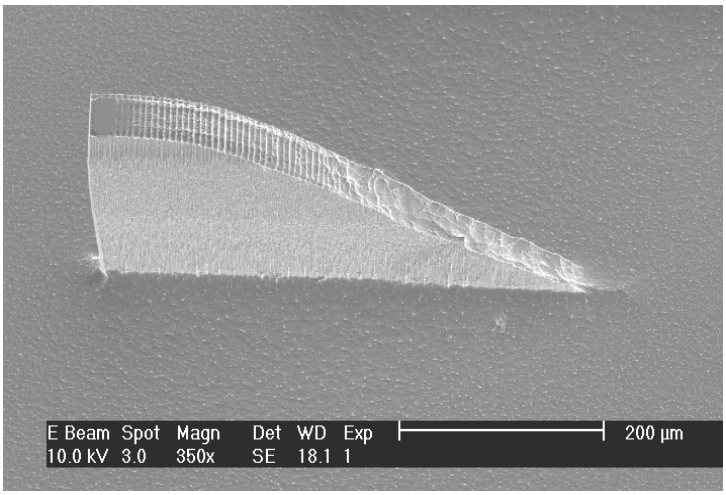

Figure 2.14: Example 200µm tall gray-scale wedge after being transferred into the underlying silicon using DRIE [17].

2.5. Technology Collaborations

The previous sections have discussed the mechanisms behind gray-scale technology, and the steps taken to improve and expand upon its capabilities. Yet these abilities and developments are best understood when discussing specific applications where precisely controlled 3-D silicon structures play a crucial role in overall system/device performance. The following sub-sections briefly describe three technology collaborations, where my research was partnered with outside organizations to develop and demonstrate unique 3-D silicon structures for enhanced performance.

2.5.1. Micro-compressor (ARL + MIT)

Researchers at the U.S. Army Research Laboratory (ARL) and Massachusetts Institute of Technology (MIT) are currently developing a micro turbine engine device,

towards portable power generation for the future soldier [108-110]. The development of such a micro-gas turbine engine requires an efficient micro-compressor design that preferably emulates their high efficiency macro-scale counterparts, which are 3-D in nature [111, 112]. While designing 3-D microstructures would not be realistic using traditional micro-fabrication techniques, with the development of gray-scale technology, the design may be driven by optimum performance goals rather than what is achievable with conventional fabrication techniques.

A micro-compressor based on the capabilities of gray-scale technology was recently designed [111, 113], and is shown in Figure 2.15. This improved design has the tops of the blades defined by the original wafer surface, while the bottom of the flow passage is etched to a variable depth. To complete the flow passage, another wafer would be bonded on top for encapsulation. The design calls for the base of the flow passage to slope from 400μm deep at the inner radius to 200μm deep at the outer radius (a 2mm long, 200μm tall slope), resulting in a mass flow inlet to exit ratio of 2:1 in the vertical dimension.

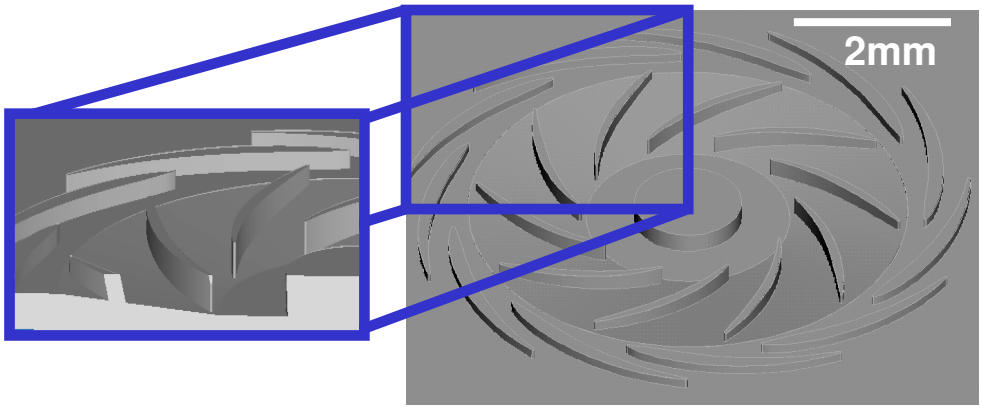

Figure 2.15: Variable height micro-compressor design exhibiting a 2mm inwardly sloped profile, where the compressor blades and veins extend above the slope to a constant height.

The first generation design, before the introduction of the Gaussian approximation, had a sloped photoresist height of ~3μm, so that a selectivity of 67 was needed. When using the base etch I from Table 2.4 a height of 210μm was achieved, and the final structure is shown in Figure 2.16 [17]. It is apparent that in this first demonstration, the sloped was quite non-linear. By using the Guassian approximation method, a 2nd design was fabricated with a linear slope, as shown in the optical profilometer scan of Figure 2.17.

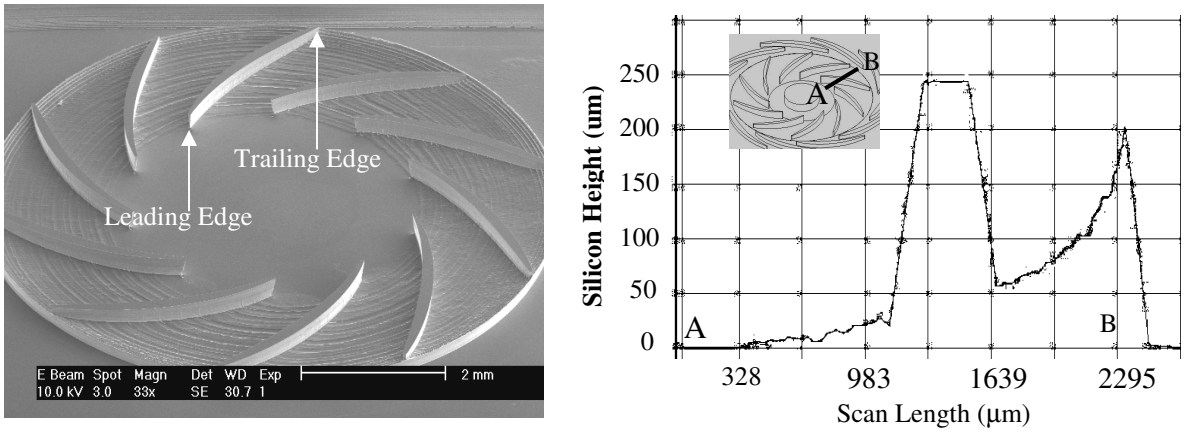

Figure 2.16: SEM and profilometer scan of the 1st generation micro-compressor [17].

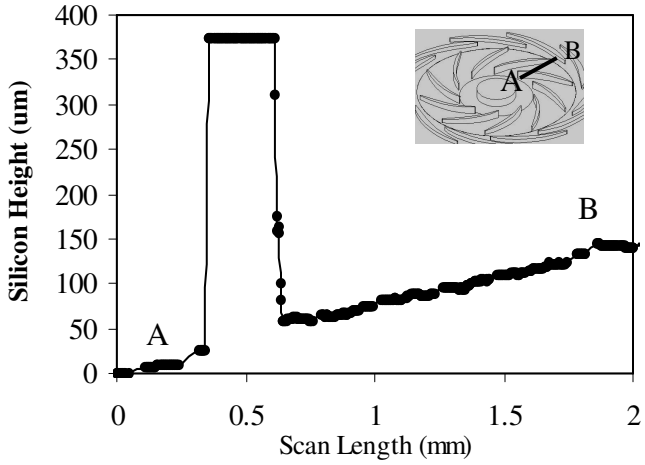

Figure 2.17: Optical profilometer scan of the 2nd generation micro-compressor using the Gaussian approximation design method.

The final step in developing this 3-D structure was its integration into an existing MIT compressor wafer process flow. A nested mask approach was developed to create the gray-scale slope and outer flow channels in separate etches, thereby eliminating the need for large single gray levels [114].

An abbreviated schematic of this process flow is shown in Figure 2.18, while Figure 2.19 is an SEM of the final variable height silicon micro-compressor with smooth outer flow channels.

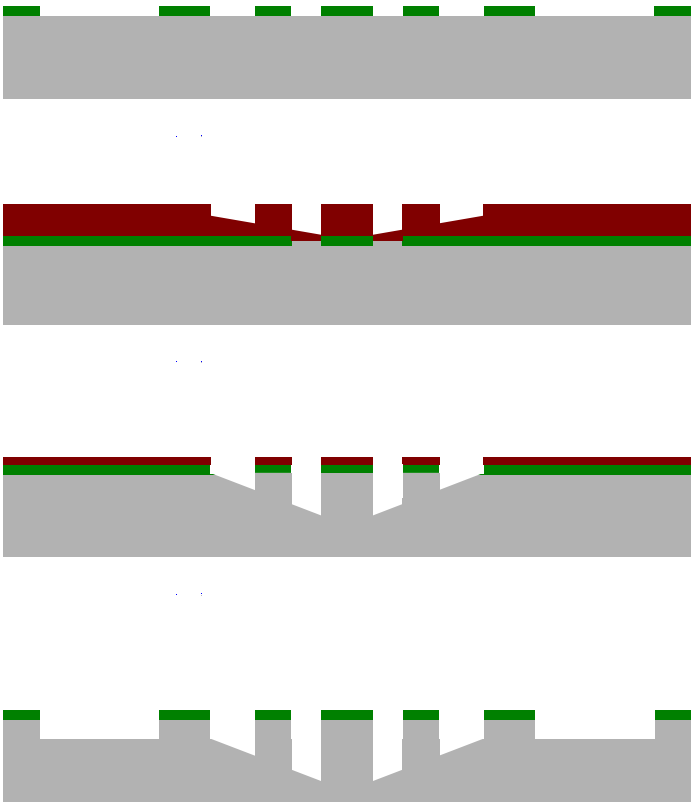

1. Deposit and pattern PECVD oxide nested mask on silicon wafer.

2. Spin and pattern photoresist using gray-scale lithography.

3. DRIE gray-scale pattern transfer using photoresist mask.

4. Remove photoresist and DRIE using the nested oxide mask.

Figure 2.18: Integrated micro-compressor level wafer process flow using a nested oxide mask.

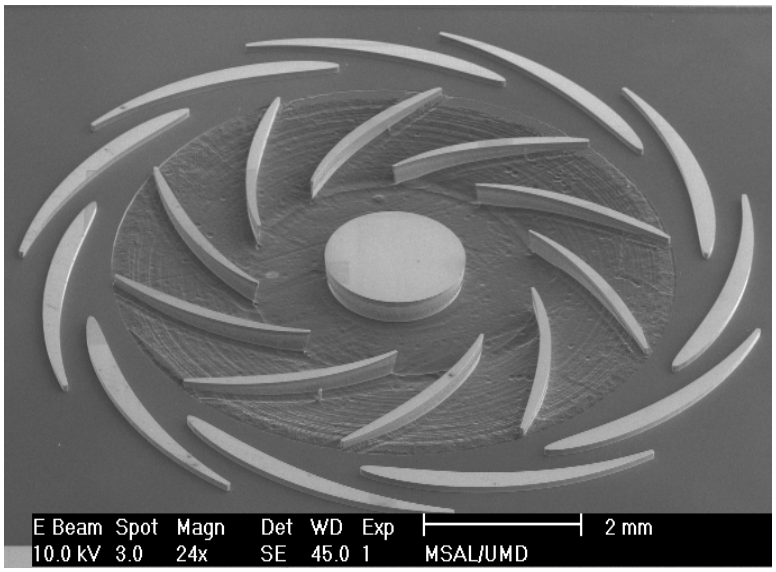

Figure 2.19: SEM of a micro-compressor fabricated using the integrated, nested oxide mask process.

At the time of this writing, the improved performance of variable height micro-compressor structures has not been confirmed in a rotating platform within the micro-engine device, largely due to the many other technical challenges associated with the project. However, our research was able to advance gray-scale technology to the point where such geometries can be achieved with regularity using the design methods and etch development guidelines described earlier.

2.5.2. Phase Fresnel Lens (NASA)

A phase Fresnel lens (PFL) is essentially a small grating that will diffract incident radiation towards its focus, while ideally producing a phase change within each grating zone to concentrate all incident power into the primary focus. Recently, G. Skinner proposed a Fresnel lens-based system for astronomical observations at hard X-ray and gamma-ray energies [115-117]. This system would have the highest diffraction-limited angular resolution of any wavelength band, resulting in a greater than 10^8 improvement over current gamma-ray imaging systems. The sensitivity of the proposed system would also be tremendous compared to typical background-limited gamma-ray instruments,

resulting in a 10^3 improvement. (Improvements based upon comparison of a 5m Fresnel lens-based system to that of INTEGRAL [117].) The main drawback is the inherently long focal length, on the order of 10^6 km, requiring that the lens and detector be located on separate spacecraft and aligned appropriately. (A detailed mission study indicated that given current propulsion technology, a large focal length is not prohibitive [118]).

To demonstrate the superior imaging properties of a PFL, scaled down lenses were developed for ground testing at lower X-ray energies as part of my masters thesis work [16, 18]. The thickness (t) of a PFL, as a function of radius (r), is defined as [119]:

$$t(r) = t_{2\pi} * MOD\left[\left(\frac{r}{A}\right)^2, 1\right] \quad \textbf{(19)}$$

where $t_{2\pi}$ is the thickness of material required to produce a phase shift of 2π, and *A* is a function of focal length (*f*) and target photon energy (*E*), given by:

$$A = 49.8 * \sqrt{\frac{f(m)}{E(keV)}}\mu m\,. \quad \textbf{(20)}$$

Neglecting absorption effects, the lens profile can also be extended to higher phase depths, such as 4π, 6π, etc [120]. Making a step approximation to the ideal profile leads to an expression for the efficiency (η_{Lens}) of a multi-level diffractive lens, given the number (*N*) of steps used to approximate the profile [121-123]:

$$\eta_{Lens} = \left[\frac{\sin\left(\pi/N\right)}{\left(\pi/N\right)}\right]^2. \quad \textbf{(21)}$$

Therefore, a traditional binary lens (2 steps) has a maximum theoretical efficiency of 40.4%. For example, By increasing the number of steps using gray-scale technology to 8, the maximum theoretical efficiency reaches 95.0%.

Using the photoresist profile and etch selectivity control methods described earlier, silicon PFL's with diameters as large as 4.7mm were designed and fabricated. Figure 2.20 shows an optical profiler scan of a fabricated silicon PFL profile (red) along with the designed profile (blue). The close agreement over the measured profile, demonstrates the precise profile control possible using the gray-scale techniques developed in this research. A phasor-based profile evaluation method was developed in combination with optical profiler scans of silicon PFL profiles to estimate the efficiency of the fabricated structures [18, 36]. Efficiencies of >87% were obtained for 1.2mm diameter PFL's assuming 8.4keV photons and f=118m [18]. An SEM of a 1.6mm diameter silicon PFL is shown in Figure 2.21 [16].

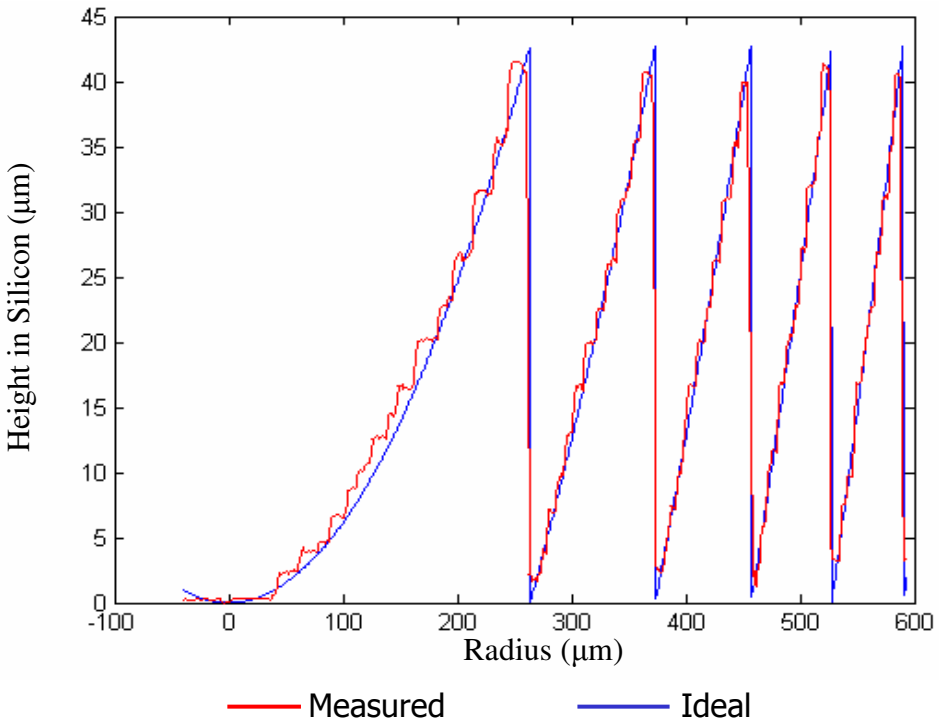

Figure 2.20: Measured silicon PFL profile compared to the ideal case, with efficiency >87%.

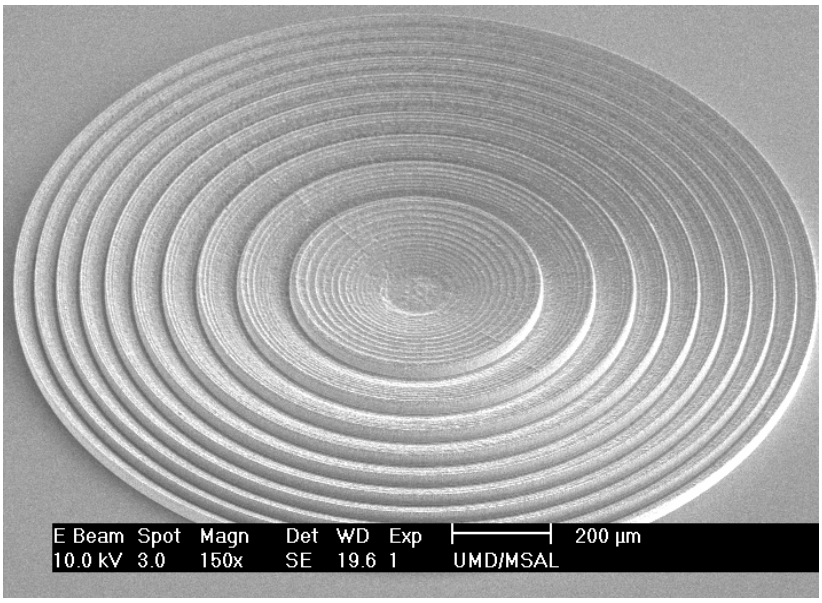

Figure 2.21: SEM of a 1.6mm silicon PFL fabricated using gray-scale technology [16].

Similar test PFL's with diameter of 3mm and 4.7mm were fabricated on 70µm silicon-on-insulator wafers using identical design and fabrication techniques. To minimize absorption, a backside through-wafer etch was added to remove the bulk silicon beneath each test lens. A few such lenses have been fabricated for testing in a new 600m x-ray beam line at the NASA-Goddard Space Flight Center [124]. Preliminary results show prominent focusing by the lenses, however significantly more testing and characterization is needed to properly evaluate the performance of the lenses and the beam line itself. At the time of this writing, this research is being pursued by my collaborators at NASA. Figure 2.22 is a raw data image from a cooled x-ray CCD camera, where each point indicates a single x-ray absorption event. As shown in the histograms (at bottom and right), a Gaussian-shaped distribution is evident from the collected photons.

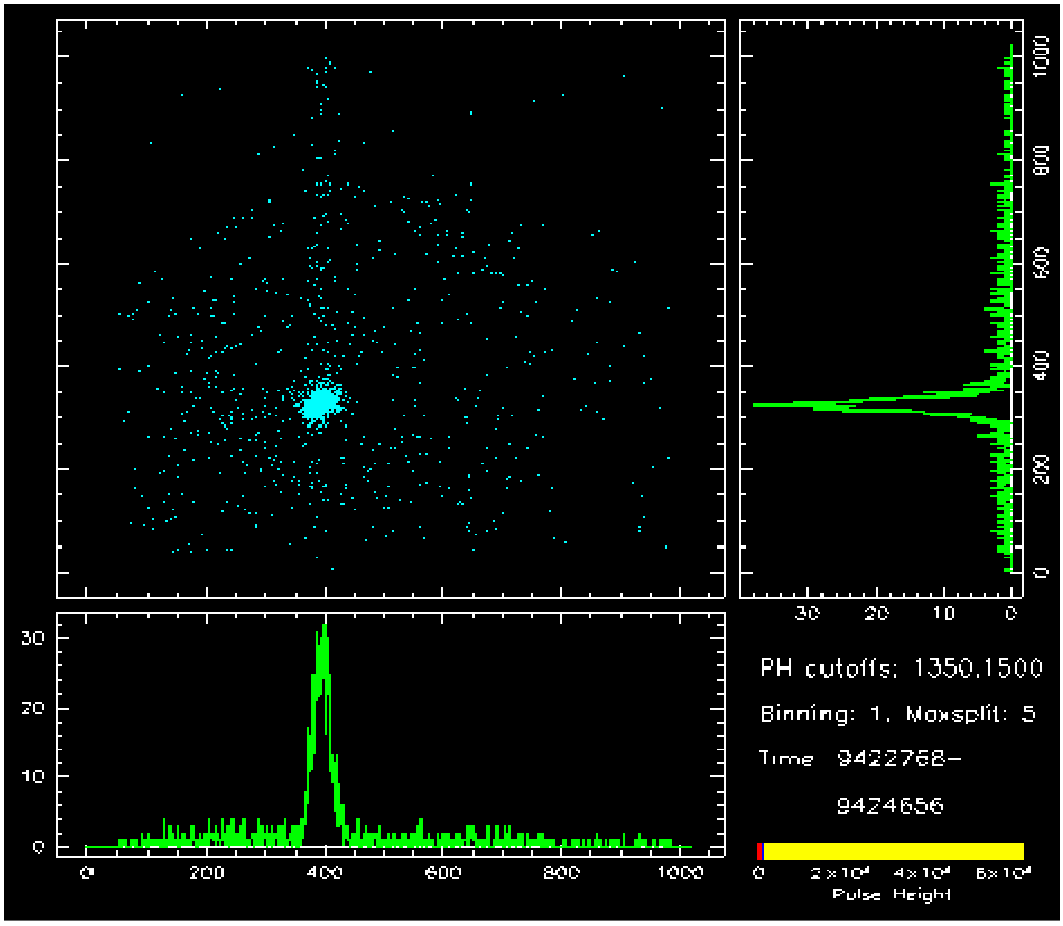

Figure 2.22: Raw data from X-ray beam line testing of 3mm silicon gray-scale PFL's on SOI substrates – filtered around the k_alpha line of a copper target (8keV). Each blue point corresponds to a single X-ray, with histograms for both axes are provided in green.

2.5.2.1. Compensated Aspect Ratio Dependent Etching (CARDE)

My research on silicon PFLs with decreasing ridge width and focal length revealed that aspect ratio dependent etching (ARDE) [34, 102, 106] caused significant changes in overall profile accuracy, as small ridges at large radii did not etch as deeply as larger ridges towards the center [16]. This problem is expected to limit future PFL efficiency because the annular ring created by each ridge has an identical collection area, so the accuracy of small outer ridges dominates PFL performance. Since gray-scale technology is already being employed to define the vertical dimensions of the PFL

features, a photoresist biasing technique using gray-scale lithography was created to counteract the subsequent ARDE. Specifically, a vertical bias was introduced to the design of variable-height photoresist nested masks to locally modulate etching time according to feature size and pattern density, creating a compensated aspect ratio dependent etching (CARDE) process [36, 125].

The conventional, or uncompensated, PFL profile thickness profile, *t(r)*, given a desired focal length of 17.1m and 6.4 keV photons, can be defined as [36]:

$$t(r) = PR_{\max} \cdot MOD\left[\left(\frac{r}{81.4\sqrt{2}}\right)^2, 1\right] \tag{22}$$

which normalizes the periodic modulo function to the maximum photoresist height (PR_{max}) available in the design. An investigation of Equation 22 reveals that as the radius increases, each ridge becomes thinner and thus has a higher aspect ratio.

For the CARDE PFL, a compensating function ($\delta(r)$) was introduced to the above design. Since the widths of the PFL ridges steadily decrease as the radius increases, a linearly decreasing compensation function was used for simplicity:

$$\delta(r) = -\left(\frac{\delta_0}{R_{\max}}\right) r + \delta_0 \tag{23}$$

where R_{max} is the radius at which no compensation will be used and δ_0 is the maximum normalized offset in the center ($r=0$) of the PFL. The compensation function is then incorporated into the thickness profile of Equation 22:

$$t(r) = \left\{\left(PR_{\max} - \delta(r)\right) \cdot MOD\left[\left(\frac{r}{81.4\sqrt{2}}\right)^2, 1\right]\right\} + \delta(r). \tag{24}$$

An example of the normalized compensated and uncompensated PFL profiles is shown in Figure 2.23. The large, fast-etching ridges at the center of the lens are now

defined using higher gray levels (i.e. thicker photoresist). These large central ridges will begin etching after a delay, while the thin outer ridges will begin transferring into the silicon immediately, effectively getting a head start. At a certain point later during the etch, the large central ridges will catch up to the thin outer ridges and a consistent etch depth/ridge height will be achieved. This behavior is confirmed in the two silicon PFL profiles shown in Figure 2.24. For the uncompensated case, the ridge height/depth decreases at large radii as the aspect ratio increases. However, for the CARDE case, a consistent ridge height/depth is achieved.

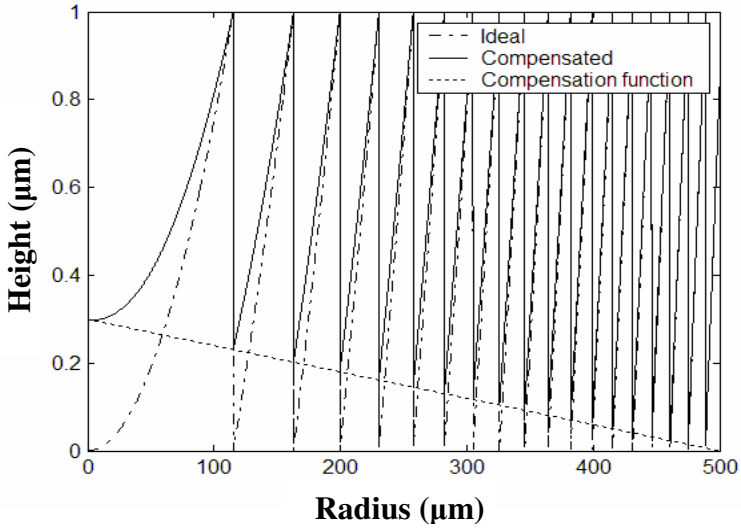

Figure 2.23: Normalized ideal and compensated PFL photoresist profile, showing the linearly decreasing compensation function.

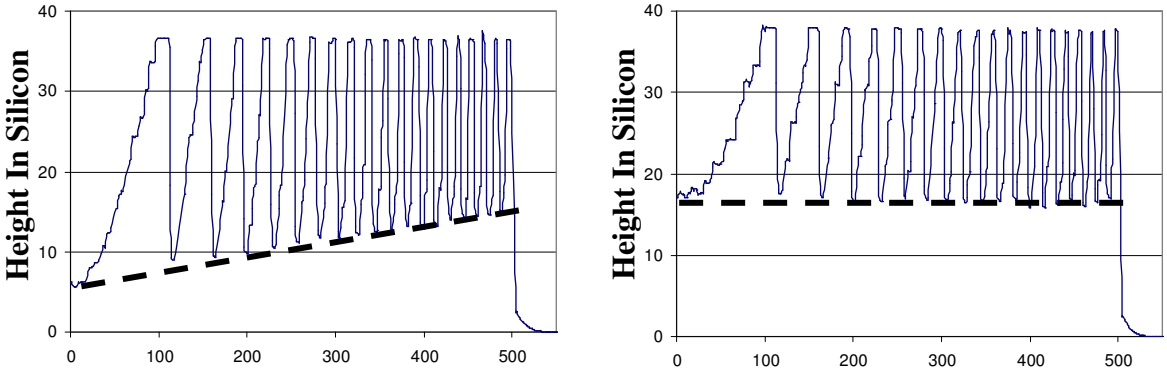

(a) (b)

Figure 2.24: Silicon profiles measured using an optical profiler for an (a) uncompensated and (b) compensated PFL design. The latter has different width ridges with the same height/etch depth.

Using the profile evaluation method developed in [18, 36], we calculated the efficiency of ridges at the edge of 1mm PFL profiles (r>400μm) for both compensated and uncompensated PFL designs to be 55% and 54%, respectively. This similarity at the edge of the PFL is expected since the small outer ridges receive no compensation. Note, these calculated efficiencies also easily exceed the maximum theoretical efficiency of a binary Fresnel lens profile (~40%) that would be possible using planar fabrication techniques. Optical profilometer scans were taken over the first 4 ridges (r=0→250μm) and their efficiencies calculated. For the uncompensated profile, an efficiency of only 43% was calculated for the center of the PFL, while a calculated efficiency of 80% was measured for the CARDE PFL. Thus, by introducing the compensation function to the PFL design, the calculated efficiency for the CARDE PFL was almost twice as high as the uncompensated PFL.

This photoresist biasing technique clearly offers the ability to control the vertical dimensions of a 3D silicon profile despite changes in feature size that causes different etch rates across the pattern. Such a technique could be utilized for the integration of gray-scale structures with silicon-on-insulator (SOI) actuators, since electrostatic MEMS actuators often incorporate a wide range of feature sizes and over-etching of large features, gray-scale or otherwise, may be undesirable.

2.5.3. 3-D Substrates for Packaging (Toshiba)

Researchers at the Toshiba Corporation (Corporate Manufacturing Engineering Center, Yokohama, Japan) desired to reduce the size of their metal-oxide-semiconductor field effect transistor (MOSFET) relay – a switching device for small electrical signals

commonly used in measurement equipment. Therefore, a new, smaller MOSFET relay package configuration based on a 3-D silicon substrate was proposed and demonstrated using gray-scale technology at UMD [126, 127].

The outline of a conventional MOSFET relay package, shown in Figure 2.25(a), contains three separate devices: a light emitting diode (LED), the MOSFET, and the Driver chip. Traditionally, the chips are connected by wire bonding and the package is shielded by plastic molding. The proposed relay package, at approximately one-half the size of the conventional package is shown in Figure 2.25(b). The combination of a 3-D silicon substrate (in place of the lead-frame) and flip-chip bonding to connect the MOSFET and Driver chips enables more dense packing of the components to reduce overall package size by 50%.

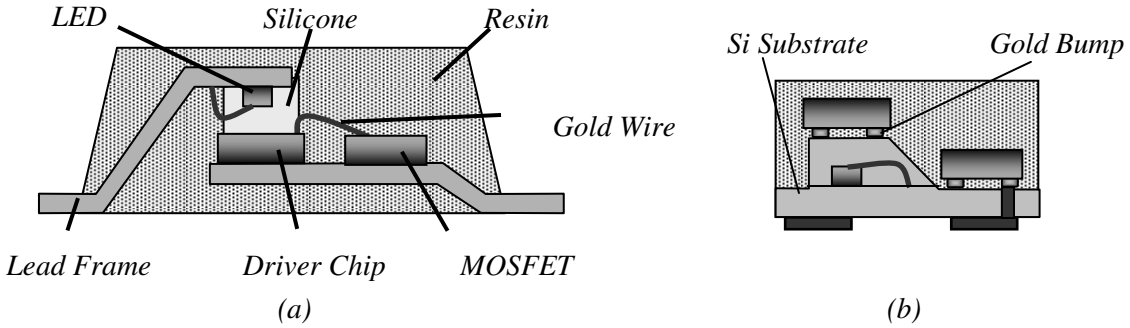

Figure 2.25: Schematic cross-sections of (a) the conventional MOSFET relay package, and (b) the proposed MOSFET relay package utilizing a 3-D silicon substrate.

The new design requires a tall, sloped silicon bulge that must be metallized to provide electrical connection between the base of the substrate and the second vertical level containing the Driver chip. Wiring of large, isotropically etched surfaces has been demonstrated by *Sharma et al* [128], however isotropic etching in general is rather limited in the structures and geometries that can be achieved. In contrast, gray-scale technology can make nearly arbitrary profiles in silicon at the necessary scale.

The basic design of the 3-D substrate is shown in Figure 2.26. The substrate has three primary features. First, backside electrodes are connected to the substrate surface using large through-hole interconnects. Second, two large bulges are used to provide a vertical platform for attaching the Driver chip above the LED. And third, electrical connection between the top and bottom of the bulges is accomplished by patterning wires on a large, sloped surface on the side of the bulges.

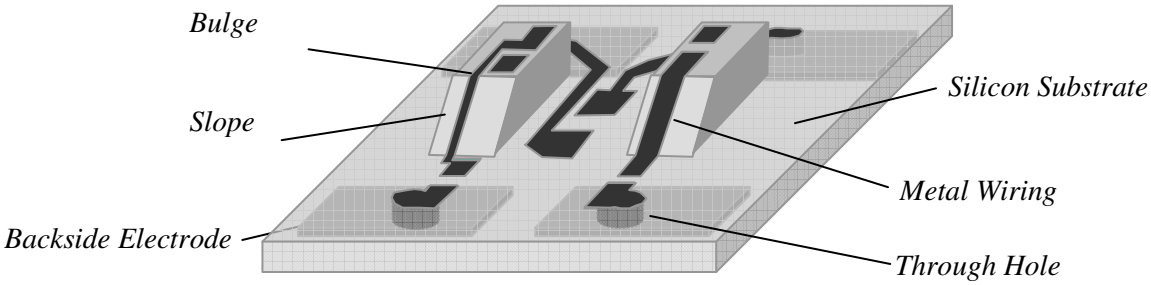

Figure 2.26: Schematic of the MOSFET relay 3-D substrate incorporating two bulges with sloped wiring and through-hole interconnects.

The major fabrication challenge is to optimize the gray-scale technology process to achieve sloped wiring connections between multiple levels vertically separated by >100μm. The primary concern for developing sloped interconnects is the surface morphology of the slope, since a single large step could prevent electrical continuity.

Using a minimum spot size of S_0=*100nm* as the increment in pixel width or length, a set of >50 pixels was created for a pitch of 3.0μm on the mask. Using a fixed increment in pixel *width* creates a change in pixel area proportional to its *length* (ΔArea = Increment x Length), and vice versa. Thus, there will be a large increment in pixel area between two large pixels, creating larger gray level steps at the top of photoresist structures (this was also apparent previously in Figure 2.11). Since a single gray level step of only a few micrometers could prevent electrical connection down the tall

(>100μm) gray-scale slope, post-processing of the photoresist and silicon slopes was investigated.

A hard-bake step was added to a 10μm version of the gray-scale lithography process (following the development step) in an attempt to cause limited photoresist re-flow and improve the smoothness of the slope. Figure 2.27 shows profilometer scans of two photoresist structures before and after the hard bake step.

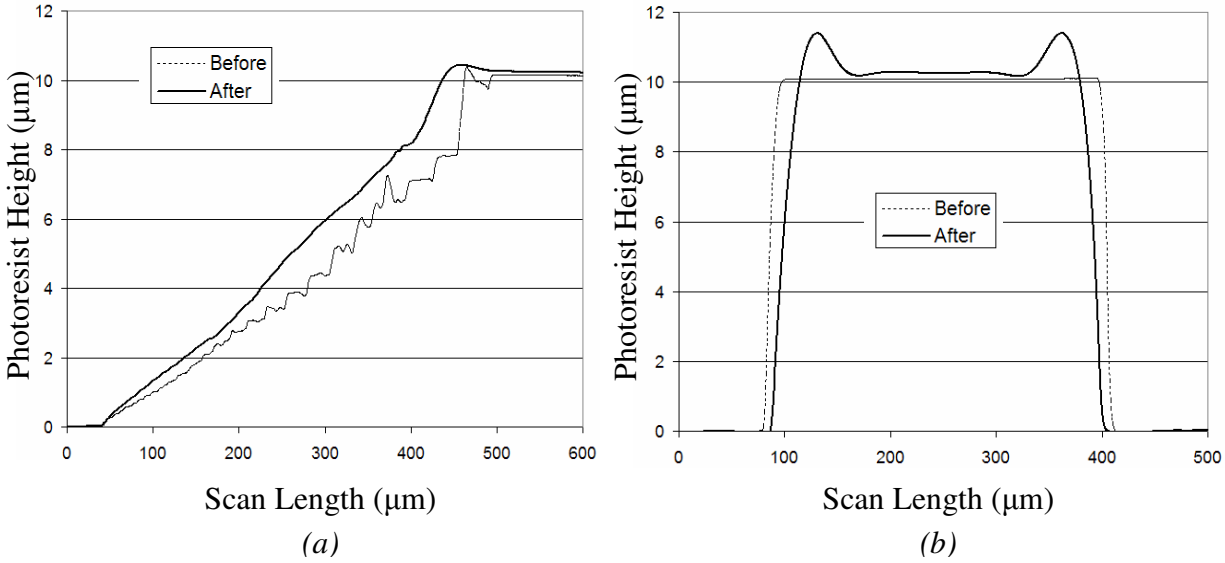

Figure 2.27: Profilometer scans of (a) gray-scale photoresist slope and (b) planar structure, before and after a hard bake step. The gray-scale slope becomes remarkably smoother, while the planar structure loses some dimensional accuracy.

In the case of the gray-scale slope, Figure 2.27(a), the bottom of the slope is initially quite smooth, while the top of the slope contains gradually larger steps due to the constant pixel increment discussed earlier. After the hard bake step, the photoresist re-flow has significantly improved the smoothness of the entire profile. However, Figure 2.27(b) shows a large planar structure before and after the hard bake, where the photoresist horizontal dimensions and sidewall profile have changed. The dimensional change of 15-20μm for this large planar structure is acceptable for the MOSFET relay substrate, as only large planar structures are defined during this step. However, for

applications requiring strict planar dimension control, the photoresist re-flow method may be inappropriate or require further optimization (such as tailoring baking temperature and/or time). The change in photoresist sidewall profile (no longer vertical) may also result in rough silicon sidewalls due to mask erosion during the DRIE step.

These photoresist profiles were subsequently transferred into silicon, where the average roughness on the gray-scale slopes immediately after DRIE was measured to be less than 50nm. Simple post-processing steps, such as isotropic plasma etching and thermal oxidation, have been used to further improve the sloped surface morphology. Alternative methods, such as hydrogen annealing [129], could be used for dramatic smoothing of the silicon profile if desired.

The final step in developing 3D sloped interconnects was to define metal traces on the slope and verify electrical continuity. A Ti/Au (60nm/300nm) layer was evaporated over the entire substrate. Since the substrate has already undergone DRIE, photoresist spray coating was performed at the Toshiba Corporate Manufacturing Engineering Center in Yokohama, Japan to coat the complex topography. Contact lithography was used to pattern this photoresist layer and wet etching removed the excess metal, leaving various metal traces on the 3-D substrate, as shown in Figure 2.28(a).

Electrical continuity was verified between the top of this 170μm tall bulge and the bottom of the etched open area, using standard wafer probes. These results confirm that the final gray-scale silicon slope was sufficiently smooth for even a thin (360nm) metal layer. Figure 2.28(b) shows example IC's after flip-chip bonding, demonstrating the ability to interconnect multiple IC's at different elevations on the same substrate.

(a)

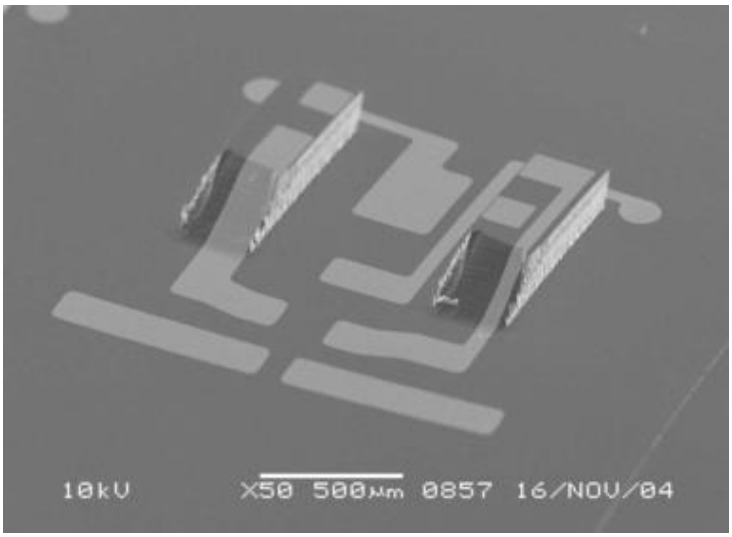

(b)

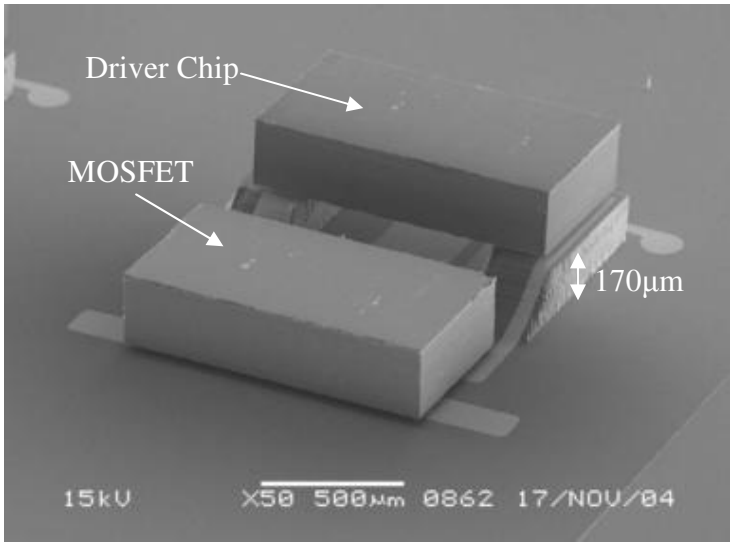

Figure 2.28: (a) Silicon substrate with patterned metal traces providing electrical contact between the two levels. (b) Flip-chip bonding of multiple IC's illustrates the potential configuration for a MOSFET relay.

2.6. Conclusion

This chapter has reviewed the research performed on the core gray-scale technology process, an attractive and flexible batch fabrication technique capable of creating variable height structures in silicon using a single lithography and etching step. Developments presented include precise 3-D photoresist profile design techniques, and

etch selectivity characterization for controlling the vertical amplification of photoresist profiles into final 3-D silicon structures. Multiple applications were pursued as collaborations on this technology, where the developed techniques were shown to be effective and precise. This research has laid the foundation for gray-scale technology serve as a platform technology for 3-D MEMS actuator development, towards improving device performance and enabling unique actuator behavior.

CHAPTER 3: ELECTROSTATIC COMB-DRIVES USING GRAY-SCALE TECHNOLOGY

3.1. Introduction

As discussed in previous chapters, the majority of fabrication techniques used in the area of microelectromechanical systems (MEMS) are planar technologies. While myriad MEMS actuators have been developed using these techniques, the design space is severely constricted due to fabrication limitations. Thus, actuator designs must often compromise between desired performance and the ability to be fabricated. In particular, electrostatic MEMS actuators are extremely sensitive to their surrounding geometries, so the ability to design with 3-D structures, can offer a significant performance advantage.

This chapter will review the basic mechanisms at work in electrostatic MEMS comb-drives, as well as highlight the areas where improvements can be made by incorporating 3-D components. Novel methods for tuning comb-drive performance using gray-scale technology in both the comb-fingers and the suspension structure will be discussed. Comb-drive actuators with 3-D comb-fingers and reduced height suspensions are demonstrated that enable customized displacement characteristics and lower driving voltages without increasing device footprint. The integrated process flow and comb-actuators developed here will serve as a building block for the development of tunable resonators (Chapter 4) and optical fiber aligners (Chapters 5 and 6).

3.2. Electrostatic Actuation Fundamentals

Planar electrostatic actuators, and in particular comb-drives, have been developed with planar techniques by many groups [46-57]. In order to properly utilize the

capability to now design comb-drives in the vertical dimension, we will first consider the relevant equations for the planar case. Referring to Figure 3.1, two sets of interdigitated fingers are used to form a parallel plate capacitor. By applying a potential (V) across the capacitor, an attractive force is generated between the fingers causing their overlap to increase (assume one set of comb-fingers to be suspended and the other fixed).

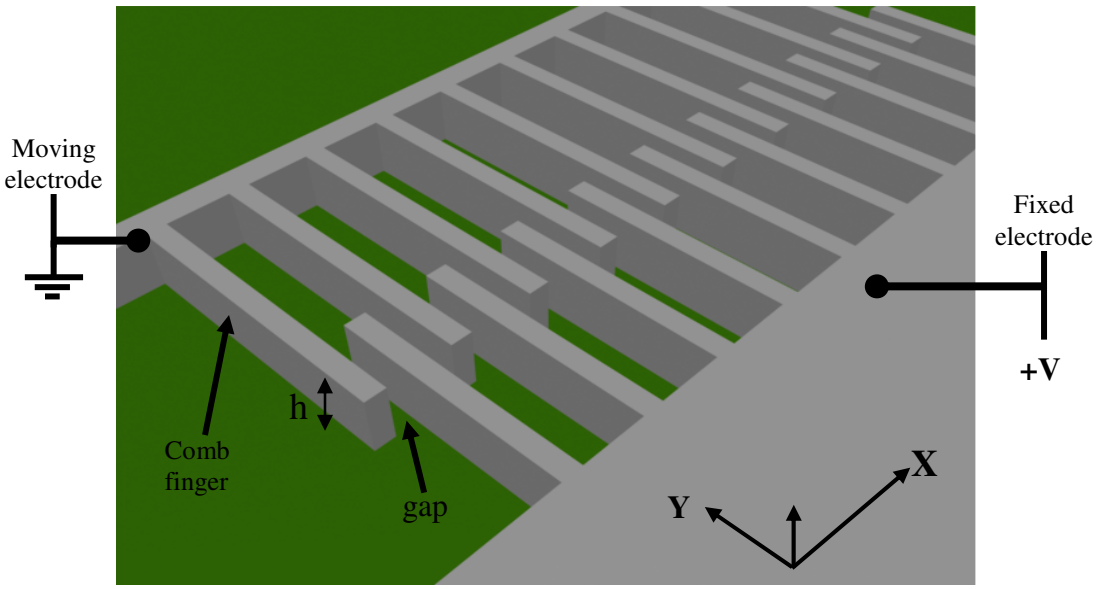

Figure 3.1: Perspective view of a comb-drive actuator.

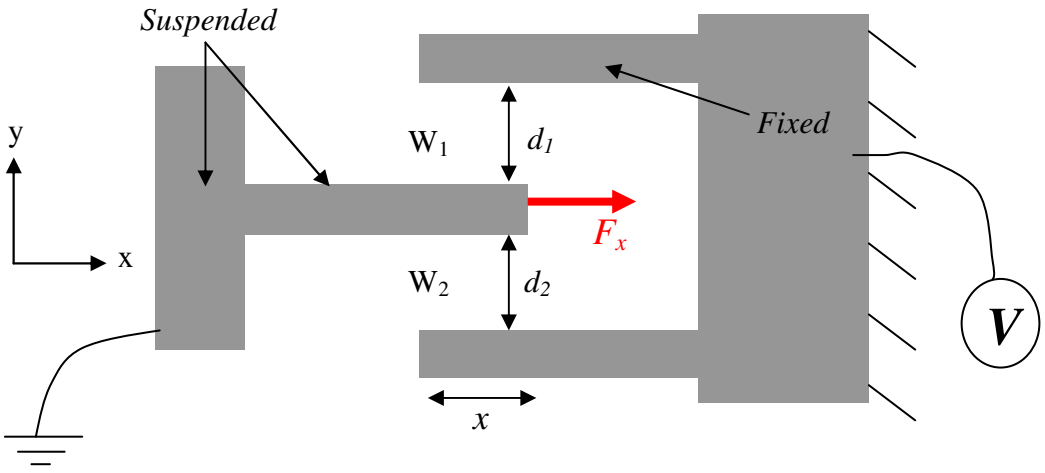

Figure 3.2: Schematic of a typical comb-drive actuator with fixed and suspended comb-fingers. The suspended set of comb-fingers is often electrically grounded to minimize any attractive force to the ground plane below.

The behavior of a comb-drive is typically described by considering a single comb-pair, shown in Figure 3.2, where we write the electric potential co-energy (W^*) as [130]:

$$W_1^* = \frac{C_1 V^2}{2}, W_2^* = \frac{C_2 V^2}{2} \tag{25}$$

where C is the capacitance between the two conductors for a particular position of the suspended fingers. In the voltage constrained case, as one side of the capacitor moves, the electrostatic force involved is the positive spatial derivative of the stored potential energy [131]. Thus, we can write the forces in the x- and y-directions:

$$F_x = \frac{\partial}{\partial x}\left(W_1^* + W_2^*\right)\Big|_V = \frac{V^2}{2}\left(\frac{\partial C_1}{\partial x} + \frac{\partial C_2}{\partial x}\right) \tag{26}$$

and

$$F_y = \frac{\partial}{\partial x}\left(W_1^* + W_2^*\right)\Big|_V = \frac{V^2}{2}\left(\frac{\partial C_1}{\partial y} + \frac{\partial C_2}{\partial y}\right). \tag{27}$$

Once the comb-fingers are overlapped, the contribution of fringing fields on the derivative of capacitance is essentially negligible [132]. Thus, the capacitance for overlapping section of a single comb-finger is often estimated using a parallel plate approximation:

$$C_{1,2} = \frac{\varepsilon_0 \cdot h \cdot x}{d_{1,2}} \tag{28}$$

where ε_0 is the permitivity of vacuum (and approximately that of air), h is the height of the comb-fingers, x is the amount of overlap, and d is the gap between comb-fingers. First considering the force in the y-direction, we see that when the suspended comb-finger is equidistant from both sides ($d_1=d_2$), the force generated from each of the capacitors (C_1 and C_2) will be equal in magnitude, but in opposite direction, canceling

each other out. Note that this issue will be revisited later in Section 3.3.3 as it relates to instability of the comb-drive. Using the same assumption (d_1=d_2), the force in the x-direction can also be calculated as:

$$F_x = N \frac{\varepsilon_0 \cdot h}{d} V^2 \tag{29}$$

where N is the number of comb-fingers and V is the applied voltage. For a planar comb-drive where the height of the comb fingers (h) is constant, the derivative of capacitance with respect to position is also constant. Thus, the force generated by a comb-drive is independent of the overlap of the comb-fingers and proportional to the square of the applied voltage.

The total displacement of a comb-drive actuator is the point where the generated force and restoring spring force are equal in magnitude. Assuming a linear spring constant (k), the displacement of a planar comb-drive (Δx) is also a quadratic function of applied voltage, V:

$$\Delta x = N \frac{\varepsilon_0 \cdot h}{k \cdot d} V^2. \tag{30}$$

Plugging in some example numbers from structures achievable with DRIE, Figure 3.3 shows a plot of the resulting displacement versus voltage curve. A few characteristics of this graph, and comb-drives in general, should be noted: first, displacements >10μm can be easily achieved using <100V, making this an attractive technology for large displacements at the micro-scale. Second, the quadratic relation between displacement and voltage results in large displacements, but at the cost of significantly decreasing resolution at large deflections.

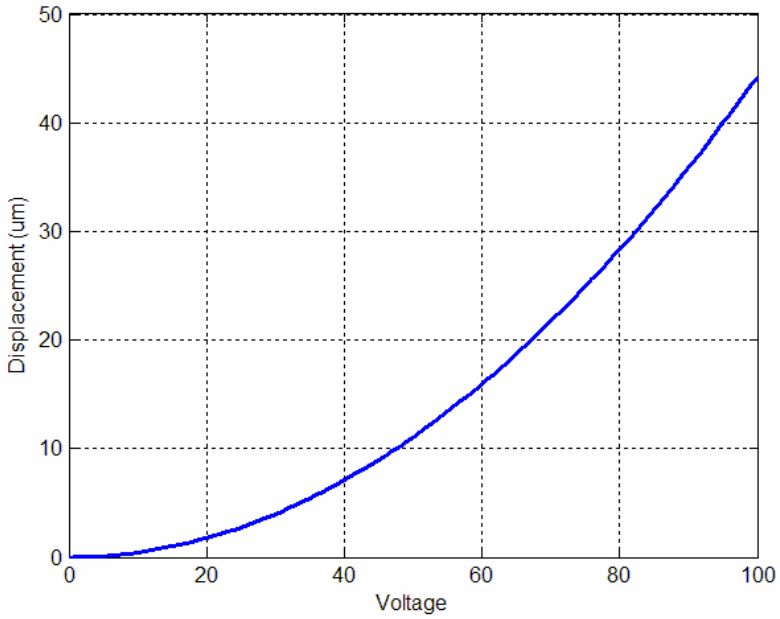

Figure 3.3: Example calculated displacement versus voltage plot for an electrostatic comb-drive assuming N=50, K=5 N/m, d=10µm, and h=100µm.

We can define the actuation resolution (R, in meters/volt) at a particular displacement as the derivative of the displacement-voltage curve at that point:

$$R(\Delta x) = \left.\frac{\partial \Delta x(V)}{\partial V}\right|_{V'} = \frac{2N \cdot \varepsilon_0 \cdot h}{k \cdot d} V' \tag{31}$$

where V' is the voltage required to cause Δx displacement:

$$V' = \sqrt{\frac{k \cdot d \cdot \Delta x}{N \cdot \varepsilon_0 \cdot h}} \tag{32}$$

Resulting in a displacement resolution that depends on the present displacement:

$$R(\Delta x) = 2\sqrt{\frac{N \cdot \varepsilon_0 \cdot h}{k \cdot d}} \sqrt{\Delta x}\,. \tag{33}$$

For applications working with optics or nanomechanics testing, sub-nanometer resolution may be important over large distances (~1mm) [133]. Referring to the case of Figure 3.3, the resolution at 5µm is three times better than the resolution at 40µm displacement (*R(5µm)=133nm/V*, while *R(40µm)=376 nm/V*).

3.3. Tailored Comb-finger Design and Simulation

To meet a specific resolution, we see that the actuator design can be adjusted through many parameters (suspension, gap, etc). However, in order to meet a required resolution at large displacement, we see that the resolution at small displacements will far exceed that which is necessary. This means we are essentially "wasting" voltage during small displacements of the device since we unnecessarily created extremely high resolution at those points. Ideally, a constant resolution over the entire range would be the most effective use of applied voltage. Thus, the resolution at large displacements should be improved while keeping the resolution at small displacements unchanged.

Since traditional planar comb-drives use a constant gap between the moving and stationary fingers, they have a constant change in capacitance per unit length and generate a force that is independent of the relative finger position. However, by locally modifying the capacitance profile, the force-engagement profile can be changed, enabling the resolution to be tailored as the displacement changes. For example, as the voltage is increased, the generated force scales as V^2. If the change in capacitance (i.e. force) decreased as the actuator is displaced, the effect of squaring the voltage (V^2) would be offset. The net effect would be the improved resolution at large deflections without over-engineering small displacements.

As mentioned in Chapter 1, previous approaches for tailoring the capacitance (and force) characteristics have varied the gap, $d \rightarrow d(x)$, between the moving and fixed comb-fingers. However, such variable-gap approaches cause large increases in the wafer real-estate required for each comb-pair (frequently >50%), resulting in a much larger device footprint [60, 61]. One group realized that with a variable height profile, $h \rightarrow h(x)$, the generated electrostatic force can also be made position dependent without increasing

device footprint. They expanded their simulated designs to include shaping in the vertical dimension, yet eventually conceded that their designs could not be fabricated due to manufacturing limitations [62].

The following sub-sections describe new 3-D comb-finger designs that use gray-scale technology to locally reduce the height of comb-fingers to alter the capacitance profile, as shown in Figure 3.4. Such an approach does not increase the area occupied by each comb-pair, while enabling similar tuning of displacement-voltage profiles. Both analytical and finite element analysis will be used to investigate the effects of shaping comb-drive components within the constraints of gray-scale technology. To enable the extension of these actuators to the optical fiber alignment systems developed in Chapters 5 and 6, 100μm silicon-on-insulator (SOI) wafers will be considered.

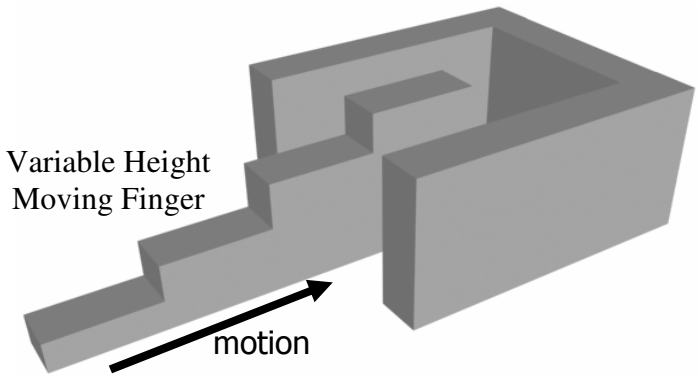

Figure 3.4: Schematic of a single variable height comb-finger moving between two constant height stationary fingers to achieve tailored comb-drive displacements.

3.3.1. Analytical Displacement Simulations (2-D)

To further establish the intuition for tailoring comb-fingers, analytical simulations using 2-D parallel plate approximations for the capacitance were used. This method was then extended to simulate the displacement-voltage behavior of a profile given a position

dependent capacitance change (*dC/dx*) [134]. Much of the analysis and designs will use 10:1 aspect ratios, which are readily achievable in DRIE, making the initial *gap=10μm* for 100μm SOI wafers. Determining the displacement-voltage characteristics of a comb-drive design starts by estimating the capacitance at each position of an individual comb-pair. The device behavior is then calculated by using an incremental method to determine the voltages required to create small displacements.

Let us consider our proposed design which locally varies the height of each comb-finger using gray-scale technology, $h \rightarrow h(x)$. The static displacement, $\Delta x(V)$, of this comb-drive is the point at which the generated comb-drive force and the restoring spring force are equal in magnitude. Assuming a linear spring constant, *k*, the displacement of a planar comb-drive was easily described as a quadratic function of applied voltage and linearly proportional to the other design parameters in Equation 30, and is repeated here using a height that changes with position, *h(x)*:

$$\Delta x = N \frac{\varepsilon_0 \cdot h(x)}{k \cdot d} V^2 . \tag{34}$$

Looking at Equation 34, we see that by changing the height profile of the comb-finger to scale as the inverse of displacement ($h(x) \propto 1/\Delta x$) will create a relationship where both displacement and voltage scale together quadratically:

$$\Delta x \propto N \frac{\varepsilon_0 \cdot \frac{1}{\Delta x}}{k \cdot d} V^2 \rightarrow \Delta x^2 \propto N \frac{\varepsilon_0}{k \cdot d} V^2 . \tag{35}$$

An example of a $(1/\Delta x)$ profile is shown in Figure 3.5. Essentially, as the displacement (Δx) increases with voltage, the height (*h*) decreases to offset the squaring of the applied voltage. This decrease in height is analogous to the gradual increase in gap between comb-fingers investigated by other groups [60, 61], but in our case the overall device

footprint remains unchanged. Similarly, the opposite effect can be produced by creating comb-fingers that gradually increase in height to give cubic or other force/displacement profiles (analogous to decreasing the gap).

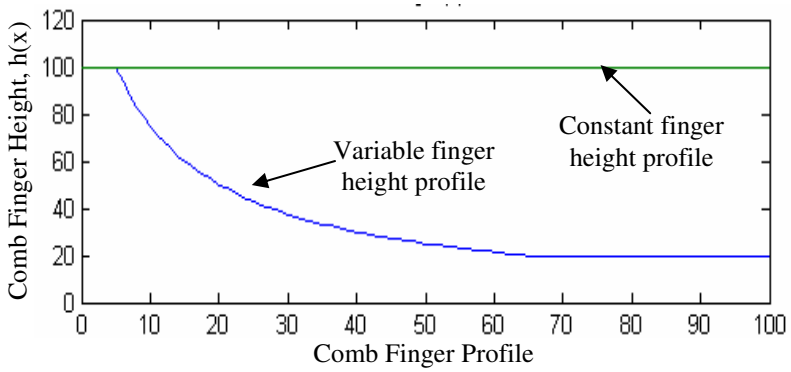

Figure 3.5: An example variable height comb-finger profile compared to the constant height case.

Assuming the capacitance is known as a function of position, an iterative method was introduced to simulate the displacement-voltage behavior of the device. First, an incremental movement, Δx_i, is defined. Then, Equation 34 is inverted to calculate the incremental voltage, ΔV_i, required to produce this incremental movement given the local change in capacitance:

$$\Delta V_i^{\,2} = \frac{k \cdot \Delta x_i}{N} \left(\frac{dC}{dx_i} \right)^{-1} \tag{36}$$

A running calculation of voltages is then used to assemble the voltage as a function of displacement, where ΔV_i is typically 0.1V:

$$V(x_i) = \sqrt{V(x_{i-1})^2 + \Delta V_i^{\,2}}\,. \tag{37}$$

Using a parallel plate approximation, we initially assume the change in capacitance with position (dC/dx) to simply be proportional to the local height of the moving comb-finger, $h(x_i)$. Figure 3.6 shows simulated displacement characteristics for

the height profiles shown in Figure 3.5, assuming N=200 comb-fingers, a gap of d=10μm, and a linear spring constant of 5 N/m.

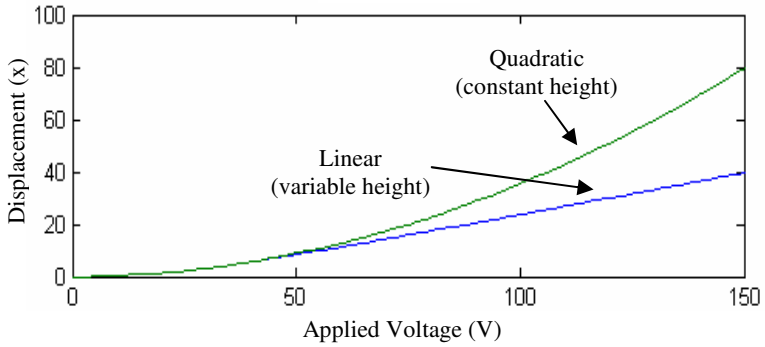

Figure 3.6: Calculated displacement as a function of voltage for designs using the constant height or variable height comb fingers shown previously in Figure 3.5.

As expected from the analysis presented earlier, the constant finger height profile results in a quadratic displacement-voltage curve, while the variable height comb-finger profile (now possible using gray-scale technology) creates a displacement-voltage curve that stays linear. In the variable height case, the incremental movement (dx) created at large voltages is reduced giving improved resolution of the comb-drive positioning. While this method is used here for the simplest case of $h(x) \propto 1/\Delta x$, it can be adapted to any C(x) relationship to predict the corresponding actuation behavior.

3.3.2. Finite Element Analysis (3-D)

The glaring difference between the planar and variable height case is the importance of fringing fields, which are neglected in planar devices. Given the dimensions and aspect ratios involved, simply reducing the height by 50% will not reduce the capacitance at each comb-position by exactly 50%. Thus, our parallel plate model must be extended to include the effects of fringing fields on the capacitance-position profiles to accurately predict actuator behavior using Finite Element Analysis (FEA). During our simulation, limitations imposed by fabrication processes must be considered,

as achievable comb-finger gaps and feature aspect ratios will be fabrication dependent. Our analysis and designs will continue to assume 100μm SOI wafers and 10:1 feature aspect ratios, giving an initial gap of $d=10\mu m$ as done before.

FEA models were constructed in the FEMLAB (V3.0) Electrostatics Module to emulate a grounded, variable height comb-finger moving between two stationary comb-fingers (held at a potential of V=1 Volt). The behavior of a device with N comb-pairs was estimated by multiplication. Top and side view schematics of the basic model geometry simulated are shown in Figure 3.7. While $h(x) \propto 1/\Delta x$ profiles were discussed earlier for intuition, it will be shown that fringing fields cause a height step to act in a similar manner. All comb-fingers were 100μm long with a maximum height of 100μm. The moving comb-finger has an initial 15μm full-height section, followed by 85μm long section with a reduced constant height, H. A ground plane was included 10μm below the comb-fingers to simulate a grounded substrate below the moving fingers. The system was bounded by a 3mm by 3mm grounded box. A mesh containing approximately 200K elements was found to be sufficient to ensure convergence of our solution.

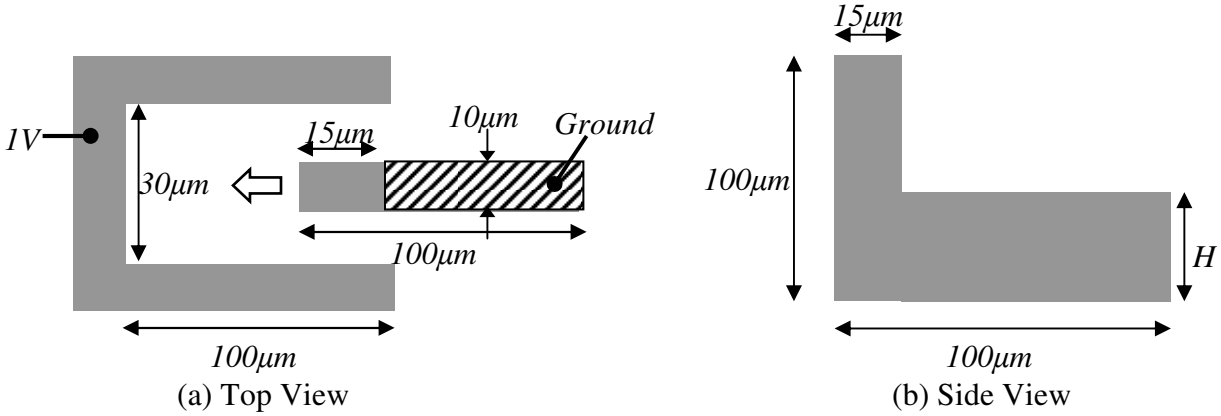

Figure 3.7: (a) Top view and (b) side view schematics of the FEA models built in FEMLAB. The moving comb-finger has an initial full-height section, followed by a section with reduced height (simulating a single gray level).

Rather than solve the Laplace equation ($\nabla^2 V = 0$) directly, FEMLAB was used to minimize total system energy in order to find the voltage distribution. This distribution specifies the electric field, and therefore electric energy density, in each discrete element. By integrating over the volume, the total electric potential energy of the system was obtained. The capacitance is then calculated using this total electric potential energy and the applied potential of 1V in Equation 25. The FEA simulated capacitance as a function of comb-finger overlap is shown in Figure 3.8 for values of H = 100μm (planar), H=40μm, and H=10μm. While the absolute value of capacitance will be different for each case, all curves were shifted vertically to a common origin to ease interpretation. This does not effect the force profiles since they depend only on the derivative.

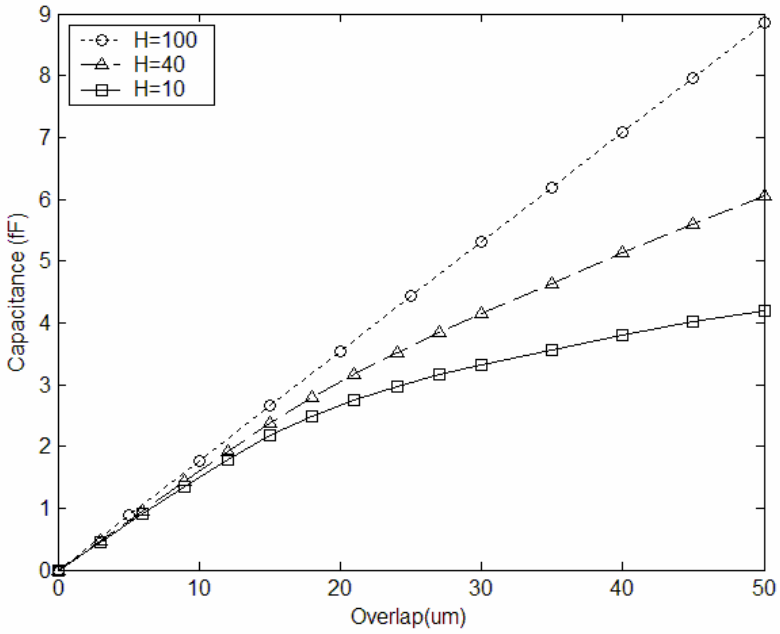

Figure 3.8: Simulated capacitance vs finger overlap for different height gray levels (H=100μm, 40μm, and 10μm) using FEMLAB.

Using 6th order polynomial curve fits, the derivative of each simulated case was calculated, see Figure 3.9. These curves represent the normalize force of each actuator as

a function of position. As evident in Figure 3.9, the planar case results in a constant force that is independent of position, consistent with the simple parallel plate model.

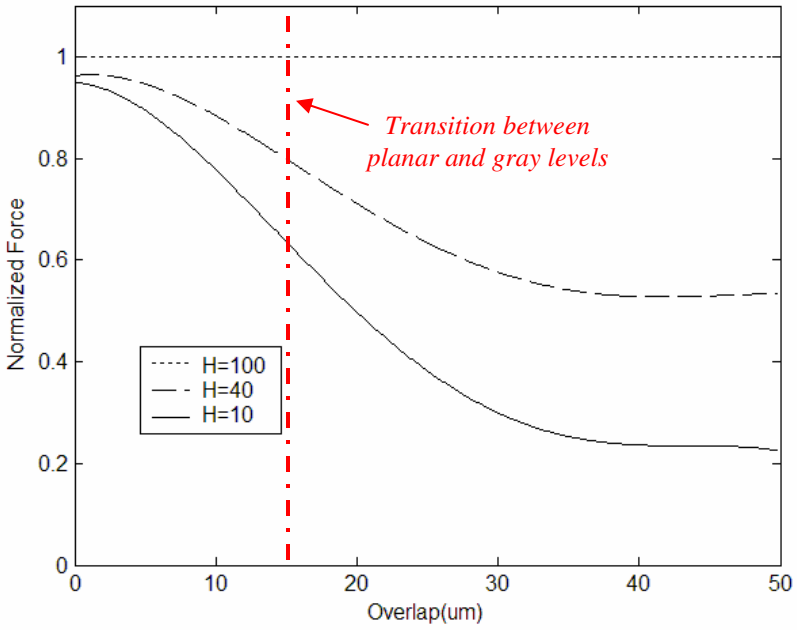

Figure 3.9: Normalized force vs. position for different height gray levels. Fringing fields cause the gradual transition. For H=10µm, the force is reduced by 75% at 40µm overlap.

From the FEA simulation results, we see that the effects of fringing fields on the capacitance profile are significant. If a parallel-plate approximation was sufficient for the variable-height case, the normalized force profile would resemble the stepped height profile, *h(x)*, shown in the side view of Figure 3.9. However, the fringing fields and our FEA model are able to "see" the change in height far before the reduced-height section arrives between the stationary fingers at an overlap of 15µm. Consequently, the force profile changes gradually around the transition point, and eventually settles to a smaller constant value. For the case of H=10µm, the total force is reduced by 75%, which should cause a corresponding improvement in displacement resolution of the actuator. Both the

analytical and FEA simulated force profiles will be compared to the experimental results of the fabricated gray-scale actuators in Section 3.6.1.

3.3.3. Instability Considerations

One issue that has been ignored to this point is the stability of the comb-drive actuator. In the analysis presented in Section 3.2, it was assumed that all forces in the y-direction (perpendicular to the stroke) will cancel. However, that assumption is premised on the moving comb-fingers being *exactly* ½ way between the stationary fingers. In reality, the comb-fingers are always slightly off-center and the force in the y-direction is non-zero:

$$F_y(\Delta x) = N\frac{\varepsilon_0 \cdot A(\Delta x)\cdot V^2}{2}\left(\frac{1}{(d-\Delta y)^2}-\frac{1}{(d+\Delta y)^2}\right) \quad \textbf{(38)}$$

Where $A(\Delta x)$ is the effective overlap area of a parallel plate capacitor on each side of the moving comb-finger. While $A(\Delta x)$ does not explicitly take fringing fields into account, any capacitance value including fringing fields can be represented as an equivalent parallel plate case ignoring fringing fields.

We can now define a virtual spring constant in the y-direction ($k_{y\text{-}virtual}$) as the derivative of F_y with respect to y, evaluated at the $\Delta y=0$ (center) position:

$$k_{y-virtual}(\Delta x) = \left.\frac{\partial F_y}{\partial y}\right|_{\Delta y=0} = \frac{2N\cdot\varepsilon_0\cdot A(\Delta x)\cdot V^2}{d^3} \quad \textbf{(39)}$$

This spring constant essentially represents the amount of instability present due to electrostatic forces. When this virtual spring constant of the electrostatic force exceeds the real mechanical spring constant of the suspension in the y-direction ($k_{y\text{-}real}$), an instability point is reached and both sets of comb-fingers will likely 'snap' together. If

we set $k_{y\text{-}virtual} = k_{y\text{-}real}$, we can find the maximum stable deflection point (Δx_{max}). For the case of a traditional, planar comb-drive, we start by re-arranging Equation 30 to be:

$$V^2 = \frac{k_x \cdot d}{N \cdot \varepsilon_0 \cdot h} \Delta x \,. \tag{40}$$

Substituting this V^2 expression into Equation 39 (set to $k_{y\text{-}real}$), and using the fact that for the planar case $A(x)=h\cdot\Delta x$, yields:

$$k_{y-real} = \left(\frac{2N \cdot \varepsilon_0 \cdot h \cdot \Delta x}{d^3} \right) \left(\frac{k_{x-real} \cdot d \cdot \Delta x}{N \cdot \varepsilon_0 \cdot h} \right). \tag{41}$$

Collecting terms and solving for Δx, we find the maximum stable deflection point for a traditional, planar comb-drive to be:

$$\Delta x_{\max} = d \cdot \sqrt{\frac{k_{y-real}}{2k_{x-real}}} \,. \tag{42}$$

Thus, the maximum displacement is actually dictated by the ratio of spring constants in the x- and y-directions, rather than their absolute value. It should be noted that the spring constants in Equation 42 are real, instantaneous values. While an approximation, Equation 42 can be used as a reasonable guideline for choosing a suspension design to suit your desired displacement needs. Further discussion on the design and performance of comb-drive suspensions is provided in Section 3.4.

For the case of a gray-scale tailored comb-finger however, Equation 42 is no longer applicable. Since the height is now a function of displacement, we must write $A(\Delta x)$ as an integral:

$$A(\Delta x) = \int_0^{\Delta x} h(x)dx \tag{43}$$

Making Equation 39:

$$k_{y-virtual} = \left.\frac{\partial F_y}{\partial y}\right|_{y=0} = \frac{2N \cdot \varepsilon_0 \cdot \int_0^{\Delta x} h(x)dx \cdot V^2}{d^3}. \quad \textbf{(44)}$$

Similarly, Equation 40 no-longer holds as the $V^2(x)$ relationship is now a complicated function dependent on $h(x)$, Δx, k_x, N, ε_0, and d:

$$V^2 = f(h(x), \Delta x, k_x, N, \varepsilon_0, d) \quad \textbf{(45)}$$

Substituting into Equation 44 gives $k_{y\text{-}virtual}$ for a variable height comb-finger:

$$k_{y-virtual}(x) = \frac{2N \cdot \varepsilon_0 \cdot \int_0^{\Delta x} h(x)dx \cdot f(h(x), \Delta x, k_x, N, \varepsilon_0, d)}{d^3}. \quad \textbf{(46)}$$

Given a particular $h(x)$ profile of the comb-finger, we can solve Equation 46 numerically for different values of displacement (explicit code is given in Appendix A). Using the comb-finger profiles and assumptions from Figure 3.5, $k_{y\text{-}virtual}$ was calculated as a function of displacement, as shown in Figure 3.10:

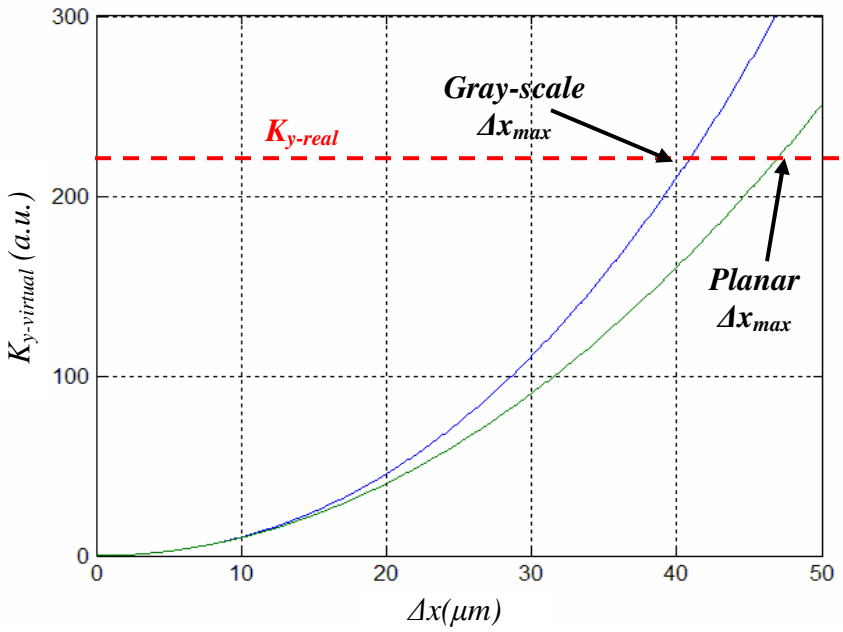

Figure 3.10: Calculated virtual spring constants for both planar and variable height gray-scale comb-finger designs.

In Figure 3.10 a fictitious line has been added to represent an arbitrary value for $k_{y\text{-}real}$. It is clear that a device with gray-scale variable height fingers will reach this limiting threshold earlier than a corresponding planar device would. Such behavior is expected from the gray-scale design because improved resolution was obtained by increasing the voltage required to generate the same displacement. Even though the overlap area of the gray-scale comb-fingers is smaller than the planar case, the fact that force scales with V^2 over-compensates for the reduction in overlap area. Thus, vertically shaped gray-scale comb-fingers can be expected to have a net decrease in stability compared to traditional planar comb-drive designs.

3.4. Reduced Height Suspensions

While shaping comb-fingers in the vertical dimension can alter the force generated by the comb-drive, gray-scale technology may also be used to locally reduce the height of comb-drive suspensions, for tailoring spring constants and/or resonant frequencies. Significant research has been performed regarding the various suspension designs possible for electrostatic actuators [50, 52-54, 135]. The 'folded-flexure' suspension design, shown schematically in Figure 3.11, is one of the simplest designs and has a relatively high compliance in the direction of the stroke, while providing stability in the direction perpendicular to the stroke (i.e. large Δx_{max}). The approximate spring constant in the direction of motion, $k_{Suspension}$, of the 'folded-flexure' design is [50]:

$$k_{Suspension} = \frac{2Ehb^3}{l^3} \tag{47}$$

where E is Young's Modulus, h is the spring height, l is the leg length, and b is the width of each leg. For planar designs, the spring constant is usually changed by adjusting the

spring length (at the expense of increased device area), or the spring width (at the expense of higher aspect ratio). However, gray-scale technology offers the possibility of tuning the suspension without increasing device area or aspect ratio.

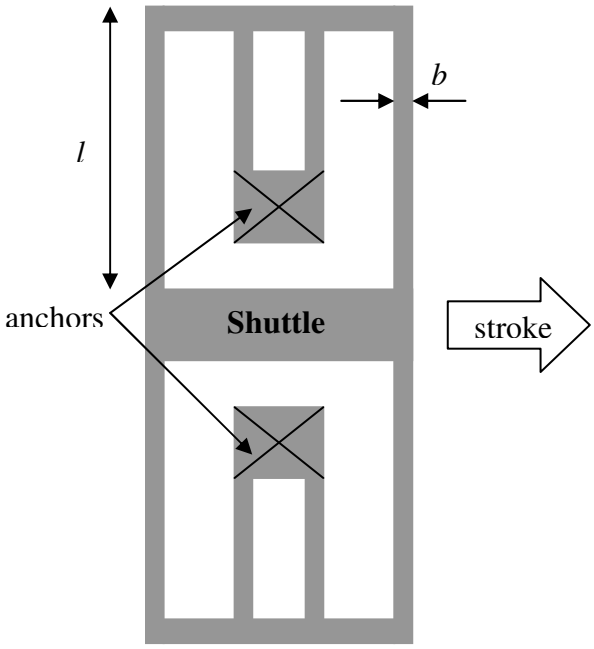

Figure 3.11: Top view schematic of a 'folded-flexure' suspension.

Assuming that the leg width, b, is limited to some minimum width, modulating the suspension height is the only method for decreasing $k_{Suspension}$ without increasing device area (i.e. length). Reducing the thickness of the entire device would reduce the spring constant, however this simultaneously reduces the force generated by the comb-drive in an identical ratio, offsetting the effect (see Equation 29). By fabricating the suspension using gray-scale technology, the spring height may be reduced without changing the comb-drive force, resulting in larger displacements at corresponding voltages. The change in spring constant will also cause a change in resonant frequency, ω_0, in accordance with:

$$\omega_0 = \sqrt{\frac{k_{Suspension}}{m_{resonator}}}. \qquad \textbf{(48)}$$

For the devices discussed later, the suspension mass is approximately 18% of the entire resonator mass, $m_{resonator}$. However, since the beam velocity varies along the length of the suspension, it should be described with an effective mass (m^*). For a simple cantilever beam, $m^* = 0.24 \cdot m$ [136], making the effective mass of the spring closer to 5% of the overall mass, of which only part is removed by reducing the suspension height. Thus, Equation 48 can be used for reasonably accurate predictions of resonant frequency shifts.

3.5. Fabrication

In order to integrate 3-D structures within an electrostatic MEMS actuator, the gray-scale process must be developed as part of an appropriate process flow. The fabrication process developed in this work, and outlined in Figure 3.12, is based on silicon-on-insulator (SOI) technology, where a silicon dioxide sacrificial layer is sandwiched between two crystalline silicon substrates of customized thickness.

Metal liftoff is first used to pattern contact pads and alignment marks. Gray-scale lithography is then performed in a projection lithography system (GCA-Ultratech) at the Laboratory for Physical Sciences (LPS) using a specifically designed gray-scale optical mask. DRIE is used to transfer the planar and variable height structures into the silicon simultaneously. As discussed in Chapter 2, the etch selectivity is controlled to properly define the vertical dimensions of each *gray-level* in silicon. Before removing the remaining photoresist, the wafer is dipped in buffered hydrofluoric acid (BHF 1:6) to remove the sacrificial silicon dioxide layer. Soaking in successive solutions of isopropyl alcohol (IPA) enables released structures without significant stiction problems due to its lower surface tension. Oxygen plasma is used to strip any remaining photoresist. Explicit process details are given in Appendix B.

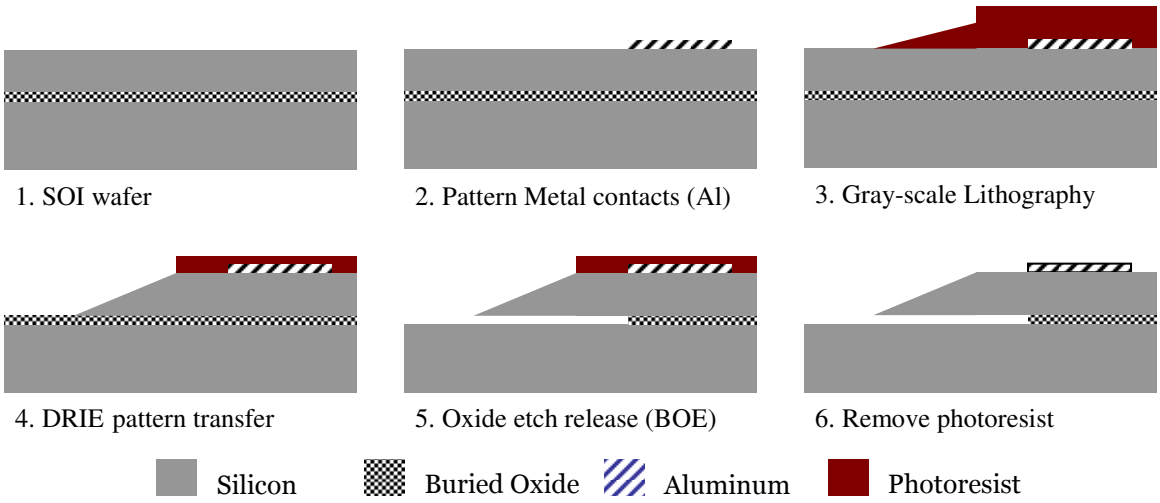

Figure 3.12: Integrated process flow for creating electrostatic MEMS actuators with 3-D suspended components.

An initial SOI device layer of 100μm and a buried oxide layer of 2μm were used, where the device layer was chosen to be appropriate for further extension to the actuation an optical fiber (125μm in diameter) later in Chapters 5 and 6. It is imperative to note that this 3-D actuator process flow is no more complex than the planar case, although each step must be precisely controlled to produce the desired results.

The design and fabrication challenges for such devices fall into two main categories: optical mask design and DRIE control. For designing the optical mask, a small offset was introduced between the desired structure edge and the pixilated design, according to the characterization of Section 2.3.1. For variable height comb-fingers, this offset was very important to ensure that the gap between fingers was constant. For DRIE, it was necessary to control the etch selectivity while etching high aspect ratio structures (10:1) and combating aspect ratio dependent etching (ARDE), as discussed previously in Chapter 2 [34]. In the case of variable-height comb-fingers, this means the etch selectivity inside the fingers is different from that in open areas. By using the buried

oxide layer as an etch stop, over-etching of the sample was used to further etch the gray-scale structures without significantly affecting adjacent planar structures.

An SEM of the initial variable height comb-finger design after DRIE is shown in Figure 3.13. A single gray-level 30μm long and 10μm high was used to remove a 'notch' from a planar comb-finger. It is important to note that the roughness seen on the gray level is easily removed with short isotropic plasma etching steps, and as such should have negligible effect on the capacitance and device performance. Figure 3.14 shows an SEM of a different variable height comb-finger design after fabrication and a short isotropic plasma etching step. The roughness is essentially gone, leaving a smooth reduced height surface. An example of a reduced height suspension fabricated with gray-scale technology is shown in Figure 3.15, where roughness is inconsequential for the mechanical properties of the suspension.

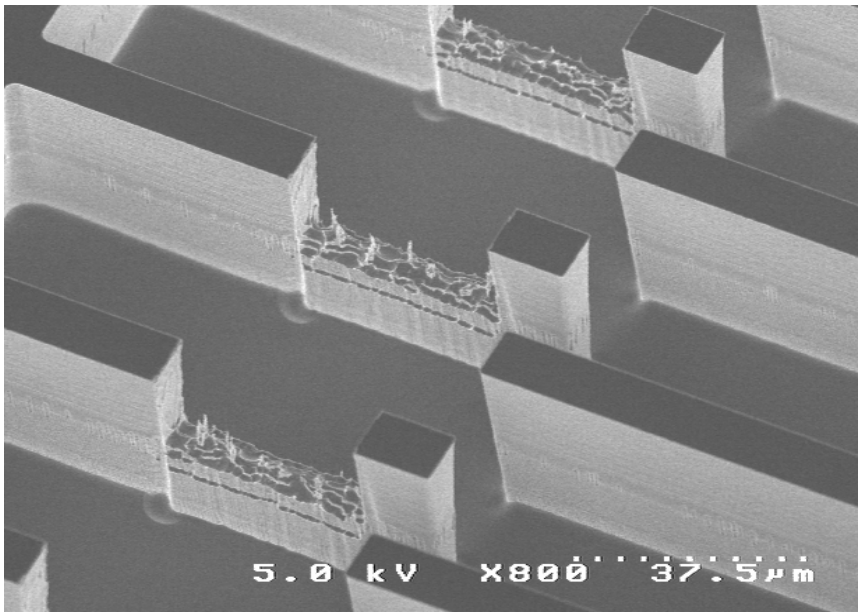

Figure 3.13: SEM of variable height comb-fingers incorporating a single intermediate gray level. Roughness may be reduced with post-processing.

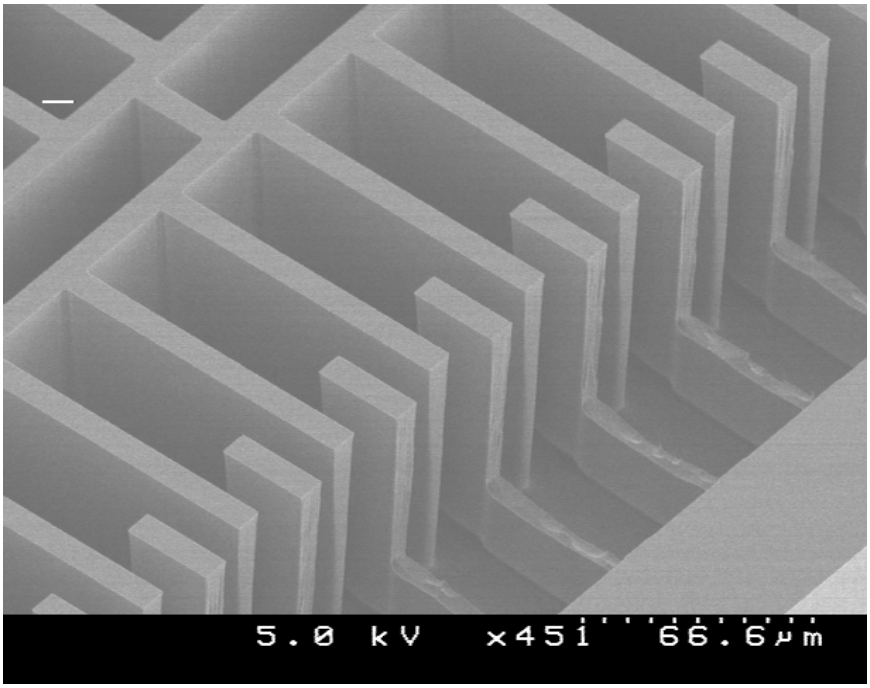

Figure 3.14: SEM of another variable height comb-drive where isotropic plasma etching leaves the gray-scale comb-fingers smooth.

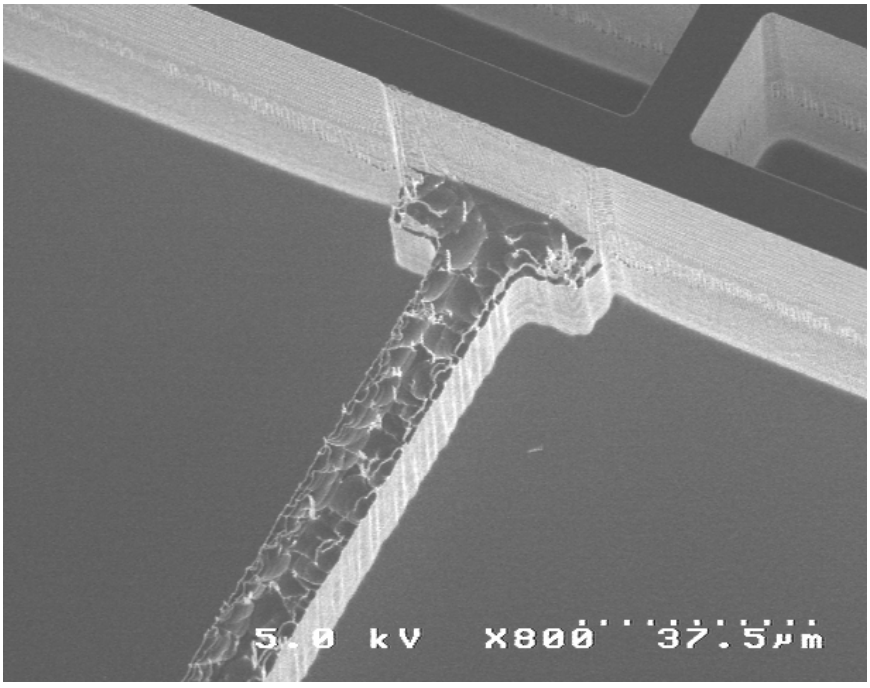

Figure 3.15: SEM of reduced height comb-drive suspensions fabricated with gray-scale technology.

3.6. Comb-drive Testing

The simulated static and dynamic behavior of comb-drive actuators incorporating variable height gray-scale features was confirmed by fabricating two comb-drives on a single wafer, where the only difference was either in the comb-finger profile or the suspension height.

3.6.1. Reduced Height Comb-fingers

For the case of reduced height comb-fingers using gray-scale technology, devices had identical suspensions ($L=1000\mu m$, $b=10\mu m$), gap ($d=10\mu m$), and number of fingers ($N=100$). Two comb-drive devices were fabricated, one planar device and one with a gray-scale notch (as shown in Figure 3.13). The deflection of these two devices was then measured under an optical microscope for various DC applied voltages to compare static deflection characteristics. The approximate spring constant for the suspension was extracted from the planar actuator using its measured actuator dimensions in silicon and analytical equations to estimate the force. The measured dimensions of the gaps/finger widths in silicon were also imported into the FEMLAB model to account for fabrication errors. Using the iterative technique described previously in Section 3.3.1, the displacement characteristics were simulated for comparison to experimental results.

Figure 3.16 shows the measured displacement as a function of applied voltage for each of the two actuator types: planar and variable height (with gray level height of 40μm). The behavior of the planar actuator is accurately predicted using simple parallel plate approximations for the capacitance. For the variable height comb-finger case, we see that the parallel plate model first over-estimates, then under-estimates the actual displacement. However, the FEMLAB capacitance model along with the iterative

displacement calculation method was able to account for fringing fields and accurately predict the displacement behavior of the variable height device.

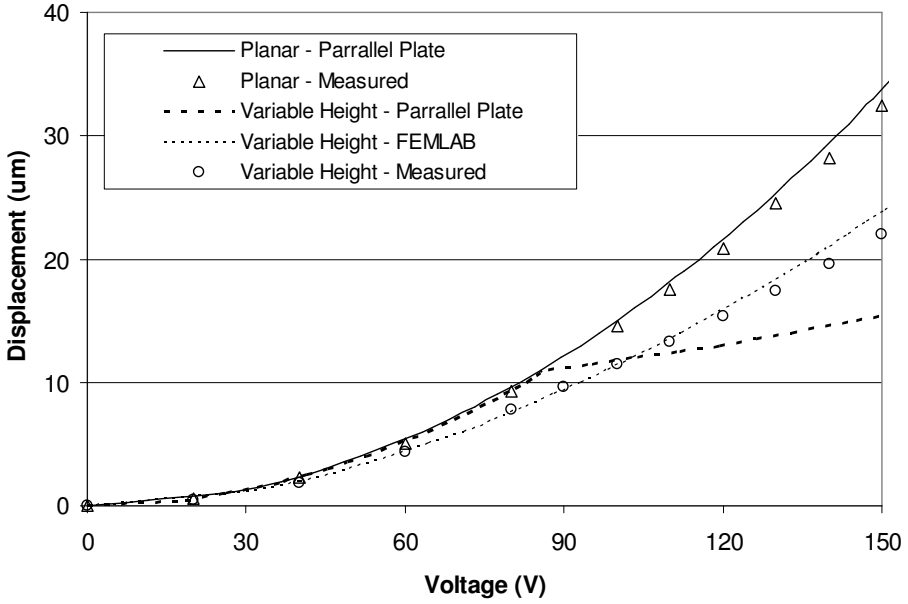

Figure 3.16: Measured displacement with simulated responses for comb-drives incorporating planar or variable height comb-finger profiles (40µm tall, 30µm long gray-scale section). FEMLAB models are able to accurately capture variable height comb-drive behavior.

A summary of the actuation magnitudes and resolutions from the data in Figure 3.16, is shown in Table 3.1. For the planar case, the amount of displacement achieved over the final 50V is *larger* than the displacement achieved over the first 100V (recall that comb-drive force scales with V^2). However, for the variable height case, the displacement measured over the final 50V is actually *smaller*, leading to a significantly better resolution at large displacements (227 vs 344 nm/V) compared to the planar case. Looking back to Equation 33, we see that a planar actuator could offer similar resolution at 20µm displacement by increasing the spring constant from 4.2 N/m (measured) to ~9.6 N/m. However, the voltage required to cause ~20µm displacement using the new spring constant would increase to 177V compared to the variable height device that requires only 140V.

Table 3.1: Displacement and resolution data for both planar and gray-scale comb-finger designs.

	Incremental Displacement (μm)		Resolution (nm/V)	
	0 → 100 V	100 → 150 V	@5μm	@20μm
Planar	14.6	17.8	141	344
Variable Height (Gray-scale)	11.5	10.5	126	227

These results confirm that our iterative technique and FEA models can be used to accurately predict the static deflection behavior of variable height comb-drives fabricated using gray-scale technology. It should also be noted that these improvements were achieved with a conservative design. Devices with lower gray level heights (than the 40μm device discussed above) should show even stronger response.

3.6.2. Reduced Height Suspensions

A second set of comb-drive actuators were designed and fabricated with identical planar comb-finger layouts to investigate the effects of locally reducing the height of the suspension structure. By using gray-scale technology to reduce the suspension height, the spring constant should be reduced proportionally with the height. This modulation comes without effecting the generated comb-drive force, resulting in a net increase in displacement for a given voltage.

Static displacement measurements were made using DC applied voltages under a microscope for two devices with identical lengths ($L=1000\mu m$) and widths ($b=10\mu m$), but different heights: $h=100\mu m$ (planar) and $h\sim30\mu m$ (variations from gray-scale uniformity). The resulting static displacement measurements are shown in Figure 3.17.

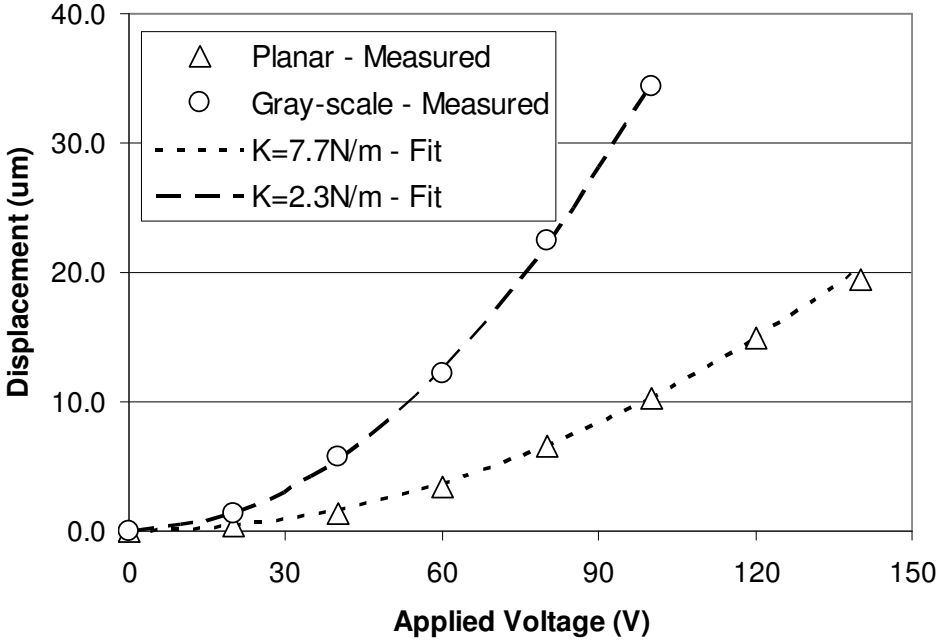

Figure 3.17: Measured displacements for comb-drives using planar or gray-scale suspensions.

By using the measured comb-finger widths/gaps and parallel plate approximation for the force, the spring constants were estimated to be 7.7N/m for the 100μm tall planar suspension and 2.3N/m for the 30μm tall gray-scale suspension. Referring back to Equation 47, we see that the spring constant should scale with the height, and in fact, our measurements confirm that reducing the spring to 30% of its original height reduces the spring constant by an identical amount.

Another consequence of a reduced height suspension design is that the dynamic behavior of the device also changes due to the reduced spring constant in Equation 48. A Veeco Wyko NT1100 Optical Profiler with DMEMS option was used to test the dynamic behavior of comb-drive devices. The Wyko uses stroboscopic white-light interferometry to measure the position of the comb-drive during a frequency sweep at a particular phase. This information was then transformed into an approximate displacement to extract the resonant frequency for each of the two devices discussed above, and the results are shown in Figure 3.18. (Note: more detail regarding the Wyko system will be given in

Chapter 4 which focuses on the dynamic characterization of tunable comb-drive resonators). Ignoring any change in resonator mass caused by reducing the suspension height (as explained earlier), the measured change in resonant peak (f_0=1630Hz→ f_0'=910Hz) corresponds well to the prediction made using the reduced spring constant and Equation 48 (f_0'=891Hz).

One drawback of reducing the suspension height is that the spring constant in the vertical direction (out of the plane of the wafer) is significantly decreased, leading to difficulty releasing the buried oxide layer with wet etching. This problem could potentially be solved by using dry vapor-etch techniques [137].

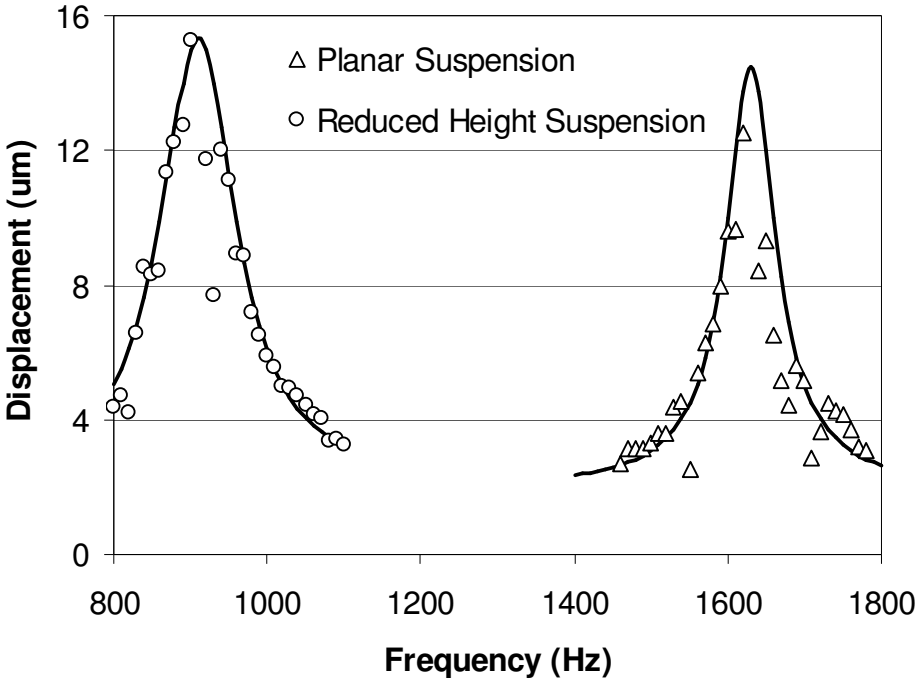

Figure 3.18: Dynamic measurements of the planar and reduced height comb-drive devices.

3.7. Conclusion

This chapter has reviewed the basic mechanisms behind electrostatic MEMS comb-drives. The design and simulation of comb-drive actuators incorporating gray-scale technology to tailor actuator properties (without increasing the device footprint) was presented using both analytical approximations and finite element analysis (in FEMLAB).

Multiple comb-drive actuators with reduced height comb-fingers and suspensions were then fabricated and tested to experimentally confirm the predicted behavior of improved resolution and reduced driving voltages. Specifically, for variable height comb-fingers, the displacement resolution at 20μm was improved from 344nm/V to 227nm/V with little effect on resolution at smaller displacements. On a separate device, suspension spring constants were reduced from 7.7N/m to 2.3N/m to enable lower driving voltages, achieving >3 times the deflection at 100V.

These results have clearly illustrated the value of using gray-scale technology within electrostatic MEMS actuators to modify device behavior without increasing overall actuator footprint. Measurements of static and dynamic actuator behavior confirm that our FEA model and iterative displacement calculation techniques are able to accurately predict 3-D actuator behavior. These results serve as the foundation for developing the tunable resonator devices presented in Chapter 4, as well as for the optical fiber alignment systems developed in Chapters 5 and 6.

CHAPTER 4: VERTICALLY-SHAPED TUNABLE MEMS RESONATORS

4.1. Introduction

Micromechanical resonators have received significant attention over the past 20 years due to their applications in thin film characterization [138], signal processing (RF and IF filters) [65, 67, 139], gyroscopes [68], electrostatic charge and field sensors [69], mass sensors for bio-chemical sensing [140], and vibration-to-electric energy conversion [141-144]. Laterally driven comb-resonators are often preferred due to their reduced damping and large travel range [49]. Vacuum sealing techniques have been used to increase the quality (Q) factor of comb-resonators to >2,000 in some cases [67].

This chapter is devoted to presenting an additional important application for the variable-height comb-drive structures presented in Chapter 3: voltage-tunable MEMS resonators. Previous MEMS tuning methods will be reviewed briefly, and the principle of vertically-shaped gray-scale electrostatic springs is introduced as a tuning mechanism. Design and simulation of vertically-shaped comb-fingers as electrostatic springs will be followed by testing results that demonstrate their bi-directional tuning capability of MEMS resonators in the 2 kHz range.

4.2. Tunable MEMS Resonator Operation

Since the inception of MEMS resonators, as far back as 1967 [70], the natural progression has been towards developing tunable resonators for use in tunable filters and other frequency dependent applications. The most popular technique is the use of an additional electrode beneath a suspended cantilever, as shown in Figure 4.1, to tune the resonant frequency down [66, 70-72, 139]. The situation can be best described using the

energy method, where the total potential energy (U) is the sum of the kinetic energy of the beam and the potential energy in stored in the tuning capacitor [72]:

$$U = \frac{1}{2} k_{eff} z^2 = \frac{1}{2} k_{mech} z^2 + \frac{1}{2} C V^2 \quad \textbf{(49)}$$

where k_{eff} is the effective spring constant, k_{mech} is the mechanical spring constant, z is the deflection magnitude, and C and V are the capacitance and voltage on the tune electrode, respectively. Assuming the voltage is constant, taking the 2nd derivative of Equation 49 yields an expression for k_{eff}, where the second term represents an electrostatic spring (k_{elec}):

$$k_{eff} = k_{mech} + k_{elec} = k_{mech} + \frac{1}{2} \frac{\partial^2 C}{\partial z^2} V^2 . \quad \textbf{(50)}$$

For the cantilever example in Figure 4.1, C can be approximated as a parallel-plate capacitor using the electrode area (A), gap (d), and dielectric constant of air (ε_0):

$$C = \frac{\varepsilon_0 A}{(d - z)} . \quad \textbf{(51)}$$

Combining Equations 50 and 51 yields:

$$k_{eff-ParallelPlate} = k_{mech} - \frac{\varepsilon_0 A}{(d - z)^3} V^2 . \quad \textbf{(52)}$$

The major drawbacks of the parallel plate tuning technique are that the electrostatic spring strength depends on the magnitude of vibration of the cantilever and the initial gap (d), which is dependent on the tuning voltage [72]. Thus, the tune and actuation voltages are inherently coupled.

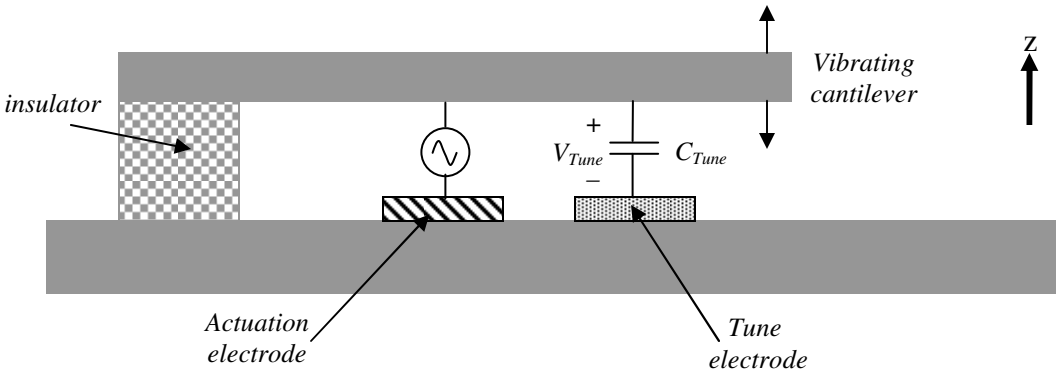

Figure 4.1: Schematic of a MEMS resonant cantilever with drive and tune electrodes for tuning the resonant frequency down.

Alternative tuning techniques have been developed that modify the capacitance-position relationship, *C(x)* for in-plane resonators; de-coupling the actuation and tuning effects, and enabling electrostatic tuning of the resonant frequency either up or down. First, so-called "fringing field actuators," have demonstrated tuning of linear and non-linear stiffness coefficients [73, 74]. These operated only over a small range of motion (~2μm) and oscillated perpendicular to the comb-finger orientation, increasing footprint and air damping.

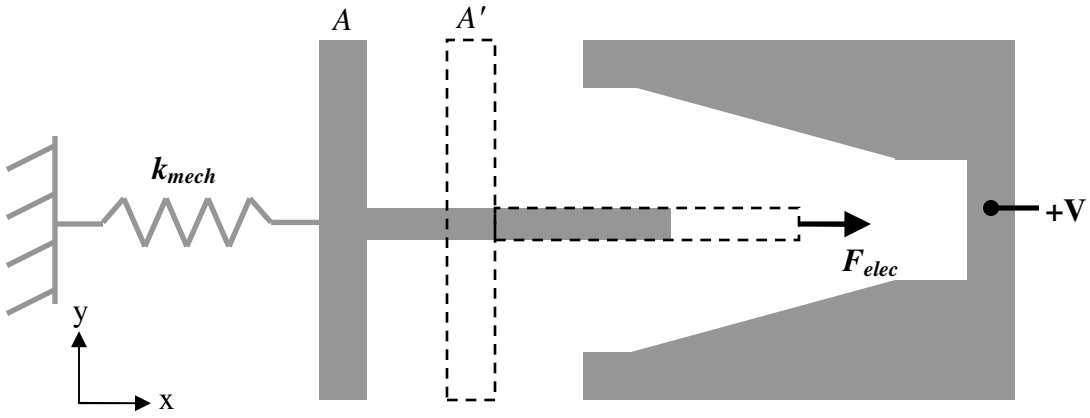

Figure 4.2: Electrostatic spring tuning via tailored capacitance-position profiles using variable-gap comb-fingers [61].

Shown in Figure 4.2 is a tuning method using familiar variable-gap comb-fingers [61]. In this case, the electrostatic force is a function of comb-finger engagement, so a

DC voltage can create an electrostatic spring over large displacements. Note that a constant gap and height comb-finger should provide a uniform mechanical force along the travel distance, so electrostatic spring would be observed.

Describing the variable gap situation using the energy method is now slightly less intuitive (but still valid) because both the gap and area of the capacitor change with distance. Instead, we can qualitatively consider the forces generated by the comb-fingers. Applying a voltage (V) to the static electrode of Figure 4.2 creates an electrostatic force in the positive x-direction on the moving finger. As the comb-finger moves from point "A" to point "A'," the electrostatic force remains in the positive x-direction and the magnitude increases, shown schematically in Figure 4.3(a). Also shown in Figure 4.3 is the mechanical restoring force (F_{mech}) created by the spring (k_{mech}). In a sense, the tuning electrode "helps" pull the resonator in the x-direction more as the engagement increases, weakening the spring ($k_{eff} < k_{mech}$). A plot of the net force (F_{net}) in Figure 4.3(b) shows the reduced k_{eff} is valid over the range where the gap changes with distance.

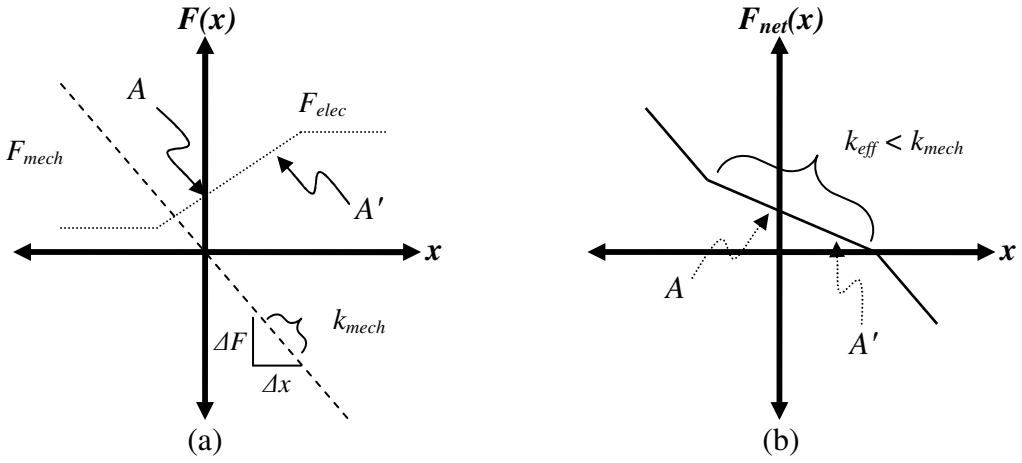

Figure 4.3: Graphic representation of the individual mechanical and electrostatic forces in (a), as well as the resulting net force in (b), for a weakening comb-finger design.

The strength of this electrostatic spring (k_{elec}) is voltage dependent, causing a change in k_{eff} and shift to a new resonant frequency (f_{tuned}):

$$f_{tuned} = \frac{1}{2\pi}\sqrt{\frac{k_{eff}}{m}} = \frac{1}{2\pi}\sqrt{\frac{k_{mech} + k_{elec}}{m}}, \quad \textbf{(53)}$$

which can also be expressed in terms of the original resonant frequency (f_0):

$$f_{tuned} = f_0\sqrt{1 + \frac{k_{elec}}{k_{mech}}}. \quad \textbf{(54)}$$

For the case shown in Figure 4.3, k_{elec} is taken as a negative since it is in the opposite direction from the k_{mech} restoring spring, essentially "weakening" k_{eff} and tuning to a lower resonant frequency. The opposite tuning behavior, a "stiffening" spring, can also be produced by using a comb-finger design where the gap increases with distance. In such a "stiffening" design, the electrostatic force would "help" significantly in the beginning, and then provide less help as the deflection increased. Thus, the spring would appear to be "stiffer" than the mechanical spring constant ($k_{eff} > k_{mech}$), and the resonant frequency would increase.

While variable gap resonators are versatile, once again their tuning ability comes at the expense of dramatically increasing the device size. However, as shown in Chapter 3, vertically-shaped gray-scale comb-fingers can provide variable force-engagement profiles over large travel ranges without increasing the footprint of a comb-finger pair.

4.3. Gray-scale Electrostatic Springs

The design, simulation, and fabrication of variable height gray-scale electrostatic springs used here are quite similar to the methods developed in Chapter 3. The following sub-sections will introduce the three types of variable-height electrostatic springs investigated in this research, as well as simulation and fabrication results to predict their relative spring constants.

4.3.1. Design

As evident from simulations in Chapter 3, a vertical step in comb-finger height creates a smoothly varying force-engagement profile (see Figure 3.9), of which a portion appears to be quasi-linear and could be used an electrostatic spring. Therefore, the three designs presented here contain only a single gray level for simplicity, and the height of the gray level (in conjunction with the applied voltage) will determine the strength of the electrostatic spring. More precise force-engagement profiles are possible by incorporating more gray levels (as will be shown with simulations in Section 4.5).

The first gray-scale electrostatic spring design is shown in Figure 4.4, where the moving comb-fingers initially engage with a reduced height section, followed by a full height (planar) section. Such a design is analogous to the decreasing gap design shown in Figure 4.2, and will thus be referred to as the "weakening" finger design.

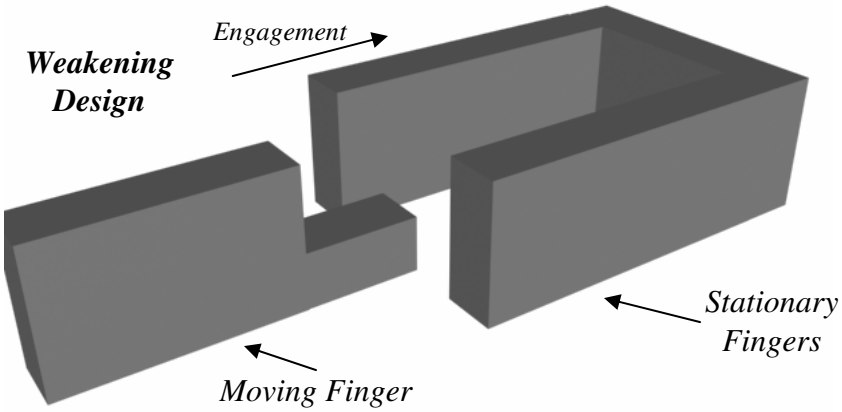

Figure 4.4: Spring-weakening comb-finger design using a single gray level on the moving finger.

A second electrostatic spring design is shown in Figure 4.5(a). The moving finger initially engages with a full-height (planar) section, followed by a reduced height section some distance later. Thus, the electrostatic force decreases as the engagement increases, analogous to an increasing gap comb-drive design. The net effect is a "stiffening" of k_{eff}.

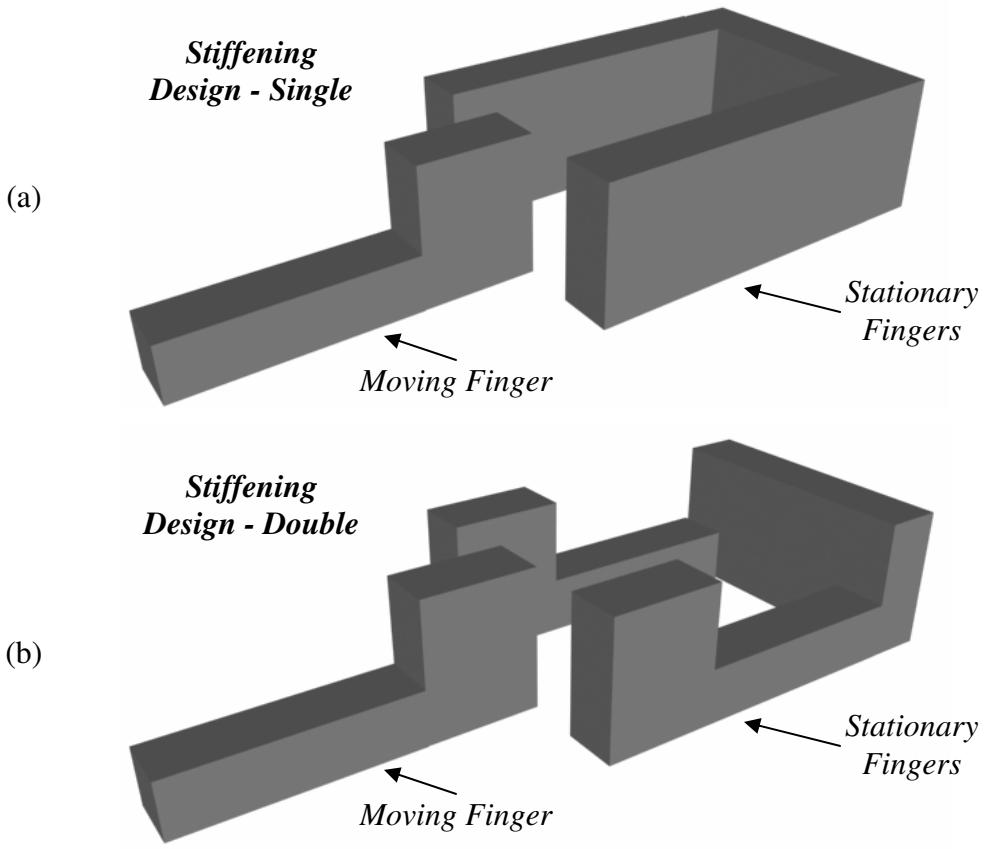

Figure 4.5: Spring stiffening designs using (a) single or (b) double vertical shaping of the comb-fingers with gray-scale technology.

Figure 4.5(b) shows an additional novel design that vertically-shapes both stationary and moving comb-fingers. As the fingers engage in this "stiffening – double" design, there should be a dramatic change in force as the two full-height sections pass each other. Since the fully engaged force will be lower for the "double" design, it is anticipated that a more dramatic electrostatic spring "stiffening" effect will be observed (assuming the change in force from max to min occurs over a similar engagement change). A variable-gap comb-finger design would have particular difficulty replicating the analog to this "double" shaping design since it would require shaping both moving and stationary fingers, leading to an increase in device footprint. It must be noted that the electrostatic spring will be non-linear for each of these three cases due to their simplistic design, a trait that will be discussed in more detail towards the end of this chapter.

4.3.2. Simulation

The capacitance as a function of engagement for each spring design was simulated using FEMLAB for different gray level heights. As in Chapter 3, 100μm SOI wafers are assumed, with 10μm comb-finger gaps and widths. Capacitance-engagement data were fit with a 6^{th}-order polynomial, and the derivative taken near the height change to obtain the local force-engagement profile. The horizontal geometry of each design and the engagement required to reach the edge height step(s) are shown in Table 4.1.

Table 4.1: In-plane design specifications for resonator designs.

Design	Planar Section Length (μm)	Gray-scale Length (μm)	Engagement to Height Change (μm)
Weakening	85	30	30
Stiffening – Single	15	85	15
Stiffening – Double	15	85	30

A derivative of the force-engagement profile near the height step was used to estimate the generated electrostatic spring constant. While in general taking multiple derivatives of polynomial fit functions can be inaccurate, later results will show that derivatives in the middle of the simulated range (near the height step) are able to predict resonator behavior with reasonable accuracy. Plots of the 1^{st} and 2^{nd} derivatives of the simulated capacitance for each type of comb-finger design are shown in Figure 4.6, Figure 4.7, and Figure 4.8, where each line indicates a specific height of the associated gray level. The plots represent example electrostatic forces (F_{elec} - left plots) and spring constants (k_{elec} - right plots) as a function of engagement for a single comb-finger.

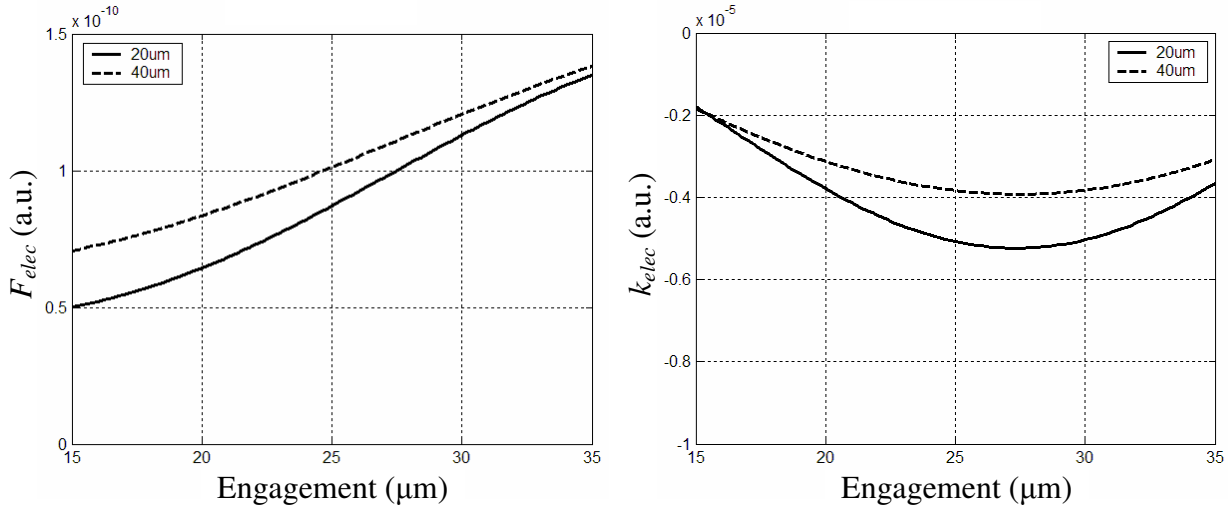

Figure 4.6: Simulated F_{elec} and k_{elec} for a "weakening" design with 20 or 40μm gray levels.

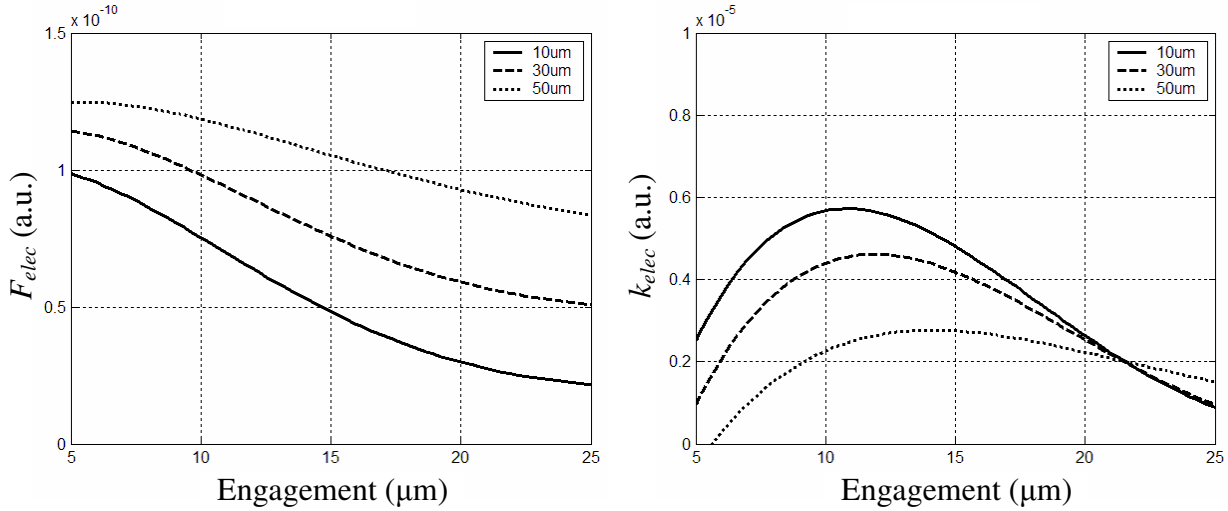

Figure 4.7: Simulated F_{elec} and k_{elec} for "stiffening–single" design with 10, 30, or 50μm gray levels.

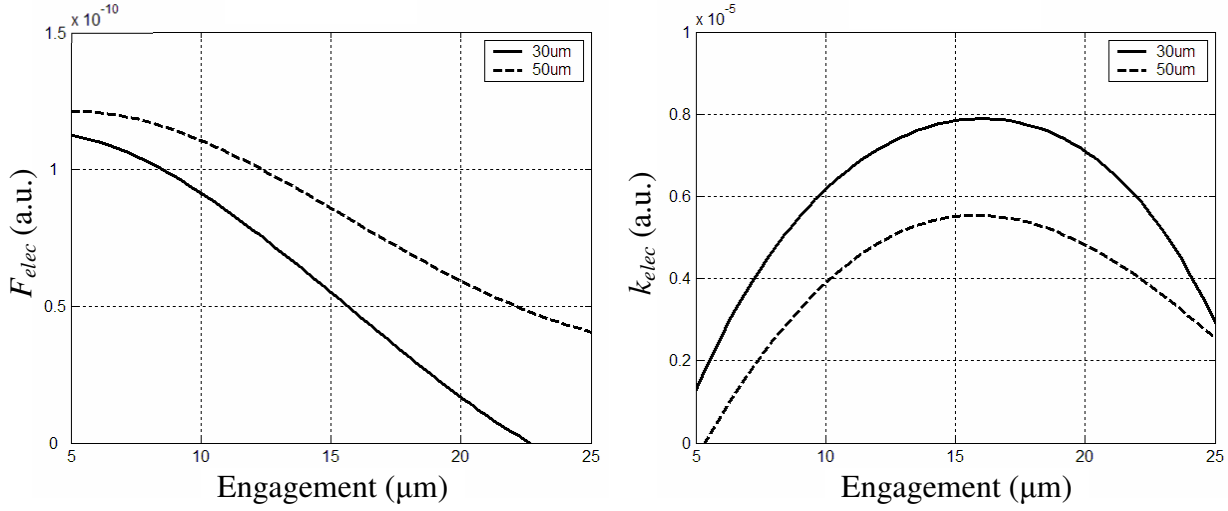

Figure 4.8: Simulated F_{elec} and k_{elec} for "stiffening–double" design with 30 or 50μm gray levels.

The 1st derivative of capacitance can be used in Equation 26 from Chapter 3 to obtain the force, while the 2nd derivative should be plugged into Equation 50 from Chapter 4 to obtain the spring constant. In each case, one must multiply by the number of comb-fingers in the system. The peak value of k_{elec} is calculated in Table 4.2 for each simulated design, assuming N=50 comb-fingers and an applied voltage of 100V. As expected, lower gray levels create larger changes in force, and thus higher magnitudes of k_{elec}. It is also clear that the "stiffening – double" design is a significant improvement over the "stiffening – single" design (1.97 N/m vs. 1.15 N/m for 30μm high gray levels).

Table 4.2: Peak simulated spring constants for different finger designs and gray level heights.

Design	**Height (μm)**	**Peak k_{elec} (*N=50, V=100*) (N/m)**
Weakening	20	– 1.31
Weakening	40	– 0.98
Stiffening – Single	10	1.43
Stiffening – Single	30	1.15
Stiffening – Single	50	0.69
Stiffening – Double	30	1.97
Stiffening – Double	50	1.39

As a rough comparison, we consider the geometry required for a planar, variable-gap model to produce tuning equivalent to the "stiffening – double" design above (using the model of *Jensen et al* [61]). For similar fabrication constraints, the gap would have to change from approximately 10μm to 20μm over a 10μm engagement length. However, by changing the gap, the density of fingers is reduced, so a device with similar footprint will only provide 2/3 the tuning of the gray-scale devices shown above. It is possible that a combination of variable-gap and variable-height comb-fingers could provide even stronger tuning effects.

4.3.3. Layout and Fabrication

The layout of tunable gray-scale resonators is based on that shown in Figure 4.9. A set of 48 stationary planar comb-fingers are connected to an actuation electrode, where the AC drive signal is applied. The "tune" electrode on the right side, which always receives a DC voltage, is attached to 48 stationary gray-scale comb-fingers. The resonant mass is made entirely of planar comb-fingers, except for the "stiffening – double" design that requires comb-fingers on the "tune" side of the resonant mass to be shaped vertically.

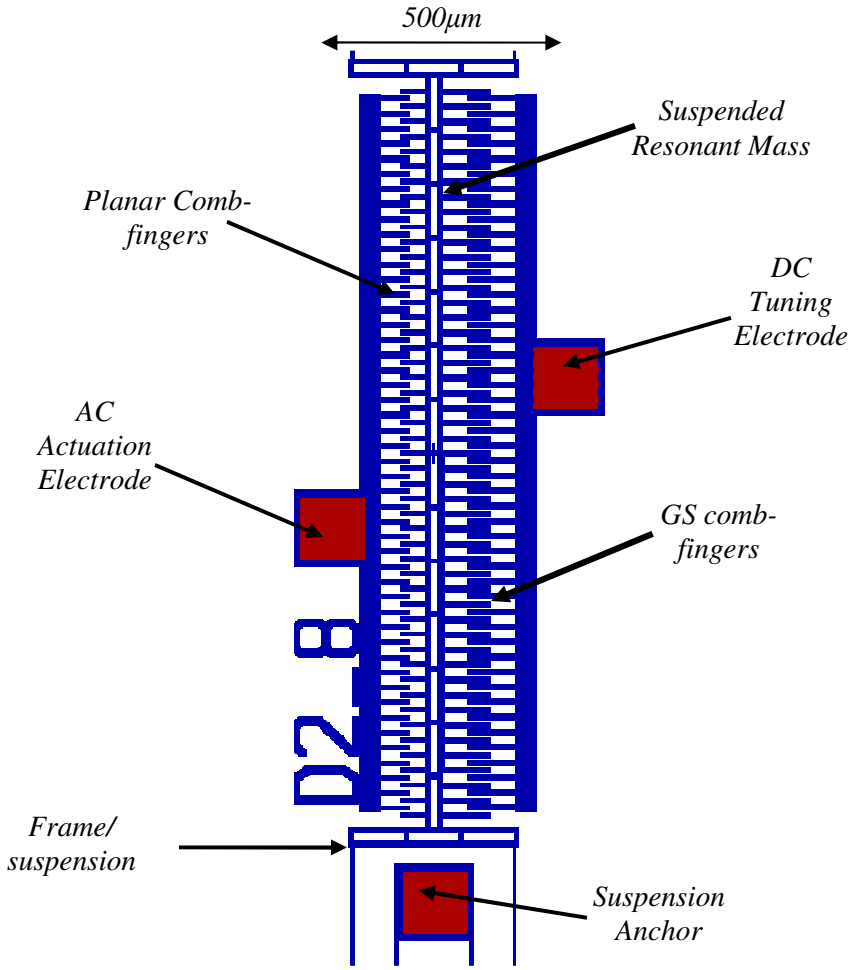

Figure 4.9: Basic layout of a tunable MEMS resonator using gray-scale comb-fingers.

The design above was developed for simplicity, however there is an obvious asymmetry of applied forces. While a small (~20V) AC signal will be used on the left side to drive the resonator, DC tuning voltages up to 100V will be applied to the tune

electrode on the right side to maximize k_{elec}. This bias will cause the device to resonate around a deflected point (5-10μm). Since k_{elec} is position dependent in Figures 4.6-4.8, static deflections will effect the magnitude of the electrostatic spring. To anticipate these offsets, the rest position of the comb-fingers was biased so that the peak k_{elec} occurs after ~5μm of deflection.

All resonator devices were fabricated using the SOI gray-scale actuator process described in Chapter 3. The approximate measured gray level height for each type of device tested in the following section is shown below in Table 4.3. For comparisons with the models presented earlier above, the simulated value closest to the measured height will be used for k_{elec} predictions.

Table 4.3: Measured heights of gray-scale comb-finger sections after fabrication.

Device	Approximate gray level height (μm)
Weakening	10-20
Stiffening – Single	~35
Stiffening – Double	~35

4.4. Testing and Characterization

Static and dynamic characterization of all resonators was performed using an optical profiler (Veeco Wyko NT1100 with DMEMS option). As with the comb-drive testing in the previous chapter, the resonating mass and bulk substrate are kept electrically grounded to avoid pull-in forces normal to the substrate. The following sections will review the methods used to test each resonator, and to extract the resonant frequency (f) and electrostatic spring constant (k_{elec}) as a function of tuning voltage.

4.4.1. Method

The Wyko NT1100 operates under the principle of white-light interferometry in both of it's primary modes, static and dynamic. Pattern recognition software can be used in either mode to measure relative structure movements in both the horizontal and vertical planes.

DC tests on the set of planar comb-fingers on each resonator were used to estimate the mechanical spring constant of the suspensions (k_{mech}). Analytical equations were used to calculate the force as a function of applied voltage (Equation 29 from Chapter 3), while the Wyko software was used to track the resonator position. The k_{mech} is then back-calculated using $F=k_{mech}x$. Example displacement vs. voltage measurements are shown in Table 4.4, where the extracted k_{mech} is relatively consistent.

Table 4.4: Displacement and voltage for planar comb-fingers to determine the mechanical spring constant.

Applied Voltage (V)	Measured Position (µm)	Displacement (µm)	Extracted k_{mech} (N/m)
0	135.28	0	-
20	135.56	0.28	5.7
40	136.55	1.27	4.9
60	138.03	2.75	5.1
70	139.02	3.74	5.1
80	140.23	4.95	5.0
90	141.49	6.21	5.0
100	142.91	7.63	5.1

Next, the dynamic measurement mode is used to determine the frequency response for different tuning voltages. In this mode, the Wyko uses an LED that is synchronized with the actuation signal to strobe the resonator at a particular phase of its periodic motion. A schematic of the periodic driving signal is shown in Figure 4.10, where the peak of the shifted sinusoid occurs at a phase of 90º.

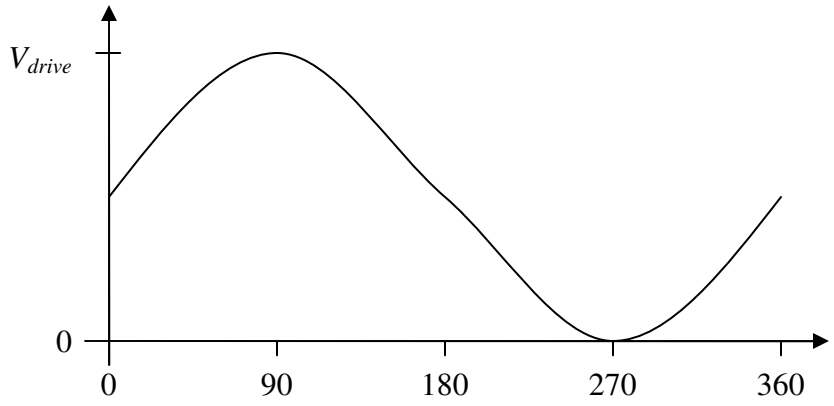

Figure 4.10: Schematic of the applied voltage as a function of phase.

To obtain the resonant frequency, we strobe the motion at a particular phase, while sweeping the actuation frequency. As the resonator passes through resonance, the drive signal and resonator motion will undergo a relative phase shift, according to the standard resonance equation [145]:

$$\delta = \frac{F/k_{mech}}{1 - \frac{\omega^2}{\omega_R^2} + j\frac{1}{Q}\frac{\omega}{\omega_R}} \tag{55}$$

where δ is the resonator displacement, F is the applied force ($F=F_0 sin(\omega t)$), Q is the quality factor, and ω_R is the resonant angular frequency. A brief inspection shows that as $\omega \rightarrow 0$, Equation 55 reduces to Hooke's Law ($\delta=F/k_{mech}$), while for the case of $\omega=\omega_R$ (resonance) we find a –90º phase shift:

$$\delta = -j\frac{QF}{k_{mech}}. \tag{56}$$

Considering this standard resonance behavior, depending on the choice of phase for the LED strobe, the measured resonator position vs. frequency will be quite different. Here we will discuss two primary examples: first, if a strobe phase of 90º is chosen, then for $f<<f_0$ the measured resonator position will be at its maximum deflection (during the

peak of the V_{drive} signal). As the drive frequency approaches f_0, the resonant amplitude will gradually increase. However, at resonance, the 90º phase shift causes the mechanical vibration and LED strobe to be 90º out of phase. Thus, the resonator will now be strobed in the middle of its travel range, appearing as negligible movement even though the amplitude of vibration is maximized. As the frequency increases further to $f>>f_0$, another 90º phase shift causes the strobe and mechanical motion to be 180º out of phase, and the measured resonator deflection is at the maximum deflection in the opposite direction. This sequence is depicted in Figure 4.11(a), where the point that the resonator position crosses the rest position indicates the approximate point of resonance. Yet, the odd shape of such a plot makes it difficult to determine f_0 accurately with a limited number of data points.

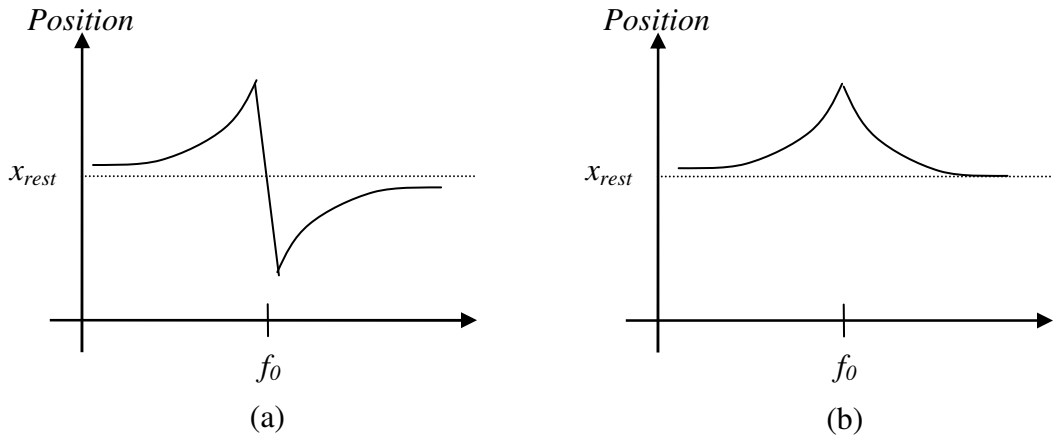

Figure 4.11: Schematic of resonator position vs. frequency for a strobe phase of (a) 90º and (b) 0º.

Alternatively, a phase of 0º can be used when strobing the resonator. Initially, almost no motion is detected because the strobe occurs in the middle of any periodic motion. However, as the drive frequency approaches f_0, the 90º phase shift causes the maximum mechanical deflection to shift to the phase where it is being strobed. This method creates a plot of position vs. frequency similar to Figure 4.11(b). This second

method is preferred for the purpose of determining resonant frequency because a peak curve fit can be used to extract the center frequency of the peak with only limited data points required. For the data discussed here, a 4-parameter (a,b,x_0,y_0) Lorentzian fit in SigmaPlot was used of the form:

$$y = y_0 + \frac{a}{1+\left(\frac{x-x_0}{b}\right)^2}. \quad \textbf{(57)}$$

The quality factor (Q) of a device is often estimated using $Q=\omega_0/\Delta\omega$, where $\Delta\omega$ is the full-width half max of the power spectrum, or $1/\sqrt{2}$ of the amplitude. However, we must remember that the Wyko records the *position* of the resonator at a particular phase for each frequency, not the *amplitude* vs. frequency that is required to estimate the quality factor. Thus, the width of the Lorentzian fit to this data cannot be used to find Q. The Wyko is capable of generating amplitude vs. frequency plots, but requires a series of nested phase and frequency sweeps that is much more time consuming. However, referring back to Equation 56 for the case of $\omega=\omega_R$, we can divide the peak resonant amplitude by the displacement caused by a DC signal to obtain an approximate Q. For most resonators tested here, this method yielded Q's of ~15 in air.

4.4.2. Weakening Resonator Tests

Tests of the weakening resonator design used an AC drive voltage of 30V on a device with 10-20μm gray levels and 10μm wide suspension arms. The extracted k_{mech} from static tests was 4.7 N/m. Figure 4.12 shows the measured resonator position as a function of frequency for different applied DC tuning voltages (0-80 V). Notice that as the voltage is increased, the base of the peak shifts gradually in the +x direction by ~5μm, as expected from the asymmetric resonator design and large DC tuning voltages. As the

tuning voltage increases, the resonant peak shifts to lower frequency, consistent with a "weakening" of the mechanical spring in Equation 53. SigmaPlot curve fits show the resonant peak shifted from f_0= 1594.6 Hz at V_{tune}= 0V, to f_{tuned}= 1442.4 Hz at V_{tune}= 90V.

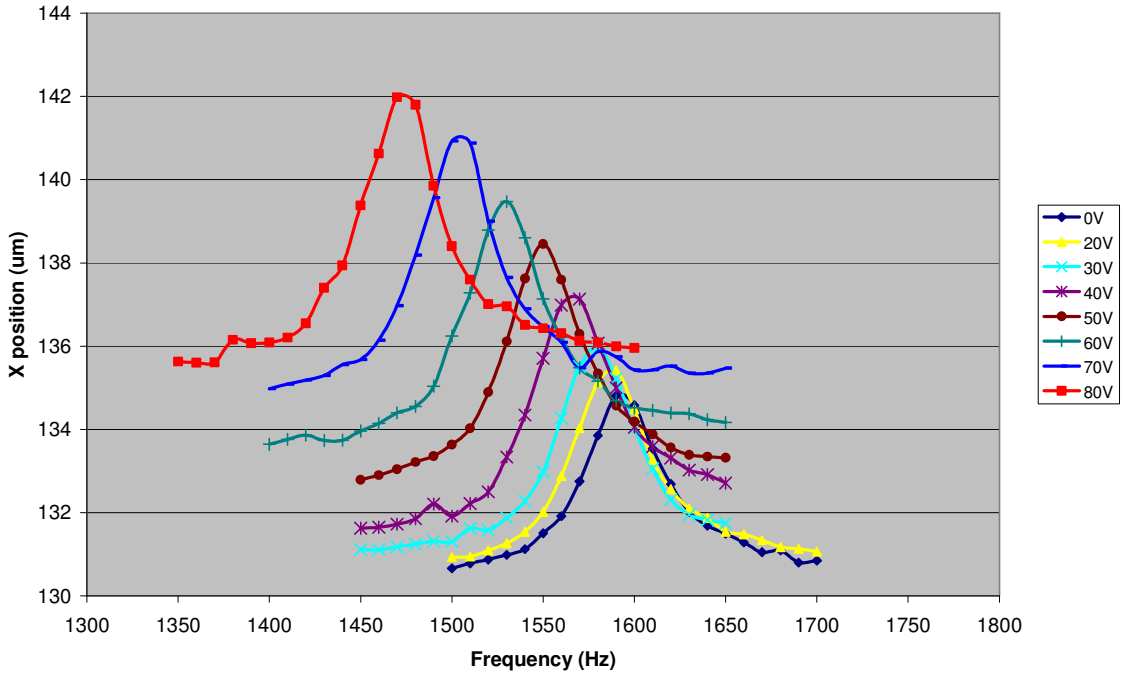

Figure 4.12: Measured position vs. frequency for different applied voltages in a weakening comb-finger design.

To compare these tuning results to our predictions, we start by taking our k_{elec} parameter from Figure 4.6 for the 20μm case at each appropriate finger engagement (accounting for the DC displacement caused by V_{tune}). Using V_{tune} and the number of comb-fingers (N=48), the expected k_{elec} is calculated for each voltage using Equation 50. This result was combined with the measured k_{mech} in Equation 54 to yield a predicted resonant frequency as a function of tuning voltage. The measured and predicted resonant frequencies match well, as shown below in Figure 4.13.

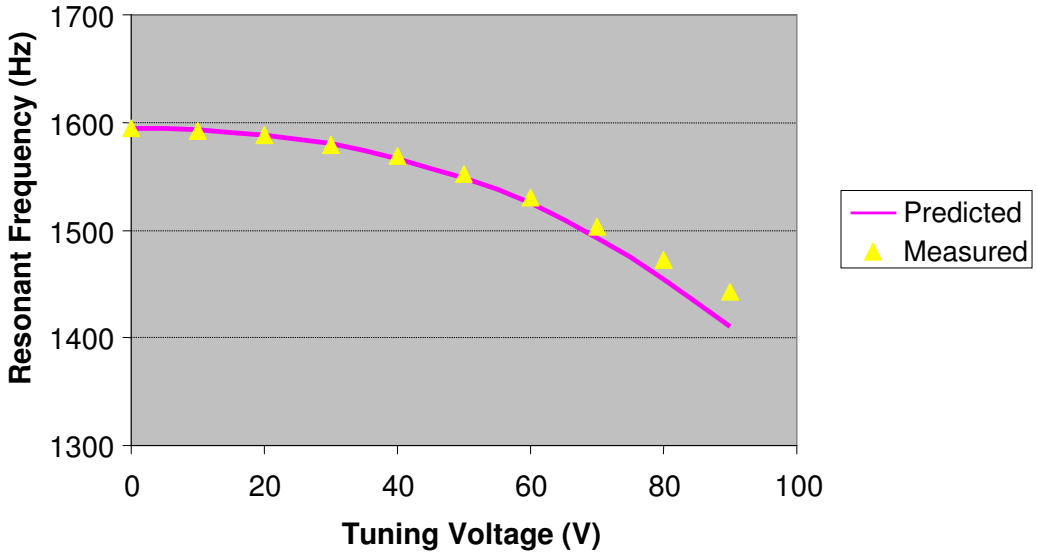

Figure 4.13: Predicted and measured resonant frequency as a function of tuning voltage for a "weakening" comb-finger design.

4.4.3. Stiffening Resonator Tests

For the "stiffening" resonators, we will first consider the "stiffening – single" design. The suspension arms are 10μm wide and the gray-levels were measured to be ~35μm tall. The extracted k_{mech} from static tests was 5.7 N/m and an AC drive voltage of 20V was used. Once again, we extract the k_{elec} parameter from FEMLAB simulations and combine it with k_{mech} in Equation 54 to calculate the predicted new resonant frequency. The measured and predicted resonant frequencies agree well and are shown in Figure 4.14. As expected, increasing the tuning voltage causes the resonant peak to shift to higher frequencies, indicating a "stiffening" of k_{eff}. SigmaPlot curve fits show that the resonant peak shifted from f_0 = 1965.9 Hz at V_{tune} = 0 V, to f_{tuned} = 2151.5 Hz at V_{tune} = 100 V.

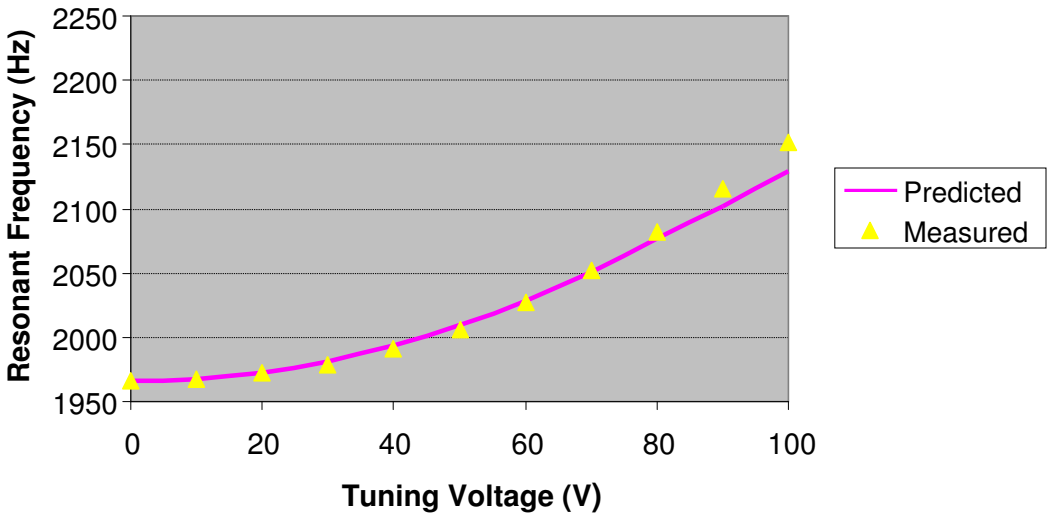

Figure 4.14: Predicted and measured resonant frequency as a function of tuning voltage for a "stiffening – single" comb-finger design.

Next, we consider the "stiffening – double" design, which according to our simulations, is expected to produce even stronger tuning characteristics. The gray levels were measured to be ~35μm tall, but the suspension width in this case was only 8μm. Since the suspension spring constant scales with the width^3 (see Equation 47 from Chapter 3), the extracted k_{mech} from static tests was only 3.2 N/m. Figure 4.15 shows both the measured and predicted resonant frequencies (using FEMLAB simulations and Equations 50 and 54) as a function of tuning voltage. The rapid increase in frequency is larger compared to the "stiffening – single" finger design due in part to the smaller k_{mech}, but also because of the larger k_{elec} produced. SigmaPlot curve fits show that the resonant peak shifted from f_0 = 1332.5 Hz at V_{tune} = 0 V, to f_{tuned} = 1560.2 Hz at V_{tune} = 70 V, a 17% increase in resonant frequency.

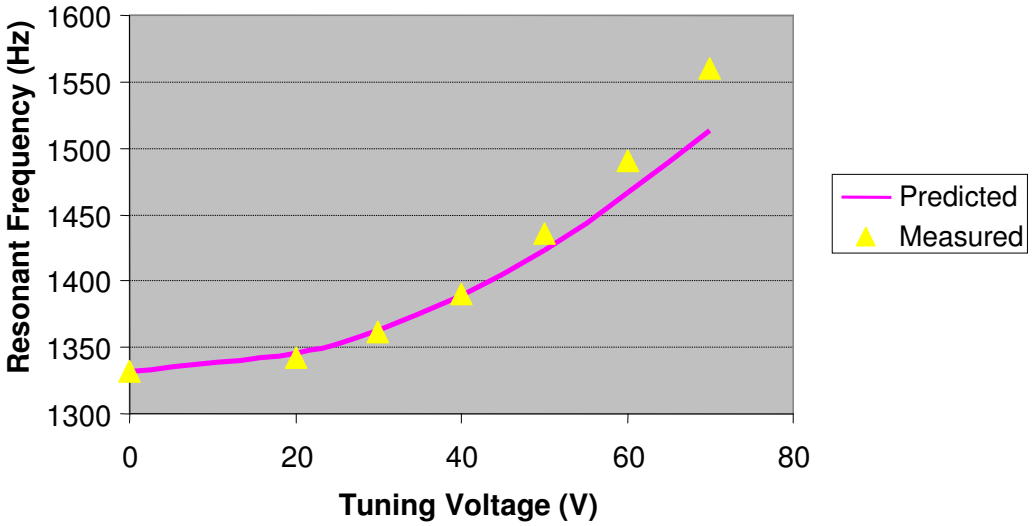

Figure 4.15: Predicted and measured resonant frequency as a function of tuning voltage for a "stiffening – double" comb-finger design.

4.4.4. Tuning Summary

The previous sections have demonstrated multiple tuning configurations for stiffening and weakening gray-scale comb-finger designs. Since each device is tested separately, and their k_{mech} and masses are slightly different, it is helpful to compare their extracted k_{elec} magnitude using Equation 54. Figure 4.16 shows the extracted k_{elec} for the three gray-scale comb-finger designs, as well as for a planar design where negligible tuning is expected. We see that in each case the measured and predicted values from our model show reasonable agreement, even at high voltages.

For the planar case, we observe a slight spring stiffening effect even though a simplified model of constant height comb-fingers would indicate no electrostatic force gradient there. However, since the resonator layout is asymmetric (with tune fingers only on one side), we should include the capacitor formed by the comb-finger tips. For an order of magnitude estimate, we consider the area created by the comb-finger tips as a parallel plate capacitor, and then use the analysis presented in Equations 50-52. We find

that a V_{tune} = 100 V would produce electrostatic springs on the order of 0.05 N/m, which is ~1/3 of the extracted k_{elec} for the planar design. We attribute the discrepancy to fringing fields that increase the effective area of the finger tip, causing an underestimation of the capacitive tuning. We believe this small asymmetry also caused a slight stiffening shift in all of designs, as evident from the consistent slight underestimation in the figure.

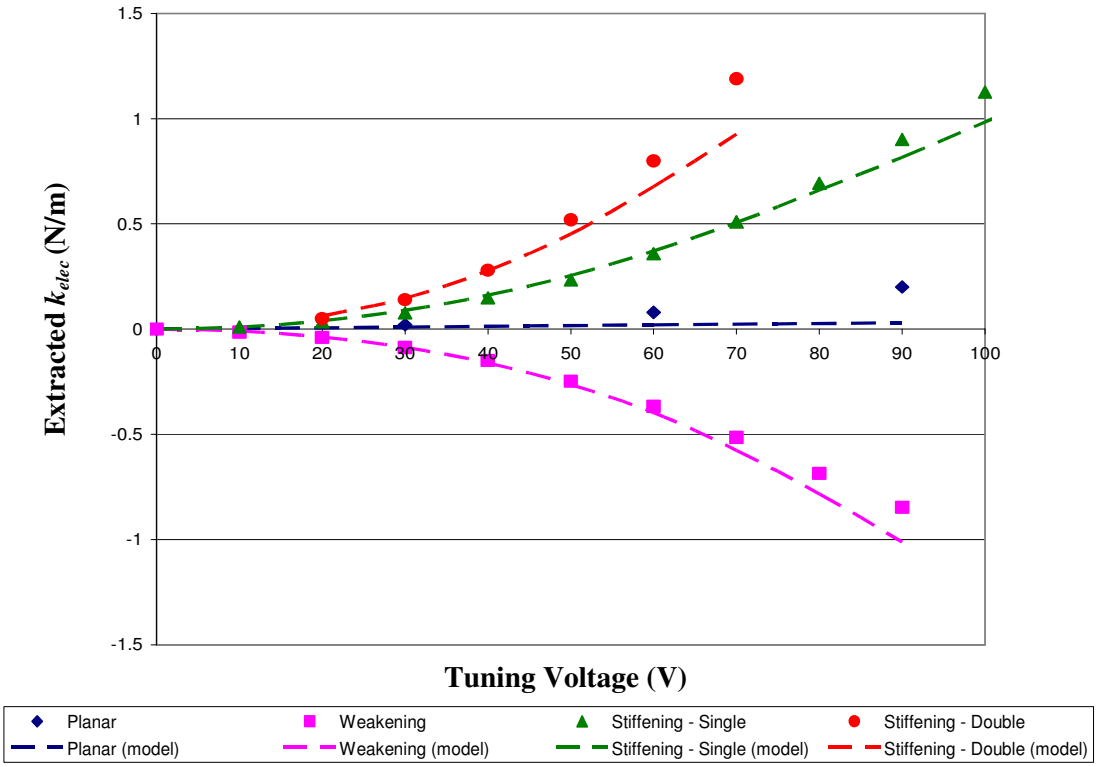

Figure 4.16: Extracted electrostatic spring constant (k_{elec}) for the 3 types of gray-scale springs and the planar case for comparison.

As expected from our simulations, the strongest relative tuning is achieved with the "stiffening – double" comb-finger design, where an electrostatic spring of 1.19 N/m is created using only 70 V. However, above 70 V, this resonator became unstable due to it's asymmetric design. Thus, the largest absolute tuning was actually achieved by the "stiffening – single" design since it was able to maintain a stable k_{elec} up to 120V, resulting in an extracted k_{elec} of 1.66 N/m. Resonator designs with tuning comb-fingers

on either side of the resonating mass should eliminate any resonator offset induced by the large DC tuning voltages. This would enable the devices to stay in their linear range up to larger tuning voltages; however the versatility and utility of variable-height gray-scale electrostatic springs has been clearly demonstrated.

4.5. Non-linear Stiffness Coefficients

As mentioned in the previous section, the k_{elec} created by the gray-scale comb-fingers has a limited range over which the spring behaves linearly. Thus, at large deflections or large DC tuning voltages, the presence of non-linear stiffness coefficients becomes important. An example of this non-linear behavior for the "weakening" resonator design presented earlier is shown in Figure 4.17 (un-tuned f_0=1594.6 Hz). For each of the 4 cases shown, the tuning voltage was held constant at 80V, but the amplitude of the drive signal was changed from 10V to 40V. At the lowest drive voltage of 10 V, the tuned resonant frequency was 1472.5 Hz. In a linear system, the peak should simply change height as driving amplitude changes. However, the figure shows that large drive amplitudes cause the peak to bend/creep towards the original f_0.

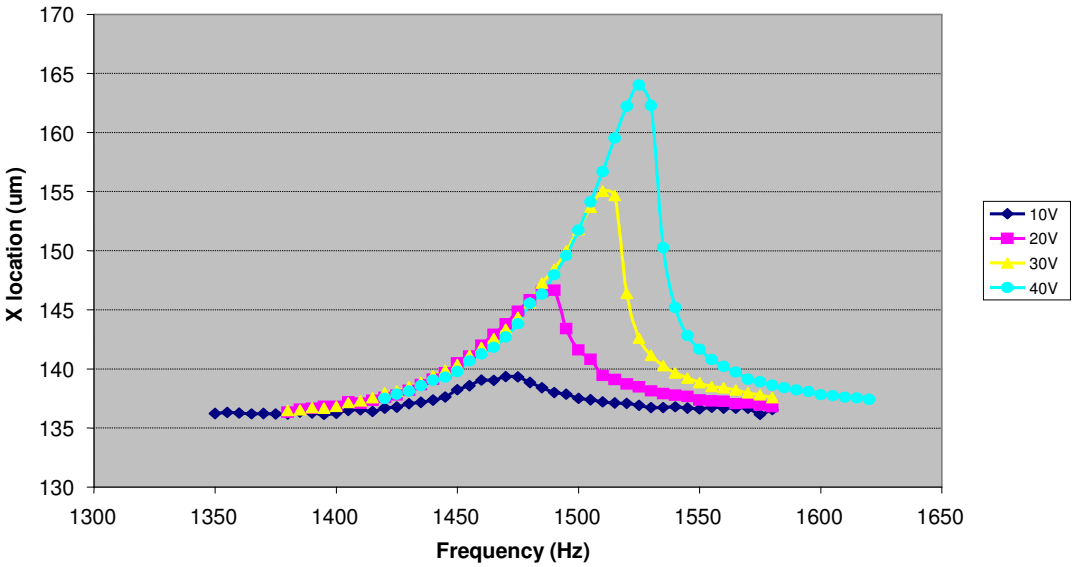

Figure 4.17: Measured resonant peak for a single resonator with a constant tune voltage of 80V, but different drive voltages.

In general, such a system can be described by the Duffing equation [146]:

$$m\ddot{x} + \xi\dot{x} + kx + \gamma x^3 = b\cos(\omega t) \quad \textbf{(58)}$$

where ξ is the damping coefficient and γ represents a third-order term in the spring constant, such that:

$$F = kx \pm |\gamma| x^3 . \quad \textbf{(59)}$$

Exact solutions to the Duffing equation are not, in general, available [138], but the concept of both "hard" ($\gamma>0$) and "soft" ($\gamma<0$) springs are shown in Figure 4.18. In some frequency ranges, multiple stable solutions exist and the resonator may 'jump' from one position to the next as the frequency changes [138], an undesirable effect in most cases.

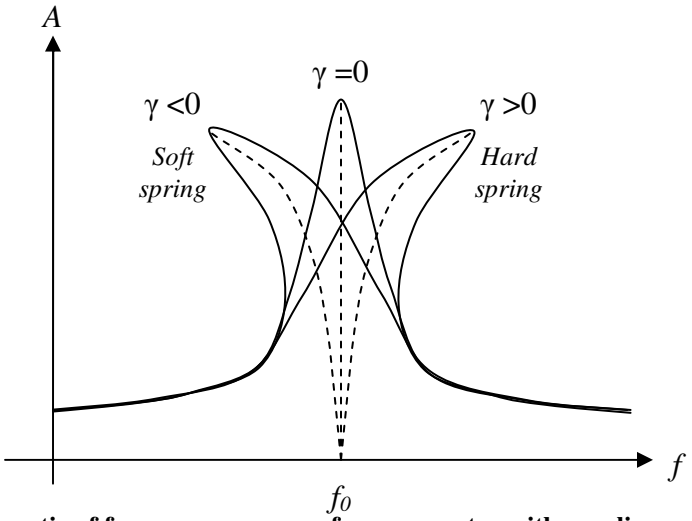

Figure 4.18: Schematic of frequency response for a resonator with non-linear stiffness coefficients.

For a typical un-tuned resonator, as the resonant amplitude increases, cubic stretching terms in the suspension spring constant [147, 148] can become non-trivial, leading to a "hard" spring behavior [138, 146]. Parallel plate electrostatic springs have been found to exhibit "soft" spring behavior [146], an inherent artifact of their cubic dependence on amplitude and gap from Equation 52.

In contrast, the tendency of vertically shaped resonators developed in this work is to bend towards the original f_0 (i.e. a "weakening" design shows "hard" spring behavior and a "stiffening" design shows "soft" spring behavior). This occurs because k_{elec} at the rest position is typically at a peak value, so large vibrations move the resonator to regions of significantly lower k_{elec} and the amount of tuning decreases.

Two potential methods will now be presented to deal with these non-linear effects. First, multiple gray levels can be used to further tailor the capacitance profile to extend the linear range of the electrostatic spring. For example, Figure 4.19 shows the simulated electrostatic force and spring constant for a single gray level design ("stiffening – single," 10μm tall) compared to a multi-gray level design (three additional 10μm long intermediate steps with heights of 70μm, 50μm, and 30μm). As evident from the figure, the single gray level design provides a steep change in force over a short distance. The multi-gray level design provides the same total change in force, but it now takes place over a large engagement distance, leading to a slightly smaller spring constant that is more consistent with engagement.

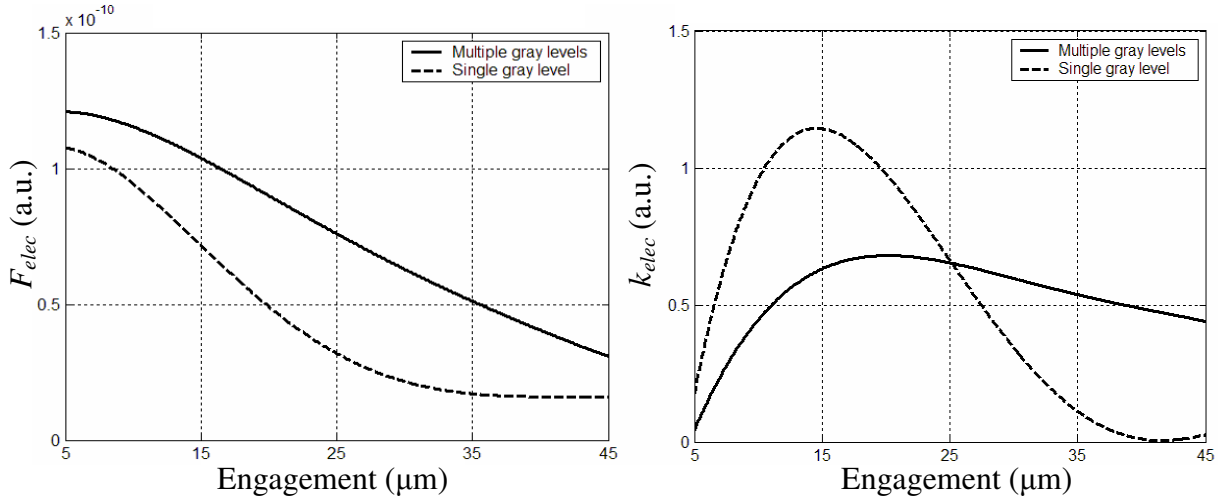

Figure 4.19: Simulated electrostatic force and spring constant for a multiple gray level finger design.

Complex force-engagement profiles could be developed through simulation to tailor spring behavior, though the simulation process is quite slow. However, a second method for extending the linear range of electrostatic springs is also briefly introduced below. By staggering the relative engagement of single-gray level comb-fingers, by δ as shown in Figure 4.20, the sum of appropriately spaced electrostatic springs could be used to create a wide linear range of operation. In this case, a single gray level design can be simulated accurately in 3-D FEA and the result manipulated easily within a simpler programming language (such as MATLAB).

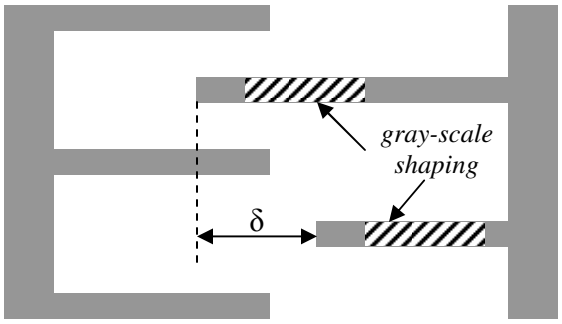

Figure 4.20: Schematic of a variable-engagement comb-finger design.

To investigate this concept in more depth, we start by considering the simulated spring constant as a function of engagement for a single finger, as done previously in Figure 4.6 – Figure 4.8. We then use the sum of many staggered fingers to create an arbitrary k_{elec}-engagement profile:

$$k_{elec}(x) = \sum_n k_0(x - \delta_n) \tag{60}$$

where $k_0(x)$ is the k_{elec}-engagement profile of a single un-shifted finger and δ_n is the shift of each individual finger. For the simplest case of shifting *A* fingers forward and *B* fingers backward by an identical amount, we have:

$$k_{elec}(x) = A \cdot k_0(x + \delta_0) + B \cdot k_0(x - \delta_0). \tag{61}$$

Thus, the problem has reduced to simply finding two coefficients, A and B, which determine the relative number of comb-fingers with each shift ($+\delta_0$ or $-\delta_0$).

For example, Figure 4.21 shows a simulated electrostatic spring without any offset, where the magnitude of k_{elec} changes dramatically with engagement. However, when an offset of δ_0=8μm is used (with $A = 5/8$ and $B = 3/8$), a plateau >20μm wide is created where there is negligible change in k_{elec}. Thus, a tunable resonator with 48 fingers (like before) would be designed with 30 fingers shifted forward and 18 fingers shifted backward from a neutral point. More complicated combinations of offsets and coefficients could be used to extend and/or tailor the k_{elec}-engagement profile as desired. In some instances, this manipulation of high-order stiffness coefficients may prove useful for purposes beyond improving linearity (such as incorporating "soft" electrostatic springs to compensate for "hard" mechanical spring behavior due to material stretching).

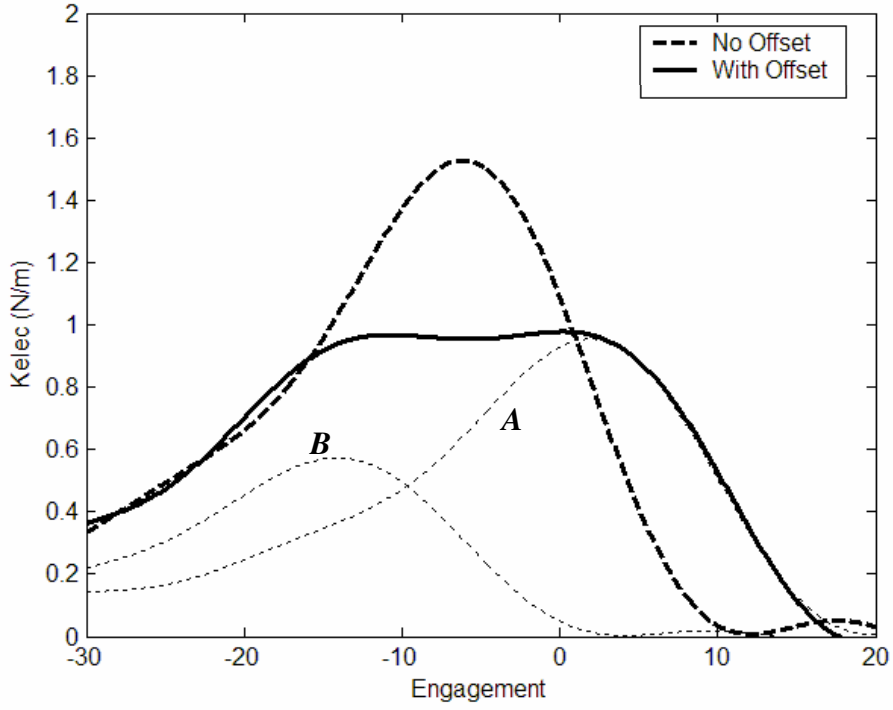

Figure 4.21: k_{elec} characteristics possible with a binary variable-engagement design.

4.6. Conclusion

This chapter has reviewed the mechanisms behind electrostatic tuning of MEMS resonators through modifications to the force-engagement profile of comb-drive actuators. Variable-height comb-finger tunable resonators were designed, simulated, fabricated, and tested for the first time. Such devices can provide similar tuning to variable-gap comb-finger designs, however without the penalty of increasing the device footprint. Electrostatic springs as high as 1.19 N/m (using 70V) or 1.66 N/m (using 120V) were demonstrated, with a maximum frequency tuning of 17% of the original f_0. Although most designs discussed in this work utilized a single gray-level, simulations were able to show that finer control of the force-engagement profile is possible by using the many intermediate heights available through gray-scale technology.

As a direct result of the development and integration of gray-scale technology presented in the first 3 chapters of this dissertation, all of the above tuning and frequency response control is provided without increasing the overall resonator footprint. While the resonant frequency and Q-factor of the devices discussed were kept low, the design and simulation principles developed can be applied to virtually any of the resonator applications mentioned previously [65, 67-69, 138-144].

CHAPTER 5: GRAY-SCALE FIBER ALIGNER I: Concept, Design, and Fabrication

5.1. Introduction

Alignment of an optical fiber within an optoelectronic module is a continuing challenge in optoelectronic packaging, and often dominates module cost [76]. Ultimately, passive alignment and packaging techniques would be preferred for their simplicity. Passive systems utilizing silicon waferboards and flip-chip bonding have reported alignment accuracies of 1-2μm [149-151], mostly through attempts to improve process and dimensional control (and in turn increasing processing cost). Common sources of error that make passive sub-micron alignment difficult include fiber core eccentricity, fiber diameter, v-groove width and placement, or variation in etch angle [88]. Particular difficulty in configurations using flip-chip bonding has been encountered with non-uniform solder ball volume distribution, which can cause vertical shifts in alignment [152-154].

Even if high-accuracy fabrication and flip-chip bonding can be accomplished, such tight tolerances increase the cost of processing and assembly, and severely limit throughput. For example, relaxing placement tolerances from the 1μm to 20μm level can increase throughput of a pick-and-place machine by an order of magnitude [75]. Further complicating the drive for passive techniques, groups now report up to 3dB of loss from only 1-2μm of axial misalignment [155]. Thus, as current alignment requirements approach 0.2μm [85], passive alignment becomes unrealistic regardless of the amount of process control. Multi-axis on-chip methods for final alignment of the optical fiber are therefore attractive replacements for the expensive and slow macro actuators currently required to achieve sub-micron alignment.

The primary challenge for on-chip fiber alignment systems is realizing both horizontal and vertical actuation of the fiber to compensate for shifts in either direction, such as vertical shifts from solder ball irregularities [152-154]. Previous MEMS fiber actuators have demonstrated multi-axis on-chip alignment [90, 95]. However, these systems typically require specialized fiber preparation (attachment of permanent magnets to the fiber tip [90]) or rare fabrication techniques (LIGA [95]). Such requirements limit their feasibility as a packaging option. In contrast, the 2-axis fiber actuator developed in this research requires no special fiber preparation and is realized using gray-scale technology – a batch technique using standard MEMS equipment. This *gray-scale fiber aligner* exploits the coupled motion of opposing in-plane actuators with integrated 3-D wedges). The device creates a dynamic v-groove (controlled via MEMS in-plane actuators) to modify the horizontal and vertical position of the optical fiber [156, 157].

The developed optical fiber alignment system can act as a platform for integrated packaging of optoelectronics devices, addressing one of the most costly and time-consuming aspects of mass-producing such components. Integrated packaging platforms using the chosen fabrication techniques are inherently mass-producible and compatible with electronics integration, promoting dense integration of optical and electronic systems in a single component.

Section 5.2 will discuss the concept of operation and layout of the developed MEMS gray-scale fiber aligner. Section 5.3 will discuss the competing optical loss mechanisms in the device which serve as guidelines for system design. The layout and dimensions of each actuator component are described in Section 5.4, while the fabrication and assembly of the device are detailed in Section 5.5 and 5.6. Finally, a brief

demonstration of the actuation mechanism using an optical profiler is provided in Section 5.7. The following chapter will discuss optical testing results.

5.2. Device Concept

Contrary to traditional *fixed* v-groove designs obtained by wet chemical etching [78-83, 149], the fiber alignment mechanism developed in this research creates a *dynamic* v-groove using opposing sloped, silicon wedge structures to hold the optical fiber in a particular alignment location. The basic alignment mechanism is illustrated in Figure 5.1. In Figure 5.1(a), the system is "at rest" with the fiber lying at the bottom of the dynamic v-groove. However, in Figure 5.1(b), after an in-plane displacement of one silicon alignment wedge, the bottom of the dynamic v-groove has been translated in both the *in-plane* and *out-of-plane* directions, altering the alignment of the optical axis. Thus, through coupled in-plane motion of opposing wedge structures, alignment of an optical fiber in the X-Y plane can be achieved.

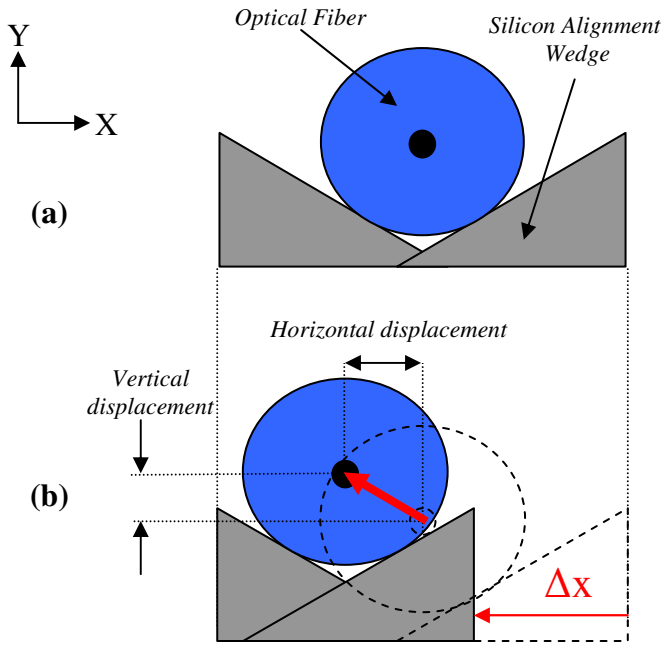

Figure 5.1: Optical fiber (a) at rest and (b) after actuating a single wedge, causing horizontal and vertical displacement of the fiber [156], essentially creating a dynamic v-groove.

3-D and top-view schematics of the 2-axis optical fiber alignment system are shown in Figure 5.2 and Figure 5.3. A flexible fiber cantilever is created by anchoring one end of the fiber in a static v-groove or trench located a few millimeters away. The static v-groove provides approximate passive alignment such that the free end of the flexible fiber cantilever rests between two sets of 3-D shaped wedges. Each set of wedges is attached to an in-plane MEMS actuator, such as comb-drives, which provide the requisite forces. The movement of each in-plane actuator allows the position of the fiber tip to be changed; improving alignment to a target device – in the case of Figure 5.2, the target is a chip with a waveguide. After achieving the desired alignment, the fiber could be secured using various types of epoxy or possibly a clamping mechanism (more discussion on this topic in Chapter 7). It is anticipated that fiber tip actuation of >10μm will be required to compensate for fabrication and assembly errors within an optoelectronic module [152].

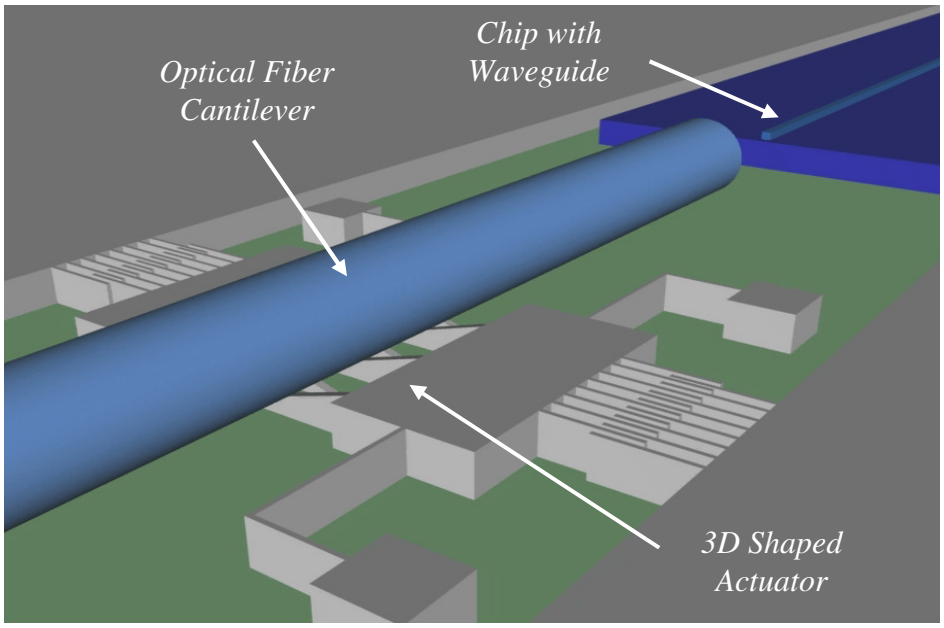

Figure 5.2: Concept of on-chip active MEMS fiber alignment system using opposed sloped alignment wedges to create a dynamic V-groove. Shown with simplified suspensions and planar comb-drives.

As mentioned earlier, the sloped alignment wedges are fabricated using gray-scale technology. Since the integration of gray-scale technology with an SOI MEMS actuator process flow has already been developed in Chapter 3 of this dissertation, only the results of the process will be given later when the fabrication is discussed. Additionally, since the gray-scale alignment wedges are purely mechanical elements, they are not limited too conductive or magnetic materials, as may be the case in other types of actuators.

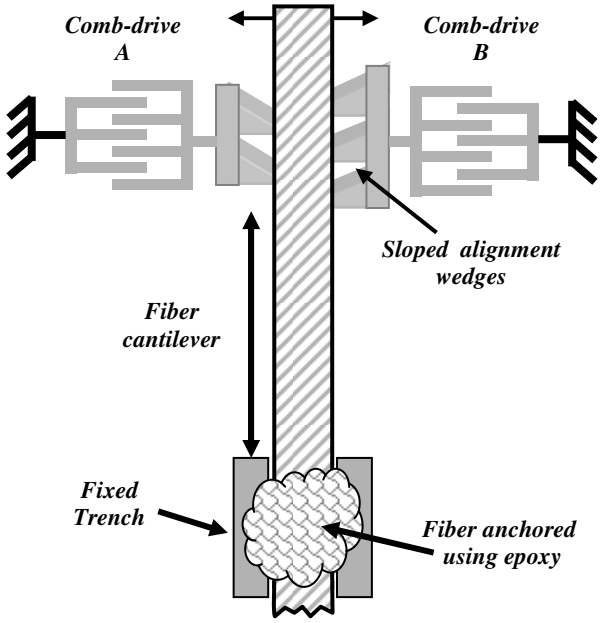

Figure 5.3: Top view schematic of the 2-axis optical fiber actuator [157]. The opposing actuators are aligned with a static v-groove trench to provide approximate passive alignment.

5.3. Fiber Coupling Loss Analysis

The goal of the gray-scale 2-axis fiber aligner is to eliminate axial misalignment by bending the fiber to an appropriate position. However, bending the fiber inherently introduces some loss as well. Thus, three primary sources of optical loss, shown in Figure 5.4, should be considered and analyzed: longitudinal (along the axis of light propagation), axial (perpendicular to light propagation), and angular. The coupling analysis in this section is based on the Gaussian coupling model presented by *Joyce and*

DeLoach in 1984 [158]; however adaptations have been introduced to specifically model the behavior of the gray-scale fiber aligner. This approach requires beams to be represented by their nearest equivalent Gaussian mode, which while an approximation, provides useful insight to the coupling for a variety of optical and mechanical configurations of the gray-scale fiber aligner. The following analysis will assume fiber-fiber coupling, but can be applied to other source/sink combinations with approximately Gaussian modes. Similar treatment of Gaussian coupling can be found in [159, 160].

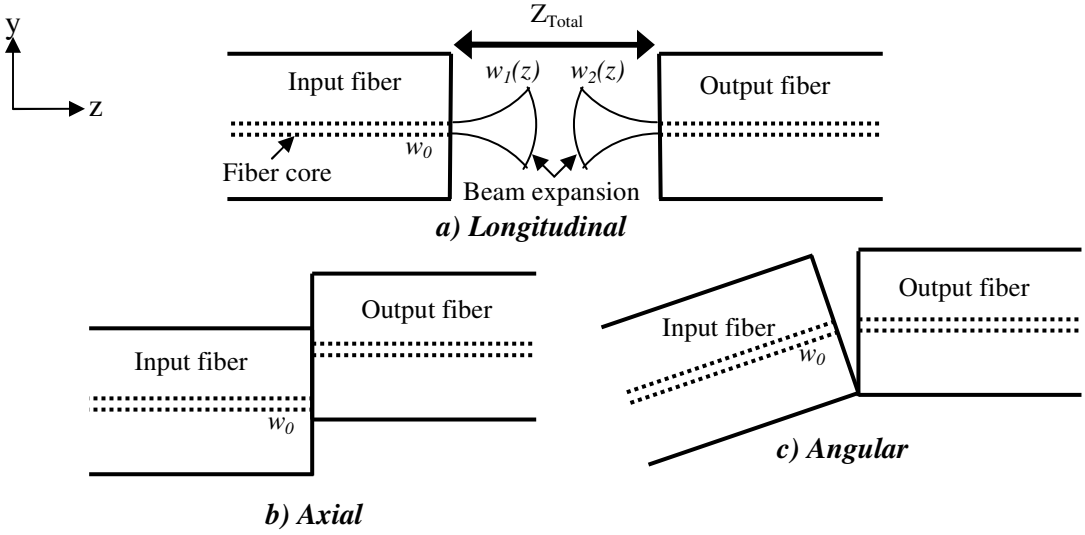

Figure 5.4: Three primary sources of loss in fiber-fiber coupling.

The simplest case to consider initially is that of purely longitudinal separation between two co-axial fibers, as shown in Figure 5.4(a). Since the optical mode is no longer confined upon entering the gap between the two fibers, the beam waist (w) will expand as it propagates in the z-direction according to:

$$w(z) = w_0\left[1+\left(\frac{2z}{kw_0^{\,2}}\right)^2\right]^{1/2} \tag{62}$$

where $k=2\pi/\lambda$ and w_0 is the original beam waist inside the fiber core. The term w is known as the half-width or beam waist, where the amplitude of the electric field drops to

1/e of the peak, or where the intensity drops to $1/e^2$. For the simulations below, and most subsequent experiments in the following chapter, 8.2μm core single mode optical fibers were used (Corning SMF-28e), with $2w=10.4\mu m$[†], and an operating wavelength of $\lambda = 1550\ nm$ to match the preferred low loss window of optical fibers [161].

For elliptical mode profiles, the coupling efficiency (τ) between co-axial fibers for either the *x* or *y* primary axes, can be calculated separately to be [158]:

$$\tau = \frac{\sqrt{2}}{\left[\left(\frac{w_{01}}{w_{02}} + \frac{w_{02}}{w_{01}}\right)^2 + \left(\frac{2}{k w_{01} w_{02}}\right)^2 Z_{Total}^{\ 2}\right]^{1/2}} \tag{63}$$

where w_{01} and w_{02} are the original beam waists for the input and output fibers respectively, and Z_{Total} is the separation distance between them. Assuming circular symmetry and identical input/output fibers, the coupled power transmission coefficient ($T_{Longitudinal}$) can be simplified to:

$$T_{Longitudinal} = \tau_x \tau_y = \tau^2 = \frac{4}{\left[4 + \frac{4 Z_{Total}^{\ 2}}{k^2 w_0^{\ 4}}\right]}. \tag{64}$$

We can plot this transmission as a function of separation to evaluate the anticipated loss resulting from only longitudinal separation, see Figure 5.5 below. From the graph it is clear that the magnitude of separation (|z|) has a large influence over the coupled power between fibers, and should therefore be kept as small as possible. However, small changes (Δz) about a certain separation have little effect on the total transmission ($T(z+\Delta z) \approx T(z)$). For example, assuming only 5μm longitudinal placement accuracy for |z|=20μm, the difference in coupled power between 20μm and

[†] Material data sheet (www.corning.com/photonicmaterials/pdf/pi1446.pdf, accessed 3/16/05).

25μm separation is <0.08dB. As will be shown shortly, this difference in coupling is virtually negligible compared to the change in coupling that would be caused by similar levels of axial misalignment. Other studies have also shown the longitudinal axis to be the least critical of the misalignment components considered here [159, 160].

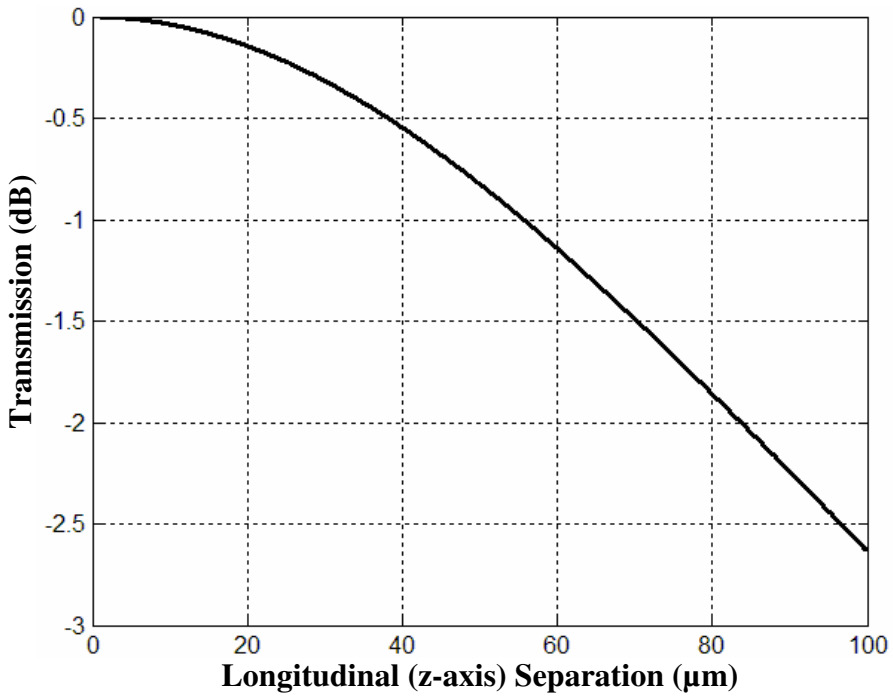

Figure 5.5: Calculated coupling as two co-axial single-mode fibers are separated longitudinally.

Thus, we can conclude that while the magnitude of fiber separation is important, active fiber positioning along the axis of transmission at the sub-micron level is unnecessary. Passive techniques for fiber placement along this axis can be utilized instead, meaning the gray-scale fiber aligner can restrict itself to 2-axis optimization of the more important axial and angular alignment components. Ultimately, for other devices or applications, the longitudinal fiber position may be more important than shown here, but positional requirements should still be more forgiving than along the other axes.

For the gray-scale fiber aligner, we will assume some constant separation value (Z_{Total}) between two fibers that are also offset both axially and angularly. The representative configuration is shown schematically in Figure 5.6. An input fiber is secured at one end to create a cantilever. The cantilever has an initial axial misalignment of Y_0. The cantilever tip is then displaced (Δy) by the gray-scale fiber aligner in an attempt to maximize the coupled power. For the purposes of this analysis, we will assume that the misalignment in the x-direction (into the page) is negligible.

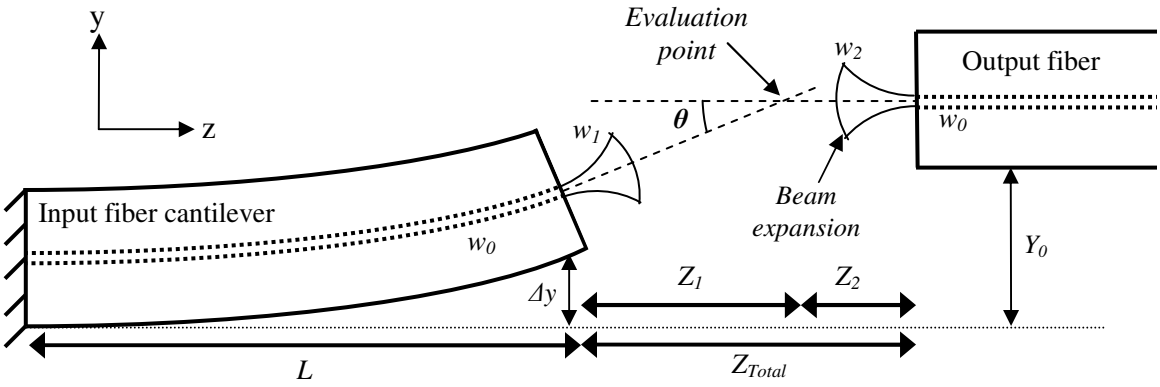

Figure 5.6: Alignment schematic for a bent fiber cantilever coupling to a fixed output fiber.

The fiber cantilever length (L) and tip displacement (Δy) dictate the included angle (θ) between the extended propagation axes of each fiber (see Appendix C):

$$\theta = \frac{2}{\left(\frac{L}{\Delta y} + \frac{\Delta y}{L}\right)} \approx \frac{2\Delta y}{L} \ . \tag{65}$$

For such separated fibers with an included angle (θ), *Joyce and DeLoach* were able to show that the transmission (T) can be now be written as [158]:

$$T = T_{Longitudinal} \exp\left[-\left(\frac{\theta}{\theta_e}\right)^2\right] \tag{66}$$

where θ_e is an angular tolerance parameter:

$$\theta_e = \frac{\sqrt{2}}{\pi\tau\left[\left(\frac{w_1(z_1)}{\lambda}\right)^2 + \left(\frac{w_2(z_2)}{\lambda}\right)^2\right]^{1/2}}. \quad \textbf{(67)}$$

The important aspect of Equations 66 and 67 is that the beam waists (w) must be evaluated at the appropriate (z) location corresponding to the intersection of the extended propagation axes. Thus, we can calculate the propagation distance for evaluation of w (Z_1 and Z_2) based on the geometry of Figure 5.6:

$$Z_1 = \frac{Y_0 - \Delta y}{\tan(\theta)} \quad \textbf{(68)}$$

$$Z_2 = Z_{Total} - Z_1 \quad \textbf{(69)}$$

Strictly speaking, the path traveled by the input beam will be the hypotenuse of the triangle created by Z_1 and $(Y_0-\Delta y)$. However, since the angles involved will be small for practical lengths and deflections ($\theta<0.02$ *rad* for $L=5mm$ and $\Delta y=50\mu m$), Z_1 is a reasonably good approximation of the path length.

Pure axial misalignment can be viewed as a special case of Equations 67 and 68, where the included angle becomes infinitesimally small angle ($\theta=d/z$ as $z\rightarrow\infty$). Thus, as $z\rightarrow\infty$, Equation 63 approaches $w\rightarrow 2z/kw_0$ and Equations 67 and 68 reduce to [158]:

$$T = T_{Longitudinal} \exp\left[-\left(\frac{d}{d_e}\right)^2\right] \quad \textbf{(70)}$$

where:

$$d_e = \frac{\sqrt{2}}{\tau\left[\frac{1}{w_{01}^{\ 2}} + \frac{1}{w_{02}^{\ 2}}\right]^{1/2}}. \quad \textbf{(71)}$$

These expressions are equivalent to those derived elsewhere for the case of pure axial misalignment of Gaussian modes [159].

We will now use Equations 62-69 to simulate the transmitted power (T) as a function of fiber cantilever tip displacement and analyze the losses corresponding to each component. Shown in Figure 5.7 is the transmitted power for a cantilever ($L=5mm$) with various tip deflections. The target fiber location has been fixed at $Y_0=20\mu m$ with longitudinal separation of $Z=30\mu m$. Also plotted in Figure 5.7 are lines indicating the loss that would be caused by each type of misalignment (longitudinal, axial, and angular) if they occurred independently of the other two. Strictly speaking, the three loss components are not entirely separable. However, for the geometries being considered, Figure 5.7 suggests that (to first order) they can be qualitatively viewed as components whose sum approximates the loss behavior near the coupling peak.

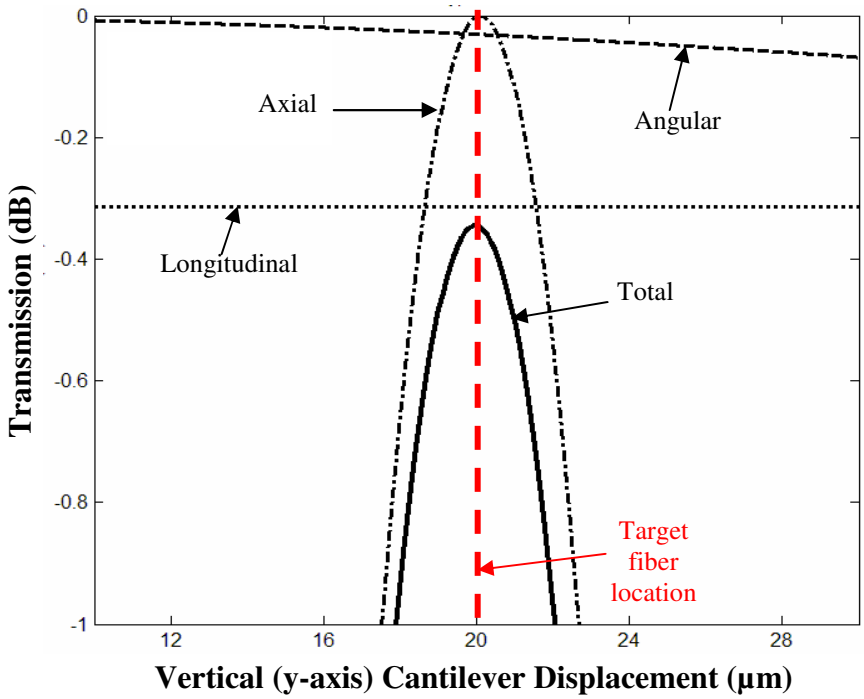

Figure 5.7: Various loss components for a single target fiber location @ Y_0=20µm.

As evident from the figure, the longitudinal loss caused by 30µm separation essentially causes a vertical shift across the entire range of tip displacements (0.31 dB). In contrast, the axial loss changes dramatically with tip deflection, where a 2µm

misalignment should cause >0.5 dB of loss. While the relative sensitivity to axial misalignment should be independent of target location, Figure 5.7 shows that the angular misalignment loss (0.03dB for $Y_0=20\mu m$) increases with cantilever tip displacement (increasing θ). Since the gray-scale fiber aligner reduces the amount of axial loss by introducing a small angular loss, the location of the target fiber is extremely important as it dictates the angular loss penalty introduced by the device.

Looking more closely at the angular loss penalty, Figure 5.8 plots the maximum transmission for different fiber cantilever lengths and tip displacements (temporarily assuming no longitudinal separation). For long cantilevers (10mm), the angle created by bending the fiber tip 50µm is still rather small. However, for shorter cantilevers (5mm), the angle resulting from the same displacement is larger (see geometry analysis in Appendix C), leading to more optical loss. For comparison, the loss caused by 1µm pure axial misalignment is also shown.

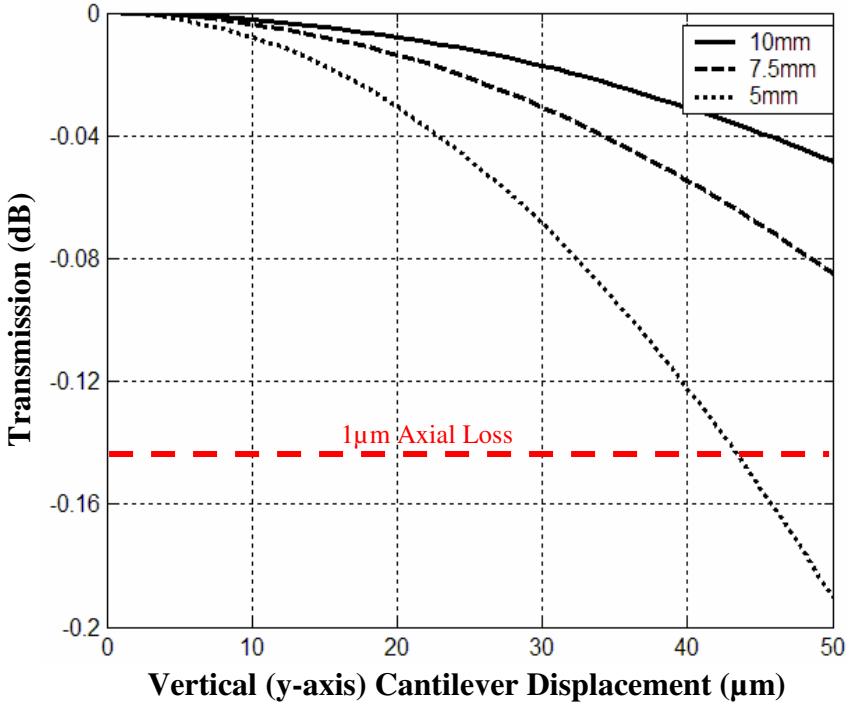

Figure 5.8: Max transmission depending on fiber cantilever length and tip displacement, compared to the loss caused by 1µm axial misalignment with no angle between input/output.

We see that a 5mm cantilever with 45μm tip displacement actually introduces greater angular loss than would be caused by 1μm axial misalignment. This means that for cases of short fiber cantilevers and large deflections, the gray-scale fiber aligner may not provide a significant advantage over other alignment techniques. As a general rule, the angular loss introduced by the gray-scale fiber aligner should be small compared to the equivalent axial loss tolerance we are trying to obtain. Thus, Figure 5.8 illustrates that this device will have inherent limitations in actuation range when the length of the fiber cantilever is scaled down.

Another way interpret the introduction of angular misalignment is that the axial misalignment must be improved in order to compensate and maintain the same total transmitted power. This concept of angular/axial alignment tradeoffs has been derived analytically in multiple forms as an "alignment product" of angular and axial tolerance terms [158, 159]. Fiber splices requiring high axial resolution are insensitive to angular misalignment, while fiber splices requiring high angular resolution are less sensitive to axial misalignment. As the fiber tip is deflected by the gray-scale fiber aligner, many combinations of angular and axial losses occur. Thus, the power transmission curves for an *L=5mm* cantilever have been calculated numerically for different target fiber positions to investigate the tradeoff between tip deflection (angle) and required resolution (see Figure 5.9). The loss caused by a 1μm axial misalignment is also plotted for reference.

As evident in Figure 5.9, target fibers located at large tip deflections have progressively lower peak transmission due to increased angular loss. Thus, axial alignment resolution must improve to <1μm in order to surpass the equivalent of 1μm axial misalignment with no tip deflection. Table 5.1 shows the maximum transmission

and axial resolution required to achieve coupling equivalent to a 1μm pure axial misalignment. We see that for a 5mm cantilever and a target fiber at Y_0=*40μm*, the axial resolution must improve from 1μm to 0.40μm to achieve power transmission equivalent to 1μm pure axial misalignment.

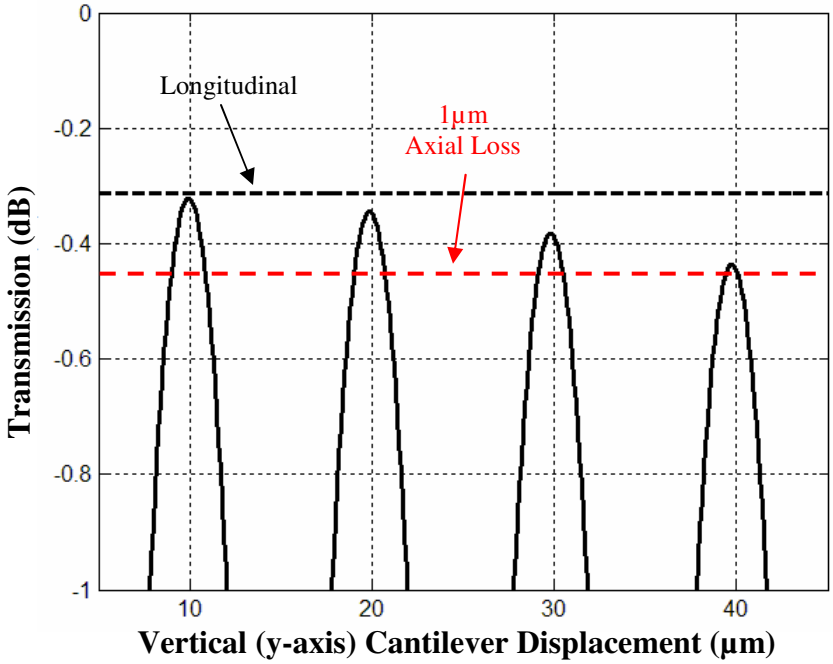

Figure 5.9: Transmitted power as a function of tip displacement for different target locations.

Table 5.1: Max transmission and required equivalent resolution for different fiber tip locations (assuming L=5mm and longitudinal separation of 30μm).

Target Location (μm)	Max Transmission (dB)	1μm Equivalent Resolution (μm)
0	-0.31	1.00
10	-0.32	0.96
20	-0.34	0.87
30	-0.38	0.72
40	-0.44	0.40

While a 1μm axial loss for cleaved fiber-fiber coupling has been used here for comparison purposes, the tolerances involved will be heavily device and application dependent (e.g. coupling to laser diodes with lensed vs. cleaved fibers has much different tolerances [162]). Most importantly, the preceding coupling analysis serves as a guideline

to estimate limitations of the proposed device. One must use similar analysis to determine what advantage the gray-scale fiber aligner can provide in a specific application.

In this research, to avoid significant angular loss, and for mechanical reasons discussed in the following section, fiber cantilevers with $L \geq 10mm$ were used. For the lengths and deflections considered here, the radius of curvature for bent fibers is >1m, making bending losses inside the optical fiber negligible.

5.4. Design

The principle of operation of an out-of-plane actuator based on opposing sloped alignment wedges was shown previously in Figure 5.1. Translating the alignment wedges alters the location of a cylindrical optical fiber resting within a dynamic v-groove. Since initial embodiments in packaging applications will require only a single use, it is not required that the actuator be either low-voltage or low-power, allowing a large amount of flexibility in actuator design. Planar electrostatic MEMS comb-drives will initially serve as the actuation mechanism for translating the sloped alignment wedges. This enables the use of the same process flow to fabricate both comb-drives and sloped alignment wedges simultaneously. Future devices could integrate variable-height comb-drives for improved displacement resolution, but such improvements lie beyond the initial goals of this thesis. For feasibility in packaging applications, the gray-scale fiber aligner should be capable of compensating for accumulated packaging and assembly errors to the order of 10μm initial misalignment [152]. The following sections discuss in more detail the design of the actuation mechanism and the design of the opposing sloped alignment wedges.

5.4.1. In-Plane Actuators (Comb-drives)

Design of the in-plane electrostatic MEMS actuator will largely focus on achieving the desired fiber deflection magnitude. As shown previously in Figure 5.3, the

anchor point for the optical fiber provides approximate passive alignment of the optical fiber, similar to a passive v-groove, such that the fiber's free end rests between the sloped alignment wedges. The location of this anchor point determines the length, and therefore spring constant, of the cylindrical optical fiber cantilever, according to [163]:

$$k_{fiber} = \frac{3\pi E r^4}{4l^3} \tag{72}$$

where E is Young's Modulus of the fiber ($\sim 70GPa$), r is the radius of the fiber (typically $r=62.5\mu m$), and l is the length of the fiber cantilever. As an example, a 10mm cantilever results in $k_{fiber}= 2.5\ N/m$. To first order, this spring constant can be modeled as part of the spring constant of the in-plane MEMS actuator suspension.

To achieve a desired range of motion, the actuation mechanism and fiber cantilever length must be considered jointly. Electrostatic comb-drive actuators have well-characterized force behavior, simplifying both design and control. The force generated by a comb-drive was presented earlier in Chapter 3 (Equation 29), and is repeated here:

$$F = N\frac{\varepsilon_0 h}{d}V^2 \tag{73}$$

where N is the number of comb-fingers, ε_0 is the permittivity of free space, h is the comb-finger height, d is the gap between fingers, and V is the applied voltage. Making some basic assumptions ($N=100,\ h=100\mu m,\ d=10\mu m,\ V=100V$), we can estimate a generated force of 89μN. If this force were applied directly to the fiber cantilever discussed above, the deflection would be >35μm ($F=kx$). However, one must also consider two additional factors for this device: first, the sloped wedges push the fiber at an angle, causing the fiber deflection magnitude to be slightly smaller than the comb-drive deflection

(assuming 45º wedges). Second, part of the generated comb-drive force is used to bend the comb-drive suspension, reducing the force delivered to the fiber. However, it is still reasonable to expect fiber actuation on the order of 10's of micrometers using comb-drive voltages of 100-150V on fiber cantilevers in the range of 10-12mm long. The use of comb-drive actuators also provides interesting possibilities for integrating the gray-scale comb-fingers discussed in Chapter 3 for improved positioning resolution of the fiber.

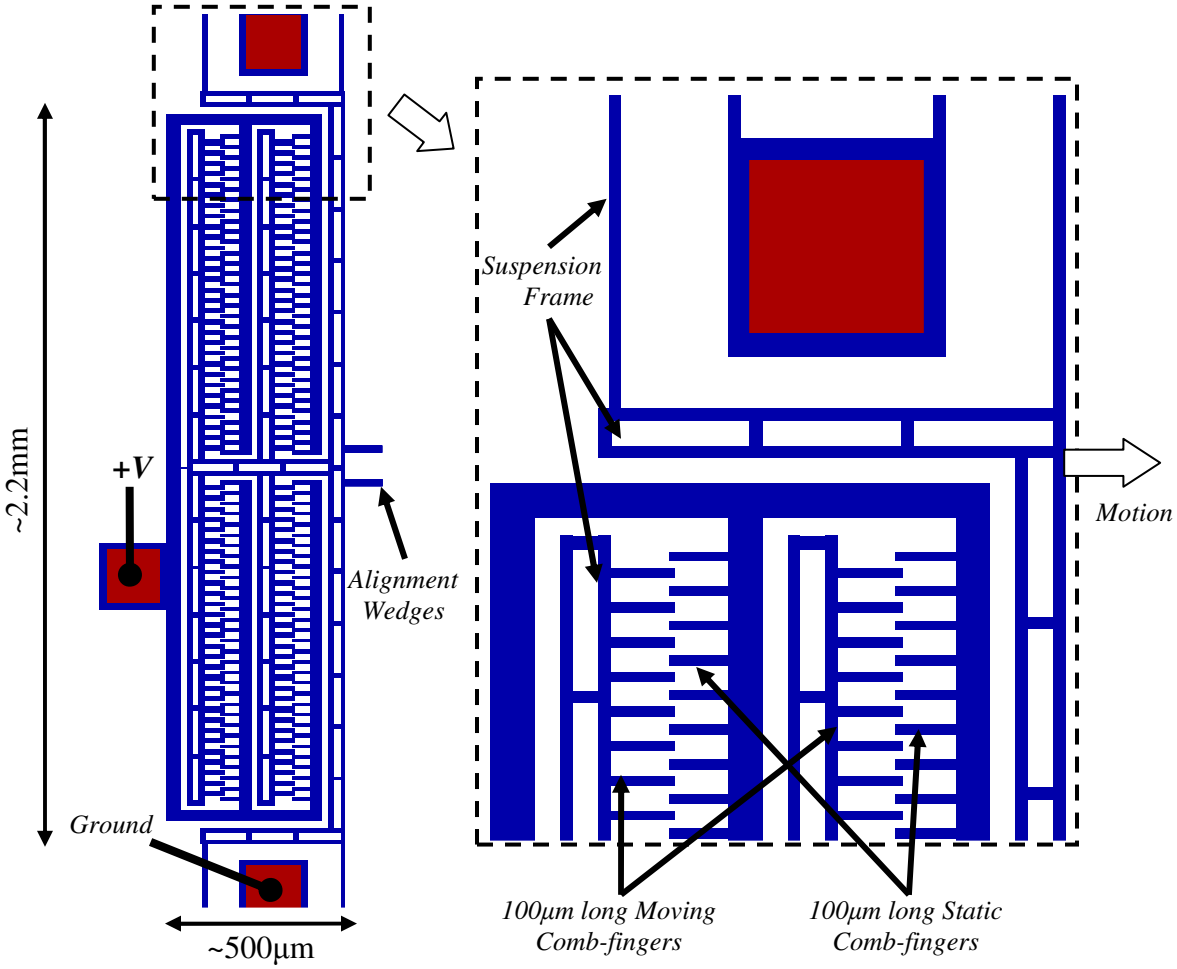

Figure 5.10: L-edit layout of a comb-drive actuator for actuating an optical fiber (gray-scale fingers would sit at the edge of the suspension frame where the arrow indicates the direction of motion).

One complication of using comb-drives is that the electrostatic force is always attractive, yet the device requires that the wedges 'push' on the fiber. Figure 5.10 shows

the novel approach taken in this research to create a "repulsive electrostatic comb-drive". Starting from a single electrode, the static comb-fingers were arranged on arms that reached around and point back towards the aluminum (Al) contact pad. The suspended comb-fingers meanwhile are attached to a stiff suspension frame that extends between the static electrode arms. Upon applying a voltage to the Al contact pad, the suspended structures get pulled to the right by the wrapped-around comb-fingers. Thus, a pushing motion has been created from the perspective of the electrode. One drawback of this design is its size. Wrapping the suspension frame inherently takes extra space, and a device with 100 comb-fingers per side requires significant real-estate on the wafer. The area required for one side of the actuator shown in Figure 5.10 is ~1.1mm^2. Given the size of the suspensions (1mm long each) and length of the cantilever (~10-12mm), an entire device is in the range of ~7mm^2.

For devices investigating the design, fabrication, operation, and control of this new type of actuator, the relatively large overall footprint is acceptable. However, for packaging applications, it is imperative that these systems be reduced in size, particularly for packaging of fiber arrays with a small pitch (250-500μm). Two primary approaches for developing such systems will be discussed in Chapter 7 as extensions of this work: (1) the use of reduced cladding fiber (r=40μm) for shorter/more flexible cantilevers, and (2) integration of higher force actuators that have potentially smaller footprints (such as thermal [45]).

The rest position of a fiber tip between sloped alignment wedges can be calculated using geometry (see Appendix D). We will always assume that the restoring force of the bent fiber cantilever causes it to rest at the bottom of the dynamic v-groove.

For the case of 45º alignment wedges and comb-drive actuators, we can plot the rest position of the fiber as a function of applied voltage. Figure 5.11(a) shows the possible v-groove alignment area, where each point represents a case of discrete applied voltages to comb-drives A and B from Figure 5.3. Taking the point (0,0) as the initial fiber resting place before actuation, the center of an optical fiber can be moved to any point within the boundaries of this imaginary diamond-shaped alignment area. Note that the uneven spacing of points in Figure 5.11(a) derives from the quadratic displacement of planar comb-drive actuators, resulting in alignment resolution that varies with position. Future devices could incorporate the variable-height gray-scale comb-drives discussed in Chapter 3 which could improve alignment resolution at large displacements, as shown in Figure 5.11(b).

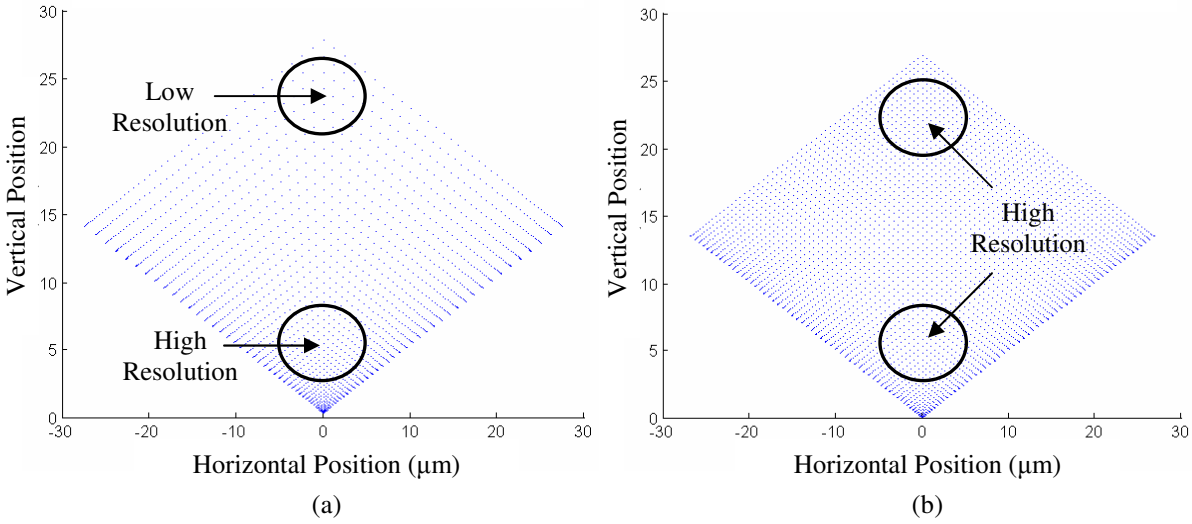

Figure 5.11: Possible alignment area covered (in the X-Y plane of Figure 9) for (a) a planar comb-drive actuator (k=5 N/m, gap=10µm, N=200, V_{max}=90V), where the displacement resolution varies depending on position, and (b) a gray-scale tailored force actuator exhibiting improved resolution at large deflections (k=5 N/m, gap=10µm, N=200, V_{max}=120V).

5.4.2. Alignment Wedges

The most critical components of this fiber actuator are the opposing sloped alignment wedges, since they contact the fiber directly and enable the out-of-plane

actuation. Once again, gray-scale technology will be used to integrate the required 3-D silicon wedges with in-plane electrostatic MEMS comb-drives. The primary difficulty when designing the alignment wedges is balancing the wedge angle, ARDE effects (see Section 2.5.2.1), and number of gray levels (i.e. morphology).

The exact angle of the wedges is not critical, but excessively shallow or steep angles could cause slippage or jamming of the fiber. A target angle of approximately 45º was chosen as the initial goal for the wedge design, ideally resulting in similar horizontal and vertical resolution. The alignment wedges are located within the open fiber trench, which is almost an order of magnitude wider than the comb-drive finger spacing (200μm vs. 30μm). This large size difference will lead to significant ARDE between the two structures. To anticipate the over etching required to fully define the comb-drive fingers/spaces, the alignment wedges were designed to have a ~30μm vertical shift (created by introducing a constant offset in the CARDE process discussed in Chapter 2).

The selection of the gray-scale mask pitch and pixel set for defining the alignment wedges is extremely important. Ideally, after fabrication, the sloped wedges should be smooth compared to the size of the optical fiber (*diameter=125μm*) to enable continuous motion. Yet, considering the mask design limitations discussed in Chapter 2, tall and smooth slopes are a challenge when using a single gray-scale exposure. Compounding this difficulty is the fact that the CARDE offset renders a large number of lower gray levels unusable. Thus, the importance of pitch selection can be seen in the following simulations, based on the Gaussian approximation and pixel limitations discussed earlier in Chapter 2. Two different gray-scale alignment wedge profiles were simulated, both assuming an etch selectivity of 60:1 and a 30μm over-etch (due to ARDE). The first

profile, shown in Figure 5.12(a), uses a mask pitch of 2.8µm with only ~25 useable gray levels, resulting in a prominent stair stepped profile. In contrast, Figure 5.12(b) shows a simulated profile using a pitch of 3.2µm, which enables ~50 gray levels within the desired range (pixel sets are given in Appendix E). Given these simulated profiles, the 3.2µm pitch is expected to produce smoother fiber motion, but still has room for improvement. These alignment wedges could be an excellent candidate for the double-exposure lithography technique introduced in Chapter 2, however it would require significantly more characterization.

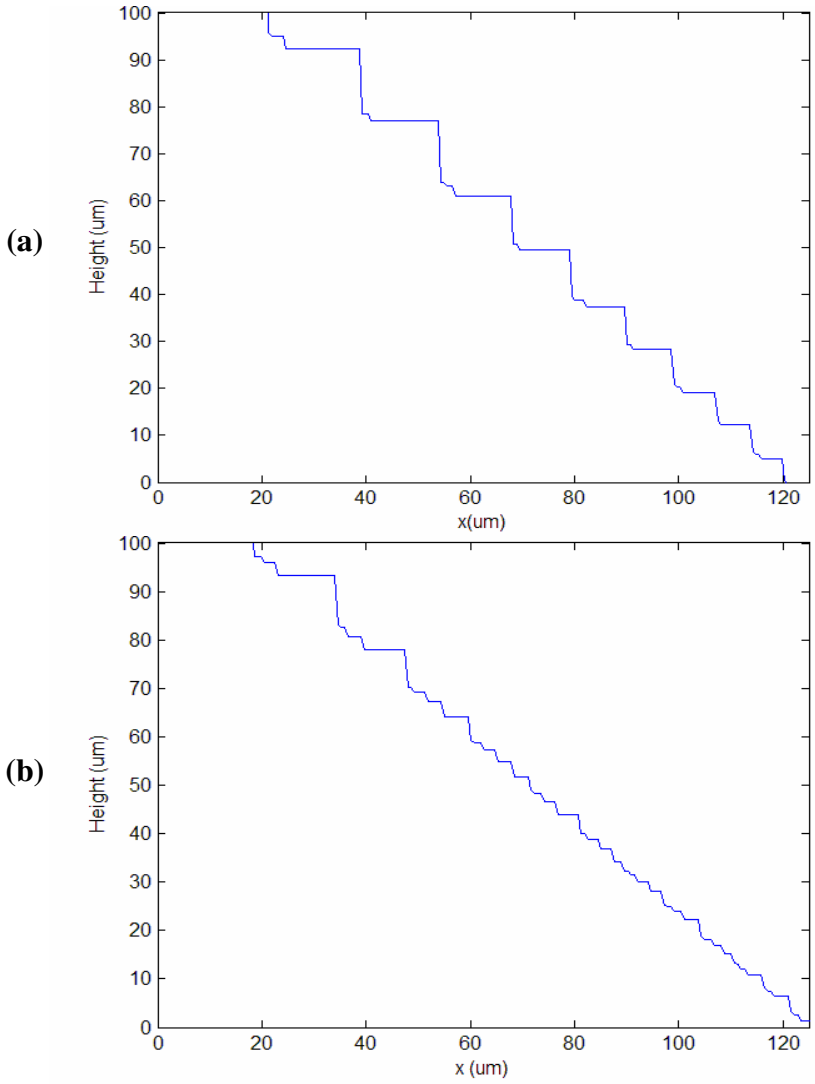

Figure 5.12: Simulated gray-scale alignment wedge profiles using (a) 2.8µm pitch with ~25 levels, or (b) 3.2µm pitch with ~50 gray levels.

5.5. Fabrication

The fabrication of the gray-scale fiber aligner follows the same gray-scale SOI comb-drive process flow presented previously in Chapter 3 (hence both fiber aligners and comb-drives can be fabricated simultaneously). Figure 5.13 shows optical and SEM micrographs of fabricated gray-scale alignment wedges in photoresist. In Figure 5.13(a), the opposing wedges appear with rainbow colors that are indicative of the changing photoresist thickness. The small holes evident in the wedge in Figure 5.13(b) are caused by partial re-construction of the pixels on the optical mask since the chosen pitch (3.2μm) is slightly above the projection lithography system resolution (a tolerable effect in our current application).

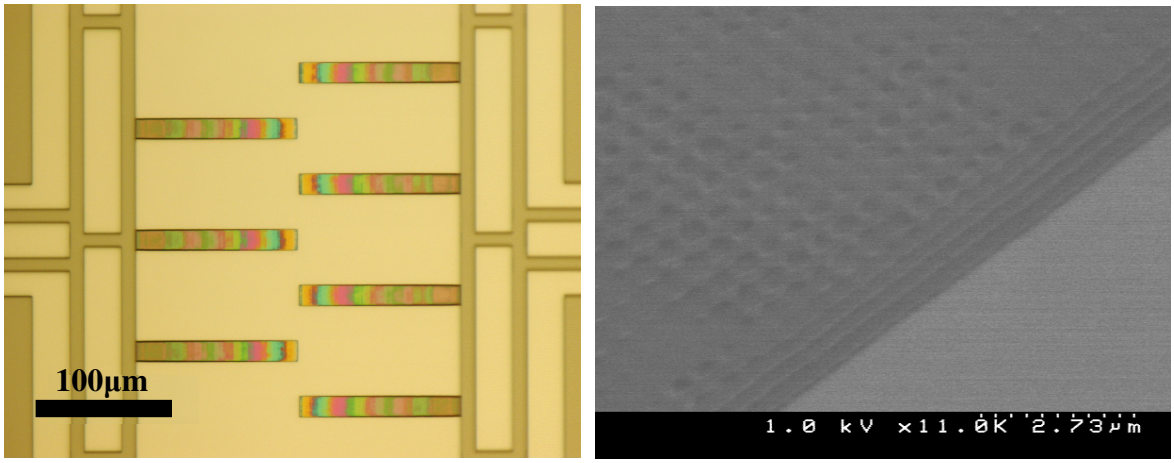

(a) (b)

Figure 5.13: (a) Optical and (b) close-up SEM micrographs of photoresist gray-scale alignment wedges using a 3.2μm pitch.

After DRIE pattern transfer, the difference in morphology between the 2.8μm pitch (25 gray levels) and the 3.2μm pitch (50 gray levels) is significant. Released silicon electrostatic actuators with integrated 3D wedges are shown in Figure 5.14 and Figure 5.15, for the 2.8μm and 3.2μm pitch designs, respectively. Figure 5.14(b) clearly shows the wedge has distinct steps on the gray-scale slope, similar to the simulated profile of Figure 5.12(a). In contrast, the close-up SEM in Figure 5.15(b) shows a much improved

slope, as expected from Figure 5.12(b), where micron-level roughness has been achieved over the majority of the slope. Note that the holes in photoresist shown previously in Figure 5.13(b) are not evident in the silicon after DRIE pattern transfer. Due to the size and location of the wedges, profilometer tips could not reliably trace the alignment finger profiles, and white light interferometry did not capture sufficient reflected light from the angled surface. Thus, quantitative roughness measurements were impractical without destructive testing that makes it impossible to relate roughness to device performance.

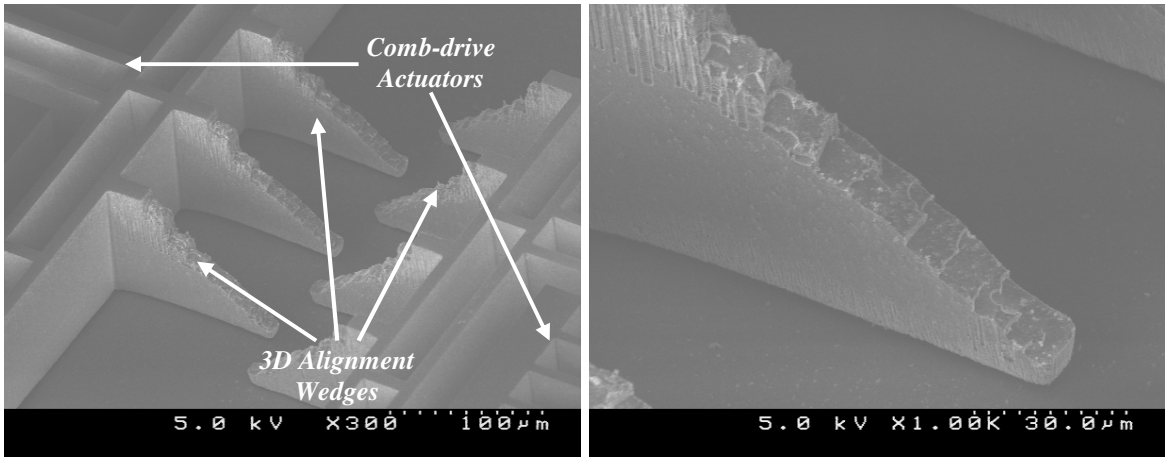

(a) (b)

Figure 5.14: (a) Far-field and (b) close-up SEM's of alignment wedges fabricated with 25 gray levels using a 2.8µm pitch.

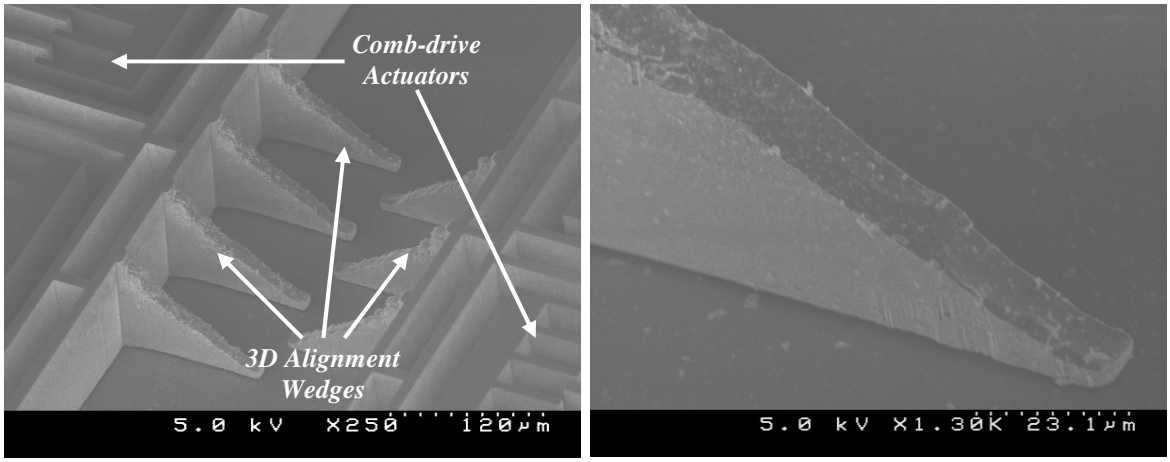

(a) (b)

Figure 5.15: (a) Far-field and (b) close-up SEM's of alignment wedges fabricated with 50 gray levels using a 3.2µm pitch. Notice that the small holes in photoresist are not evident on the slope.

5.6. Assembly

To prepare the sample for testing, a length of single mode optical fiber (Corning SMF-28e) was manually stripped and cleaved. The cleaved free end of the fiber is placed between the alignment wedges (attached to the comb-drives), while the bulk of the fiber passes through the static trench. In order to enable coupling to other devices (either optical fibers or indium-phosphide (InP) waveguides), the cleaved facet of the fiber cantilever hangs slightly off the edge of the SOI chip (<1mm).

The bulk fiber is secured in the static trench with UV-curing epoxy (Norland Products, Inc.) to create a flexible cantilever. Small drops of epoxy are applied using a piece of optical fiber dipped in un-cured epoxy. Due to the lack of control over drop volume, the UV lamp must shine on the sample immediately after the drop is applied to avoid excessive spreading of the epoxy. The effect of spreading epoxy is most noticeable when it wicks along the bottom of the fiber beyond the static trench, effectively shortening the fiber cantilever length. Since the extents of epoxy flow are easily viewed under a microscope, an adjusted fiber cantilever length can be estimated to account for this effect. A device after fiber attachment is shown in Figure 5.16.

Since the fiber attachment process is entirely manual, it is difficult to ensure that the fiber touches both wedges in its rest state. Reliable operation can be achieved with small gaps between the wedge and fiber, but requires a voltage offset to move both sets of wedges into contact before the fiber begins to move. The inconsistencies with manual fiber attachment and epoxy dispensing should be remedied by moving towards automated pick and place machines with controlled liquid dispensing capabilities [164]. Alternative methods for fiber attachment, such as laser spot welding could also be investigated [165].

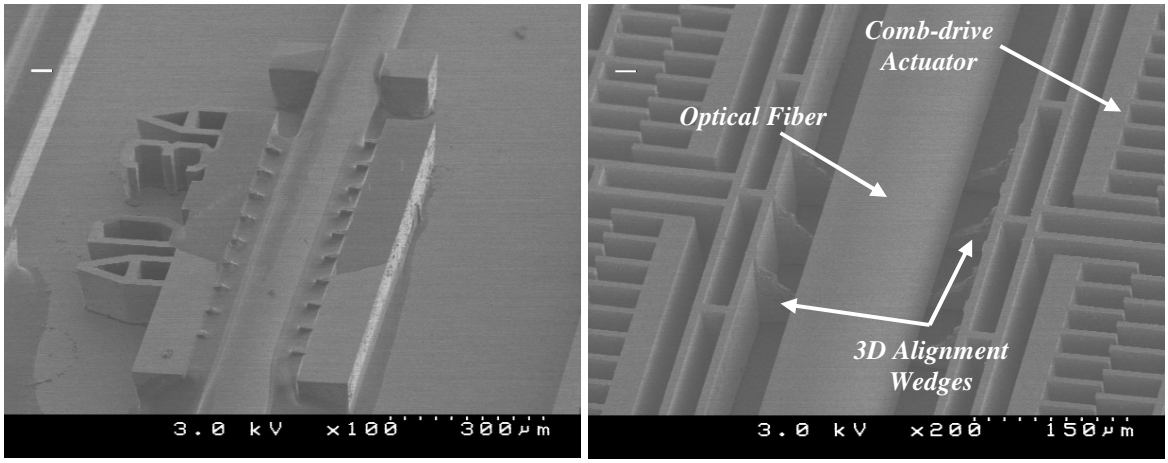

(a) (b)

Figure 5.16: SEM's of (a) fiber secured in the static trench with UV-curing epoxy and (b) the free end resting between the 3-D alignment wedges.

5.7. Actuation Concept Demonstration

The proposed new fiber actuation mechanism was first evaluated using a white-light optical profiler (Veeco WYKO NT1100) to track both horizontal and vertical movement of the fiber caused by actuating the sloped wedges. In static mode, this profiler uses reflected light from horizontal surfaces to create a full-field 3-D height map in only a few seconds. Since an optical fiber is cylindrical, appreciable reflected light is only collected from a thin strip (1-2µm wide) representing the top of the fiber. The silicon actuators in the background serve as a vertical reference point, enabling changes in both the horizontal and vertical location of the fiber to be determined. Due to limited magnification available in the system and changing light conditions as a fiber is deflected, the accuracy of measurement is estimated at only <2µm. While this measurement method is clearly not intended to evaluate alignment to another fiber, it is adequate for demonstrating the principle of operation of the gray-scale fiber aligner.

Figure 5.17 shows the measured location of the optical fiber for different sets of applied voltages (up to 120V). Three primary actuation trajectories are shown.

Actuating each set of wedges independently (while holding the opposite set at 0V) results in points along two trajectories that are tilted with respect to the X-Y axis (labeled #1 and #3 in the figure). Purely vertical motion of the fiber is achieved by applying an identical voltage to each actuator (#2 in the figure). Intermediate voltage combinations should result in fiber positions within the diamond-like bounds of these measurements. This test successfully demonstrates the basic operation of our gray-scale fiber aligner, where an optical fiber cantilever is deflected in both the horizontal and vertical directions using coupled in-plane motion of sloped silicon wedges.

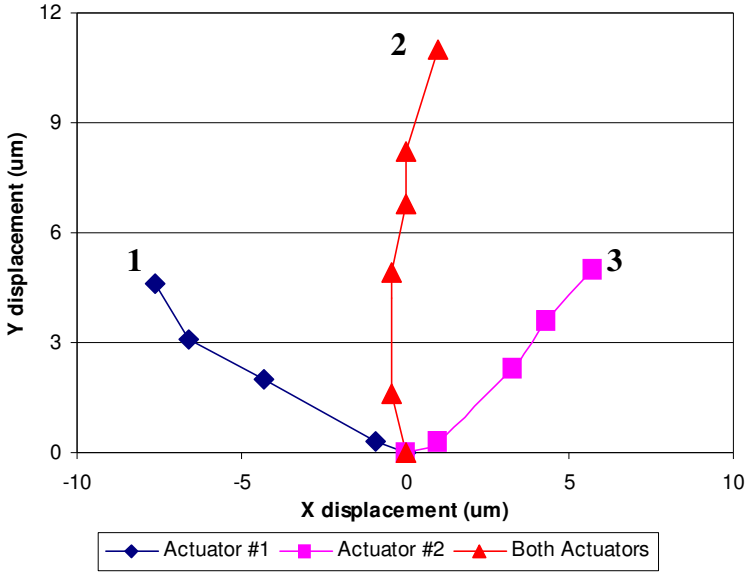

Figure 5.17: Fiber locations measured using an optical profiler for different actuation voltage combinations. Each colored path represents a trajectory caused by actuating either wedge by itself (angled trajectories #1 and #3) or both wedges together (straight up #2).

5.8. Conclusion

This chapter has introduced a new on-chip method for actuating an optical fiber in 2-axes. Opposing electrostatic comb-drives with integrated 3-D wedges create a dynamic v-groove capable of altering the horizontal and vertical alignment of an optical fiber

cantilever. All structural components of this new device can be fabricated in silicon using gray-scale technology, making it conducive to batch fabrication. This device is attractive for on-chip active alignment of fiber optics to edge-coupled optoelectronic devices.

Analysis of the primary sources of optical coupling loss between two fibers showed that 2-axis alignment is sufficient to eliminate the dominant source of loss (axial misalignment). However, the amount of angular misalignment introduced by bending the fiber cantilever must also be considered. The design and fabrication of the gray-scale alignment wedges showed that ~50 gray levels were able to produce a relatively smooth slope, which should result in nearly continuous fiber actuation (experimental results discussed in the following chapter). Simple actuation and measurement results clearly demonstrated the fundamental operation of the 2-axis gray-scale fiber aligner.

The following chapter will focus on evaluating the performance of gray-scale fiber aligners in an optical coupling setup. Of particular interest will be the fiber actuation range and resolution, as well as hysteresis behavior between the sloped wedges and optical fiber due to friction. Automated alignment algorithms will be developed as part of this evaluation process to demonstrate the flexibility of this device.

CHAPTER 6: GRAY-SCALE FIBER ALIGNER II: Optical Testing and Characterization

6.1. Introduction

The previous chapter has introduced the design, modeling, and fabrication of a novel 2-axis optical fiber alignment platform, the *gray-scale fiber aligner*, for systems requiring in-package active fiber alignment. The development of this device is directly aimed towards addressing some of the primary challenges identified by ITRS in the area of optoelectronic packaging [77]. While the basic mechanical operation of this device was briefly demonstrated, the overriding purpose of this device is to optimize optical coupling between an optical fiber and a corresponding target (another fiber, waveguide, laser, etc). Therefore, this chapter is dedicated to the static and dynamic characterization of the gray-scale fiber aligner through multiple optical coupling configurations.

The development of an experimental setup for testing both fiber-fiber and fiber-waveguide coupling will first be discussed in Section 6.2. Static testing results will then be reviewed in Section 6.3, with particular emphasis on evaluating actuation range and controlling movement of the fiber tip. Section 6.4 will discuss auto-alignment algorithms for both coarse and fine alignment, with testing results focused on speed and resolution presented in Section 6.5. Discussion of testing results will be given in Section 6.6. Concluding remarks are provided in the final section.

6.2. Experimental Setup

All infrastructure and experimental testing discussed in this chapter was developed in the MEMS Sensors and Actuators Lab (MSAL) at UMD. The following sub-sections will describe both the hardware assembled for optical testing and some characterization of the system limitations.

6.2.1. Hardware

The optical setup developed to test the gray-scale fiber aligner is shown schematically in Figure 6.1. A 1550nm laser diode is used as the optical source. The target fiber is fixed on a calibrated electrostrictive XYZ stage controlled via LabVIEW. In some cases, the target fiber is aligned to an indium-phosphide (InP) chip with suspended waveguides [166, 167]. The gray-scale fiber aligner holds the output fiber and is fixed on a second electrostrictive XYZ stage. In general, the location of the gray-scale fiber aligner chip is not altered during alignment testing to avoid repositioning the electrical probes. The output fiber is connected directly to an optical power meter, which is sampled by LabVIEW. Actuation voltages for the gray-scale fiber aligner are provided through two analog-out channels on a data acquisition (DAQ) card and a high-voltage (HV) MEMS amplifier. The limited current output of the DAQ card (5 mA), coupled with the low input impedance of the HV amplifier (50Ω), made it necessary to add an op-amp buffer circuit to increase current output in order to achieve high voltages (up to 200V). The primary components and associated model numbers are listed in Table 6.1.

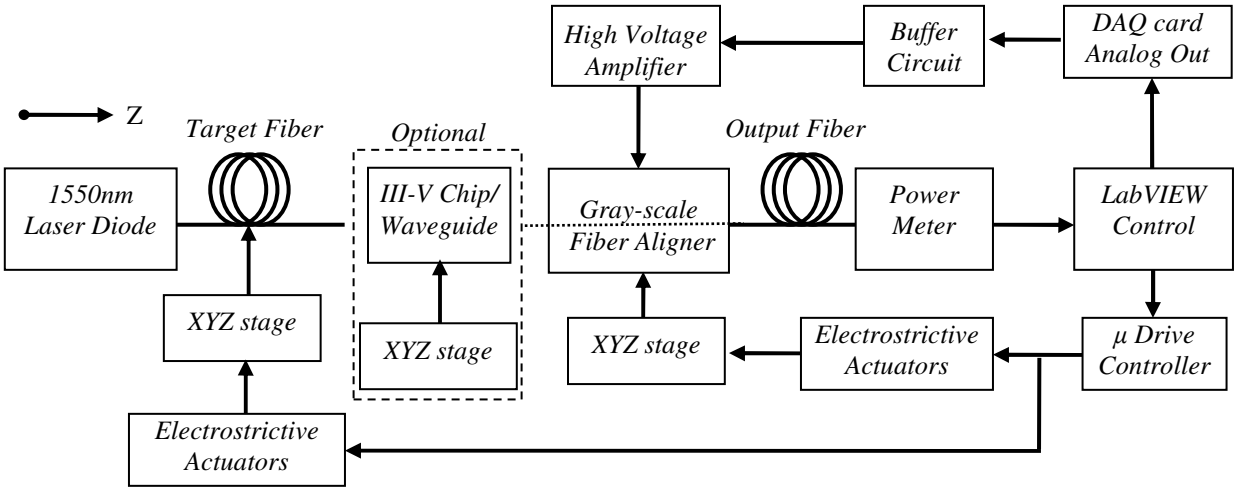

Figure 6.1: Optical test setup for auto-alignment of MEMS-actuated fiber to cleaved fibers or InP waveguides.

Table 6.1: Primary hardware components used in the optical testing setup.

Manufacturer	Product	Model #
Newport	Optical Power Meter	1830-C
Newport	IR Detector	818-IR
Newport	Laser diode	LD-1550-21B
Newport	Laser diode driver	501
Newport	μ Drive Controller	ESA-C
Newport	Electrostrictive Actuator	AD-100
Newport	Mechanical Positioning Stages	561D
National Instruments	Data Acquisition Card	6221
Pragmatic	High Voltage MEMS Amplifier	100X
ST Microelectronics	Operational Amplifier	LM324N
Corning	Single mode fiber (9/125μm)	SMF-28e
Corning	OptiFocus Lensed Fiber	3.3μm MFD

6.2.2. Instrumentation Characterization and Limitations

Prior to testing devices, it was necessary to characterize the limitations of the experimental setup. Since optical coupling is position sensitive, mechanical drift between input and output was a particular concern. Two fibers were manually aligned with the XYZ stages to peak coupling and the power monitored over the course of a few hours. As shown in Table 6.2, slight drift between stages caused <2% change in coupled power over a 3 hour period. Since peak coupling could be restored using X-Y positioners, we concluded that negligible drift occurred along the Z-axis. This fact is important because the gray-scale fiber aligner already adjusts for X-Y position, but changes in separation would alter the peak power which must remain stable during alignment tests. Therefore, the stability of the peak power is limited by optical noise (source and detector variations) and mechanical vibrations in the system; estimated to be <1% for short coupling experiments.

Table 6.2: Mechanical drift of stage causes slight change in coupled power between aligned fibers.

Time	Power (μW)	Drift (%)
12:25pm	496.0	--
12:42pm	497.2	0.2
1:35pm	502.6	1.3
2:16pm	504.0	1.6
3:02pm	504.5	1.7
3:31pm	507.4	1.9

One essential function this setup must perform is to locate the position and value of the maximum coupled power. The facet of the input fiber can be scanned in the X-Y plane using a custom LabVIEW module (developed by MSAL member Jonathan McGee) to control the electrostrictive XYZ stage while monitoring the coupled power. This facet scan creates a 2-D map of coupled power vs. position to quantify the relative locations of the target and output fiber before and after each alignment experiment. An example 2-D coupled power map is shown in Figure 6.2. The coupling profile is approximated using a 3-parameter Gaussian fit to quantify the shape of the peak:

$$y = a \cdot \exp\left[-\frac{1}{2}\left(\frac{x - x_0}{b} \right)^2 \right]. \tag{74}$$

This Gaussian fit is imperative for measuring the sharpness of the peak, as shown in Figure 6.3, which provides a numerical correlation between the coupled power and axial misalignment between input/output. As a worst case scenario estimate, the "true" peak power is inferred using the Gaussian width parameter by assuming the highest recorded power during the facet scan was 0.5μm misaligned (½ way between two points on the 1μm scan grid). If a higher power is observed during the alignment tests, potentially due to nearly "perfect" alignment or small noise fluctuations, the higher

power is taken as the "true" peak power instead. Since the peak in Figure 6.3 is relatively wide, achieving alignment resolutions of ~1.5μm will require final coupling thresholds close to 95% of the peak power.

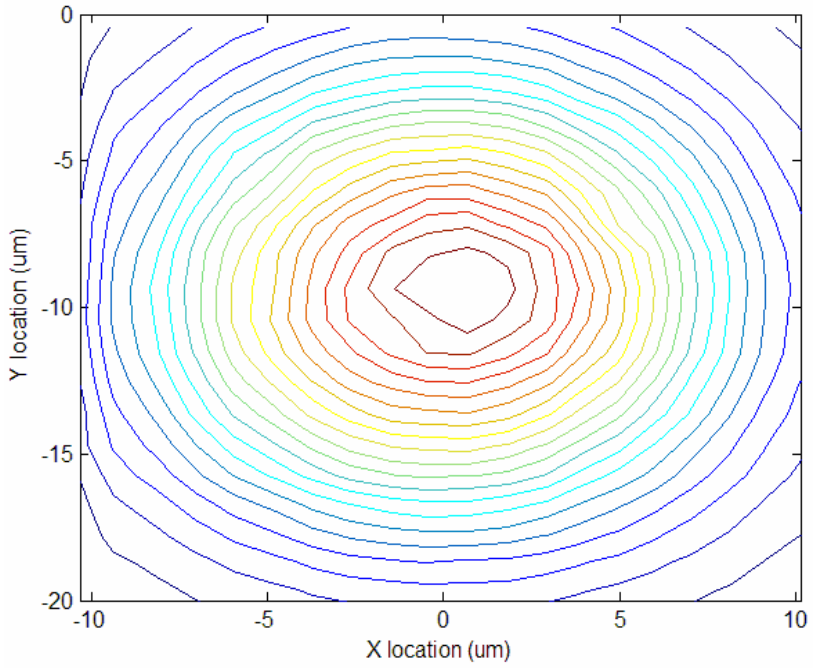

Figure 6.2: Example coupled power contours using a LabVIEW module to scan the facet of the fiber. Measures location and sharpness of coupling profile.

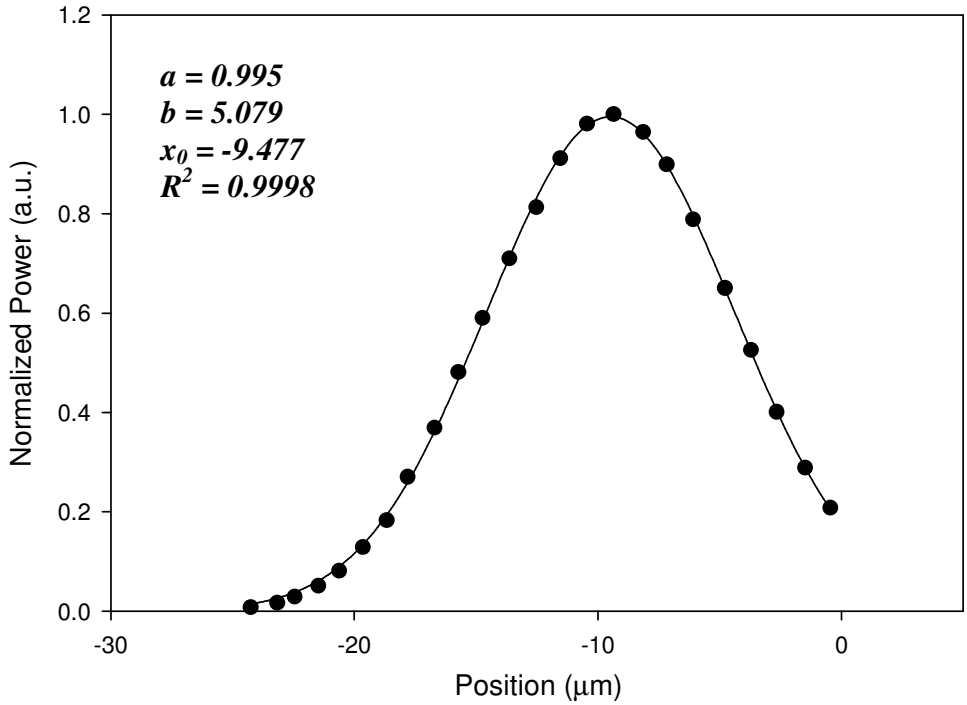

Figure 6.3: Cross-section of fiber-fiber coupled power profile after 3-parameter Gaussian fit.

The final important characteristic of our experimental setup pertaining to the gray-scale fiber aligner is the delay between fiber movements required by the control program to properly asses the new coupled power. There are two possible contributors to this delay: first, a finite time is required for the fiber to physically move and switch positions. Second, the LabVIEW control program and associated components need time to be updated and/or queried. Thus, the control program must periodically pause after initiating a voltage change to allow the fiber to reach its new position and sample the optical power meter, all before actuating the fiber again.

First, transient fiber-fiber coupling experiments were conducted to evaluate the switching speed of the gray-scale fiber aligner. The optical power meter was temporarily replaced with a high-speed photoreceiver (New Focus 1811 IR-DC 125MHz Low Noise Photoreceiver). Note that this photoreceiver is noisy compared to the optical power meter and has a small dynamic range, making it ill-suited to alignment experiments but acceptable for assessing transients. The gray-scale fiber aligner was initially partially aligned with an output fiber such that a small amount of coupled power was received. The fiber was then actuated to a position of different coupling while recording the actuation voltage and photoreceiver output voltage simultaneously via the DAQ card.

Measurements of fiber aligner switching were taken during both “Up” and “Down” actuation trajectories (starting and ending voltage combinations), as shown in Figure 6.4. During the “Up” trajectory, the fiber was sometimes observed to slightly over-shoot the final position, possibly due to momentum carrying it off the surface of the alignment wedges. It is expected that the switching speed will depend slightly on the size and direction of the fiber trajectory, yet typical switching speeds of <1ms were observed.

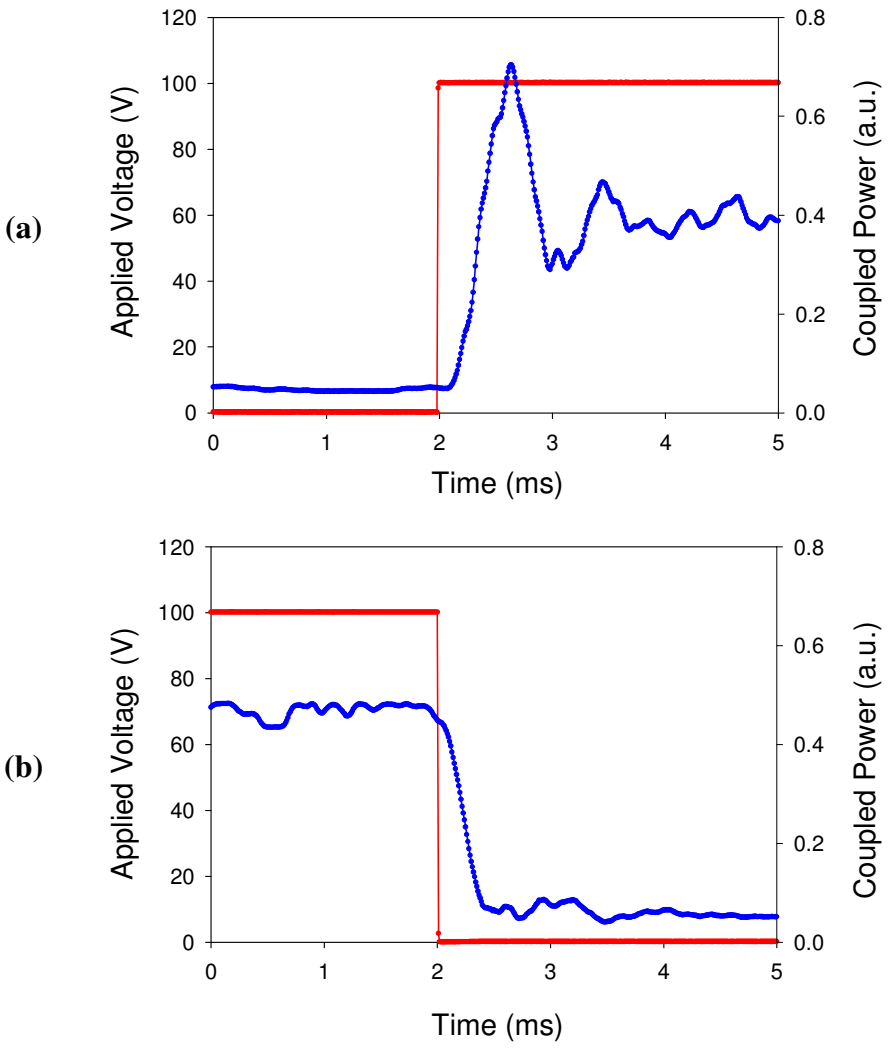

Figure 6.4: Actuation speed of the gray-scale fiber aligner during (a) "Up" and (b) "Down" actuation trajectories. In some "Up" experiments, the fiber over-shoots the final position, as in (a).

We now turn our attention to assessing how quickly and reliably we can change actuation voltages and sample the optical power meter. Thus, a *settling time* (pause) parameter was introduced in LabVIEW as a delay between sending the actuation signal and measuring the power at a new position. The same fiber-fiber coupling setup as above was used with the optical power meter, and the received power was recorded after different settling times. Fiber settling experiments were conducted for different fiber

trajectories, the results of which are depicted graphically in Figure 6.5, where the transition from one fiber position to the other is obvious.

Since the fiber actuation occurs in ~1 millisecond, these tests confirm that the required settling time is limited by the LabVIEW control program and power meter. Although the optimum settling time for each fiber trajectory may be different, our results indicate that a universal settling time of at least 300ms should be used between fiber movements. While changes to the experimental setup could potentially increase this actuation speed, later fiber alignment tests will show that such speeds have still produced fast and reliable fiber alignment.

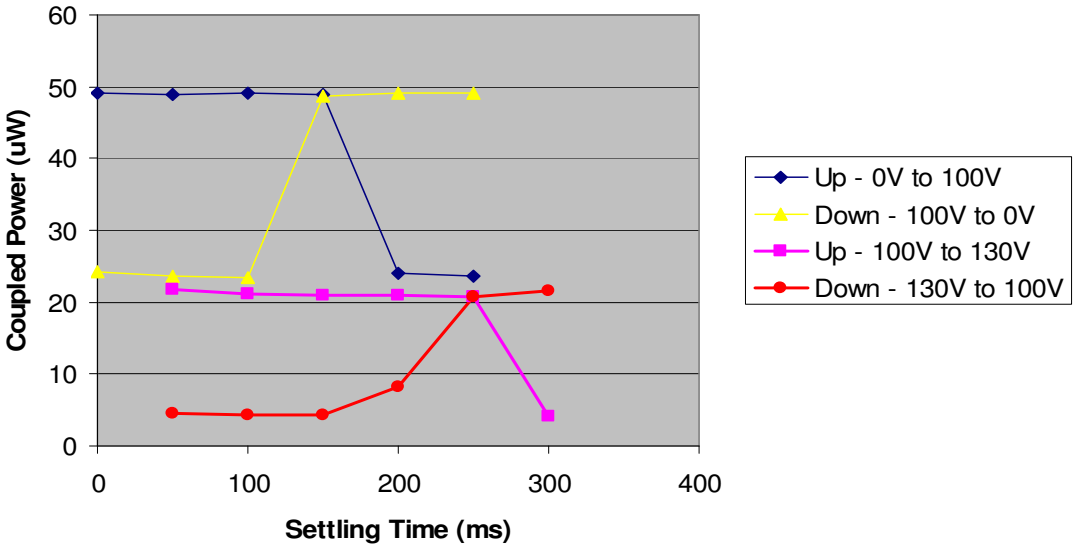

Figure 6.5: Measured power as a function of settling time for different fiber trajectories, showing the delay between sending the actuation signal and the fiber completing it's motion. Settling times of 300ms were deemed sufficient for complete fiber switching.

6.3. Static Testing

The next step in characterizing the gray-scale fiber aligner motion is to measure static movements intended to create motion along easily predictable patterns. The tests described below seek to characterize the range, flexibility, and hysteresis of fiber

actuation. Such static movements will serve as the foundation for the auto-alignment algorithms discussed in later sections. Unless otherwise mentioned, tests described in this and the following sections utilize devices with a fiber cantilever length of L=12mm.

6.3.1. "Diamond" Extents

The actuation mechanism of the gray-scale fiber aligner inherently defines a diamond-shaped area over which a fiber tip can be aligned, as described in Chapter 5. Thus, to establish the overall range of operation for this device, we must measure the size of this diamond-shaped area corresponding to the extreme movements of each alignment wedge. The voltage on either actuator was limited to 0-140V to avoid breakdown of the 2μm buried oxide (based on experience), restricting the overall travel range.

Four discrete voltage combinations were applied to the two actuators to move the fiber to the four corners of the diamond-shaped alignment area. The location of the cleaved fiber tip was measured for each case using the facet scanning capability described earlier (with Gaussian fits). The voltage combinations, as well as absolute and relative fiber locations for this device, are given in Table 6.3. These four points, shown graphically in Figure 6.6, create a relatively symmetric diamond. Fiber positions within the diamond-shaped bounds of these measurements (37μm tall, 48μm wide) should be achievable with the appropriate set of applied voltages.

Table 6.3: Measured fiber locations for discrete actuation voltages. These 4 points form the corners of a diamond shaped alignment area.

Ch A (V)	Ch B (V)	X Position (μm)	Y Position (μm)	ΔX (μm)	ΔY (μm)
0	0	-5.5	-3.0	0	0
0	140	-29.5	17.6	-24.0	20.6
140	0	18.8	16.7	24.3	19.7
140	140	-5.4	34.0	0.1	37.0

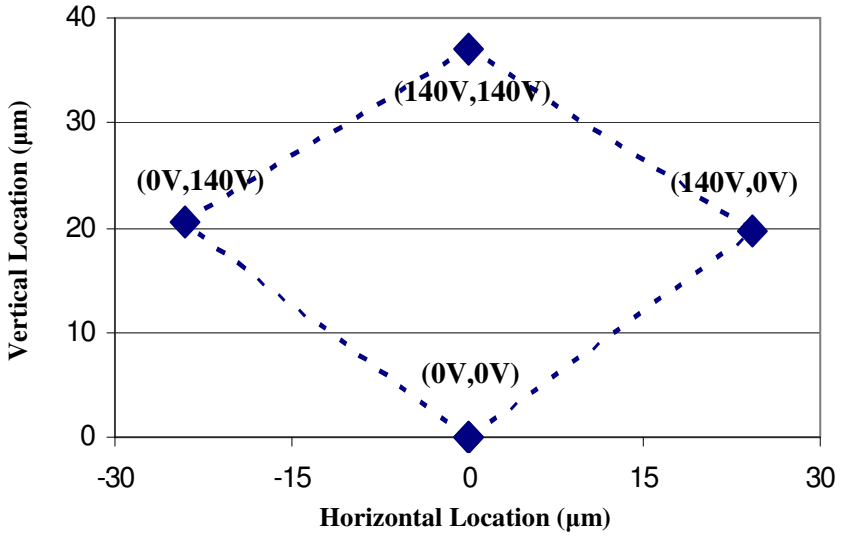

Figure 6.6: Measured fiber location for extreme actuation voltages, which form a diamond-shaped alignment area.

The fiber tip displacements measured in Figure 6.6 are slightly larger than the fiber displacement at the alignment wedges because the fiber tip extends beyond the wedges for ease of testing, causing a small additional tip displacement. More discussion on this subtle point is given in Appendix C.

6.3.2. Power Mapping

The diamond extents test was simply a demonstration of large single movements. Yet, we would also like to show that the gray-scale fiber aligner provides some of the same functionality as the electrostrictive XYZ stages. Using LabVIEW, we implemented a raster actuation routine to map the fiber-fiber coupled power as a function of applied voltages to channels A and B of the gray-scale fiber aligner. This scan is analogous to the 2-D facet scan performed by the electrostrictive stages.

Shown in Figure 6.7 are coupled power contours that are plotted vs. voltage squared (since comb-drive force scales with V^2). The concentric circular power contours clearly demonstrate that movements of each alignment wedge behave predictably and rather symmetrically. The single dominant coupling peak is a result of the fiber-fiber

setup being used in this test; however optimizing coupling to devices with secondary peaks is always a concern during fiber alignment and will be discussed in later sections.

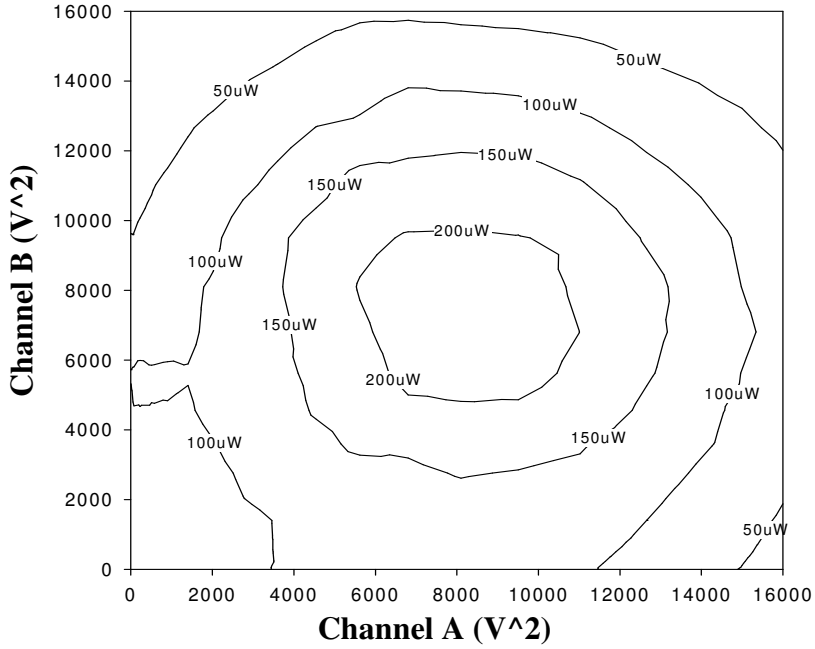

Figure 6.7: Coupled power contours created using the gray-scale fiber aligner for a fixed target fiber location as voltage combinations are applied to the device.

6.3.3. Cartesian Control

As evident from the diamond test, when one wedge is kept stationary and the other moved, the fiber tip will trace out an angled trajectory parallel to one side of the diamond-shaped alignment area shown in Figure 6.6. This essentially leads to a rotated coordinate system (in V^2 space) where moving one actuator creates fiber movement along a tilted axis. Yet, in some cases it may be advantageous to move the fiber along Cartesian coordinates; for example, to map optical sources with complicated modes.

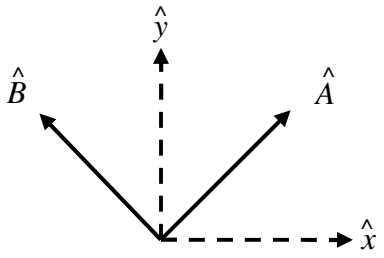

Figure 6.8: Relation between Cartesian and wedge primary axes.

Referring to Figure 6.8, we see that the Cartesian axes are simply summations of the angled fiber trajectories caused by individual wedge movements:

$$\hat{x} = \left(\hat{A} - \hat{B}\right)/\sqrt{2} \quad \textbf{(75)}$$

$$\hat{y} = \left(\hat{A} + \hat{B}\right)/\sqrt{2} \quad \textbf{(76)}$$

Thus, a coordinate transform from wedge to Cartesian axes can be made by assuming symmetrical 45º wedges and an initial point in voltage space (V_A, V_B). We can then define an arbitrary desired Cartesian trajectory (U) to be:

$$\vec{U} = \alpha \cdot \hat{x} + \beta \cdot \hat{y} \quad \textbf{(77)}$$

where α and β are coefficients in units of $Volts^2$ because the comb-drive force scales with voltage squared. The set of new voltages ($V_{A\text{-}new}$, $V_{B\text{-}new}$) required to create this trajectory can then be calculated as:

$$V_{A-new} = \sqrt{V_A{}^2 + \alpha + \beta} \quad \textbf{(78)}$$

$$V_{B-new} = \sqrt{V_B{}^2 - \alpha + \beta}\,. \quad \textbf{(79)}$$

Using these transforms, the fiber tip can be directed in any Cartesian direction from any starting point within the diamond alignment area. To show this capability, the fiber was actuated along trajectories every 45º for $|U|=2000V^2$ and $|U|=4000V^2$, starting from the middle of the actuator range (99V, 99V). The measured fiber locations after actuation are shown in Table 6.4 and Figure 6.9. For the angled trajectories, one wedge remains stationary while the other wedge slides the fiber up/down the slope. For the vertical and horizontal trajectories, the wedges must move in tandem to produce the desired fiber movement.

Table 6.4: Cartesian control results for the 45º primary axes starting from center of diamond shaped alignment area (99V, 99V).

Desired Angle (º)	Desired |U| (V^2)	ΔX (μm)	ΔY (μm)	Measured |U| (μm)	Measured Angle (º)	Resolution (μm / |U|=1000V^2)
0	2000	8.7	-0.1	8.7	-0.5	4.3
0	4000	15.7	1.0	15.7	3.8	3.9
45	2000	5.0	4.9	7.0	44.5	3.5
45	4000	10.5	9.8	14.3	42.8	3.6
90	2000	-1.1	6.3	6.4	99.5	3.2
90	4000	-1.2	12.9	13.0	95.3	3.2
135	2000	-6.5	5.0	8.2	142.4	4.1
135	4000	-12.6	10.0	16.1	141.4	4.0
180	2000	-8.6	0.6	8.6	175.9	4.3
180	4000	-15.7	1.0	15.7	176.3	3.9
-135	2000	-4.7	-4.7	6.7	-135.0	3.3
-135	4000	-9.4	-9.4	13.4	-135.0	3.3
-90	2000	1.2	-7.8	7.9	-81.1	4.0
-90	4000	2.1	-13.8	14.0	-81.4	3.5
-45	2000	5.8	-5.1	7.7	-41.7	3.9
-45	4000	12.1	-10.6	16.1	-41.0	4.0

For most cases of Table 6.4 and Figure 6.9, the measured and desired trajectory angles are within a few degrees. The resolution parameter calculated in the last column indicates that a movement of 3-4μm can be expected from a |U|=1000V^2 size trajectory; this information will become important during fine resolution fiber alignment tests later in this chapter. The slight non-linearity and variability over these 16 tests (and their ~30μm travel range) is attributed to small asymmetries in wedge morphology and fiber rest position.

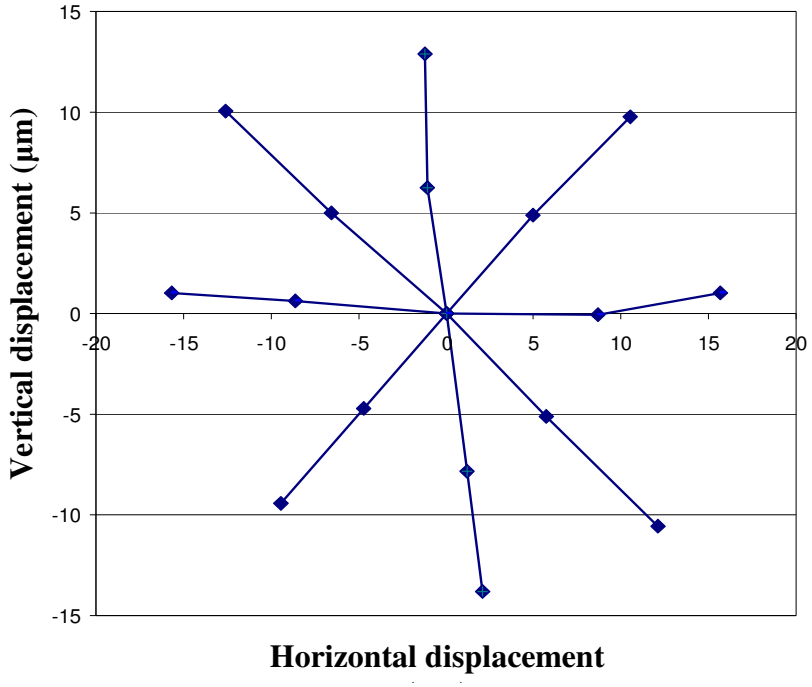

Figure 6.9: Primary axes of movements show trajectories along ~45º, demonstrating that Cartesian control of fiber is possible.

As a brief demonstration that the Cartesian control principle produces similar results starting from an arbitrary point (not the center), a module was created in LabVIEW to automatically create successive fiber movements at the behest of an operator. The LabVIEW module (shown in Figure 6.10) allows the user to define a starting location and then press buttons to determine the direction and magnitude of the next fiber movement. While buttons only exist for every 45º in the figure, arbitrary angles can also be manually entered with slight changes to the program. To demonstrate this operability, the letter "M" was traced out with the fiber tip using sequential movements and facet scans to measure fiber location (see Figure 6.11). Both vertical and angled trajectories across the diamond alignment area were necessary to create the desired shape. Once again slight non-linear motion was observed.

The 45º trajectories and "M" tests have clearly demonstrated that Cartesian control of the fiber tip location can be achieved using simplified geometrical transforms

to control the coupled motion of two alignment wedges. Improvements in wedge morphology and angle are expected to improve the symmetry of fiber movement.

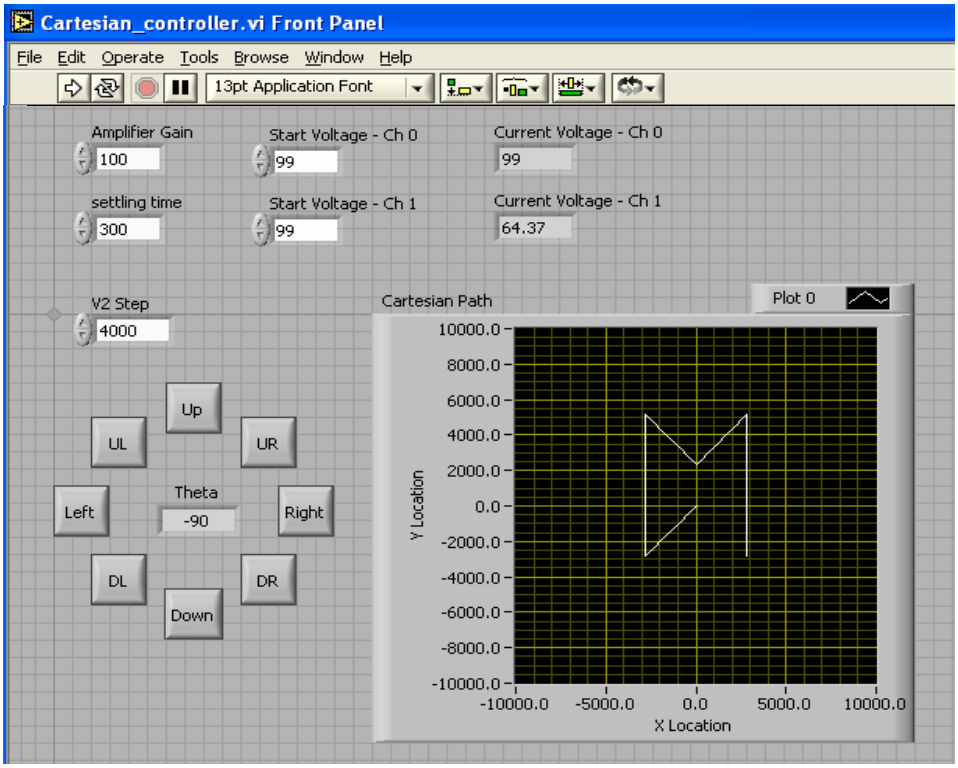

Figure 6.10: LabVIEW module for creating arbitrary fiber movements.

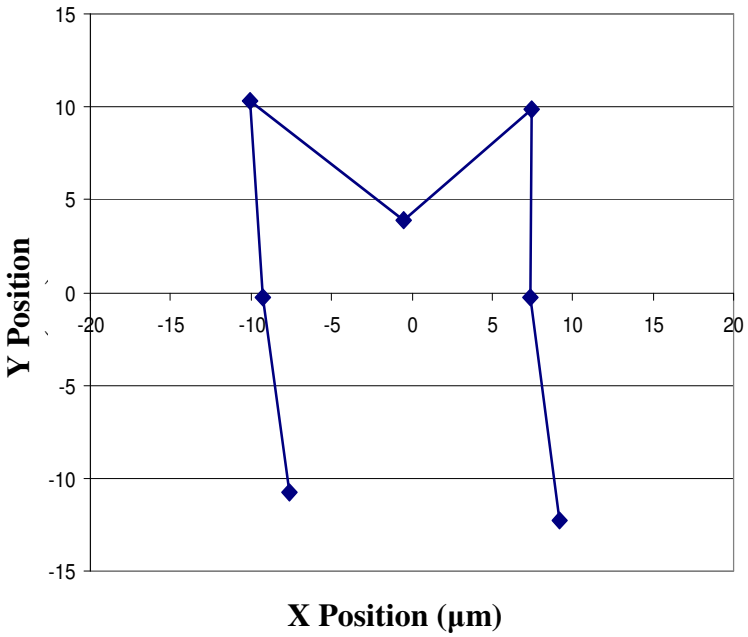

Figure 6.11: Cartesian control was used to trace out the letter "M".

6.3.4. Hysteresis Evaluation

Another important quasi-static characteristic to investigate is hysteresis of the fiber motion, primarily caused by the morphology of the gray-scale wedges. The main forces on the fiber during an "Up" cycle are shown in Figure 6.12, where both wedges move towards each other to create purely vertical motion. In the absence of friction, each wedge transmits the electrostatic force of the comb-drive into a net angled force on the fiber ($F_{net\ A}$ and $F_{net\ B}$). These forces combine to produce a net force/movement "Up," which is balanced by a restoring spring force ($F_{restore}$) that points back toward the original fiber location ("Down" in this case). However, as the fiber slides "Up" each wedge, there is a frictional force on each wedge face ($F_{f\text{-}A}$ and $F_{f\text{-}B}$) that will oppose the fiber's upward motion.

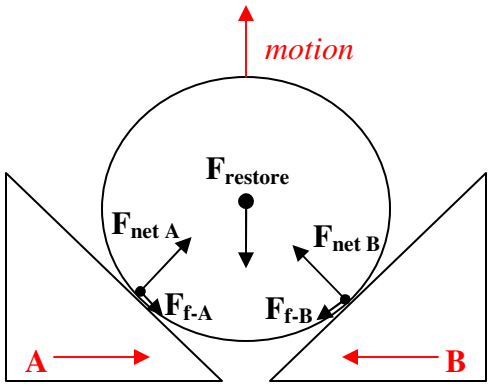

Figure 6.12: Force diagram during the "up" portion of a hysteresis test, where the frictional forces oppose the net force acting on the fiber from each alignment wedge.

These frictional forces between the wedges and optical fiber will oppose the fiber motion on any actuation path, causing hysteresis. To test the magnitude of this effect, a fiber was fixed with a vertical offset compared to the gray-scale fiber aligner. During a sequence of increasing then decreasing voltages, the gray-scale fiber aligner tip passes through the point of peak coupling both on its way "Up" and on its way back "Down." The coupled power between fibers was then measured as the gray-scale fiber aligner was

actuated "Up" and "Down" over multiple cycles. As shown in Figure 6.13, there is definite hysteresis between the two actuation paths. (While a single cycle is shown here, the hysteresis is quite repeatable). Essentially, friction from the wedge surfaces increase the force (i.e. V^2) required to move the fiber "Up," and then delays the fiber's return "Down" to a lower state. Using facet scans taken with the calibrated electrostrictive stages, this 'lag' is estimated to be equivalent to a shift of ~4μm between the two coupling peaks.

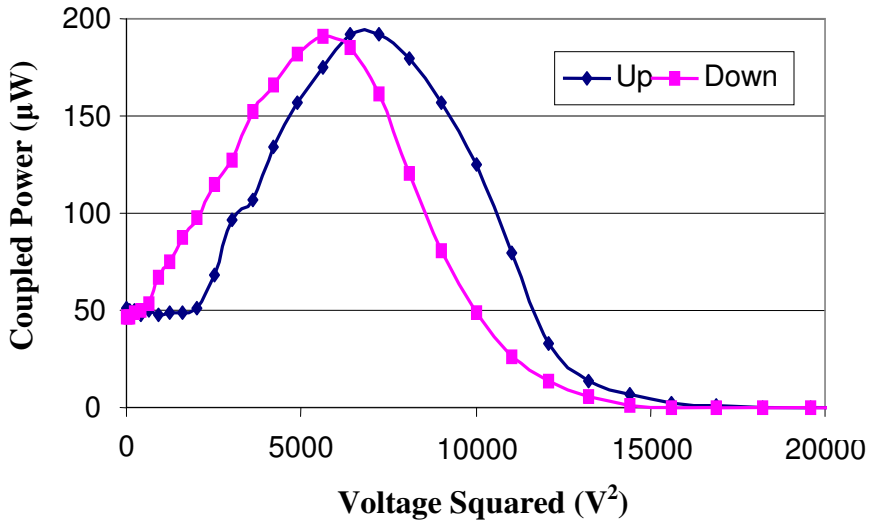

Figure 6.13: Actuating both sloped wedges identically creates a vertical up/down motion that exhibits definite hysteresis [168].

It should be possible to reduce this hysteresis effect by improving the wedge morphology through a combination of design and/or fabrication, although the observed roughness is already small (1-2μm) compared to the 125μm fiber. Since the fundamental principle of operation of this device relies upon two sliding surfaces, it is not expected that hysteresis could be totally eliminated in practice. As will be shown in later sections, fiber alignment using closed-loop control has proven robust with the current structures despite these small hysteresis effects.

6.4. Auto-alignment Algorithms

The motivation for developing the gray-scale fiber aligner is rooted in automating the optical fiber alignment and packaging process. Thus, it is only prudent to demonstrate the capabilities of said actuator for auto-alignment of a fiber to various targets. Alignment algorithms can be considered a field unto itself and the development of entirely new algorithms is not the primary focus of this work. Rather, the following sub-sections will provide a brief overview of general alignment schemes, and focus instead on the adaptation of popular alignment schemes to the gray-scale fiber aligner. Of primary interest will be the impact and/or limitations imposed by the developed novel fiber actuation mechanism on the achievable alignment time and resolution.

6.4.1. Overview and Background

The majority of alignment algorithms developed in the literature utilize external stages or fiber positioners capable of manipulating the fiber position in multiple axes [169-176]. Nearly all alignment sequences make use of multiple algorithms in order to minimize cycle time and improve reliability. Most begin with a coarse alignment step to achieve "first light" and meet some intermediate threshold power. This coarse threshold power is often designed high enough to avoid noise and secondary peaks. Once coarse alignment has been reached, a fine alignment step optimizes the alignment via a different algorithm.

The majority of alignment algorithm implementations use a "step-and-read" approach, where the fiber is moved incrementally and the coupled optical power is measured at the new fiber location. "If-then-else" types of logic are popular [174], however more complicated Hamiltonian [170] or fuzzy logic [171] approaches have potential advantages for simultaneously aligning many fibers with multiple degrees of

freedom. Some algorithms also take advantage of *a priori* knowledge regarding the expected coupling profile shape (such as beam ellipticity) to reduce the overall alignment time [176].

The coarse and fine algorithms implemented in this work are adaptations of standard algorithms in order to characterize the performance of the gray-scale fiber aligner. To this end, our testing uses targets with symmetric coupling profiles, allowing us to infer alignment accuracy regardless of the direction of misalignment. After characterizing the performance of the gray-scale fiber aligner and demonstrating its flexibility, it would be possible to implement more complex alignment algorithms, but is considered beyond the scope of this work.

The coarse and fine alignment experiments discussed in the rest of this chapter will follow the same general sequence: (1) the longitudinal separation between the target and gray-scale fiber aligner is set manually under a microscope. (2) Electrostrictive XYZ stages are controlled via LabVIEW to create a facet scan of the target in order to correlate the coupled power to positional misalignment. (3) The target is intentionally misaligned with regards to the gray-scale fiber aligner. (4) A LabVIEW program, utilizing coarse and/or fine algorithms, optimizes alignment by modifying voltages supplied to gray-scale fiber aligner while monitoring the coupled optical power. (5) Upon satisfying all relevant thresholds, or giving up due to some failure, pertinent data is logged electronically. (6) Finally, the facet is re-scanned via the electrostrictive XYZ stages to verify that negligible drift occurred during the test(s).

6.4.2. Coarse Algorithms

We have implemented two separate coarse alignment scans using the gray-scale fiber aligner to show its versatility and evaluate achievable speed and accuracy. It will be shown that the fundamental choice and settings of each algorithm has a significant effect on the speed with which the threshold is reached. For these coarse algorithm tests, cleaved fiber-cleaved fiber coupling was used for simplicity and ease of re-configuration. Coarse threshold powers of 50-75% peak power were typically used to simulate avoidance of side modes, but the observed coupling profile remains a single Gaussian-shaped peak as shown earlier.

The simplest coarse alignment routine is that of a raster scan. The voltage on the 1st actuator is held fixed, while the voltage on the 2nd actuator is swept through its range. The voltage on the 1st actuator is then incremented, and the sweep repeated on the 2nd actuator. The primary variable to control during a raster algorithm is the step size between successive fiber locations (ΔV^2 because we are using comb-drives). Using a raster scan coarse algorithm, Figure 6.14 shows the time required to achieve a coarse alignment threshold of 75% peak coupling for different positions of the target fiber. The slope of the alignment wedges cause the time contour lines to be tilted with respect to the X-Y axes, a result of the sequential angled fiber trajectories caused by sweeping the 2nd actuator from one extreme to the other, as indicated in the figure. Note that times >36sec in Figure 6.14 indicate failure to achieve threshold, loosely illustrating the diamond-shaped possible alignment area of this device.

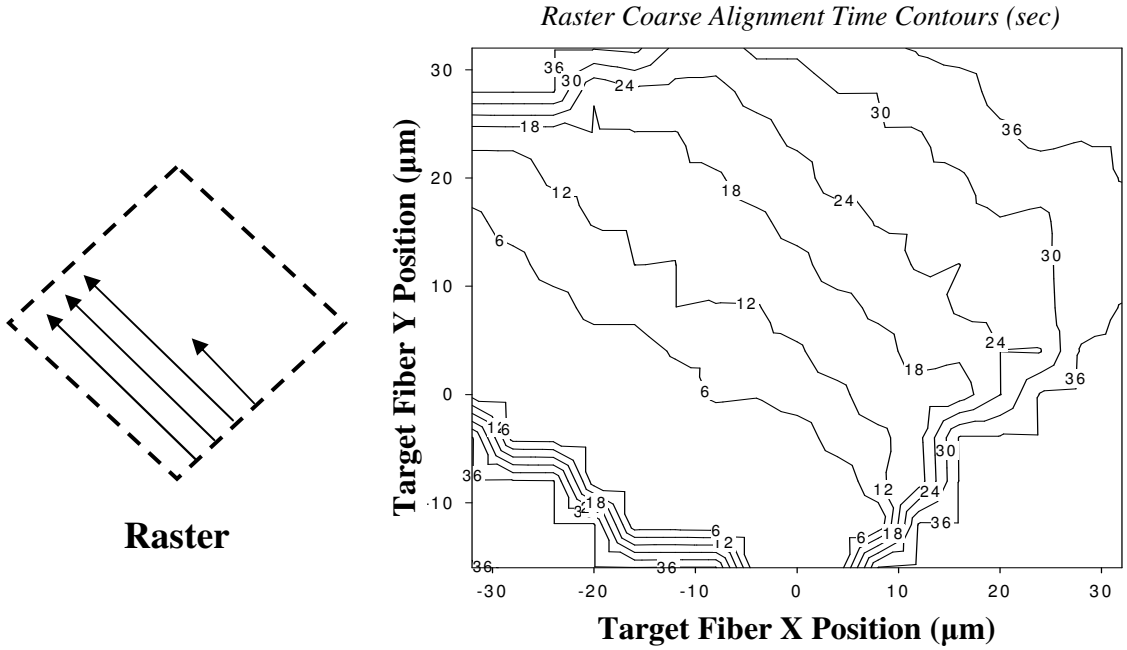

Figure 6.14: Coarse alignment contours for different target fiber locations using raster algorithm [168].

As mentioned above, the raster coarse algorithm performance can be tailored by adjusting the step size (ΔV^2) between successive points (mesh density). For example, Table 6.5 shows the time required to achieve a 75% coarse threshold power to a fixed target location for different step sizes. As the step size increases, the time required to achieve coarse threshold scales by approximately the square of the step size ratio (ΔV^2_{old} / $\Delta V^2_{new})^2$, essentially an area term. However, reducing the coarse alignment time by using larger steps has the inherent risk of missing important peaks altogether.

Table 6.5: Coarse alignment time to achieve 75% peak coupling as a function of step increment within raster algorithm for a single target location.

Step Size (ΔV^2)	Coarse Threshold Alignment Time (sec)
2000	30.1
3000	15.9
4000	9.7

The primary drawback of a raster scan for packaging applications is that it begins searching for the peak in a presumably unlikely position (the very edge of the travel range at the bottom of the diamond alignment area). Ideally, an optoelectronic module design would have the target in the center of the alignment area such that shifts/errors in any direction could be corrected. However, even for perfect fabrication and assembly, a raster scan would still require 12-18 seconds to achieve coarse alignment to a centrally located target; meaning precise fabrication and assembly could require longer alignment times than in cases of poor assembly.

To address the paradox of perfect assembly requiring longer alignment times, a spiral search algorithm was also developed and implemented for the gray-scale fiber aligner to compare with the raster scan. Rather than beginning at the edge of fiber travel range, the spiral algorithm begins in the center of achievable motion, and spirals outward to progressively less-likely positions until the coarse alignment threshold is reached. Furthermore, a spiral scan is significantly more interesting from a device characterization standpoint since it requires coupled motion of both alignment wedges to create a spiral fiber trajectory (whereas the raster scan moves one alignment wedge at a time). The spiral trajectory used here was made of concentric circles of increasing radius. Both the radius of each ring and the angular spacing between successive fiber positions can be adjusted to tailor the speed and resolution of the fiber trajectory.

Figure 6.15 shows the measured coarse alignment time for the same target positions as in the case of a raster scan. The time contours appear in concentric circles, as expected from the desired fiber trajectory. For locations near the center, we observed coarse alignment times <6 seconds, confirming that the spiral algorithm is more efficient

when the target is near the center, as likely in a packaging application. It should be noted that the total time required to scan the entire alignment area was kept approximately the same (>30sec) for both raster and spiral algorithms to emulate a similar scan point density in the X-Y plane.

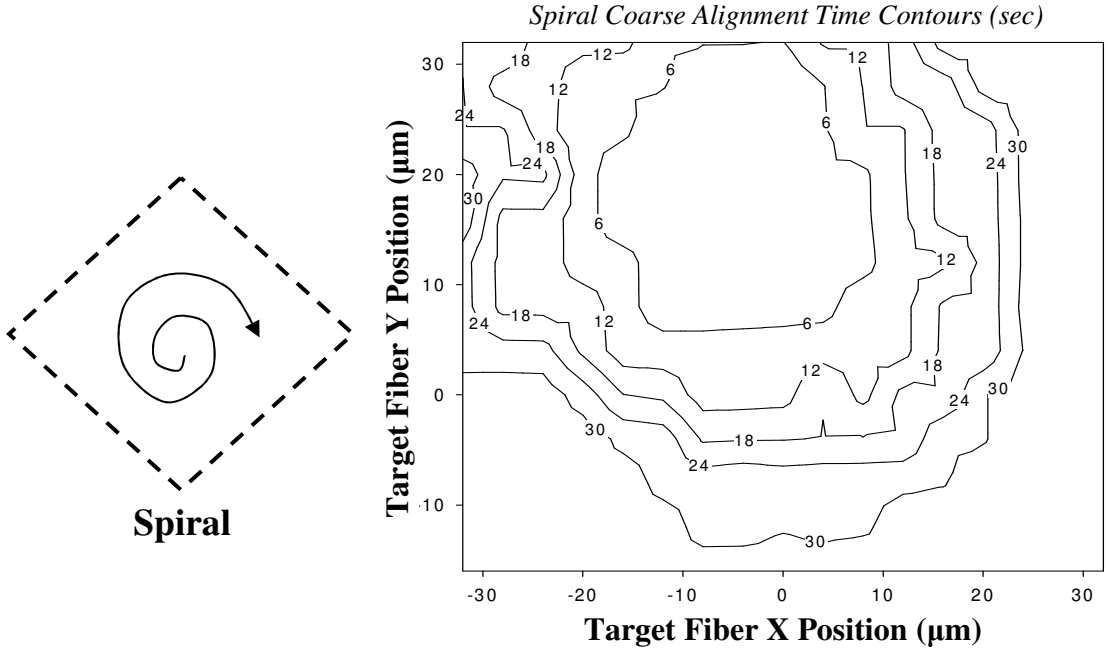

Figure 6.15: Coarse alignment time contours for different target fiber locations using a spiral algorithm [168].

While only two basic coarse algorithms have been implemented so far, the spiral results clearly reinforce the previous claim that nearly arbitrary 2-axis motion of a fiber tip can be achieved through the coupled motion of sloped gray-scale wedges. Thus, any other 2-D coarse algorithm of interest could be implemented using the gray-scale fiber aligner.

6.4.3. Fine Algorithm

The ability to move a fiber tip in arbitrary patterns means that virtually any 2-D search algorithm could be used for the fine alignment step. As mentioned previously,

Hamiltonian [170] and fuzzy logic [171] approaches tend to be most useful when aligning multiple fibers with many degrees of freedom, while the spot size method [176] requires 3 degrees of freedom and an optically elliptical target. The most popular algorithm for fine alignment is a "gradient search" or "hill-climbing algorithm" [174, 175] due to its simplicity of implementation.

A basic hill-climbing algorithm is shown in Figure 6.16. Coupled power measurements are taken at two successive fiber locations. If the coupled power increased, then the search continues in the same direction, "up" the hill. If the power change is negative, the algorithm assumes it is going "down" a hill, away from the optimum location. The search then turns around and reduces it's step size (assuming it somehow jumped "past" the optimum peak because the step was too large). Since this process is 1-dimensional, the hill-climb loop for turning around is executed for each axis independently, usually switching between axes after every few changes in direction. This sequence continues until the ultimate threshold is reached (or the program gives up).

The primary drawback of the hill-climbing technique is the susceptibility to trapping in false peaks. This limitation can sometimes be addressed using a quasi-momentum term within a hill-climbing algorithm [171]. Alternative fine alignment algorithms have been developed that work better in the presence of side modes, such as the simplex method discussed in [175]. However, these algorithms can be quite complex, making it difficult to distinguish between algorithm complications and actuator performance. Since the targets used in this research operate with a single fundamental mode, and the coarse threshold is intended to avoid side modes, a hill-climbing algorithm is sufficient for this device characterization.

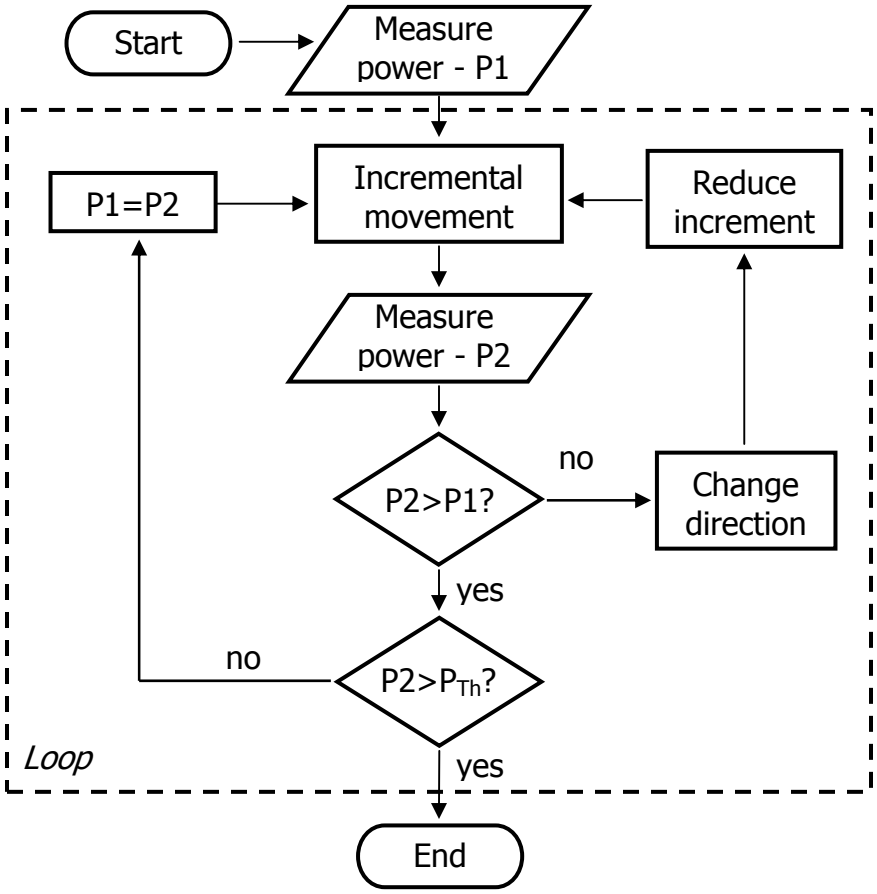

Figure 6.16: Simplified hill-climbing algorithm block diagram.

The most important parameters to be used during the hill-climbing algorithm are the step sizes and the ultimate fine threshold power. The initial step size determines how coarse a mesh the first 1-D search will be, and after each reversal of direction the step size is reduced (typically by ½). Large step sizes will climb the hill fast, but may over-shoot the optimum position and require many step size reductions to achieve the resolution required for final alignment. Small step sizes will take longer to climb a single hill, but should finalize alignment quickly once there. Use of small steps does make one more vulnerable to local false peaks caused by either secondary modes or artifacts of actuator motion (like sticking or hysteresis). Ideally, a compromise must be found

between speed and reliability. A time-out function was also included to avoid infinite attempts to climb a hill that peaks outside of the possible area.

6.5. Automated Fiber Alignment Results

The experimental results presented in this section were performed entirely using the developed test setup described in Section 6.2. These tests were intended to specifically investigate the performance and limitations of the gray-scale fiber aligner using the implemented auto-alignment algorithms discussed in the previous section. Of specific interest are both the speed and resolution of the alignment process, each of which is focused on independently in the following two sections. Note that these tests make use of either lensed fibers or InP waveguides with approximately circular modes. While elliptical targets (like LEDs) may provide more coupling sensitivity along 1-axis, each power could correspond to multiple misalignment positions, significantly complicating evaluation of our device.

6.5.1. Cleaved Fiber – InP Waveguide (Speed)

The first auto-alignment tests using the gray-scale fiber aligner investigate the effect of algorithm parameters on speed of alignment within the constraints of the developed actuator and test setup. All experiments in this section utilized InP suspended waveguides (courtesy of fellow MSAL graduate student Jonathan McGee) [167] in an attempt to simulate in-package alignment to III-V photonic devices. It must be noted that due to the sensitive coupling between both facets of InP waveguides, alignment tests to InP waveguide were performed for a limited number of waveguide positions.

Initially, InP ribbed waveguides (2 by 2μm core with 400nm rib height) [167] were used as the alignment target, vertically misaligned by ~20μm with respect to the

gray-scale fiber aligner. The waveguide location was somewhere towards the middle of the aligner's range, but the precise location was left unknown to simulate 'blind' alignment. The final alignment threshold used for this first test was 92% peak, corresponding to ~3.5μm misalignment due to the wide central mode emerging from the ribbed waveguide. While this resolution is far from the micron-level goal of this research, these tests serve to ensure that all alignment algorithms were implemented correctly.

The total alignment time for different coarse threshold powers and settling times, all using a raster coarse algorithm, are shown in Figure 6.17. The total alignment time scales linearly with settling time from 1000ms down to 300ms. However, experiments using settling times <300ms consistently failed due to insufficient time for the fiber to reach its new position. For a single settling time, we observed that lower coarse threshold powers (50% vs 75%) produced faster overall alignment results, but this improvement comes with higher risk of getting trapped in side peaks during fine alignment. Since the ribbed InP waveguide had insignificant side modes, this trapping was not a problem. Overall, the total alignment time for a single waveguide location was reduced from 34.2 seconds to 8.5 seconds by decreasing the settling time (from 1000ms to 300ms) and coarse threshold level (from 75% to 50% peak). While the position and sharpness of the target will influence the exact alignment times, these trends should be universal.

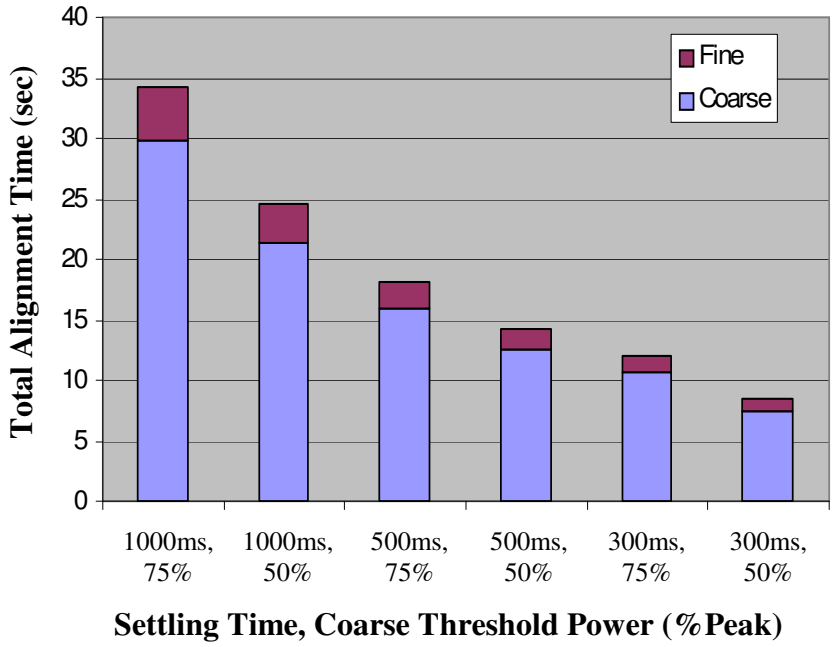

Figure 6.17: Alignment times to an InP waveguide for different settling times and coarse threshold power (% peak).

It is obvious that for all cases in Figure 6.17, the total alignment time is dominated by achieving a coarse threshold power. Thus, some changes to the experimental conditions were implemented. First, we wanted to compare results when the raster coarse algorithm was replaced with the spiral coarse algorithm. And second, a 2μm square InP waveguide (tighter optical confinement than ribbed waveguide) was used in conjunction with a final threshold of 95% peak coupled power to decrease the required alignment resolution to 1.6μm (rather than the unimpressive 3.5μm). Once again, the InP waveguide was fixed in a single location approximately ~20μm vertically shifted from the gray-scale fiber aligner. The time required to achieve final alignment (<1.6μm) was then recorded as it relates to coarse algorithm selection (raster vs spiral) and incremental actuator step size ($\Delta Voltage^2$ applied to comb-drives). The results are shown in Figure 6.18. Note that alignment results to a single target location were extremely repeatable ($\Delta t<0.1$sec).

As expected for a quasi-centrally located target, the coarse alignment time dominates the total alignment time when a raster algorithm is used, especially for smaller ΔV^2 (a finer scan mesh). Using the spiral algorithm dramatically decreased the coarse alignment time, but large ΔV^2 increments caused the fiber to temporarily overshoot the target location. The fastest alignment times (routinely <10 seconds) were achieved using the spiral algorithm in conjunction with the smaller ΔV^2.

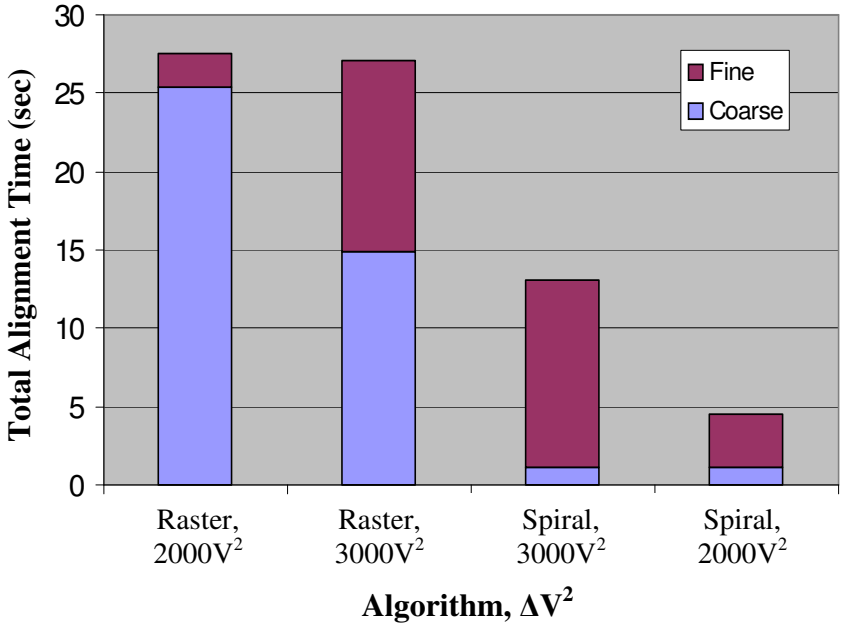

Figure 6.18: Time to align within 95% peak power (<1.6μm) to a fixed InP waveguide, as a function of coarse search algorithm and ΔVoltage^2 setting [168].

6.5.2. Cleaved Fiber – Lensed Fiber (Resolution)

The previous experiments have established that high resolution alignment can be obtained quickly to a few particular points in the gray-scale fiber aligner range. However, the achieved resolution (<1.6μm) in the InP waveguide experiments could have been an artifact of the particular waveguide locations tested. To fascilitate testing of many target locations, the InP waveguide was replaced with a lensed fiber on the electrostrictive XYZ stage as the new target. This setup enables quick reconfiguration of

the target location (i.e. lensed fiber) to determine if high resolution can be achieved over the majority of the alignment area.

The custom LabVIEW module developed for executing the alignment tests at multiple target locations is shown in Figure 6.19. Universal hardware setup parameters are controlled in the bottom left section. The operator then selects either "raster" or "spiral" coarse search algorithm via a toggle switch, with the associated power threshold levels and ΔV^2 increments. The position of the XYZ stage with lensed fiber is controlled using the "Electrostrictive Position Settings" on the right side. For each position of the XYZ stage and target fiber, the chosen alignment algorithm is executed and alignment results for both the coarse and fine steps are displayed and logged for analysis.

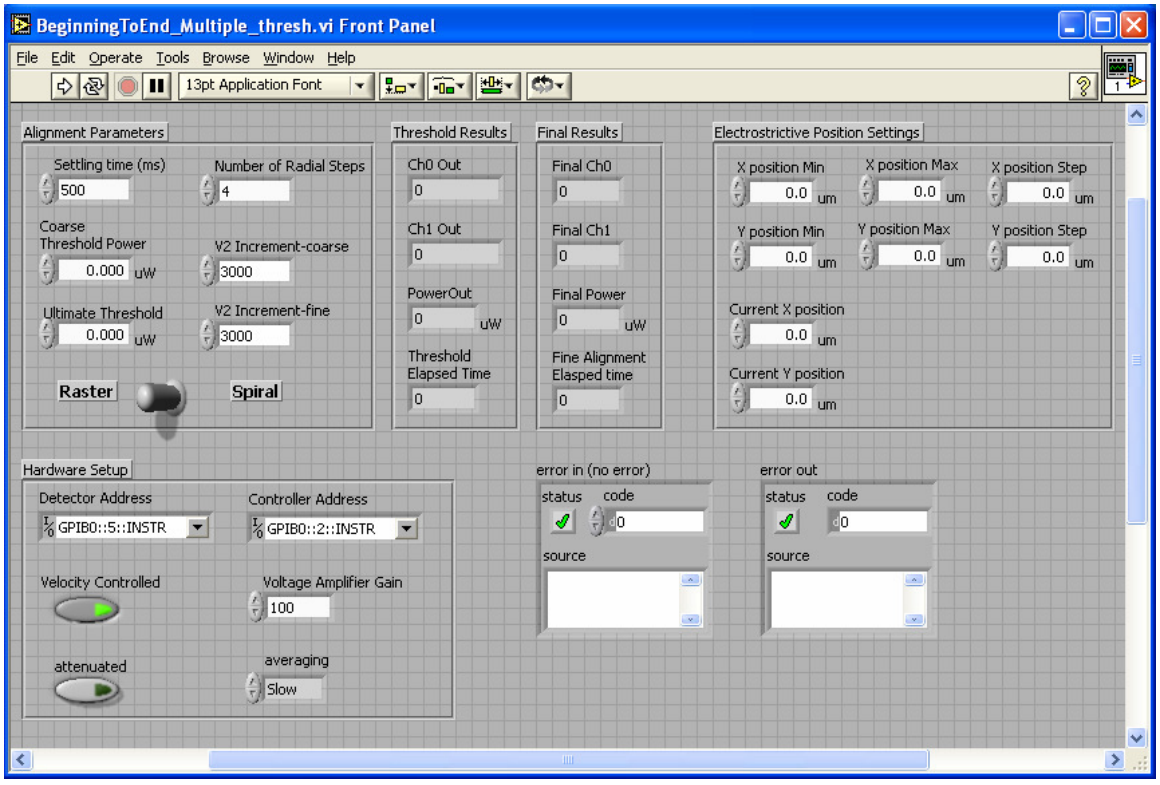

Figure 6.19: LabVIEW module for auto-alignment testing of multiple target fiber locations.

A 20 by 20μm grid was selected within the diamond shaped alignment area (shown in the inset of Figure 6.21), with 2.5μm spacing between target locations. For

each position of the input fiber, the gray-scale fiber aligner attempted to align within 97% peak coupling (1.25μm accuracy when calibrated with electrostrictive stages). Initial results indicated success rates of only 73%, meaning the gray-scale fiber aligner failed to achieve the required alignment for 27% of the target locations (failed points were randomly scattered). A histogram of the best alignment accuracy achieved for each location using standard actuation is shown in Figure 6.20.

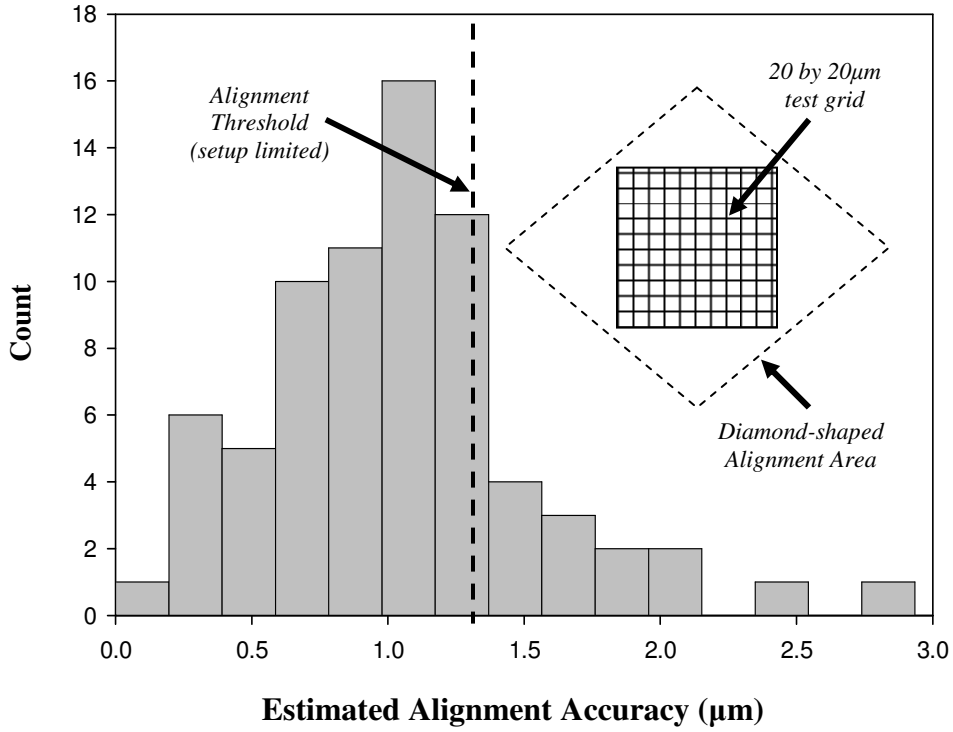

Figure 6.20: Estimated alignment accuracy histogram for 20 by 20μm area using standard actuation.

Upon further inspection, the problem with failed alignments was identified to be between our actuator and the hill-climbing algorithm. Typically, hill-climbing algorithms step towards a peak and after passing a peak, turn around and scan again with a reduced step size. (For intuition on the step sizes required for this level of alignment, refer back to Section 6.2.3 where |U|=1000 created 3-4μm of movement). However, small step sizes did not always cause any appreciable movement, an effect we attribute to static friction

between the wedges and fiber. Thus, depending on target location, hysteresis, and friction conditions, decisions within the algorithm were often based simply on noise, causing the alignment to eventually fail.

We then altered the fiber actuation scheme to include a 100ms pulse of (0V, 0V) prior to the intended actuation voltage to "un-stick" and reset the fiber. While this method slows alignment slightly, it enables small ΔV^2 steps to create real changes in the fiber location. Alignment tests were then performed over the same 20 by 20μm area, but now using this 'pulse' method of actuation in the fine alignment step. As shown in the histogram of the estimated resolution in Figure 6.21, the 1.25μm required threshold was achieved with 100% success across the entire area (all 81 measured points).

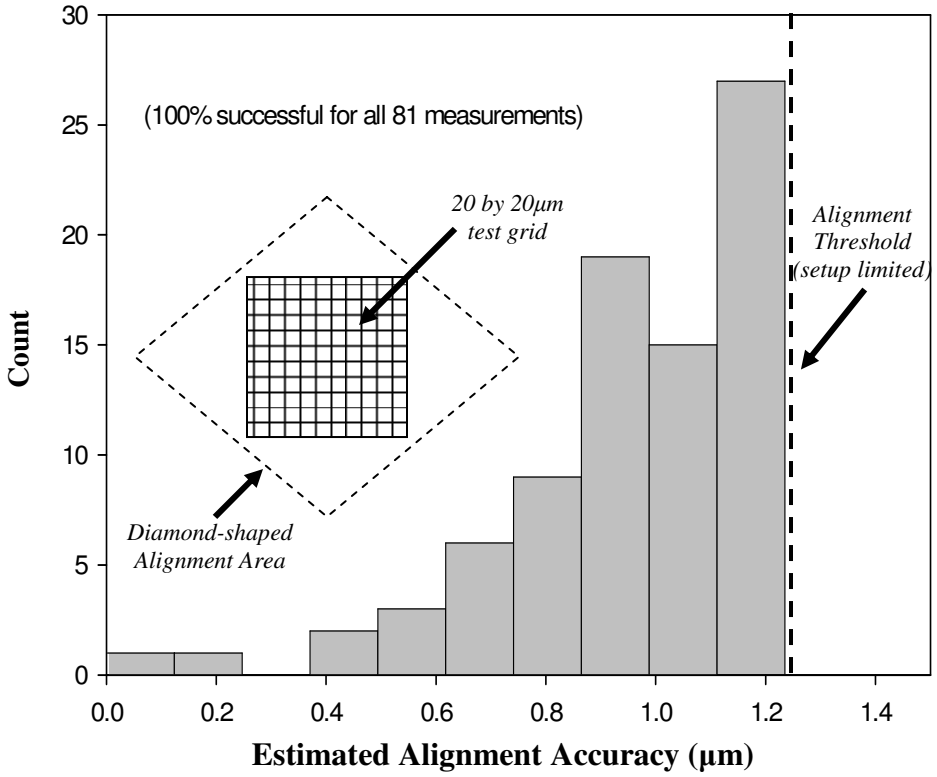

Figure 6.21: Estimated alignment accuracy histogram for a 20 by 20μm area (with 2.5μm grid), where alignment better than 1.25μm (setup limited) was achieved with 100% success.

6.6. Testing Summary and Discussion

While the exact time required to align to particular device depends on its location, our tests show that an accuracy of <1.6μm could be routinely achieved on the order of 10 seconds to InP waveguides initially misaligned by ~20μm. Direct comparison of such alignment times to previous research is difficult because externally actuated systems typically optimize degrees of freedom beyond the 2-axis optimization performed by our gray-scale fiber aligner. Although previous simulations showed that our gray-scale fiber aligner is optimizing alignment along the two most important axes. Nonetheless, the alignment speed of the gray-scale fiber aligner (at ~10 seconds for 2-axes) compares favorably to active alignment times reported using external actuators (~30 seconds for 3-axes) [174]. Many algorithm parameters could also be adjusted to tailor the alignment speed and/or resolution for particular applications.

The alignment resolution achieved with the gray-scale fiber aligner (<1.25μm) is competitive with the best reported passive alignment techniques [84], with the advantage that extreme control over all fabrication and assembly tolerances is not required. Pulse testing results imply that continuous small displacements by the gray-scale fiber aligner are limited by friction between the wedges and fiber. Thus, improving the sloped wedge surface morphology should lead to more continuous movement and finer alignment accuracy. Re-design of the gray-scale slope using more gray levels could minimize wedge roughness in photoresist at the expense of increasing optical mask cost. Alternatively, techniques such as short isotropic silicon etching or hydrogen annealing [129] are candidates for post-process smoothing of the surface, but would require careful process control to avoid effecting other geometries on the device. However, as shown

with the pulse actuation method, fibers can already be positioned with accuracy below the minimum continuous movement threshold.

Use of a 9μm core cleaved fiber makes evaluating the desired sub-micron resolution nearly impossible with the current optical setup. As stated previously, the FHWM is currently ~10μm, so <1μm misalignment corresponds to <0.1dB of loss, which is too near the noise threshold of our system (<1% ≈ 0.04dB) to be reliable. It would be preferable to work with a setup similar to *Kang et al* [155] where they reported a 3dB loss for only 1-1.2μm misalignment of a lensed fiber to an InP chip. However, manually assembly of lensed fibers in the gray-scale fiber aligner would be exceedingly difficult and expensive given the equipment available. (Assembly yield would be extremely low since lensed fiber tips are delicate and manual insertion/epoxying of the fiber often does not result in good contact between the fiber and both alignment wedges.)

6.7. Conclusion

The static and auto-alignment testing presented in this chapter was able to clearly demonstrate three key abilities of the gray-scale fiber aligner. First, controlled actuation of the optical fiber in both the horizontal and vertical directions was achieved over a range >35μm in each axis with switching speeds of ~1ms. Second, auto-alignment results illustrated that standard search algorithms could be implemented using the gray-scale fiber aligner with predictable and intuitive behavior; optimizing alignment to fiber and waveguide targets on the order of 10 seconds. Thirdly, alignment using the pulse actuation method was able to confirm that an alignment resolution <1.25μm was achievable over a 20 by 20μm area. Gray-scale fiber aligners have also proven robust, in

some instances actuating $>10^5$ times in numerous testing configurations without any observed change in performance.

The developed gray-scale fiber aligner system is a significant step towards in-package alignment of optoelectronic components. The most realistic packaging configuration would likely include flip-chip bonding of III-V or SOI photonic circuits onto a silicon substrate containing one or more fiber alignment devices (and possibly relevant control electronics). The gray-scale fiber aligners would then provide individually optimized alignment to minimize optical losses. While only basic device configurations and control algorithms were presented here, there remain numerous avenues for optimizing active alignment time and accuracy for particular applications. In addition, testing has shown that nearly arbitrary control methods and search algorithms could be adapted to work with this device.

CHAPTER 7: CONCLUSION

7.1. Summary of Accomplishments

This PhD dissertation has investigated electrostatic MEMS actuators incorporating 3-D features fabricated with gray-scale technology. While traditional MEMS actuators have been limited to planar design and fabrication, the integration of 3-D components has enabled improved performance and increased (or otherwise impossible) functionality. This research is the first to demonstrate such a beneficial marriage between MEMS actuators and a batch 3-D fabrication technique. Developed devices include static 3-D comb-drives, tunable MEMS resonators, and a novel 2-axis fiber alignment device.

The specific accomplishments of this PhD dissertation are as follows:

1. **Gray-scale Technology Development:** Complex 3-D photoresist and silicon profiles were controlled through a developed empirical model of the gray-scale lithography process and extensive DRIE pattern transfer characterization. A double-exposure technique was demonstrated as a method to exponentially increase the vertical resolution of 3-D structures, while the CARDE process was introduced as an effective technique for anticipating aspect ratio limitations during DRIE. Static applications of gray-scale technology were demonstrated through three technology collaborations: (a) Development of a variable span microcompressor *(U.S. Army Research Laboratory and Massachusetts Institute of Technology);* (b) Design and fabrication of 3-D substrates for a MOSFET relay package *(Toshiba Corporation);* (c) Design, fabrication, and testing of x-ray phase Fresnel lenses *(NASA-Goddard Space Flight Center).*

2. **Compact Tailored Electrostatic MEMS Comb-drives:** Variable height gray-scale structures were integrated with electrostatic MEMS actuators for the first time. Analytical and FEA methods were developed to model comb-drives with variable height comb-fingers, enabling tailored displacement characteristics without increasing device area. Local reduction of actuator suspension height enabled dramatic (70%) reductions in spring constant, leading to lower driving voltages. The design and fabrication techniques developed to integrate gray-scale technology within an electrostatic MEMS actuator process flow serves as a platform for developing more complex 3-D shaped actuators.
3. **Vertically-Shaped Tunable MEMS Resonators**: Research on vertically shaped comb-drive actuators was extended to create new compact tunable MEMS resonators. Voltage-controlled electrostatic springs were designed, modeled, and fabricated; capable of bi-directional resonant frequency tuning of in-plane comb resonators. Simulations showed that multi-step comb-finger profiles or variable-engagement comb-finger designs can be used to minimize non-linear stiffness coefficients during large amplitude resonator oscillations. MEMS resonators in the low kHz range demonstrated electrostatic springs as strong as 1.19 N/m (@70V) and enabled tuning of the resonant frequency by up to 17.1%.
4. **Gray-scale Fiber Aligner**: A novel 2-axis optical fiber alignment system using 3-D wedges (fabricated with gray-scale technology) was created for the first time. Without the integration of these 3-D components, this new class of actuators would be otherwise impossible or impractical. Devices were designed, fabricated and tested based on experience with comb-drive actuators and gray-scale integration.

Auto-alignment algorithms were developed and implemented to demonstrate the ability of final devices to align an optical fiber to a specific target, with particular emphasis on comparing overall alignment time and achievable resolution. Methods for Cartesian control and evaluating hysteresis of these actuators were also developed. Device switching speeds were measured to be consistently <1ms, while alignment times of <10sec to a fixed 2μm square indium phosphide (InP) waveguide with <1.6μm resolution were commonly achieved. Ultimately, gray-scale fiber aligners were able to achieve alignment ranges as large as 40μm (at fiber tip) in both the in-plane and out-of-plane directions, with alignment resolution of <1.25μm. These results represent a significant step towards cost effective in-package fiber alignment in optoelectronic packaging.

7.2. Future Work

The following sections will briefly comment on areas for future work based on this PhD dissertation.

7.2.1. Gray-scale Technology: Resolution and Uniformity

The discussion on the gray-scale technology process presented in this research was primarily concerned with design and process control for individual devices. However, the wide acceptance of this technique will hinge upon developments in two primary areas of future work: resolution and uniformity.

As discussed briefly in Chapter 2, the horizontal resolution of gray-scale photoresist structures is limited by the pixilated technique being used during the mask design process (recall that horizontal resolution is inversely proportional to vertical resolution due to mask vendor limitations). Additionally, a finite number of pixels is

required to create a distinct gray level in photoresist. The double-exposure technique introduced in Section 2.3.3 could exponentially increase the number of gray levels available without sacrificing horizontal resolution, but will require significantly more modeling and process optimization in order to reliably produce complex 3-D profiles. Another interesting possibility is to use the 2nd exposure to "sharpen" the edges of an initially defined gray-scale feature to remove edge effects from the pixilated mask design, thereby reducing the minimum gray-scale feature size.

The manufacturability of MEMS devices utilizing gray-scale technology will ultimately be limited by the uniformity and repeatability of both the lithography and etching steps. During the current research, the lithography was largely manual, allowing limited control over the uniformity. However, one area observed to have a potentially large effect on uniformity was the baking step, as soft baking photoresist on an uneven hot-plate caused dramatic differences in structure heights across the wafer. Changing to an oven soft bake could lead to more uniform photoresist solvent content and therefore developing properties, but will require significant characterization and process control. Automation of the development step should also improve wafer to wafer repeatability, although puddle techniques have been problematic due to the finite time required to cover the wafer. It is recommended that spray development techniques be investigated as an alternative.

Etching uniformity during DRIE is already a large field of interest [34, 100, 101, 105, 177-179]. In general, low silicon loading is preferred for uniformity [178] where transport is ion limited, compared to high loading that is neutral limited [100]. Groups have reported techniques for modeling uniformity effects from pattern layouts [179], or

even introducing dummy structures to minimize pattern dependent processing [180]. Other research has focused on tuning the plasma for lower pressure and high coil power to improve uniformity [101]. However, each change to the layout and/or plasma process for uniformity purposes will also effect the etch selectivity of the 3-D photoresist transfer into silicon. Thus, it is suggested that a database relating etch uniformity and selectivity for high and low loading conditions be developed in order to anticipate realistic manufacturing tolerances and tuning ability when developing a device.

These interesting and exciting areas of future work on the core gray-scale technique are currently being pursued by another graduate student, Mr. Lance Mosher, as part of his Masters Thesis research (at MSAL at UMD). The author can envision developments in this fabrication technique opening up applications in micro-molding, micro-fluidics, or on-chip inductors and interconnects.

7.2.2. Vibrational Energy Harvesting

The voltage-tunable MEMS resonators discussed in Chapter 4 have relatively low resonant frequencies (~2 kHz) and would likely require significant modifications for RF applications. However, the dimensions and frequencies discussed are close to those of interest in vibrational energy harvesting (100's of Hz), an active topic of research in MEMS and distributed wireless sensor networks [141-144] .

The development and deployment of wireless sensor networks could be felt in a variety of applications, such as embedded sensors in buildings and bridges [141]. However, such systems will rely on small low power nodes that must be autonomous and maintenance free. While approaches such as micro-batteries are being investigated [181], stored power sources for applications requiring multiple years of operation are currently

extremely challenging. Thus, energy scavenging approaches, such as photovoltaics and vibration harvesting, have received increasing attention. While the power available from these sources is small (typically 100's of $\mu W/cm^3$ [144]), wireless RF transmitters with 10m range and <1mW power consumption have been demonstrated that rely entirely on solar and vibrationally scavenged energy [143].

For vibrational energy harvesting, *Williams and Yates* [141] developed a simplified model to calculate the maximum available power (P) from a vibrational source with an angular frequency of ω (independent of power conversion technique):

$$|P| = \frac{m\zeta\omega^3\left(\frac{\omega}{\omega_R}\right)Y^2}{\left[1-\left(\frac{\omega}{\omega_R}\right)^2\right]^2+\left[2\zeta\frac{\omega}{\omega_R}\right]^2} \quad \textbf{(80)}$$

where m is the vibrating mass, Y is the amplitude of vibration, ζ is a damping coefficient, and ω_R is the resonant frequency of the vibrating mass.

As evident from Equation 80, the power scales with mass, so most designs seek to include the largest proof mass possible within size limitations. The power also scales with the cube of resonant frequency, and the square of amplitude, making fast high amplitude vibrations preferable for high power output (with some designs requiring stable operation for >30μm amplitudes [141]). Near resonance, the amplitude of vibration is inversely proportional to the damping coefficient ($Y \propto 1/\zeta$), meaning low damping will lead to high power, at the expense of making the resonator more frequency selective. Other terms in Equation 80 also show that the frequency of input vibrations must match the resonant frequency of the resonator in order to maximize power. Since the frequency and acceleration of the source vibrations are inherent properties of each

environment, the capability for a single node design to adapt (tune) it's resonant frequency is quite attractive.

Looking at the vibration spectrums measured by *Roundy et al* [144], common ambient environments have acceleration peaks in the 100-300 Hz range. Such frequencies could be obtained using a 1000μm silicon cube held by 3 N/m springs, giving an approximate resonant frequency of 182 Hz. In the case of large damping coefficients, this single device could cover a wide range of frequencies at the cost of dramatically reducing the power available from any particular frequency. Conversely, designs using a minimal damping coefficient could increase power dramatically, but the optimal range of frequencies for generation would be small. Thus, it would be necessary to design and fabricate many devices to be able to cover the desired range. An alternative could be to include vertically-shaped electrostatic springs to enable resonant frequency tuning (either up or down) of a single optimized design in order to maximize power output at any given frequency in the range of interest.

The paradox in such a proposal is that energy harvesting typically uses low voltages to minimize power consumption, while the electrostatic springs discussed previously in this chapter require >50V to create significant tuning. However, there are multiple potential solutions. First, reservoir capacitors could be precisely pre-charged on tuning "islands" that are isolated from the remaining system. Since the tuning mechanism is capacitive, virtually no energy should be consumed during operation and the capacitor voltage should remain stable. Note that the reservoir capacitor should be much larger than the capacitance of the comb-fingers themselves. A second option could be the inclusion of electret's (permanent electrostatic charges), which have been shown to

hold up to 100 Volts for >3 years [182]. Electrets would require corona charging as a post-processing step after resonator fabrication (possibly using shadow masks) to serve as the permanent tuning mechanism.

A potential tunable resonator configuration utilizing "tuning islands" and extra comb-fingers for an electrostatic generator (like the generator in [142]) is proposed in Figure 7.1. Both stiffening and weakening electrostatic fingers could be included on separate "islands" to enable tuning of the resonant frequency either up or down. This approach would enable a single optimized design to be fabricated and subsequently tuned to a final desired frequency as a post-processing step. Using the gray-scale electrostatic springs demonstrated in Chapter 4, the 182 Hz system discussed earlier could be tuned from 154 Hz (-0.85 N/m) to 227 Hz (1.66 N/m). Altering basic design parameters, such as the number of fingers and/or their spacing, could easily extend this range significantly.

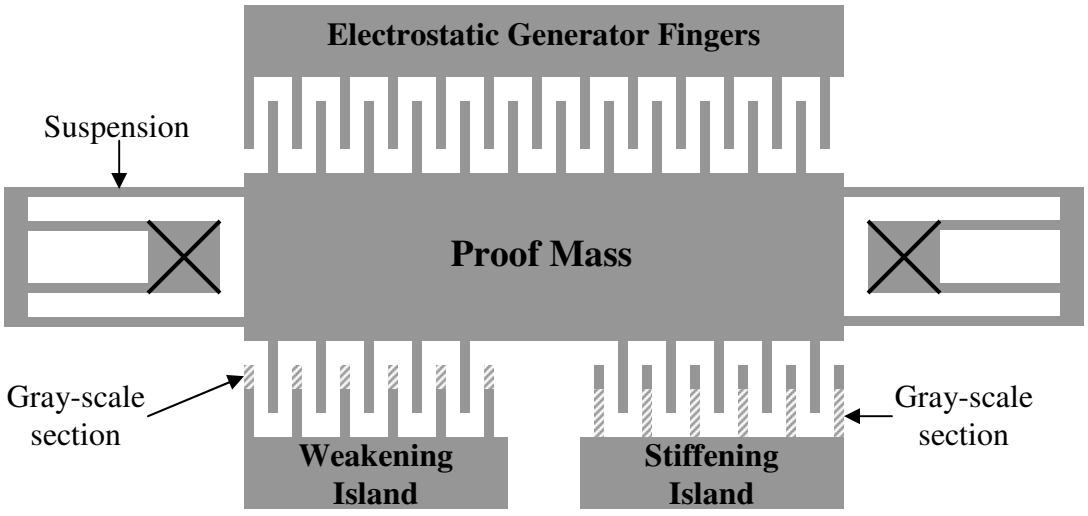

Figure 7.1: Schematic of a vibrational energy scavenger using stiffening and weakening gray-scale electrostatic spring islands.

While high voltage capacitive reservoirs and electrets are not commonly integrated with MEMS technology at the present time, further development of these areas

could provide numerous opportunities for on-chip tuning and actuation of electrostatic MEMS devices. Thus, vertically-shaped gray-scale tunable resonators could have direct applications in vibrational energy harvesting, and the topic is worthy of further study.

7.2.3. Fiber Aligner Miniaturization

The device footprint of the gray-scale fiber aligner is currently large, requiring cantilever lengths >10mm and multiple actuators measuring approximately 0.5 by 4mm. This design was initially chosen to minimize angular loss and enable the use of well understood comb-drive actuators. Yet for acceptance as a packaging technique, the layout should be more compact and compatible for array packaging. Both the fiber cantilever length and MEMS actuator size could be reduced by making some basic modifications to the design.

First, the use of a reduced cladding (RC) fiber (r=40μm vs 62.5μm) would have a dramatic effect on fiber spring constant because $k_{fiber} \propto \text{radius}^4$ (see Equation 72). Thus, an RC fiber cantilever of only 5.5mm would have the same spring constant as a 10mm cantilever of normal fiber. RC fiber is already commercially produced, often as bend-insensitive fiber (see www.StockerYale.com), making it a potentially viable solution.

A second design modification could be the migration to MEMS electrothermal actuators as the source of in-plane actuation [43-45]. Such actuators are capable of much higher forces compared to electrostatic devices, offering up to 0.67mN @ 7mA per beam [45]. The fabrication process for electrothermal actuators with 3-D components could be virtually identical to that used for the gray-scale electrostatic devices discussed in this research. Multiple electrothermal beam actuators could also be cascaded to increase the generated force, with the footprint still being smaller than most comb-drive designs.

Smaller footprints could lead towards compact fiber array packaging schemes, such as that shown schematically in Figure 7.2.

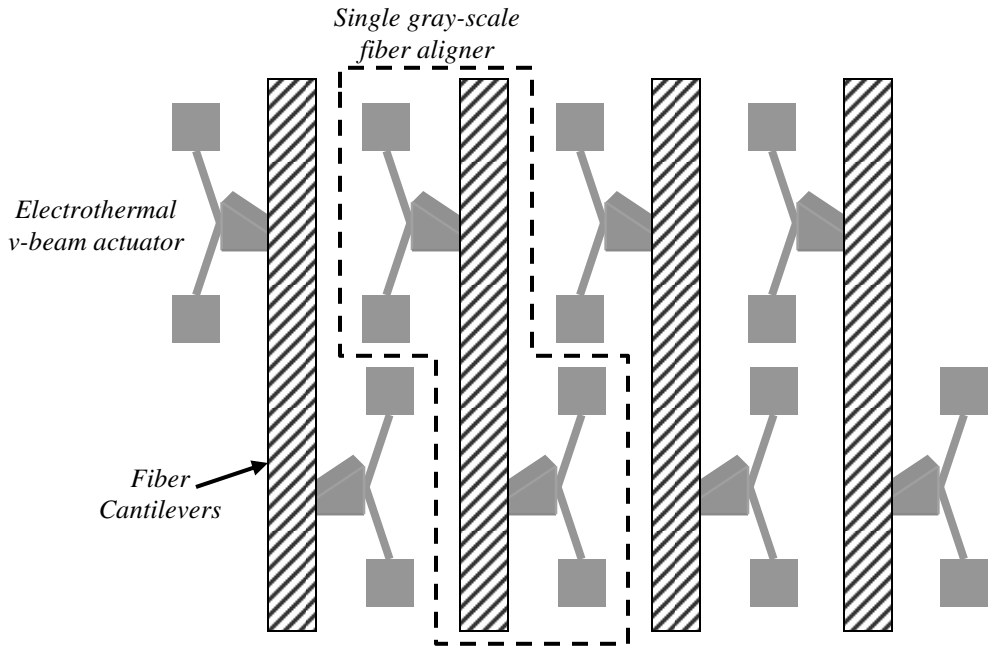

Figure 7.2: Schematic of compact gray-scale fiber aligner array configuration using electrothermal v-beam actuators with attached alignment wedges.

Electrothermal actuators were not originally used because they introduce additional design, fabrication, and testing variables that would make evaluation of the fiber actuation mechanism difficult. Since the mechanism of fiber actuation has now been established, electrothermal actuators could prove instrumental for reducing the gray-scale fiber aligner footprint of future. However, while RC fiber and electrothermal actuators could make short cantilever devices mechanically feasible, optical considerations discussed in Chapter 5 may become the limiting factor in fiber aligner designs.

Methods for improving and evaluating the alignment accuracy of gray-scale fiber aligners are also of great interest, but are more related to the core gray-scale technology and equipment limitations discussed previously. This actuation mechanism could also be extended for use in other applications, such as 1 x N switches or micro-robotics.

7.2.4. Maintaining Fiber Alignment

Once acceptable coupling has been achieved by the gray-scale fiber aligner, to whatever tolerance is required, the device currently requires a constant application of voltage to maintain the alignment. Thus, the gray-scale fiber aligner would greatly benefit from the development of a mechanism to fix the fiber in its final position, a necessary component of any fiber packaging scheme.

There are two apparent avenues to address the fiber-fixing challenge. The first option is to immobilize the fiber via epoxy or soldering, which is typically a permanent process. Some research has been pursued to study the alignment effects on a fiber within a package caused by thermal CTE mismatch of adhesives [184] and solder ball relaxation [172]. Options such as laser welding could be attractive in certain cases [155], but significant research on this topic remains.

Alternatively, a mechanical locking mechanism could potentially be introduced to immobilize the silicon actuators, and therefore indirectly immobilize the fiber. MEMS bi-stable actuators [185] could be adapted to hold the comb-drive actuators, and therefore the fiber, in the final aligned positions. A schematic of such a system is shown in Figure 7.3. The primary advantage of a mechanical clamping approach is that the locking mechanism could be reversible, enabling re-positioning of the fiber if any shifts occur during or after the clamping process. However, the additional actuators would increase the size and complexity of the overall device. Significant design, simulation and testing would be required for such a mechanism, with specific focus on it's susceptibility to shock and/or vibration.

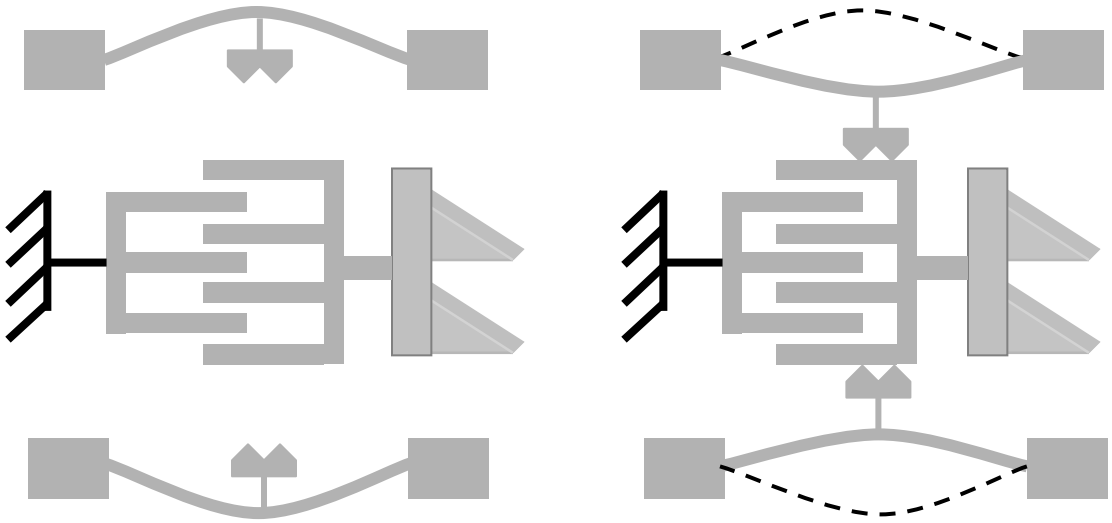

Figure 7.3: Schematic of a bi-stable clamping mechanism (a) before and (b) after fixing a fiber actuator in an optimal position.

7.3. Conclusion

This PhD dissertation research has definitively shown that electrostatic MEMS actuators incorporating gray-scale technology have significant advantages over their planar counterparts. In demonstrating that gray-scale is a viable 3-D batch fabrication technique for developing MEMS sensors and actuators, it is my sincere hope that this technology can be leveraged by the MEMS community to develop innovative solutions to many of the technical, economic, and social challenges facing the world today.

APPENDIX A: Matlab Script for Virtual Electrostatic Spring Constants

As discussed in Section 3.3.3, the instability point of a static comb-drive actuator is defined by the perpendicular virtual electrostatic spring ($k_{y\text{-}virtual}$) that is created as the voltage increases and the device deflects. To calculate this instability point, knowledge of both the actuation characteristics ($V^2(x)$) and overlap area ($A(x)$) as a function of displacement is required. However, for variable height profiles these relations are not simple analytical functions. Thus, a Matlab script was created to take any comb-finger height profile ($h(x)$) and numerically calculate $k_{y\text{-}virtual}$ as a function of displacement.

The script first defines all constants and assumptions about the comb actuator design (such as number of fingers and suspension spring constant). A height profile is then input from a text file, where it is assumed that the height profile accounts for fringing fields by scaling the physical height into an "effective" height representing dC/dx. Equation 43 is then evaluated numerically to obtain $A(x)$, while $V^2(x)$ is calculated numerically using the piecewise constant technique of Equations 36 and 37. Finally, the virtual spring constant $k_{y\text{-}virtual}(x)$ as a function of displacement is calculated using Equation 46. The code is shown below with comments in green font.

```
**********************************************************************
% Matlab code for calculating the perpendicular virtual electrostatic spring constant as a
% function of displacement for arbitrary comb-finger profiles

% Define constants and design assumptions in SI units
step = 1;
stepx = 1e-7;
epsilon = 8.85e-12;
gap = 10e-6;
num_fingers = 200;
k = 5;
max_finger_height = 100e-6;
```

```
% Input “effective” height profile from text file – can account for fringing fields
string_input = 'height_profile.txt';
fid = fopen(string_input);
height = fscanf(fid, '%f',[1 inf]);
height = height';
fclose(fid);

% Calculate overlapping area as a function of (x) by integrating over the height profile
% Corresponds to A(x) in Equation 43
area(1) = max_finger_height * stepx;
for(ii=2:length(x))
   increment = x(ii) - x(ii-1);
   area(ii) = area(ii-1) + height(ii) * increment;
end

% Calculate voltage^2 vs. displacement characteristics for V^2(x) in Equation 45
% Assumes force is proportional to the given “effective” height profile
Vtemp2 = zeros(length(x),1);
V = zeros(length(x),1);
V2 = zeros(length(x),1);
for(n = 2:length(x));
   increment = x(n) - x(n-1);
   Vtemp2(n) = increment * gap * K / (epsilon * height(n)) / num_fingers;
   V(n) = sqrt(V(n-1)^2 + Vtemp2(n));
   V2(n) = V(n) * V(n);
end

% Use A(x) and V^2(x) in Equation 46 to calculate the virtual electrostatic spring as a
% function of displacement, ky(x)
for(i=1:length(area))
   ky(i) = num_fingers * epsilon * area(i) * V2(i) * 2 / gap^3;
end

plot(x,ky)

**********************************************************************
```

APPENDIX B: Process Flow for Gray-scale SOI process

The process flow for integrating gray-scale technology within an SOI actuator required significant development. The final process was described qualitatively in Section 3.5 and the details are shown in Table B.1. The gray-scale lithography and DRIE steps were described in more detail elsewhere in this dissertation (see Chapter 2). Slight modifications would be required to adapt this process to devices having different layouts or requiring different etch selectivity.

The wafer saw step is intentionally performed before the wet oxide etch release step to maintain structural integrity during the relatively harsh sawing process. The oxide etch release required significant development as the sequence of etching in buffered oxide etch (BOE) and rinsing in DI water often effected the complete etching between high aspect ratio features. In general, 1-2 rinse steps in DI water (5 min each) helped to ensure complete undercutting of desired structures. The final die rinse process was a combination of multiple soaks in DI, followed by soaks in IPA to avoid stiction problems (due to its low surface tension).

Table B.1: Process details for electrostatic MEMS actuators incorporating gray-scale technology.

Step #	Step Name	Location	Recipe / Description
1	Starting Material	MSAL	Wafer = 100mm, p-type (1-10 ohm-cm) SOI (device layer / buried oxide layer) – 100µm / 2µm Thickness = 600-650µm (total)
2	Coat Photoresist	ARL	Karl Suss ACS 200 Recipe Name: 5214eS51 Spin: 2000rpm, 40 sec Bake: 110 C, 120 sec

3	Expose Photoresist	LPS	GCA Waferstep File: COMBS2, Pass: METAL2 Mask: 2nd Gen_M 4 by 4 array (dropping corners), 19.5mm in X & 18mm in Y Exposure = 0.17 sec, Focus = 0
4	Develop Photoresist	LPS	AZ312MIF 1:1 DI 120 seconds, light agitation → Check under microscope
5	De-Scum	LPS	PlasmaTherm 790 Recipe: dandescu.prc Gas = O_2 16sccm, Pressure = 200mTorr, Power = 100W, Time = 45 sec
6	Evaporate Metal	LPS	CHA Mark – 40 Recipe 22: Aluminum, 1000 A Rate = 4 A/sec, Power = 90%
7	Metal Lift Off	ARL	PRS – 3000 Temp = 85 C Time = 120 min
8	Inspection	ARL	Under microscope – check for line definition / delamination
9	Coat Photoresist	ARL	Karl Suss ACS 200 Recipe Name: 9245S51 Spin: 2500rpm, 60 seconds Bake: 110 C, 120 seconds
10	Gray-scale Exposure	LPS	GCA Autostep File: COMBS2, Pass: GRAY2 Mask: 2ndGen_S 4 by 4 array (dropping corners), 19.5mm in X & 18mm in Y Exposure = 1.50 sec, Focus = -1 Alignment: Align Fiducial mark to Al mark on wafer i. Align mark offset = 8mm on x-axis ii. Uses die's (3,1) and (3,4)
11	Develop Photoresist	LPS	AZ400K 1:5 DI (Fresh solution every wafer) Time = 6 min (Light agitation)
12	Inspection	LPS	Aluminum mark must be covered by larger photoresist mark Aluminum pads should be covered by photoresist squares
13	DRIE Chamber Conditioning	ARL	PlasmaTherm 770 DRIE Recipe: Clean Time = 15 min Recipe: brianm2 Time = 25 loop conditioning run with recipe below → Use dummy wafer

14	DRIE Silicon Etch	ARL	PlasmaTherm 770 DRIE Recipe: brianm2 • Coil Power = 825 W (etch), 825 W (dep) • Chiller Temperature = 20 C • Pressure = 15mTorr (etch), 15mTorr (dep) • Electrode Power = 13 W (etch), 1W (dep) • Cycle Time = 9sec (etch), 8 sec (dep) • Number of Loops = 230+
15	Inspection	ARL	Be sure area between comb-fingers is clear of silicon → darkness indicates remaining silicon!!
16	Wafer Dicing	ARL	Wafer saw at ARL – channel 1 = 18mm, channel 2 = 19.5mm (assuming wafer flat is towards the operator)
17	Oxide Etch Release	ARL	Buffered oxide etch (BOE) 6:1 → ~1000 A/min @RT Time: 50min BOE → DI 5min → 50min BOE 10 min DI soak → 5 min DI soak → 10 min IPA soak → 30 min IPA soak Release bars at least 30μm wide should be cleared
18	Photoresist Strip	LPS	PlasmaTherm 790 RIE Recipe: 02sample.prc Time: 10 min

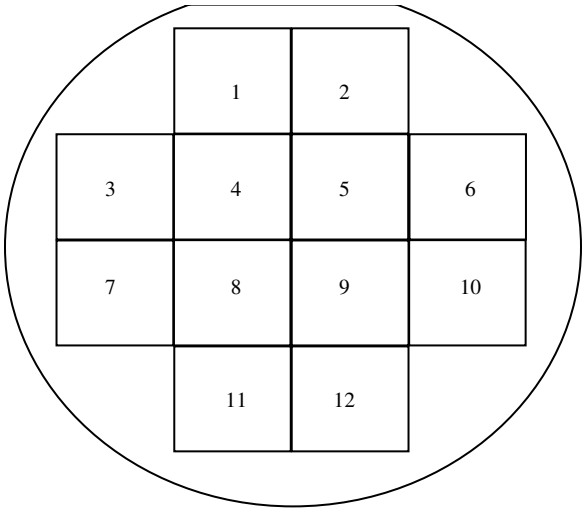

Figure B.1: Resulting die layout on a 4-inch wafer.

APPENDIX C: Fiber Deflection Geometry

For purposes of both optical and mechanical characterization of the gray-scale fiber aligner, the angles and displacements of the fiber cantilever tip during actuation must be calculated. As a slight approximation, we will assume that the deflected fiber cantilever of length (L) follows a circular arc of radius (r) due to a tip displacement (Δy), creating an angle (θ) as shown in Figure C.1. We can then write the length of the circular arc as:

$$L = r\theta \tag{C.1}$$

And the displacement in terms of the angle as:

$$\Delta y = r - r\cos\theta. \tag{C.2}$$

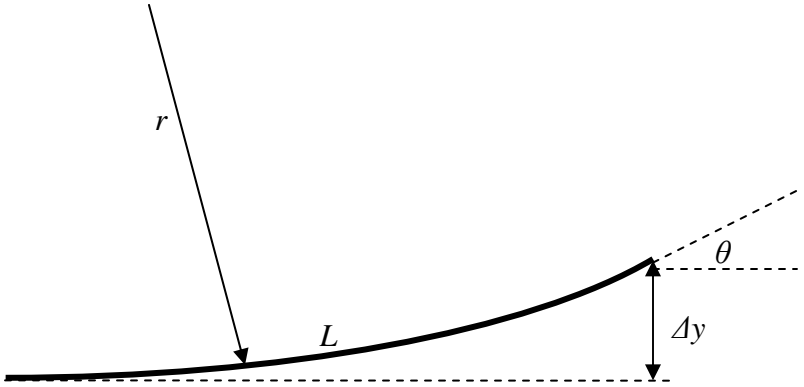

Figure C.1: Angle created by deflecting fiber cantilever tip.

Since L and Δy are known, we can substitute Equation C.1 into C.2 to eliminate r, resulting in a single equation with one unknown (θ):

$$\Delta y = \frac{L}{\theta}(1 - \cos\theta). \tag{C.3}$$

Equation C.3 can be solved for θ by converting to sin θ terms (instead of cos θ) and using the approximation of $\sin\theta \approx \theta$. Re-arranging and squaring both sides, we obtain:

$$\left(1 - \frac{\theta}{L}\Delta y\right)^2 = 1 - \theta^2. \tag{C.4}$$

Solving for θ results in Equation 65 as stated in Section 5.3:

$$\theta = \frac{2}{\left(\frac{L}{\Delta y} + \frac{\Delta y}{L}\right)}. \qquad \textbf{(C.5)}$$

For most cases $L >> \Delta y$, and Equation C.5 can be reduced to:

$$\theta = 2\frac{\Delta y}{L}. \qquad \textbf{(C.6)}$$

Knowledge of this angle is quite useful for determining the angular loss components of a deflected fiber cantilever tip, as discussed in Chapter 5.

For most implementations of the gray-scale fiber aligner, the fiber will actually extend beyond the point of contact with the alignment wedges along a straight line tangent to the curve, see Figure C.2. Thus, an additional tip displacement ($\Delta y'$) is generated that depends on the fiber angle and the length it extends past the alignment wedges (L'):

$$\Delta y' = L' \cdot \tan\theta. \qquad \textbf{(C.7)}$$

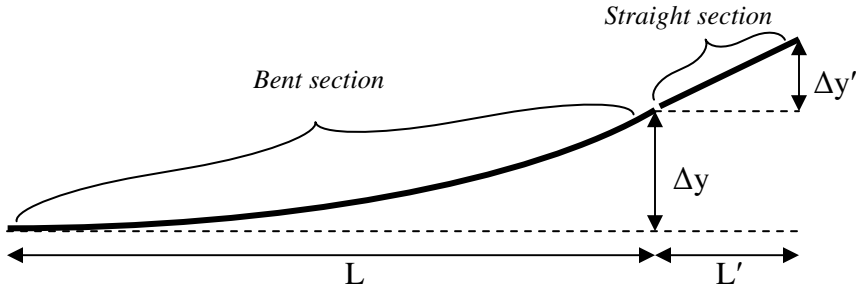

Figure C.2: Additional tip displacement due to fiber tip extending beyond the point of actuation.

Using Equations C.5 and C.6, we can now analyze the fiber displacements in Figure 6.6 more accurately. For the case of (140V,140V) in Figure 6.6, the total measured displacement ($\Delta y + \Delta y'$) was 37μm for a device with $L=12mm$ and $L'=2mm$. This means that the 37μm tip displacement was actually comprised of approximately $\Delta y=28\mu m$ at the alignment wedges and $\Delta y'=9\mu m$ due to the overhanging fiber. Although the extra $L'=2mm$ of fiber was necessitated by our testing setup, the fiber

displacement at the alignment wedges is still easily in the 10's of micrometer range that is realistically required for in-package alignment [152].

It is also possible to use this additional angular displacement to one's advantage when designing a fiber alignment system. Shown in Table C.1 are 3 possible designs for achieving 40μm tip displacement with a total fiber cantilever length of 6mm. Moving the alignment wedges from L=6mm to L=4mm reduces the fiber displacement at the alignment wedges (Δy) by a factor of two, causing a corresponding reduction in the angular losses during optical coupling. One caveat to this approach is that while the required fiber motion is smaller, the fiber spring constant will increase dramatically (recall $k_{fiber} \sim 1/L^3$ from Equation 72) and higher force actuators may be required.

Table C.1: Example designs using displacement amplification to achieve 40μm total tip movement.

L (mm)	L′ (mm)	Δy (μm)	Δy′ (μm)	θ (rad)	Max Transmission (dB)
6	0	40	0	0.0133	-0.085
5	1	28.6	11.4	0.0114	-0.063
4	2	20	20	0.0100	-0.048

APPENDIX D: Geometry for Fiber Position in V-groove

In order to design a gray-scale fiber aligner for a particular application, one must calculate the rest position of the cylindrical fiber between two overlapping wedges, as shown in Figure D.1. For this general case, we will assume that the fiber is perfectly cylindrical (with radius=R), and that each wedge makes an identical angle (θ) with the horizontal axis. The coordinates of interest will be those that define the center of the fiber as it rests between the wedges **(X,Y)**.

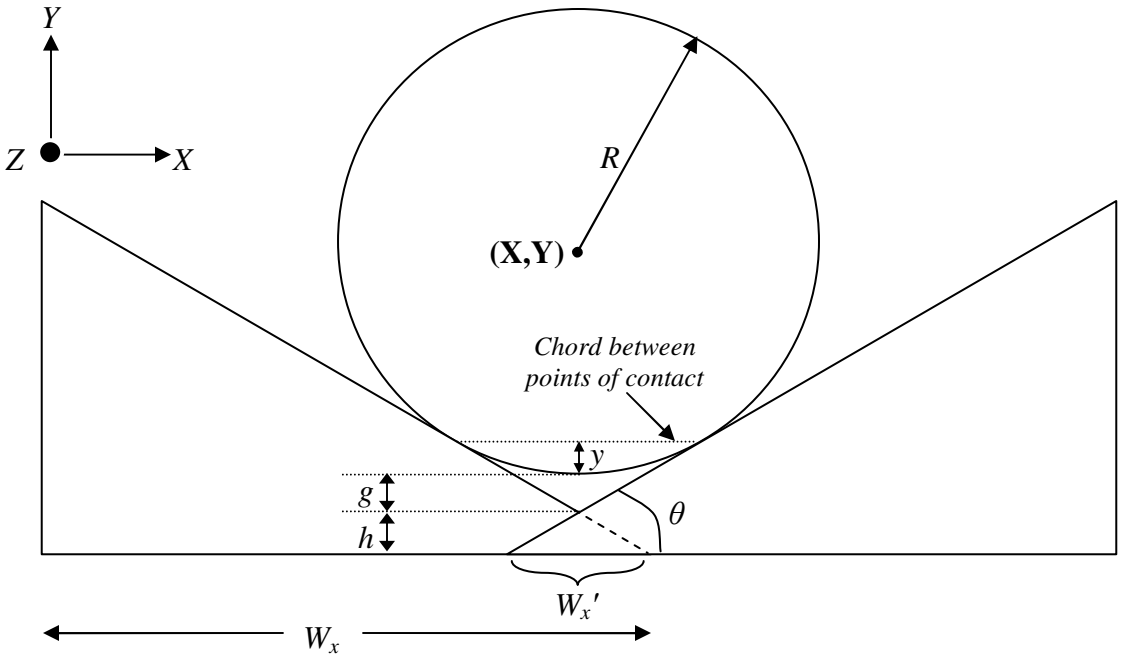

Figure D.1: Geometry for deriving the rest position of a cylindrical fiber within a v-groove.

The horizontal position (**X**) of the fiber center in relation to the edge of an individual wedge can be readily calculated using the width of that wedge (W_x), and it's overlap with the opposing wedge (W_x'):

$$X = W_x - \frac{W_x'}{2}. \qquad \textbf{(D.1)}$$

However, calculating the vertical position (**Y**) of the fiber center is more complicated because it is determined by a combination of the fiber radius (R), the gap (g) between the

fiber edge and the bottom of the v-groove, and the offset (h) created by the overlapping wedges:

$$Y = R + g + h\,. \tag{D.2}$$

Calculating the vertical offset caused by the overlapping wedges is straight forward:

$$h = \frac{W_x'}{2}\tan(\theta)\,. \tag{D.3}$$

The gap (g) between the fiber and bottom of the v-groove can be determined by first defining a chord between the two points of contact between fiber and wedges. The vertical distance between the center of the chord and the fiber edge ("y" in the figure), can then be calculated to be:

$$y = R\left(1 - \frac{1}{\sqrt{\tan(\theta)^2 + 1}}\right). \tag{D.4}$$

Using some trigonometry, the gap can then be determined in terms of y and θ:

$$g = \tan(\theta)\sqrt{R^2 - (R - y)^2} - y\,. \tag{D.5}$$

Equations D.1-D.5 explicitly define the center coordinates of a cylindrical fiber resting in a v-groove of arbitrary angle. As intuition would dictate, as the wedge angle approaches zero, the gap vanishes ($g \rightarrow 0$ and $y \rightarrow 0$) and the **Y** coordinate approaches the fiber radius ($\mathbf{Y} \rightarrow R$).

For the case of $\theta = 45^o$, as desired in this research, the calculation of the **Y** coordinate can be greatly simplified to:

$$Y = R\sqrt{2} + \frac{W_x'}{2}\,. \tag{D.6}$$

APPENDIX E: Pixel Sets for Alignment Wedges

As mentioned in Chapter 5, two different pixel sets were used during the design of the gray-scale fiber aligner wedges. The design utilizing a 2.8μm mask pitch has a total of 27 available pixels, while the design utilizing a 3.2μm mask pitch has a total of 52 available pixels. The tables below give the in-plane dimensions of each rectangular pixel, with its calculated transmission (*Tr*) and expected height in photoresist using the Gaussian approximation. The final height in silicon is then estimated by assuming an etch selectivity of 60:1, with a 30μm over etch to account for ARDE.

Table E.1: Set of pixels for 2.8μm mask pitch used to create gray-scale alignment wedges.

Level #	x (μm)	y (μm)	Calculated *Tr*	Estimated Height in Photoresist (μm)	Estimated Height in Silicon (μm)
1	2.2	2.1	0.411	2.42	115.3
2	2.1	2.1	0.438	2.10	95.8
3	2.2	2.0	0.439	2.08	94.9
4	2.3	1.9	0.443	2.04	92.3
5	2.1	2.0	0.464	1.81	78.5
6	2.2	1.9	0.467	1.78	76.9
7	2.0	2.0	0.490	1.56	63.8
8	2.1	1.9	0.491	1.55	63.1
9	2.2	1.8	0.495	1.52	61.0
10	2.0	1.9	0.515	1.34	50.6
11	2.1	1.8	0.518	1.32	49.4
12	1.9	1.9	0.540	1.16	39.4
13	2.0	1.8	0.541	1.15	38.9
14	2.1	1.7	0.545	1.12	37.2
15	1.9	1.8	0.564	0.99	29.4
16	2.0	1.7	0.566	0.97	28.4
17	1.8	1.8	0.587	0.85	20.8
18	1.9	1.7	0.588	0.84	20.3
19	2.0	1.6	0.592	0.82	19.0
20	1.8	1.7	0.610	0.72	13.0
21	1.9	1.6	0.612	0.70	12.2
22	1.7	1.7	0.631	0.61	6.4

23	1.8	1.6	0.633	0.60	6.0
24	1.9	1.5	0.636	0.58	4.9
25	1.7	1.6	0.653	0.51	0.3
26	1.8	1.5	0.656	0.49	-0.3
27	1.6	1.6	0.673	0.42	-4.8

Table E.2: Set of pixels for 3.2µm mask pitch used to create gray-scale alignment wedges.

Level #	x (µm)	y (µm)	Calculated *Tr*	Estimated Height in Photoresist (µm)	Estimated Height in Silicon (µm)
1	2.4	2.4	0.438	2.39	113.5
2	2.5	2.3	0.438	2.38	112.8
3	2.6	2.2	0.441	2.34	110.7
4	2.4	2.3	0.461	2.12	97.2
5	2.5	2.2	0.463	2.10	95.9
6	2.6	2.1	0.467	2.06	93.4
7	2.3	2.3	0.483	1.88	83.1
8	2.4	2.2	0.484	1.88	82.5
9	2.5	2.1	0.487	1.85	80.8
10	2.6	2.0	0.492	1.80	77.9
11	2.3	2.2	0.506	1.67	70.3
12	2.4	2.1	0.508	1.65	69.2
13	2.5	2.0	0.512	1.62	67.2
14	2.6	1.9	0.518	1.57	64.1
15	2.2	2.2	0.527	1.49	59.2
16	2.3	2.1	0.528	1.48	58.7
17	2.4	2.0	0.531	1.45	57.3
18	2.5	1.9	0.536	1.42	54.9
19	2.6	1.8	0.543	1.36	51.8
20	2.2	2.1	0.549	1.32	49.1
21	2.3	2.0	0.551	1.30	48.2
22	2.4	1.9	0.555	1.28	46.5
23	2.5	1.8	0.561	1.23	44.0
24	2.1	2.1	0.569	1.17	40.3
25	2.2	2.0	0.570	1.17	39.9
26	2.3	1.9	0.573	1.15	38.7
27	2.4	1.8	0.578	1.11	36.8
28	2.5	1.7	0.585	1.07	34.1
29	2.1	2.0	0.590	1.04	32.3
30	2.2	1.9	0.592	1.03	31.5

31	2.3	1.8	0.596	1.00	30.1
32	2.4	1.7	0.602	0.97	28.0
33	2.0	2.0	0.609	0.92	25.3
34	2.1	1.9	0.610	0.92	24.9
35	2.2	1.8	0.613	0.90	23.9
36	2.3	1.7	0.618	0.87	22.3
37	2.0	1.9	0.629	0.81	18.8
38	2.1	1.8	0.631	0.80	18.2
39	2.2	1.7	0.635	0.78	17.0
40	2.3	1.6	0.641	0.75	15.2
41	1.9	1.9	0.647	0.72	13.2
42	2.0	1.8	0.648	0.72	12.9
43	2.1	1.7	0.651	0.70	12.1
44	2.2	1.6	0.656	0.68	10.7
45	1.9	1.8	0.666	0.63	8.0
46	2.0	1.7	0.668	0.63	7.5
47	2.1	1.6	0.672	0.61	6.5
48	1.8	1.8	0.684	0.56	3.5
49	1.9	1.7	0.685	0.55	3.3
50	2.0	1.6	0.688	0.54	2.6
51	2.1	1.5	0.692	0.52	1.4
52	1.8	1.7	0.701	0.49	-0.7

REFERENCES

[1] A. Bertsch, H. Lorenz, and P. Renaud, "3D microfabrication by combining microstereolithography and thick resist UV lithography," *Sensors and Actuators A (Physical)*, vol. A73, pp. 14, 1999.

[2] Gal, *U.S. Patent #5,310,623*, 1994.

[3] W. Henke, W. Hoppe, H. J. Quenzer, P. Staudt-Fischbach, and B. Wagner, "Simulation and experimental study of gray-tone lithography for the fabrication of arbitrarily shaped surfaces," *Proceedings IEEE Micro Electro Mechanical Systems An Investigation of Micro Structures, Sensors, Actuators, Machines and Robotic Systems*, pp. 205, 1994.

[4] W. Henke, W. Hoppe, H. J. Quenzer, P. Staudt-Fischbach, and B. Wagner, "Simulation assisted design of processes for gray-tone lithography," *Microelectronic Engineering*, vol. 27, pp. 267, 1995.

[5] B. Wagner, H. J. Quenzer, W. Henke, W. Hoppe, and W. Pilz, "Microfabrication of complex surface topographies using grey-tone lithography," *Sensors and Actuators A (Physical)*, vol. A46, pp. 89, 1995.

[6] M. R. Whitley, R. L. Clark, J. R. Shaw, D. R. Brown, P. S. Erbach, and G. T. Dorek, *International Patent WO 02/31600 A1*, 2002.

[7] M. LeCompte, X. Gao, and W. Prather, "Photoresist characterization and linearization procedure for the gray-scale fabrication of diffractive optical elements," *Applied Optics*, vol. 40, pp. 5921-7, 2001.

[8] Y. Opplinger, P. Sixt, J.M. Stauffer, J.M. Mayor, P. Regnault, and G. Voirin, "One-step 3D Shaping Using a Gray-tone Mask for optical and microelectronic applications," *Microelectron. Eng*, vol. 23, pp. 449-454, 1994.

[9] W. Daschner, R. Stein, Pin Long, Chuck Wu, and S. H. Lee, "One-step lithography for mass production of multilevel diffractive optical elements using high energy beam sensitive (HEBS) gray-level mask," *Proc. of the SPIE: Diffractive and Holographic Optics Technology III*, vol. **2689**, pp. 153-5, 1996.

[10] *Canyon Materials, Inc., US patent 5,285,517*, 1994.

[11] D. C. O'Shea, and W. S. Rockward, "Gray-scale masks for diffractive-optics fabrication: II. Spatially filtered halftone screens," *Applied Optics*, vol. 34, pp. 7518-26, 1995.

[12] T. J. Suleski, and D.C. O'Shea, "Gray-scale Masks for Diffractive-optics fabrication: I. Commercial Slide Images," *Applied Optics*, vol. 34, pp. 7507-17, 1995.

[13] C. M. Waits, R. Ghodssi, M. H. Ervin, and M. Dubey, "MEMS-based gray-scale lithography," *International Seminconductor Device Research Symposium (ISDRS)*, pp. 182, 2001.

[14] C. M. Waits, "Investigation of Gray-scale technology for large area 3D silicon structures," *M.S. Thesis, University of Maryland - College Park*, 2003.

[15] C. M. Waits, A. Modafe, and R. Ghodssi, "Investigation of gray-scale technology for large area 3D silicon MEMS structures," *Journal of Micromechanics and Microengineering*, vol. 13, pp. 170, 2003.

[16] B. Morgan, C. M. Waits, J. Krizmanic, and R. Ghodssi, "Development of a deep silicon phase Fresnel lens using Gray-scale lithography and deep reactive ion etching," *Journal of Microelectromechanical Systems*, vol. 13, pp. 113, 2004.

[17] C. M. Waits, B. Morgan, M. Kastantin, and R. Ghodssi, "Microfabrication of 3D silicon MEMS structures using gray-scale lithography and deep reactive ion etching," *Sensors and Actuators A: Physical*, vol. 119, pp. 245, 2005.

[18] B. Morgan, "Development of a Deep Phase Fresnel Lens in Silicon Using Gray-scale Lithography and Deep Reactive Ion Etching," *M.S. Thesis, University of Maryland - College Park*, 2004.

[19] A. Bertsch, S. Jiguet, P. Bernhard, and P. Renaud, "Microstereolithography: a review," *Mater. Res. Soc., Rapid Prototyping Technologies. Symposium*, pp. 3, 2003.

[20] T. S. Ji, K. J. Vinoy, and V. K. Varadan, "RF MEMS phase shifter by microstereolithography on silicon," *Proceedings of the SPIE - The International Society for Optical Engineering*, vol. 4700, pp. 58.

[21] C. W. Hull, *U.S. Patent #4,575,330*, 1986.

[22] T. Takagi, and N. Nakajima, *4th International Symposium on Micro Machine and Human Science (MHS'93)*, 1993.

[23] S. Maruo, O. Nakamura, and S. Kawata, *SPIE-Optics for Science and New Technology*, 1996.

[24] M. Miwa, S. Juodkazis, T. Kawakami, S. Matsuo, and H. Misawa, "Femtosecond two-photon stereo-lithography," *Applied Physics A (Materials Science Processing)*, vol. A73, pp. 561, 2001.

[25] K. J. Vinoy, Y. Hargsoon, J. Taeksoo, and V. K. Varadan, "RF MEMS and reconfigurable antennas for communication systems," *Proceedings of the SPIE - The International Society for Optical Engineering*, vol. 4981, pp. 164, 2003.

[26] F. Yongqi and B. Ngoi Kok Ann, "Experimental study of microcylindrical lenses fabricated using focused-ion-beam technology," *Journal of Vacuum Science & Technology B (Microelectronics and Nanometer Structures)*, vol. 19, pp. 1259, 2001.

[27] F. Yongqi and N. K. A. Bryan, "Fabrication of three-dimensional microstructures by two-dimensional slice by slice approaching via focused ion beam milling," *Journal of Vacuum Science & Technology B (Microelectronics and Nanometer Structures)*, vol. 22, pp. 1672, 2004.

[28] S. Reyntjens and R. Puers, "Focused ion beam induced deposition: fabrication of three-dimensional microstructures and Young's modulus of the deposited material," *Journal of Micromechanics and Microengineering*, vol. 10, pp. 181, 2000.

[29] C. Khan Malek, F. T. Hartley, and J. Neogi, "Focused ion beam direct micromachining of DOEs," *Proceedings of the SPIE - The International Society for Optical Engineering*, vol. 4075, pp. 167-72, 2000.

[30] M. Mita, Y. Mita, H. Toshiyoshi, and H. Fujita, "Multiple-height microstructures fabricated by ICP-RIE and embedded masking layers," *Transactions of the Institute of Electrical Engineers of Japan, Part E*, vol. 120-E, pp. 493, 2000.

[31] C. Beuret, G. A. Racine, J. Gobet, R. Luthier, and N. F. de Rooij, "Microfabrication of 3D multidirectional inclined structures by UV lithography and electroplating," *Proceedings IEEE Micro Electro Mechanical Systems An Investigation of Micro Structures, Sensors, Actuators, Machines and Robotic Systems*, pp. 81, 1994.

[32] M. Han, L. Woonseob, L. Sung-Keun, and S. L. Seung, "3D microfabrication with inclined/rotated UV lithography," *Sensors and Actuators A (Physical)*, vol. A111, pp. 14, 2004.

[33] N. P. Pham, E. Boellaard, J. N. Burghartz, and P.M. Sarro, "Photoresist Coating Methods for the Integration of Novel 3-D RF Microstructures," *Journal of Microelectromechanical Systems*, vol. 13, pp. 491-499, 2004.

[34] A. A. Ayon, R. Braff, C. C. Lin, H. H. Sawin, and M. A. Schmidt, "Characterization of a time multiplexed inductively coupled plasma etcher," *Journal of the Electrochemical Society*, vol. 146, pp. 339, 1999.

[35] A. A. Ayon, S. Nagle, L. Frechette, A. Epstein, and M. A. Schmidt, "Tailoring etch directionality in a deep reactive ion etching tool," *Journal of Vacuum Science*

& Technology B (Microelectronics and Nanometer Structures), vol. 18, pp. 1412, 2000.

[36] B. Morgan, R. Ghodssi, and C. M. Waits, "Compensated aspect ratio dependent etching (CARDE) using gray-scale technology," *Microelectronic Engineering*, vol. 77, pp. 85, 2005.

[37] B. Morgan, C.M. Waits, and R. Ghodssi, "MEMS-based Gray-scale Technology for Large Area 3-D Structures in Silicon," presented at VC16, The 16th International Vacuum Congress, Venice, Italy, 2004.

[38] B. Morgan, R. Ghodssi, "Biasing Gray-scale Lithography for Integration with Deep Reactive Ion Etching (DRIE)," presented at 49th International Conference on Electron, Ion, and Photon Beam Technology & Nanofabrication, Grande Lakes, Florida, 2005.

[39] M. Khoo, and C. Liu, "Micro-magnetic silicone elastomer membrane actuator," *Sensors and Actuators A: Physical*, vol. A89, pp. 259-66, April 2001.

[40] D. J. Peters, and B.L. Blackford, "Piezoelectric bimorph-based translation device for two-dimensional, remote micropositioning," *Rev. Scientific Instruments*, vol. 60, pp. 138-140, Jan 1989.

[41] T. Akiyama, D. Collard, and H. Fujita, "Scratch drive actuator with mechanical links for self-assembly of three-dimensional MEMS," *Journal of Microelectromechanical Systems*, vol. 6, pp. 10, 1997.

[42] P. Krulevitch, A. P. Lee, P. B. Ramsey, J. C. Trevino, J. Hamilton, and M. A. Northrup, "Thin film shape memory alloy microactuators," *Journal of Microelectromechanical Systems*, vol. 5, pp. 270, 1996.

[43] L. Que, J.-S. Park, and Y. B. Gianchandani, "Bent-beam electrothermal actuators - Part I: Single beam and Cascaded Devices," *Journal of Microelectromechanical Systems*, vol. 10, 2001.

[44] J. M. Maloney, D. S. Schreiber, and D. L. DeVoe, "Electrothermal linear micromotors fabricated from deep reactive ion etching of single crystal silicon," *Micro-Electro-Mechanical Systems (MEMS). 2000 ASME International Mechanical Engineering Congress and Exposition*, pp. 289, 2001.

[45] J. M. Maloney, D. S. Schreiber, and D. L. DeVoe, "Large-force electrothermal linear micromotors," *Journal of Micromechanics and Microengineering*, vol. 14, pp. 226, 2004.

[46] W. C. Tang, T.-C. H. Nguyen, and R. T. Howe, "Laterally driven polysilicon resonant microstructures," *Sensors and Actuators*, vol. 20, pp. 25-32, 1989.

[47] W. C. Tang, T. C. H. Nguyen, M. W. Judy, and R. T. Howe, "Electrostatic-comb drive of lateral polysilicon resonators," *Sensors and Actuators A (Physical)*, vol. A21, pp. 328, 1990.

[48] W. C. Tang, M. G. Lim, and R. T. Howe, "Electrostatic comb drive levitation and control method," *Journal of Microelectromechanical Systems*, vol. 1, pp. 170, 1992.

[49] X. Zhang, and W.C. Tang, "Viscous Air Damping in Laterally Driven Microresonators," *Proceedings of IEEE MEMS'94*, pp. 199-204, 1994.

[50] R. Legtenberg, A. W. Groeneveld, and M. Elwenspoek, "Comb-drive actuators for large displacements," *Journal of Micromechanics and Microengineering*, vol. 6, pp. 320, 1996.

[51] O. Renken, and W. Benecke, "Electrostatically driven micromachined nickel resonators and gyroscopes," *Proceedings of the SPIE – The International Society for Optical Engineering*, vol. 3680, pp. 716-27, 1999.

[52] A. P. Pisano and C. Young-Ho, "Mechanical design issues in laterally-driven microstructures," *Sensors and Actuators A (Physical)*, vol. A23, pp. 1060, 1990.

[53] L. Saggere, S. Kota, and S. B. Crary, "A New Design for Suspension of Linear Microactuators," *Dynamic Systems and Control, ASME 1994*, vol. 33-2, pp. 671-675, 1994.

[54] G. Zhou and P. Dowd, "Tilted folded-beam suspension for extending the stable travel range of comb-drive actuators," *Journal of Micromechanics and Microengineering*, vol. 13, pp. 178, 2003.

[55] T. Hirano, T. Furuhata, K. J. Gabriel, and H. Fujita, "Design, fabrication, and operation of submicron gap comb-drive microactuators," *Journal of Microelectromechanical Systems*, vol. 1, pp. 52, 1992.

[56] C. Chihchung and L. Chengkuo, "Design and modeling for comb drive actuator with enlarged static displacement," *Sensors and Actuators A (Physical)*, vol. A115, pp. 530, 2004.

[57] J. D. Grade, H. Jerman, and T. W. Kenny, "Design of large deflection electrostatic actuators," *Journal of Microelectromechanical Systems*, vol. 12, pp. 335, 2003.

[58] C. Lee, S. Han, and N.C. MacDonald, "Multiple Depth, Single Crystal Silicon MicroActuators for Large Displacement Fabricated by Deep Reactive Ion Etching," *Solid State Sensor and Actuator Workshop, Hilton Head Island, South Carolina, June 8-11*, pp. 45-50, 1998.

[59] M. A. Rosa, S. Dimitrijev, and H. B. Harrison, "Enhanced electrostatic force generation capability of angled comb finger design used in electrostatic comb-drive actuators," *Electronics Letters*, vol. 34, pp. 1787, 1998.

[60] W. Ye, S. Mukherjee, and N. C. MacDonald, "Optimal shape design of an electrostatic comb drive in microelectromechanical systems," *Journal of Microelectromechanical Systems*, vol. 7, pp. 16, 1998.

[61] B. D. Jensen, S. Mutlu, S. Miller, K. Kurabayashi, and J. J. Allen, "Shaped comb fingers for tailored electromechanical restoring force," *Journal of Microelectromechanical Systems*, vol. 12, pp. 373, 2003.

[62] W. Ye and S. Mukherjee, "Optimal shape design of three-dimensional MEMS with applications to electrostatic comb drives," *International Journal for Numerical Methods in Engineering*, vol. 45, pp. 175, 1999.

[63] J. B. Muldavin, and G. M. Rebeiz, "X-band Tunable MEMS Resonators," *Topical Meetings on Silicon Monolithic Integrated Circuits in RF Systems*, pp. 116-117, 2000.

[64] H. D. Nguyen, H. Dooyoung, P. R. Patterson, C. Rumin, W. Piyawattanametha, E. K. Lau, and M. C. Wu, "Angular vertical comb-driven tunable capacitor with high-tuning capabilities," *Journal of Microelectromechanical Systems*, vol. 13, pp. 406, 2004.

[65] C. T.-C. Nguyen, L.P.B. Katehi, and G. M. Rebeiz, "Micromachined Devices for Wireless Communications," *Proceedings of the IEEE*, vol. 86, pp. 1756-1768, 1998.

[66] J. R. Clark, F.D. Bannon, A.-C. Wong, and C.T.C. Nguyen, "Parallel-Resonator HF Micromechanical Bandpass Filters," *International Conference on Solid-state Sensors and Actuators (Transducers'97)*, pp. 1161-64, 1997.

[67] L. Lin, R.T. Howe, and A.P. Pisano, "Microelectromechanical Filters for Signal Processing," *Journal of Microelectromechanical Systems*, vol. 7, pp. 286-294, 1998.

[68] J. Kim, S. Park, D. Kwak, H. Ko, W. Carr, J. Buss, and D. D. Cho, "Robust SOI process without footing for ultra high-performance microgyroscopes," *IEEE International Solid-State Sensors and Actuators Conference*, vol. vol.2, pp. 1691, 2003.

[69] P. S. Riehl, K. L. Scott, R. S. Muller, R. T. Howe, and J. A. Yasaitis, "Electrostatic charge and field sensors based on micromechanical resonators," *Journal of Microelectromechanical Systems*, vol. 12, pp. 577, 2003.

[70] H. C. Nathanson, W.E. Newell, R.A. Wickstrom, and J.R. Davis Jr., "The Resonant Gate Transistor," *IEEE Transactions on Electron Devices*, vol. ED-14, pp. 117-133, 1967.

[71] G. Piazza, R. Abdolvand, G.K. Ho, and F. Ayazi, "Voltage-tunable piezoelectrically-transduced single-crystal silicon micromechanical resonators," *Sensors and Actuators A: Physical*, vol. 111, pp. 71-78, 2004.

[72] J. J. Yao, and N.C. Macdonald, "A micromachined, single-crystal silicon, tunable resonator," *Journal of Micromechanics and Microengineering*, vol. 6, pp. 257-264, 1996.

[73] S. G. Adams, F.M. Bertsch, K.A. Shaw, and N.C. MacDonald, "Independent Tuning of Linear and Nonlinear Stiffness Coefficients," *Journal of Microelectromechanical Systems*, vol. 7, pp. 172-180, 1998.

[74] S. G. Adams, F.M. Bertsch, K.A. Shaw, P.G. Hartwell, F.C. Moon, and N.C. MacDonald, "Capacitance based tunable resonators," *Journal of Micromechanics and Microengineering*, vol. 8, pp. 15-23, 1998.

[75] P. Schwab, T. Bowen, R. Perko, N. Delen, J. Goodrich, and R. Anderson, "A high throughput optoelectronic module assembly process," *2004 Proceedings. 54th Electronic Components and Technology Conference*, vol. Vol.2, pp. 1475, 2004.

[76] L. Haber, "Optoelectronic Bets on Low-cost," *Lightwave*, 1995.

[77] *International Technology Roadmap for Semiconductors (ITRS) Assembly and Packaging*, pp. 11, 2003.

[78] L. Boivin, "Thin film laser-to-fiber coupler," *Applied Optics*, vol. 13, pp. 391-395, 1974.

[79] S. A. Newton, K.P. Jackson, and H.J. Shaw, "Optical fiber V-groove transversal filter," *Applied Physics Letters*, vol. 43(2), 1983.

[80] S. Sriran, and R.L. Holman, "Packaging of components for optical fiber technology," *Electronic Packaging Materials Science Symposium*, 1987.

[81] C. A. Armiento, M. Tabasky, C. J. Jagannath, T. W. Fitzgerald, C. L. Shieh, V. Barry, M. Rothman, A. Negri, P. O. Haugsjaa, and H. F. Lockwood, "Passive coupling of InGaAsP/InP laser array and singlemode fibres using silicon waferboard," *Electronics Letters*, vol. 27, pp. 1109, 1991.

[82] M. Wale, and C. Edge, "Self Aligned Flip-chip assembly of photonic devices with electrical and optical connections," *IEEE Transactions on components, hybrids and manufacturing technology*, vol. 13, 1990.

[83] R. Wilson, and R. Boudreau, "Single-mode laser/fiber coupling yields using silicon V-groove passive alignment," *AMP J. Technology*, vol. 4, pp. 41-49, 1995.

[84] J. Sasaki, M. Itoh, T. Tamanuki, H. Hatakeyama, S. Kitamura, T. Shimoda, and T. Kato, "Multiple-chip precise self-aligned assembly for hybrid integrated optical modules using Au-Sn solder bumps," *IEEE Transactions on Advanced Packaging*, vol. 24, pp. 569, 2001.

[85] W. J. Shakespeare, R. A. Pearson, J. L. Grenestedt, P. Hutapea, and V. Gupta, "MEMS integrated submount alignment for optoelectronics," *Journal of Lightwave Technology*, vol. 23, pp. 504, 2005.

[86] R. R. A. Syms, H. Zou, J. Yao, D. Uttamchandani, and J. Stagg, "Scalable electrothermal MEMS actuator for optical fibre alignment," *Journal of Micromechanics and Microengineering*, vol. 14, pp. 1633, 2004.

[87] A. Unamuno, J. Yao, and D. Uttamchandani, "Alignment and fixing of fiber optics based on electrothermal MEMS actuators," *IEEE Photonics Technology Letters*, vol. 17, pp. 816, 2005.

[88] B. Li, H. Wirz, and A. Sharon, "Optimizing Fiber Coupling with a Quasi-Passive Microoptical Bench," *Journal of Microelectromechanical Systems*, vol. 14, pp. 1339-1346, 2005.

[89] S. Kaneko, M. Noda, K. Shibata, T. Aoyagi, H. Watanabe, T. Hatta, and K. Kasahara, "Novel fiber alignment method using a partially metal-coated fiber in a silicon V-groove," *IEEE Photonics Technology Letters*, vol. 12, pp. 645, 2000.

[90] T. Frank, "Development and manufacturing of a two-dimensional microactuator for moving of an optical fibre," *Proceedings of the SPIE - The International Society for Optical Engineering*, vol. 2882, pp. 226, 1996.

[91] T. Frank, "Two-axis Electrodynamic Micropositioning devices," *Journal of Micromechanics and Microenegineering*, vol. 8, pp. 114-118, 1998.

[92] Y. Kikuya, M. Hirano, K. Koyabu, and F. Ohira, "Alignment of optical axes by using electrostatic force," *Optics Letters*, vol. 18, pp. 864, 1993.

[93] Y. Kikuya, M. Hirano, K. Koyabu, and F. Ohira, "Micro alignment machine for optical coupling," *Proceedings of Micro Electro Mechanical Systems*, pp. 36, 1993.

[94] E. S. Hung and S. D. Senturia, "Extending the travel range of analog-tuned electrostatic actuators," *Journal of Microelectromechanical Systems*, vol. 8, pp. 497, 1999.

[95] J. M. Haake, R. L. Wood, and V. R. Dhuler, "In-package active fiber optic micro-aligner," *Proceedings of the SPIE - The International Society for Optical Engineering*, vol. 3276, pp. 207, 1998.

[96] V. R. Dhuler, R. L. Wood, J. M. Haake, and A. B. Cowen, "Microsystems for three axis active fiber alignment," *Technical Digest Solid-State Sensor and Actuator Workshop*, pp. 277, 1998.

[97] H. Guckel, "High-Aspect-Ratio Micromachining Via Deep X-ray Lithography," *Proc. Of the IEEE*, vol. 86, pp. 1586-1593, 1998.

[98] C. A. Mack, "Absorption and Exposure in Positive Photoresist," *Applied Optics*, vol. 27, 1988.

[99] *Robert Bosch GmbH, U.S. Patent 4,855,017*, 1996.

[100] H. Sun, T. Hill, M. Schmidt, and D. Boning, "Characterization and modeling of wafer and die level uniformity in Deep Reactive Ion Etching (DRIE)," vol. 782, pp. A.10.2.1-6, 2004.

[101] A. A. Ayon, R. A. Braff, R. Bayto, H. H. Sawin, and M. A. Schmidt, "Influence of coil power on the etching characteristics in a high density plasma etcher," *Journal of the Electrochemical Society*, vol. 146, pp. 2730, 1999.

[102] M. A. Blauw, I. a. P. B. T. a. N. th International Conference on Electron, T. Zijlstra, and E. van der Drift, "Balancing the etching and passivation in time-multiplexed deep dry etching of silicon," *Journal of Vacuum Science & Technology B (Microelectronics and Nanometer Structures)*, vol. 19, pp. 2930, 2001.

[103] M. A. Blauw, G. Craciun, W. G. Sloof, P. J. French, and E. van der Drift, "Advanced time-multiplexed plasma etching of high aspect ratio silicon structures," *Journal of Vacuum Science & Technology B (Microelectronics and Nanometer Structures)*, vol. 20, pp. 3106, 2002.

[104] H. Jansen, M. de Boer, R. Legtenberg, and M. Elwenspoek, "The black silicon method: a universal method for determining the parameter setting of a fluorine-based reactive ion etcher in deep silicon trench etching with profile control," *Journal of Micromechanics and Microengineering*, vol. 5, pp. 115, 1995.

[105] F. Laermer, N.-E. Micro- and Nano-Engineering. 28th International Conference on Micro- and, and A. Urban, "Challenges, developments and applications of silicon deep reactive ion etching," *Microelectronic Engineering*, vol. 67-68, pp. 349, 2003.

[106] I. W. Rangelow, "Critical tasks in high aspect ratio silicon dry etching for microelectromechanical systems," *Journal of Vacuum Science & Technology A (Vacuum, Surfaces, and Films)*, vol. 21, pp. 1550, 2003.

[107] P. Verdonck, A. Goodyear, R. D. Mansano, P. R. J. Barroy, and N. S. J. Braithwaite, "Importance of fluorine surface diffusion for plasma etching of silicon," *Journal of Vacuum Science & Technology B (Microelectronics and Nanometer Structures)*, vol. 20, pp. 791, 2002.

[108] A. H. Epstein, et al, "Power MEMS and microengines," *Proceedings of the IEEE International Conference on Solid-state Sensors and Actuators (Transducers '97)*, pp. 753-756, 1997.

[109] L. G. Frechette, S.F. Nagle, R. Ghodssi, S.D. Umans, M.A. Schmidt, and J.H. Lang, "An electrostatic induction micromotor supported on gas-lubricated bearings," *Proceedings of the IEEE International Conference on Microelectromechanical Systems (MEMS 2001)*, pp. 290-293, 2001.

[110] R. Ghodssi, C.M. Waits, B. Morgan, and M.J. Kastantin, "Gray-scale technology for power MEMS silicon devices," *Proceedings of the Collaborative Technology Alliance (CTA) Annual Symposium P&E Technical Session, Inn and Conference Center, University of Maryland*, pp. 55-59, 2003.

[111] B. Sirakov, Yifang Gong, Alan Epstein, and Choon Tan, "Design and Characterization of Micro-compressor Impellers," *Proceedings of ASME Turbo Expo 2004 Power for Land, Sea, and Air (GT2004-53332)*, 2004.

[112] Y. Gong, Borislav Sirakov, Alan Epstein, and Choon Tan, "Aerothermodynamics of Micro-turbomachinery," *Proceedings of ASME Turbo Expo 2004 Power for Land, Sea, and Air (GT2004-53877)*, 2004.

[113] B. Sirakov, "Characterization and Design of Non-Adiabatic Micro-compressor Impeller and Preliminary Design of Self-Sustained Micro Engine System," *PhD Thesis, Massachusetts Institute of Technology*, 2005.

[114] R. Ghodssi, C.M. Waits, and B. Morgan, "Development and Optimization of Integrative MEMS-based Gray-scale Technology in Silicon for Power MEMS Applications," *Proceedings of the Collaborative Technology Alliance (CTA) Annual Symposium P&E Technical Session, Inn and Conference Center, University of Maryland*, 2004.

[115] G. Skinner, "Diffractive/refractive optics for high energy astronomy I: Gamma-ray phase Fresnel lenses," *Astronomy and Astrophysics*, vol. 375, pp. 691-700, 2001.

[116] G. Skinner, "Diffractive/refractive optics for high energy astronomy II: Variations on the theme," *Astronomy and Astrophysics*, vol. 383, pp. 352-9, 2002.

[117] G. Skinner, P. von Ballmoos, H. Halloin, N. Gehrels, and J. Krizmanic, "Diffraction-limited gamma-ray imaging with Fresnel lenses," *Proceedings of SPIE X-ray and Gamma-ray Telescopes and Instruments for Astronomy (J.E. Truemper and H.D. Tananbaum, eds.)*, vol. 4851, pp. 4851-163, 2002.

[118] *NASA GSFC Integrated Mission Design Center (IMDC) study, (unpublished)*, 2002.

[119] E. Hecht, and A. Zajac, *OPTICS, Addison-Wesley*, pp. 375, 1974.

[120] M. Kuittinen, H.P. Herzig, and P. Ehbets, "Improvements in diffraction efficiency of gratings and microlenses with continuous relief structures," *Optics Communications*, vol. 120, pp. 230-234, 1995.

[121] J. R. Leger, M.L. Scott, P. Bundman, and M.P. Griswold, "Astigmatic Wavefront Correction of Gain-Guided Laser Diode Array using Anamorphic Diffractive Microlenses," *Proc. SPIE*, vol. 884, pp. 82, 1988.

[122] B. Hadimioglu, E.G. Rawson, R. Lujan, M. Lim, J.C. Zesh, B.T. Kuri-Yakub, and C.F. Quate, "High-efficiency Fresnel Acoustic Lenses," *1993 Ultrasonics Symposium*, pp. 579-82, 1993.

[123] B. H. Kleemann, and R. Guther, "Zonal diffraction efficiencies and imaging of micro-Fresnel lenses," *Journal of Modern Optics*, vol. 45, pp. 1405-1420, 1998.

[124] J. Krizmanic, R. Streitmatter, N. Gehrels, K. Gendreau, Z. Arzoumanian, R. Ghodssi, B. Morgan, and G. Skinner, "Development of Ground-testable Phase Fresnel Lenses in Silicon," *Gamma Wave Workshop on Focusing Telescopes in Nuclear Astrophysics, Espace St. Jacques, Bonifacio, Corsica, September 12-15*, 2005.

[125] B. Morgan, R. Ghodssi, "Biasing Gray-scale Lithography for Integration with Deep Reactive Ion Etching (DRIE)," presented at 49th International Conference on Electron, Ion, and Photon Beam Technology & Nanofabrication, Grande Lakes, Florida, May 31 - June 3, 2005.

[126] B. Morgan, X. Hua, T. Iguchi, T. Tomioka, G. S. Oehrlein, and R. Ghodssi, "Substrate interconnect technologies for 3-D MEMS packaging," *Microelectronic Engineering*, vol. 81, pp. 106, 2005.

[127] B. Morgan, X. Hua, T. Tomioka, T. Iguchi, G. S. Oehrlein, and R. Ghodssi, "Compact packaging using MEMS-based 3D substrate interconnects," *Eurosensors 2005, Barcelona, Spain*, 2005.

[128] V. Sharma, A.B. Suriadi, F. Berauer, and L.S. Mittelstadt, "AlCu pattern generation on 3D structured wafer using multi level exposure method on electrodeposited polymer material," *Materials, Technology and Reliability for advanced Interconnects and Low-k Dielectrics Symposium*, 2003.

[129] M.-C. M. Lee, and M.C. Wu, "3D Silicon Transformation using Hydrogen Annealing," *Proceedings of the 2004 Solid-state Sensor, Actuator, and Microsystems Workshop, Hilton Head Island, South Carolina*, pp. 19-22, 2004.

[130] S. D. Senturia, *Microsystem Design, Kluwer Academic Publishers, p. 239*: CRC Press, 2001.

[131] J. D. Jackson, *Classical Electrodynamics: Third Edition, Wiley & Sons, Inc, p. 169*, 1999.

[132] M. J. Madou, *Fundamentals of Microfabrication, Second Edition, p. 548*: CRC Press, 2002.

[133] N. Sakar, C. Baur, E. Stach, Z. Jandric, R. Stallcup, M. Ellis, G. Skidmore, J. Liu, and G.K. Fedder, "Modular MEMS Experimental Platform for Transmission Electron Microscopy," *Proceedings of IEEE MEMS 2006, Istanbul, Turkey*, pp. 146-149, 2006.

[134] B. Morgan, and R. Ghodssi, "Design and Simulation of Comb-drive Actuators Incorporating Gray-scale Technology for Tailored Actuation Characteristics," *SPIE Microtechnologies for the New Millennium 2005, Seville, Spain, May 9-11*, 2005.

[135] M. Mita, Y. Mita, H. Toshiyoshi, and H. Fujita, "Multiple-height Microstructures Fabricated by ICP-RIE and Embedded Masking Layers," *T.IEE Japan*, vol. 120-E, pp. 493-495, 2000.

[136] Y. Jeong Woo, W. Y. Shih, and S. Wei-Heng, "Effect of length, width, and mode on the mass detection sensitivity of piezoelectric unimorph cantilevers," *Journal of Applied Physics*, vol. 91, pp. 1680, 2002.

[137] A. Witvrouw, B. Du Bois, P. De Moor, A. Verbist, C. A. Van Hoof, H. Bender, and C. Baert, "Comparison between wet HF etching and vapor HF etching for sacrificial oxide removal," *Proceedings of the SPIE*, vol. 4174, pp. 130.

[138] R. I. Pratt, G. C. Johnson, R. T. Howe, and J. C. Chang, "Micromechanical structures for thin film characterization," pp. 205, 1991.

[139] D. Galayko, A. Kaiser, B. Legrand, L. Buchaillot, D. Collard, and C. Combi, "Tunable passband T-filter with electrostatically-driven polysilicon micromechanical resonators," *Sensors and Actuators A (Physical)*, vol. 117, pp. 115, 2005.

[140] M. W. Pruessner, W. H. Chuang, K. Amarnath, S. Kanakaraju, and R. Ghodssi, "Micromechanical resonators with integrated optical waveguides for sensing applications," *2005 Conference on Lasers and Electro-Optics (CLEO) (IEEE Cat. No. 05TH8796)*, vol. Vol. 1, pp. 761.

[141] C. B. Williams and R. B. Yates, "Analysis of a micro-electric generator for microsystems," *8th International Conference on Solid-State Sensors and Actuators and Eurosensors IX. Digest of Technical Papers (IEEE Cat. No.95TH8173)*, vol. vol.1, pp. 369, 1995.

[142] S. Meninger, J. O. Mur-Miranda, R. Amirtharajah, A. Chandrakasan, and J. H. Lang, "Vibration-to-electric energy conversion," *IEEE Transactions on Very Large Scale Integration (VLSI) Systems*, vol. 9, pp. 64, 2001.

[143] S. Roundy, B.P. Otis, Y.-H. Chee, J.M. Rabaey, P.K. Wright, "A 1.9GHz RF Transmit Beacon using Environmentally Scavenged Energy," *ISPLED 2003, Seoul, Korea*, 2003.

[144] S. Roundy, P.K. Wright, J.M. Rabaey, *Energy Scavenging for Wireless Sensor Networks with Special Focus on Vibrations*: Kluwer Academic Publishers, 2004.

[145] H. C. Nathanson, W. Newell, R.A. Wickstrom, and J.R. Davis, Jr., "The Resonant Gate Transistor," *IEEE Transactions on Electron Devices*, vol. ED-14, no. 3, pp. 117-133, 1967.

[146] J. J. Yao and N. C. MacDonald, "A micromachined, single-crystal silicon, tunable resonator," *Journal of Micromechanics and Microengineering*, vol. 5, pp. 257, 1995.

[147] M. Pruessner, T. T. King, D. P. Kelly, R. Grover, L.C. Calhoun, and R. Ghodssi, "Mechanical property measurement of InP-based MEMS for optical communications," *Sensors and Actuators A: Physical*, vol. 105, pp. 190-200, 2003.

[148] S. D. Senturia, "Microsystems Design," *Kluwar Academic Publishers*, pp. 252, 2000.

[149] C. A. Armiento, A. J. Negri, M. J. Tabasky, R. A. Boudreau, M. A. Rothman, T. W. Fitzgerald, and P. O. Haugsjaa, "Gigabit transmitter array modules on silicon waferboard," *IEEE Transactions on Components, Hybrids, and Manufacturing Technology*, vol. 15, pp. 1072, 1992.

[150] W. Imler, K.D. Scholz, M. Cobarruviaz, V.K. Nagesh, C.C. Chao, and R. Haitz, "Precision flip-chip solder bump interconnects for optical packaging," *IEEE Transactions on Components Hybrids and Manufacturing Technology*, vol. 15, no. 6, pp. 977-982, 1992.

[151] T. Hayashi, "An innovative bonding technique for optical chips using solder bumps that eliminate chip positioning adjustments," *IEEE Transactions on Components Hybrids and Manufacturing Technology*, vol. 15, no. 2, pp. 225-230, 1992.

[152] J. Sutherland, G. George, S. van der Green, and J. P. Krusius, "Alignment tolerance measurements and optical coupling modeling for optoelectronic array interface assemblies," *1996 Proceedings. 46th Electronic Components and Technology Conference (Cat. No.96CH35931)*, pp. 480, 1996.

[153] J. Sutherland, G. George, and J.P. Krusius, "Optical coupling and alignment tolerances in optoelectronic array interface assemblies," *Proceedings of the 45th Electrical Components and Technology Conference*, pp. 577-583, 1995.

[154] J. McGroarty, P. Borgesen, B. Yost, and C.-Y. Li, "Statistics of solder joint alignment for optoelectronic components," *IEEE Transactions on components, hybrids and manufacturing technology*, vol. 16, no. 5, pp. 527-529, 1993.

[155] S.-G. Kang, S. Min-Kyu, P. Seong-Su, L. Sang-Hwan, H. Nam, L. Hee-Tae, O. Kwang-Ryong, J. Gwan-Chong, and L. Donghan, "Fabrication of semiconductor optical switch module using laser welding technique," *IEEE Transactions on Advanced Packaging*, vol. 23, pp. 672, 2000.

[156] B. Morgan, and R. Ghodssi, "On-chip 2-Axis Optical Fiber Actuator using Gray-scale Technology," *Proceedings of IEEE MEMS 2006, Istanbul, Turkey*, pp. 266-269, 2006.

[157] B. Morgan, and R. Ghodssi, "Automated Optical Fiber Alignment in 2-Axes using 3-D Shaped Actuators," *To be presented at Hilton Head 2006: A Solid State Sensor, Actuator, and Microsystems Workshop*, June 4-8, 2006.

[158] W. B. Joyce and B. C. DeLoach, "Alignment of Gaussian beams," *Applied Optics*, vol. 23, pp. 4187, 1984.

[159] D. Marcuse, "Loss analysis of a single-mode fiber splice," *Bell Systems Technical Journal*, vol. 56, pp. 703-718, 1977.

[160] S. Nemoto and T. Makimoto, "Analysis of splice loss in single-mode fibres using a Gaussian field approximation," *Optical and Quantum Electronics*, vol. 11, pp. 447, 1979.

[161] Agrawal, *Fiber Optic Communication Systems, 3rd Edition*: Wiley Inter-Science, 2002.

[162] J. V. Collins, I. F. Lealman, P. J. Fiddyment, A. R. Thurlow, C. W. Ford, D. C. Rogers, and C. A. Jones, "The packaging of large spot-size optoelectronic devices," *IEEE Transactions on Components, Packaging and Manufacturing Technology, Part B: Advanced Packaging*, vol. 20, pp. 403, 1997.

[163] C. Sy-Hann, L. Heh-Nan, and O. Pang-Ming, "Spring constant measurement of a bent near-field optical fiber probe," *Review of Scientific Instruments*, vol. 71, pp. 3788, 2000.

[164] "Newport MRSI-M5 Assembly Work Cell," *http://www.mrsigroup.com/mrsi-m5.pdf*.

[165] T. Horiuchi, J. Ono, S. Onuki, M. Ashida, Y. Kanaya, T. Arie, T. Sato, and K. Tsukamoto, "1.48-µm high power laser-diode module," *Anritsu Technical Bulletin*, pp. 48-54, 1993.

[166] D. P. Kelly, M. W. Pruessner, K. Amarnath, M. Datta, S. Kanakaraju, L. C. Calhoun, and R. Ghodssi, "Monolithic suspended optical waveguides for InP MEMS," *Photonics Technology Letters, IEEE*, vol. 16, pp. 1298, 2004.

[167] J. McGee, N. Siwak, B. Morgan, and R. Ghodssi, "In-Plane Indium Phosphide Tunable Optical Filter Using Ridge Waveguides," *International Semiconductor Device Research Symposium 2005 (ISDRS 2005), Bethesda, MD, December 7-9*, 2005.

[168] B. Morgan, and R. Ghodssi, "Automated Optical Fiber Alignment in 2-Axes using 3-D Shaped Actuators," *To be presented at Hilton Head 2006: A Solid State Sensor, Actuator, and Microsystems Workshop, Hilton Head Island, SC, USA*, June 4-8, 2006.

[169] Y. A. Peter, H. P. Herzig, and S. Bottinelli, "XY-stage for alignment of optical elements in MOEMS," *Proceedings of the SPIE - The International Society for Optical Engineering*, vol. 3513, pp. 202, 1998.

[170] M. Mizukami, M. Hirano, and K. Shinjo, "Simultaneous alignment of multiple optical axes in a multistage optical system using Hamiltonian algorithm," *Optical Engineering*, vol. 40, pp. 448, 2001.

[171] D. T. Pham and M. Castellani, "Intelligent control of fibre optic components assembly," *Proceedings of the Institution of Mechanical Engineers, Part B (Journal of Engineering Manufacture)*, vol. 215, pp. 1177, 2001.

[172] M. Datta, H. Zhaoyang, and M. Dagenais, "A novel method for fabrication of a hybrid optoelectronic packaging platform utilizing passive-active alignment," *IEEE Photonics Technology Letters*, vol. 15, pp. 299, 2003.

[173] Y.-T. Tseng and Y.-C. Chang, "Active fiber-solder-ferrule alignment method for high-performance opto-electronic device packaging," *IEEE Transactions on Components and Packaging Technologies*, vol. 26, pp. 541, 2003.

[174] J. Guo and R. Heyler, "Fast active alignment in photonics device packaging," *2004 Proceedings. 54th Electronic Components and Technology Conference*, vol. Vol.1, pp. 813, 2004.

[175] R. Zhang and F. G. Shi, "A novel algorithm for fiber-optic alignment automation," *IEEE Transactions on Advanced Packaging*, vol. 27, pp. 173, 2004.

[176] R. Zhang, G. Jingyan, and F. G. Shi, "Fast fiber-laser alignment: beam spot-size method," *Journal of Lightwave Technology*, vol. 23, pp. 1083, 2005.

[177] N. Miki, C. J. Teo, L. C. Ho, and X. Zhang, "Enhancement of rotordynamic performance of high-speed micro-rotors for power MEMS applications by precision deep reactive ion etching," *Sensors and Actuators A (Physical)*, vol. A104, pp. 263, 2003.

[178] A. A. Ayon, W. Technical Digest. Solid-State Sensor and Actuator, X. Zhang, R. Khanna, and F. Transducers Res, "Anisotropic silicon trenches 300-500 mu m deep employing time multiplexed deep etching (TMDE)," *Sensors and Actuators A (Physical)*, vol. A91, pp. 381, 2001.

[179] T. Hill, H. Sun, H.K. Taylor, M.A. Schmidt, and D.S. Boning, "Pattern Density Based Prediction for Deep Reactive Ion Etch (DRIE)," *Proceedings of the Solid-state Sensor, Actuator and Microsystems Workshop, Hilton Head Island, South Carolina, June 6-10, 2004.*, pp. 320-323, 2004.

[180] Y. Chen, A. Kahng, G. Robins, and A. Zelikovsky, "Area Fill Synthesis for Uniform Layout Density," *IEEE Transactions on CAD*, vol. 21, pp. 1132-1147, 2002.

[181] J. B. Bates, N.J. Dudney, B. Neudecker, A. Ueda, and C.C. Evans, "Thin film lithium and lithium ion batteries," *Solid State Ionics*, vol. 135, pp. 33-45, 2000.

[182] H. Amjadi, "Charge Storage in Double Layers of Thermally Grown Silicon Dioxide and APCVD Silicon Nitride," *IEEE Transactions on Dielectrics and Electrical Insulation*, vol. 6, pp. 852-857, 1999.

[183] "Multilayer ceramic butterfly type packages," *http://global.kyocera.com/prdct/semicon/oe_pkg/btf_pkg.html*, (Accessed: July 3, 2006).

[184] Z. W. Zhong, S. C. Lim, and A. Asundi, "Effects of thermally induced optical fiber shifts in V-groove arrays for optical MEMS," *Microelectronics Journal*, vol. 36, pp. 109, 2005.

[185] H. N. Kwon, H. Il-Han, and L. Jong-Hyun, "A pulse-operating electrostatic microactuator for bi-stable latching," *Journal of Micromechanics and Microengineering*, vol. 15, pp. 1511, 2005.

PERSONAL PUBLICATION RECORD

Manuscripts in Progress

1. J. Krizmanic, B. Morgan, R. Streitmatter, N. Gehrels, K. Gendreau, Z. Arzoumanian, R. Ghodssi, and G. Skinner, "X-ray Phase Fresnel Lenses in Silicon," *To be submitted to NATURE*, September 2006.

Journal Publications

2. B. Morgan and R. Ghodssi, "On-Chip Active Optical Fiber Alignment System using Gray-scale Technology," *To be published in NASA Tech Briefs, September 2006*.

3. B. Morgan and R. Ghodssi, "On-Chip 2-Axis Optical Fiber Alignment using Gray-scale Technology," *Journal of Microelectromechanical Systems, In Press*.

4. J. Krizmanic, B. Morgan, R. Streitmatter, N. Gehrels, K. Gendreau, Z. Arzoumanian, R. Ghodssi, and G. Skinner, "Development of Ground-testable Phase Fresnel Lenses in Silicon," *Submitted to Experimental Astronomy*, November 2005.

5. B. Morgan, X. Hua, T. Tomioka, T. Iguchi, G. S. Oehrlein, and R. Ghodssi, "Substrate Interconnect Technologies for 3-D MEMS Packaging," *Microelectronic Engineering*, Vol. 81, p. 106-116, 2005.

6. B. Morgan, C.M. Waits, and R. Ghodssi, "Compensated Aspect Ratio Dependent Etching (CARDE) using Gray-scale Technology," *Microelectronic Engineering*, Vol. 77, Issue 1, p. 85-94, January 2005.

7. C.M. Waits, B. Morgan, M. Kastantin, and R. Ghodssi, "Microfabrication of 3D Silicon MEMS Structures using Gray-scale Lithography and Deep Reactive Ion Etching," *Sensors and Actuators A: Physical*, Vol. 119, p. 245-253, 2005.

8. B. Morgan, C.M. Waits, J. Krizmanic, and R. Ghodssi, "Development of a Deep Silicon Phase Fresnel Lens using Gray-scale Technology and Deep Reactive Ion Etching," *Journal of Microelectromechanical Systems*, Vol 13, pp. 113-120, Feb. 2004.

Conference Papers and Presentations

9. B. Morgan and R. Ghodssi, "Compact Tunable Resonators using Vertically-shaped Comb-fingers Towards Vibration Energy Scavenging," *Submitted to PowerMEMS 2006,* Berkeley, California, November 29 – December 1, 2006.

10. Lance Mosher, B. Morgan, and R. Ghodssi, "Advanced techniques in 3-D lithography for MEMS," *To be presented at the 25th Army Science Conference*, Orlando, Florida, November 27-30, 2006.

11. B. Morgan and R. Ghodssi, "Automated Optical Fiber Alignment in 2-Axes using 3-D Shaped Actuators," *Hilton Head 2006: A Solid-state Sensor, Actuator, and Microsystems Workshop,* Hilton Head Island, South Carolina, June 4-8, 2006.

12. B. Morgan and R. Ghodssi, "On-Chip 2-Axis Optical Fiber Actuator using Gray-scale Technology," *IEEE MEMS 2006*, Istanbul, Turkey, January 22-26, 2006.

13. J. Mcgee, N. Siwak, B. Morgan, and R. Ghodssi, "In-Plane Indium Phosphide Tunable Optical Filter using Ridge Waveguides," *International Semiconductor Device Research Symposium (ISDRS) 2005*, Bethesda, MD, December 7-9, 2005.

14. B. Morgan and R. Ghodssi, "On-Chip 2-Axis Optical Fiber Actuator using Gray-scale Technology," *International Semiconductor Device Research Symposium (ISDRS) 2005*, Bethesda, MD, December 7-9, 2005.

15. J. Krizmanic, R. Streitmatter, N. Gehrels, K. Gendreau, Z. Arzoumanian, R. Ghodssi, B. Morgan, and G. Skinner, "Development of Ground-testable Phase Fresnel Lenses in Silicon," *Gamma Wave Workshop on Focusing Telescopes in Nuclear Astrophysics*, Espace St. Jacques, Bonifacio, Corsica, September 12-15, 2005.

16. B. Morgan, X. Hua, T. Tomioka, T. Iguchi, G. S. Oehrlein, and R. Ghodssi, "Compact packaging using MEMS-based 3D substrate interconnects," *Eurosensors 2005*, Barcelona, Spain, September 11-14, 2005.

17. B. Morgan and R. Ghodssi, "Biasing Gray-scale Lithography for Integration with Deep Reactive Ion Etching," *49th International Conference on Electron, Ion, and Photon Beam Technology & Nanofabrication*, Orlando, Florida, May 31-June 3, 2005.

18. R. Ghodssi, B. Morgan, and C.M. Waits, "Variable Height Precision DRIE Technology," *Power and Energy Collaborative Technology Alliance (CTA) Four-year Review,* Hyatt Regency, Crystal City, Arlington, VA, June 1-3, 2005.

19. B. Morgan and R. Ghodssi, "Design and Simulation of Comb-drive Actuators Incorporating Gray-scale Technology for Tailored Actuation Characteristics," *Proceedings of SPIE – The International Society for Optical Engineering*, Vol. 5836, *Microtechnologies for the New Millenium 2005*, Sevilla, Spain, May 9-11, 2005.

20. B. Morgan, C.M. Waits, and R. Ghodssi, "MEMS-based Gray-scale Technology for Large Area 3-D Structures in Silicon," *IVC16, The 16th International Vacuum Conference*, Venice, Italy, June 28 – July2, 2004.

21. B. Morgan, C.M. Waits, and R. Ghodssi, "Development and Optimization of Integrative MEMS-based Gray-scale Technology in Silicon for Power MEMS Applications," *Proceedings of the Collaborative Technology Alliance (CTA),* Mariott Wardman Park Hotel, Washington D.C., May 6, 2004.

22. B. Morgan, C.M. Waits, J. Krizmanic, and R. Ghodssi, "Development of a Deep Phase Fresnel Lens in Silicon," *50th AVS International Symp.*, Baltimore, MD, Nov. 2-7, 2003.

23. R. Ghodssi, C. M. Waits, B. Morgan, and M. Kastantin, "Gray-Scale Technology for Power MEMS Silicon Devices," Invited paper, *2003 CTA, P & E Technical Session*, Inn and Conference Center, University of Maryland – College Park, April 29 – May 1, 2003.

Workshop, Symposium and Meeting Posters

24. B. Morgan, L. Mosher, and R. Ghodssi, "Dual-Axis Optical Fiber Alignment using Gray-scale Technology," *MEMS Alliance Workshop*, Student Poster Session, Johns Hopkins Applied Physics Lab, April 4, 2006.

25. B. Morgan, C. M. Waits, and R. Ghodssi, "Large Displacement Electrostatic MEMS Comb-drive Actuators using Gray-scale Technology," *MEMS Alliance Workshop*, Student Poster Session, Johns Hopkins Applied Physics Lab, April 19, 2005.

26. B. Morgan, C.M. Waits, and R. Ghodssi, "Development and Integration of a 3D Silicon MEMS Technology using Gray-scale Lithography and Deep Reactive Ion Etching," *2004 Solid-State Sensor, Actuator, and Microsystems Workshop*, Open Poster Session, Hilton Head Island, S.C., June 6-10, 2004.

27. C.M. Waits, B. Morgan, and R. Ghodssi, "3-D Silicon MEMS Fabrication using Gray-scale Lithography and Deep Reactive Ion Etching," *MEMS Alliance Symp. On MEMS in Homeland Security, Defense, and Aerospace App.*, Johns Hopkins Applied Physics Lab, March 29-30, 2004.

28. C. M. Waits, B. Morgan, M. Kastantin, and R. Ghodssi, "Development of a MEMS-based Gray-Scale Technology for 3-D Silicon Structures," *MEMS Alliance Workshop*, Student Poster Session, University of Maryland, April 11, 2003.

29. C. M. Waits, B. Morgan, M. Kastantin, and R. Ghodssi, "MEMS-based Gray-scale Technology," *MEMS Alliance Workshop*, Student Poster Session, Johns Hopkins Applied Physics Lab, Nov. 25, 2002.

30. B. Morgan, S. Brida, R. Mordkin, and M. Paranjape, "A Micro-Flow Sensor for Urodynamic Monitoring." *MEMS Alliance Workshop*, Student Poster Session, Johns Hopkins Applied Physics Lab, November 6, 2001. – ***Best Student Poster Award***

Oral Seminars

31. B. Morgan, "On-Chip Optical Fiber Alignment using Gray-scale Technology," *Institute for Systems Research Faculty/Student Colloquium*, University of Maryland, May 10, 2006.

32. B. Morgan, "Electrostatic MEMS Comb-drives using Gray-scale Technology," *Small Smart Systems Center Seminar Series*, University of Maryland, April 1, 2005.

33. B. Morgan, "Deep Silicon Phase Fresnel Lens using Gray-scale Technology," *Small Smart Systems Center Seminar Series*, University of Maryland, Nov. 14, 2003.

34. B. Morgan, "Variable Height Precision DRIE Technology," *MIT Microengine Weekly Seminar Series*, Massachusetts Institute of Technology, March 4, 2003.